Mesure de la résistance thermique de parois opaques de bâtiment par méthode active

Thanh-Tung Ha

Thanh-Tung Ha. Mesure de la résistance thermique de parois opaques de bâtiment par méthode active. Thermics [physics.class-ph]. Université Paris-Est, 2020. English. NNT : 2020PESC0062 . tel-03547571

HAL Id: tel-03547571
https://theses.hal.science/tel-03547571v1

Submitted on 28 Jan 2022

UPEC
Connaissance - Action
UNIVERSITÉ
PARIS-EST CRÉTEIL
VAL DE MARNE

PROJET FINANCÉ PAR L'ANR - PROJECT FUNDED BY THE ANR
ANR

Ecole doctorale No. 531 : Sciences, Ingénierie et Environnement

Thèse de doctorat

Spécialité / discipline de doctorat :

Thermique Energétique

Thanh Tung HA

Measurement of the thermal resistance of opaque building walls by active method

Thèse dirigée par Laurent IBOS

Soutenue le 10 décembre 2020

Devant le jury composé de :

Mme SIROUX Monica	Professeur, INSA Strasbourg	Rapporteur
M. GHIAUS Christian	Professeur, INSA Lyon	Rapporteur
Mme VOGT-WU Tingting	Maître de Conférences, Université de Bordeaux	Examinateur
M. DUMOULIN Jean	Chargé de Recherche, Université Gustave Eiffel	Examinateur
M. LE NILIOT Christophe	Professeur, Aix-Marseille Université	Examinateur
M. FEUILLET Vincent	Maître de Conférences, Université Paris-Est Créteil	Encadrant
M. IBOS Laurent	Professeur, Université Paris-Est Créteil	Directeur de Thèse

Acknowledgements

Il me sera très difficile à remercier tout le monde car c'est grâce à l'aide de nombreuses personnes que j'ai pu mener bien cette thèse à son terme.

D'abord, je voudrais remercier grandement mon directeur de thèse Laurent IBOS et mon encadrant Vincent FEUILLET, pour toute leur aide. Ils ont toujours été là pour me soutenir, me conseiller et me répondre toutes mes questions pendant trois ans de ma thèse.

Monica SIROUX et Christian GHIAUS m'ont fait l'honneur d'être rapporteurs de ma thèse. Ils ont pris le temps de m'écouter et de discuter avec moi pendant ma soutenance. Leurs remarques m'ont permis d'envisager mon travail sous un autre angle. Pour tout cela je les remercie.

Je remercie Tingting VOGT WU, Christophe LE NILIOT et Jean DUMOULIN pour avoir accepté de participer à mon jury de thèse et pour la richesse d'échange pendant ma soutenance.

Je tiens à remercier Yann GARCIA, Véronique LE SANT, Alain KOENEN, Laurent PEIFFER, Eric DIMNET et Julien WAEYTENS pour m'avoir aidé de réaliser les mesures expérimentales. Sans leurs aides, il aurait été difficile d'y arriver tout seul.

Je remercie spécialement Séverine DEMEYER et Alexandre ALLARD avec leurs conseils pour l'inférence bayésienne qui est le cœur de mes études. De plus, je souhaite remercier Julien WAEYTENS, Kamel ZIBOUCHE, Simon THEBAULT et Remi BOUCHIE pour leur travail de benchmark qui m'a aidé de perfectionner mon algorithme d'estimation.

Je remercie également Jean DUMOULIN et Mario MARCHETTI pour leurs conseils scientifiques pour le développement du prototype. Il m'est impossible d'oublier Mathieu KREMER et Jean-Pierre MONCHAU pour leur aide précieuse pour le design de mon prototype.

Enfin, je tiens à remercier tous les membres du laboratoire CERTES, qui m'ont accueilli et partagé trois ans de ma thèse.

Les derniers mots sont pour ma famille et ma "MêuMêu" qui m'ont supporté pendant des années de ma vie.

Résumé

La résistance thermique est l'un des paramètres physiques permettant d'évaluer le niveau d'isolation thermique d'une paroi de bâtiment. Sa valeur influe sur le confort thermique des occupants et sur les déperditions thermiques de la paroi. Par ailleurs, la connaissance de la résistance thermique est précieuse dans le cadre de travaux de rénovation nécessitant des informations détaillées sur la performance énergétique du bâtiment considéré. Les méthodes existantes d'évaluation de la résistance thermique reposent sur deux approches distinctes, passive ou active. La technique passive consiste à réaliser le suivi thermique du mur étudié dans des conditions naturelles sans aucune interaction. La résistance thermique de la paroi est alors déduite d'un simple calcul statistique. Cependant, la durée de mesure requise est importante (plus de trois jours). La technique active est basée sur l'analyse de la réponse en température du mur consécutive à une excitation thermique produite artificiellement. La mise en œuvre expérimentale et le calcul de la résistance thermique sont dans ce cas plus complexes. Une méthode de mesure in-situ permettant d'évaluer la résistance thermique de manière simple, rapide et systématique est aujourd'hui nécessaire.

Cette thèse s'inscrit dans le cadre du projet ANR RESBATI dont l'objectif est de développer un appareil de mesure in-situ basé sur une méthode active d'évaluation de la résistance thermique d'une paroi opaque. Celui-ci doit être simple d'utilisation et fournir un résultat avec une durée de mesure plus courte que les méthodes existantes.

Un modèle d'estimation de paramètres est développé dans ce travail de thèse. Les quadripôles thermiques et la méthode « Robust Adaptive Metropolis » sont utilisés respectivement comme modèle direct et algorithme de minimisation. L'approche bayésienne mise en œuvre permet l'évaluation des incertitudes sur les paramètres estimés.

Quatre prototypes s'appuyant sur des modes de chauffage différents (par lampes ou par résistance chauffante) en surface intérieure de la paroi ont été réalisés. Après comparaison des résultats de mesure, deux prototypes ont été sélectionnés. L'utilisation d'une plaque métallique en surface de la paroi assure l'homogénéité de l'excitation thermique imposée. Les différents capteurs thermiques étant intégrés à la plaque, la durée d'installation de l'appareil est courte.

Plusieurs parois (isolation par l'intérieur ITI, isolation par l'extérieur ITE, monomur MM et mur à ossature bois OSB) ont été caractérisés pour différentes conditions environnementales (constantes, variables et naturelles) dans des enceintes climatiques (LNE, CEREMA, IFSTTAR). Les résultats d'estimation montrent que les deux prototypes conduisent à une estimation satisfaisante de la résistance thermique des murs ITI et MM pour une durée mesure de 6 heures quelles que soient les conditions environnementales. En revanche, la présence de flux latéraux importants dans les murs à ossature bois ne permet pas d'obtenir une résistance thermique pour cette typologie de paroi. Dans le cas d'une paroi ITE, l'obtention d'une résistance correcte nécessite l'installation du dispositif de chauffage du côté extérieur de la paroi.

Les résultats de cette étude ont permis de lister plusieurs recommandations garantissant la qualité de la mesure. Tout d'abord, le prototype de mesure doit être installé du même côté que la couche isolante du mur étudié. Ensuite, les irrégularités telles que les ponts thermiques doivent être évitées. Une analyse qualitative préalable doit ainsi être effectuée pour positionner correctement le prototype de mesure. Enfin, la mesure ne doit pas être effectuée durant les périodes d'ensoleillement important en raison de la sensibilité du modèle d'estimation au rayonnement solaire. La réalisation de la mesure de nuit est à privilégier. Lors des tests en journée, une protection solaire sur la surface extérieure du mur peut néanmoins être utilisée.

***Mots-clés* –** résistance thermique, paroi opaque, méthode active, problème inverse, inférence bayésienne

Summary

Thermal resistance is one of the physical parameters used to assess the level of thermal insulation of a building wall. Its value influences the thermal comfort of the occupants and the heat losses through the wall. In addition, knowledge of the thermal resistance is useful in the context of refurbishment work requiring detailed information on the energy performance of the building considered. Existing methods for evaluating the thermal resistance rely on two distinct approaches: passive or active. The passive technique consists in performing a thermal monitoring of the studied wall under natural conditions without any interaction. The thermal resistance of the wall is then deduced from a simple statistical calculation. However, the required measurement time is long (more than three days). The active technique is based on the analysis of the temperature response of a wall following an artificial thermal excitation. The experimental implementation and the calculation of the thermal resistance are in this case more complex. A method of in-situ measurement allowing the evaluation of the thermal resistance in a simple, fast and systematic way is currently necessary.

This thesis is part of the ANR RESBATI project whose objective is to develop an in-situ measurement device based on an active method to evaluate the thermal resistance of an opaque wall. This device should be easy to use and lead to shorter measurement times than existing methods.

A parameter estimation model is developed in this thesis work. Thermal quadrupoles and the “Robust Adaptive Metropolis” method are used as direct model and minimization algorithm, respectively. The Bayesian approach implemented allows the evaluation of uncertainties on the estimated parameters.

Four prototypes using different heating modes (by lamps or by heating resistance) on the wall internal surface are investigated. After analysis of the homogeneity of the wall surface temperature and of the numerical estimation results, two prototypes using an aluminum plate are selected. The metal plate ensures the homogeneity of the thermal excitation imposed. In addition, the thermal sensors being integrated into the plate, the installation time is very fast.

Several walls (Internal Wall Insulation IWI, External Wall Insulation EWI, Single Wall SW and Wood Frame Wall WFW) are studied experimentally under different environmental conditions (constant, variable and natural) in climatic chambers (LNE, CEREMA, IFSTTAR).

Estimation results show that the two prototypes lead to a good estimation of the thermal resistance of the IWI and SW walls for a measurement duration of 6 hours for every tested condition. In contrast, only half of the thermal resistance of the WFW wall is detected due to a strong lateral heat diffusion in this wall. In the case of the EWI wall, a correct thermal resistance estimation requires the installation of the heating system on the wall external surface.

The results of this study made it possible to list several recommendations ensuring the quality of the measurement. First, the measurement prototype must be installed on the same side as the insulating layer of the studied wall. Then, irregularities such as thermal bridges must be avoided. A prior qualitative analysis must therefore be carried out to find the correct position of the measurement prototype. Finally, the measurement should not be performed during periods of strong sunshine because of the sensitivity of the estimation model to solar radiation. A measurement during the night should be preferred. During daytime testing, a sun protection on the wall external surface can still be used.

***Keywords* –** thermal resistance, opaque wall, active method, inverse problem, Bayesian inference

Introduction

In recent years, the concept of the low-carbon economy or low-fossil-fuel economy or decarbonized economy has become more and more popular at every conference related to climatic problems. This kind of strategy is proposed to reduce CO_2 emissions due to the high-speed development of technology in the world nowadays.

The BP® Energy Outlook in 2019 [1] shows that fossil sources (as coal, gas, and oil) remain the largest suppliers for energy demand until now and in the near future (Cf. Figure 0.1). Even though there are several options to reduce their contribution, such as renewable energy, fossil fuel can not be replaced in just a few years. To lower CO_2 emissions, a drastic reduction in energy consumption in all sectors is strongly recommended.

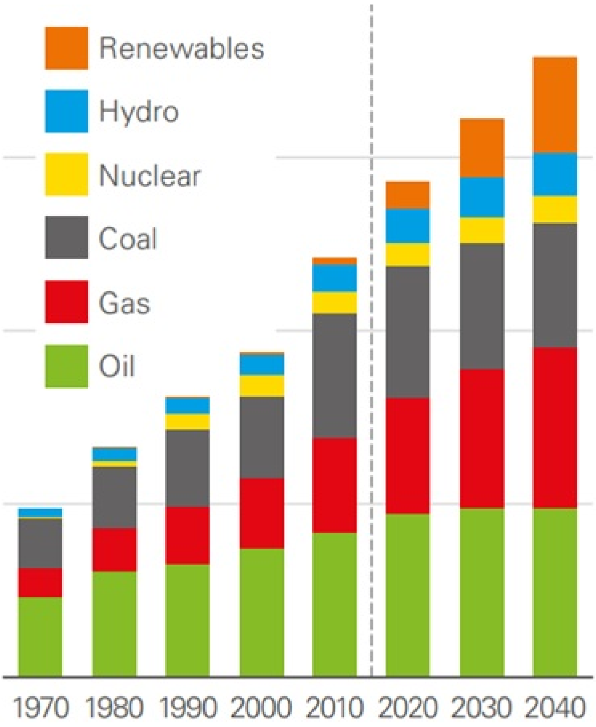

Figure 0.1: Distribution of different energy sources [1].

According to recent surveys about energy consumption (see Figure 0.2 for instance), the building sector, which is currently the second largest contributor to primary energy consumption, is seen as an interesting potential source of energy savings. This sector contributes nearly 25% of global CO_2 emissions. Statistics of the European Commission, as shown in Figure 0.3, announce that 64.1% of energy in the house is used for space heating, which may be reduced by insulation improvement [2].

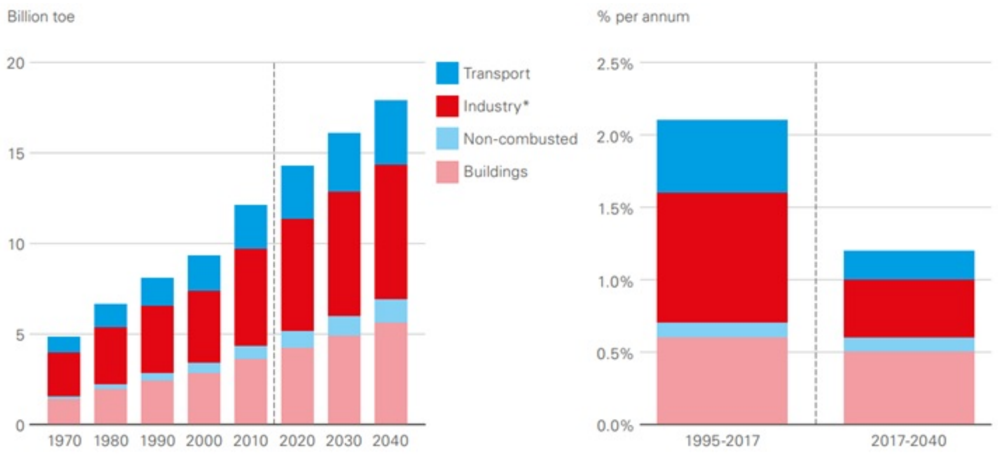

Figure 0.2: Primary energy consumption by end-use sector (left) and their annual demand growth (right) [1].

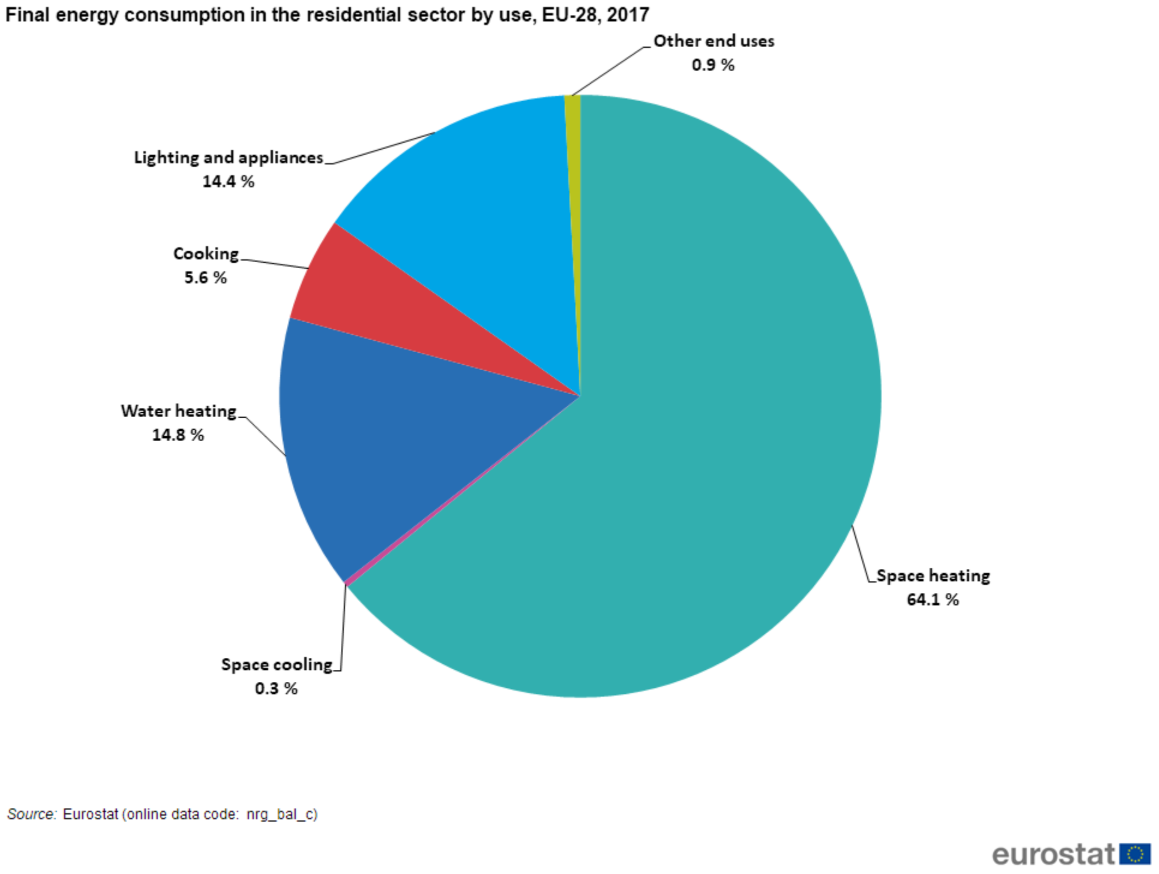

Figure 0.3: Statistics of energy consumption in residential house in 2017 in European Union [2].

In France, about two-thirds of the buildings (apartment blocks, private houses, etc.) were built before the first thermal regulation in 1975 and are generally uncomfortable because of a poor level of insulation. Renovation works have been undertaken to improve resident thermal comfort and achieve an overall energy saving objective. In 2012, the French thermal regulation

RT2012 [3] fixed a limit of primary energy consumption at 50 kWhep.m^{-2}.year^{-1} and entailed a requirement of thermal insulation for new or renovated buildings. The thermal insulation of a building envelope can be assessed by the thermal resistance value (or by the thermal transmittance value). The consumption objectives imposed by the RT 2012 result in a minimum resistance value of about 4 m^2.K.W^{-1} for an opaque building wall. In comparison, this value was 3 m^2.K.W^{-1} according to the consumption objectives of the RT 2005. It is also important to note that these requirements will continue to increase in the next regulation.

In fact, several points must be checked before knowing if a building satisfies the insulation requirement. In the case of a new building, we need to estimate the global heat transfer coefficient of the envelope, but an old building renovation requires more than that. We have to determine the part of the building that needs to be renovated and how much we have to improve the insulation level. All of these works need a robust *in-situ* measurement method for determining the insulation level, or thermal resistance value, of a given wall in a building, and not only the global U-value of the building.

Research works have been conducted to develop an efficient method for estimating an opaque building wall's thermal resistance, but the estimation capability of the existing methods is quite limited. To avoid unwilling error coming from measurement, they require some strict environmental conditions which are not always available on site. Moreover, for obtaining acceptable results, the measurement duration needed is quite long (from 3 days to 2 weeks). These methods are, therefore, difficult to apply to occupied buildings. The balance between accuracy, measurement duration, and robustness is a challenge for any researcher working on this subject.

In this context, a research project called RESBATI (*Mesure in situ de RESistance thermique de parois de BATIment* in French) and funded by the French National Research Agency (namely *ANR* in French) was launched in 2016. Several industrial and academic partners are involved in this project: CERTES, IFSTTAR (recently renamed Université Gustave Eiffel), CEREMA, CSTB, LNE, Themacs Ingénierie, and AFNOR. This project's main objective is to develop an *in-situ* measurement prototype to evaluate the thermal resistance of an opaque building wall (large surface without irregularities, such as thermal bridges or openings). Specifications of the prototype were defined at the beginning of the project:

- requiring short measurement duration (less than 24 h);

- being available at any time of the year whatever the weather conditions;

- being usable not only to assess opaque walls upon delivery of new buildings or to run diagnostics on existing buildings, but also for self-monitoring on construction sites (no need for any specific installation on the surface or inside of the wall);

- being easily transportable and easy to use by professionals.

Project planning is shown in Figure 0.4.

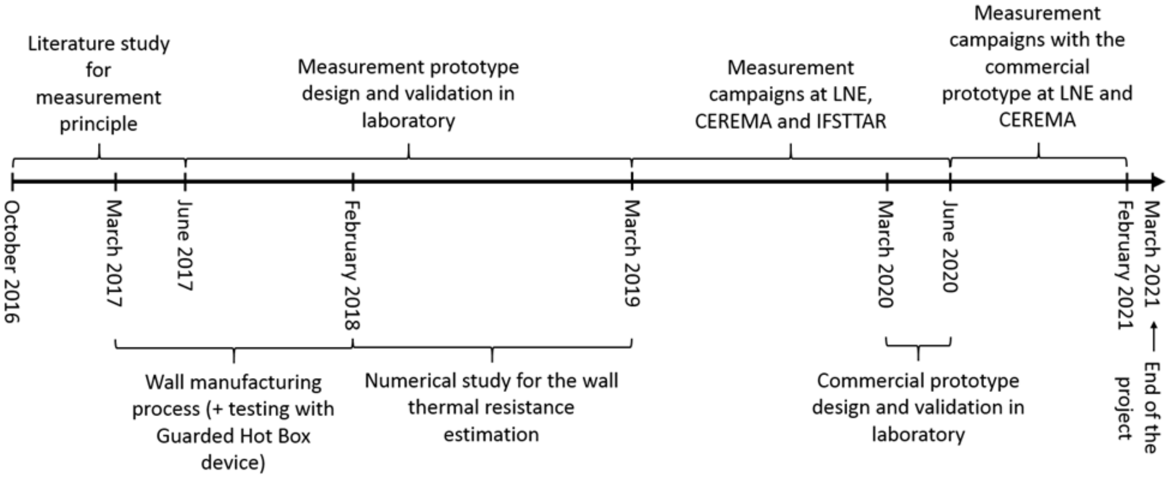

Figure 0.4: RESBATI project planning.

The present Ph.D. work is a part of the RESBATI project. It consists in participating in the numerical study for the wall thermal resistance estimation, the prototype development and validation, and the measurement campaigns with both laboratory and commercial prototypes. The thesis main objective is to develop a measurement prototype and validate it in laboratory and controlled climatic chambers. It will be the core of the commercial prototype developed at the end of the project.

This document contains six chapters.

The first chapter describes the literature research about existing measurement methods related to the evaluation of wall thermal resistance. There are two main methods: active and passive. The passive technique can calculate the wall thermal resistance by a simple equation but requires a long measurement duration. On the other hand, by using a dynamic heat transfer model more complex than the passive equation, the active method needs a shorter measurement duration. Based on these methods, several studies are reviewed to determine from which method this thesis work will be derived.

The second chapter presents the theory of the thermal quadrupole method (namely QUAD), which is used in this work to simulate heat transfers in building walls and to develop the direct model of the estimation process. Two models are presented: Excitation With Convection (namely EWC) and Absorbed Flux (namely AbF) models. They are based on the same heat transfer equation but use different boundary conditions. COMSOL Multiphysics® is used as a reference simulation generator to validate the thermal quadrupole simulation.

The third chapter details the definition of the inverse problem and several parameter estimation algorithms such as Gradient Descent, Metropolis-Hastings, etc.. A wall thermal resistance estimation is proposed using the Robust Adaptive Metropolis algorithm and the 1D QUAD model. Several numerical cases under different boundary conditions are studied to verify the estimation process ability to determine a wall thermal resistance.

The fourth chapter presents four measurement prototypes developed during the RESBATI project and based on an active method. Two types of thermal excitation sources are proposed: using lamps or a heating resistance. After verifying the homogeneity of the surface temperature and the pros and cons in the estimation, two prototypes are selected for use in laboratory measurement.

The fifth chapter details the measurement campaigns launched on real walls at LNE, CEREMA, and IFSTTAR, including the environmental conditions (constant, variable and natural), the tested walls (Internal Wall Insulation, External Wall Insulation, Wood Frame Wall and Single Wall), the climatic chambers, the heating power, etc.. Several measurements using standard methods are carried out to determine each tested wall thermal resistance, which will be used as reference values for the estimation.

The sixth chapter shows the measurement results of all tests presented in the previous chapter. The influence of the measurement configuration (external air temperature, heating power, position, etc.) on the wall thermal resistance estimation results is studied to define the prototype estimation limit. At the end of the chapter, several recommendations to be followed to obtain a correct estimation are listed.

Nomenclature

Greek symbols

T	Temperature [°C or K]
θ	Transformed temperature by Laplace transform [°C.s or K.s]
q	Heat flux density or heat flux [W.m^{-2}]
ϕ	Transformed heat flux by Laplace transform [W.s.m^{-2}]
R	Thermal resistance [m^{2}.K.W^{-1}]
U	Thermal transmittance [W.m^{-2}.K^{-1}]
C	Thermal capacitance [W.s.m^{-2}.K^{-1}]
λ	Thermal conductivity [W.m^{-1}.K^{-1}]
ρC_p	Volumetric heat capacity [J.m^{-3}.K^{-1})]
b	Thermal effusivity [W.s$^{1/2}$.K^{-1}.m^{-2}]
τ	Time constant [s]
a	Thermal diffusivity [m^{2}.s^{-1}]
x,y,z	Cartesian coordinates [m]
α,β	Eigenvalue of integral transform [m^{-1}]
t	Time [s]
p	Laplace variable [s^{-1}]
S	Surface [m^{2}]
h	Heat transfer coefficient [W.m^{-2}.K^{-1}]
ϵ	Emissivity []
σ	Stefan-Boltzmann constant (5.67$\times$10^{-8} kg.s^{-3}.K^{-4})
v	Wind speed [m.s^{-1}]
L	Luminance [cd.m^{-2}]

Subscripts and superscripts

rad	Radiation
$conv$	Convection
$surr$ or env	Surrounding environment
S	Surface
a	Air
I	Interior
E	Exterior
Ref	Reference
$\hat{X}$	Transformed X by integral transform

Acronyms

IR	Infrared
QUAD	Thermal quadrupoles computation
EWC	Excitation with convection
AbF	Absorbed flux
IWI	Internal Wall Insulation
EWI	External Wall Insulation
SW	Single Wall
WFW	Wood Frame Wall
MCMC	Markov Chain Monte Carlo method
CGD	Conjugated Gradient Descent method
LM	Levenberg-Marquardt method
TR	Trust-Region method
RWM	Random Walk Metropolis
RAM	Robust Adaptive Metropolis

Contents

1 Literature studies 1

1.1 Introduction 1

1.2 Passive methods for measuring wall thermal resistance 1

1.2.1 Definition 1

1.2.2 ISO 8990-1994 method 2

1.2.3 ISO 9869-1 method 3

1.2.4 Studies based on ISO 9869-1 standard 5

1.2.5 Studies using heat flux computation approaches 8

1.2.6 Passive studies using a physical model for thermal resistance estimation 16

1.3 Active methods for measuring wall thermal resistance 18

1.3.1 Definition 18

1.3.2 Studies based on the active approach for measuring wall thermal resistance 19

1.4 Comparison of methods for measuring wall thermal resistance 25

1.5 Conclusions 32

2 Theory of heat transfer modelling 35

2.1 Introduction 35

2.2 Simulation configuration and considered walls 35

2.3 Thermal quadrupole computation 40

2.3.1 Thermal quadrupoles in unidirectional (1D) model 41

2.3.2 Steady-state computation 45

2.3.3 Thermal quadrupoles in high dimensional model (3D) 46

2.3.4 Boundary conditions in thermal quadrupole method 48

2.4 Applied transforms in thermal quadrupole model 50

2.4.1 Laplace transform: continuous and discrete 50

2.4.2 Inverse Laplace transform 53

2.4.3 Integral transform 55

2.5 Model validation 57

2.5.1 Comparison of 1D EWC model with COMSOL simulation 58

2.5.2 Comparison of 3D EWC model with COMSOL simulation 62

2.5.3 Comparison of AbF model with EWC COMSOL simulation 66
2.6 Conclusions 70

3 Theory of parameter estimation 71
3.1 Introduction: definition of an inverse problem 71
3.2 Least-squares minimization methods 74
3.2.1 Gradient Descent method 74
3.2.2 Gauss-Newton method 75
3.2.3 Levenberg-Marquardt method 76
3.2.4 Trust-region method 77
3.3 Bayesian approach: Parameter and uncertainty estimation 78
3.4 Markov chain generation methods 81
3.4.1 Metropolis-Hastings method 81
3.4.2 Gibbs sampling method 83
3.4.3 Hamiltonian Monte Carlo method 84
3.4.4 Adaptive Metropolis method 86
3.5 Comparison of estimation methods: from simple to complex cases 88
3.6 Identification model in use 94
3.7 Estimation capability validation with 3D numerical data 98
3.7.1 Parameter sensitivity study 99
3.7.2 Prediction of estimation capability via numerical studies of heat flux . . 107
3.7.3 Estimation results of the cases under constant conditions by using 1D EWC model 111
3.7.4 Estimation results of the cases under variable conditions by using 1D EWC model 113
3.7.5 Estimation results of the cases under constant conditions by using 1D AbF model 116
3.7.6 Estimation results of the cases under variable conditions by using 1D AbF model 117
3.8 Conclusions 119

4 Measurement prototype development 123
4.1 Introduction of chapter 123
4.2 Difficulties of existing active method prototypes 123

4.3 Proposed measurement prototypes 128
4.3.1 Prototype 1: excitation with strong lamp 128
4.3.2 Prototype 2: excitation with a lamp box 131
4.3.3 Prototype 3: excitation with a lamp box and an aluminum plate 137
4.3.4 Prototype 4: excitation with a heating resistance and an aluminum plate 145
4.3.5 Comparison between four measurement prototypes 147
4.4 Conclusions 148

5 Measurement setup 149

5.1 Introduction of chapter 149
5.2 Presentation of the tested walls 149
5.3 Evaluation of the wall thermal resistances by the standard methods 153
5.3.1 Measurements with the Guarded Hot Box (ISO 8990) 154
5.3.2 Measurements with the ISO 9869-1 standard 155
5.4 Presentation of the climatic chambers 157
5.5 Testing conditions of the measurement campaigns with the third prototype . . . 159
5.5.1 Constant conditions 161
5.5.2 Variable conditions 163
5.5.3 Natural conditions 165
5.6 Testing conditions of the measurement campaigns with the fourth prototype . . 167
5.7 Conclusions 168

6 Measurement results 171

6.1 Measurement campaign no. 1: constant conditions 171
6.1.1 IWI results by using the third prototype 171
6.1.2 IWI results by using the fourth prototype 174
6.1.3 EWI results 175
6.1.4 SW results 179
6.1.5 WFW results 181
6.2 Measurement campaign no. 2: variable conditions 183
6.2.1 IWI results with the third prototype 184
6.2.2 IWI results with the fourth prototype 186
6.2.3 SW results 188

6.3 Measurement campaign no. 3: natural conditions 192
6.3.1 IWI results 192
6.3.2 SW results 195
6.4 Conclusions 196

7 Conclusions and perspectives 199

References 205

Appendix 213
A1 Calculation of quadrupole transfer matrix 214
A2 Table of Laplace transform functions for the thermal quadrupole computation . 216
A3 Noise measurement in laboratory 218
A4 Residuals of thermal resistance estimations of the measurement campaigns . . . 220

List of Figures

0.1 Distribution of different energy sources [1]. vii
0.2 Primary energy consumption by end-use sector (left) and their annual demand growth (right) [1]. viii
0.3 Statistics of energy consumption in residential house in 2017 in European Union [2]. viii
0.4 RESBATI project planning. x
1.1 ISO 8990 standard [8]: (left) Schematic view of the experimental set-up and (right) Guarded hot box equipment. 2
1.2 Schematic view of the experimental set-up of ISO 9869-1 standard. 4
1.3 Diagram representing the various thermal phenomena in [12]. 5
1.4 Measurement configuration in [14]. 9
1.5 Conduction heat flux transferred on the surface of the wall: (left) heat flux meter measurements and (right) thermography measurements [14]. 10
1.6 View of the experimental arrangement from inside the building in [19]. 11
1.7 2D U-value field obtained on the whole wall in [20]. 11
1.8 Variation of the U-value depending on the reflected temperature and the emissivity of the wall [21]. 12
1.9 Outline of first additional element in [25]. 13
1.10 Diagram of the experimental device used in [25]. 14
1.11 Diagrams of the experimental device used in the SEID method [27]. 15
1.12 *In situ* experimental test bench in [28]. 17
1.13 Measured and estimated interior-exterior temperature difference in [28]. 17
1.14 General diagram of experimental set-up in [33]. 19
1.15 The real view of (left) the heating box and of (right) the experimental setup on the front face of the wall in [33]. 20
1.16 Results obtained for the values of R and C optimised from active experiment in [33]. 21
1.17 Active thermography experimental device in [34]. 22
1.18 Results of thermal resistance estimation in [34]. 22
1.19 Basic diagram of the EPM method [35]. 23
1.20 Experimental device developed in [35]. 23
1.21 Evolution of measurement data during a QUB/e test with 8 hours of heating phase (red line) and 8 hours of cooling phase (blue line) in [38]. 25

1.22 Comparison between ISO 9869-1 and QUB/e methods in [38]. 25

1.23 (left) Visible and (right) infrared image of the observed wall [39]. 27

2.1 Global diagram for simulating heat transfer in a building wall on-site subject to an active excitation on the interior side of the building. 36

2.2 External air temperature and solar radiation in Trappes and Carpentras measured by Météo France. 37

2.3 The difference of 1D-3D data as a function of heating surface. 39

2.4 Schematic view of the indoor thermal excitation. 39

2.5 Homogeneous and isotropic wall considered in 1D computation. 42

2.6 Multi-layer wall. 45

2.7 Equivalent electrical circuit of a wall in steady-state regime. 46

2.8 Original data (blue line) and sub-series data (red line). 51

2.9 Comparison between original data (blue line) and the rebuilt data by using discontinuity correction term (DATA 1, red line) and not using (DATA 2, yellow line). 52

2.10 An example of two simulations using Stehfest's and de Hoog's algorithms and their computation time (in seconds). 55

2.11 Internal temperature horizontal profiles at the center of the wall surface after 24 hours of heating computed by 3D COMSOL for 3 different walls: IWI 1, EWI and SW. 58

2.12 Temperature profiles of internal and external surfaces of the IWI 1 wall with the external environmental condition of Trappes simulated by 1D QUAD and 1D COMSOL and their differences. 59

2.13 Absorbed heat flux profiles of internal and external surfaces of the IWI 1 wall with external environmental condition of Trappes simulated by 1D QUAD and 1D COMSOL and their differences. 59

2.14 Temperature and absorbed flux on the internal surface of the IWI 1 wall with external environmental condition of Trappes simulated by 1D QUAD and 1D COMSOL and their differences during first ten minutes of heating. 60

2.15 Temperature profiles of internal and external surfaces of the IWI 1 wall with the external environmental condition of Carpentras simulated by 1D QUAD and 1D COMSOL and their differences. 61

2.16 Absorbed heat flux profiles of internal and external surfaces of the IWI 1 wall with external environmental condition of Carpentras simulated by 1D QUAD and 1D COMSOL and their differences. 61

2.17 Temperature and absorbed flux on the internal surface of the IWI 1 wall with external environmental condition of Carpentras simulated by 1D QUAD and 1D COMSOL and their differences during first ten minutes of heating. 62

2.18 Two considered profiles in 3D comparison. 63

2.19 Internal temperature horizontal profiles of EWI wall computed by 3D QUAD and 3D COMSOL and their difference after 5 hours of heating with varied truncated orders. 63

2.20 Internal temperature diagonal profiles of EWI wall computed by 3D QUAD and 3D COMSOL and their difference after 5 hours of heating with varied truncated orders. 64

2.21 Temporal profiles of temperature at the center of the internal surface of EWI wall computed by 3D QUAD and 3D COMSOL and their difference with varied truncated orders. 64

2.22 External temperature horizontal profiles of EWI wall computed by 3D QUAD and 3D COMSOL and their difference after 5 hours of heating with varied truncated orders. 65

2.23 Comparison between the temporal internal surface temperature evolution computed by 1D AbF model in using different time steps for absorbed heat flux and 1D EWC model with the computation time corresponding. 66

2.24 Internal absorbed flux residuals computed by 1D and 3D EWC models with 5 considered walls. 67

2.25 Comparison of the computed temperature profile of the internal surface of IWI configurations by using 3D EWC model and 1D AbF using 3D flux. 68

2.26 Comparison of computed temperature profile of internal surface of EWI and SW configurations by using 3D EWC model and 1D AbF using 3D flux. 69

2.27 Internal absorbed flux horizontal profile for the EWI wall after 5 hours of heating computed by 3D QUAD model. 69

3.1 General representation of the direct and inverse problems. 71

3.2 General diagram of inverse problem process. 73

3.3 Histogram of parameter distribution generated by the Metropolis-Hastings method (blue line) and its fitted Gaussian form (red line). 82

3.4 Exponential example without noise: original (blue) and estimated (black) profiles by using the Conjugate Gradient Descent, Levenberg-Marquardt, and Robust Adaptive Metropolis methods. 91

3.5 Exponential example with noise: original (blue) and estimated (black) profiles by using the Conjugate Gradient Descent, Levenberg-Marquardt and Robust Adaptive Metropolis methods. 91

3.6 Periodic example without noise: original (blue) and estimated (black) profiles by using the Conjugated Gradient Descent, Levenberg-Marquardt, Trust-region and Robust Adaptive Metropolis methods. 92

3.7 Periodic example with noise: original (blue) and estimated (black) profiles by using the Conjugated Gradient Descent, Levenberg-Marquardt, Trust-region and Robust Adaptive Metropolis methods. 93

3.8 Thermal resistance estimation process used in this study. 97

3.9 Example of an estimation case: (blue line) measurement data, (red line) estimated data and (black line) estimated thermal resistance with corresponding uncertainty. 98

3.10 Reduced sensitivity coefficients of parameters computed with the EWC model for the IWI 1 wall. 100

3.11 Temporal evolution of estimated thermal resistance by varying the internal global heat transfer coefficient. 101

3.12 Reduced sensitivity coefficients computed with the 1D EWC model for the IWI 1 wall. 102

3.13 Correlation coefficients of reduced sensitivity coefficients computed with the 1D EWC model for the IWI 1 wall. 102

3.14 Reduced sensitivity coefficients computed with the 1D AbF model for the IWI 1 wall. 103

3.15 Correlation coefficients of reduced sensitivity coefficients computed with the 1D AbF model for the IWI 1 wall. 104

3.16 Reduced sensitivity coefficients computed with the 1D EWC model for the EWI wall. 105

3.17 Correlation coefficients of reduced sensitivity coefficients computed with the 1D EWC model for the EWI wall. 105

3.18 Reduced sensitivity coefficients computed with the 1D AbF model for the EWI wall. 106

3.19 Correlation coefficients of reduced sensitivity coefficients computed with the 1D AbF model for the EWI wall. 106

3.20 Reduced sensitivity coefficients computed with the 1D EWC model for the SW wall. 107

3.21 Correlation coefficients of reduced sensitivity coefficients computed with the 1D EWC model for the SW wall. 108

3.22 Reduced sensitivity coefficients computed with the 1D AbF model for the SW wall. 108

3.23 Correlation coefficients of reduced sensitivity coefficients computed with the 1D AbF model for the SW wall. 109

3.24 Longitudinal heat flux isolines in IWI wall after 24 hours of heating. 110

3.25 Longitudinal heat flux isolines in EWI wall after 24 hours of heating. 110

3.26 Longitudinal heat flux isolines in SW wall after 24 hours of heating. 111

3.27 Ratio between the theoretical and estimated thermal resistances for the five considered walls under constant conditions according to the heating duration by using the EWC model. 112

3.28 Ratio between the theoretical and estimated thermal resistances for the five considered walls under variable condition of Carpentras according to the heating duration by using the EWC model. 115

3.29 Ratio between the theoretical and estimated thermal resistances for the five considered walls under variable condition of Trappes according to the heating duration by using the EWC model. 116

3.30 Ratio between the theoretical and estimated thermal resistances for the five considered walls under constant condition according to the heating duration by using the AbF model. 118

3.31 Ratio between the theoretical and estimated thermal resistances for the five considered walls under variable condition of Carpentras according to the heating duration by using the AbF model. 119

3.32 Ratio between the theoretical and estimated thermal resistances for the five considered walls under variable condition of Trappes according to the heating duration by using the AbF model. 120

4.1 Light beam form of a lamp. 124

4.2 Distance from 150W Metal Halide light source versus light intensity (measured and calculated, PAR: Photosynthetically Active Radiation) [82]. 125

4.3 Heat flux distribution when using the contact heating element (left: without guarded insulation, right: with guarded insulation). 126

4.4 Measured heat flux on the wall surface by a heat flux meter fixed on the surface during an active measurement. 127

4.5 Schematic view of the first prototype. 129

4.6 Real view of the first prototype. 129

4.7 Thermal image of the tested surface with horizontal and vertical temperature profiles taken during the measurement with the first prototype. 130

4.8 Measurement on the IWI wall under constant condition (internal/external air temperature = 20°C/0°C) and its estimation result when using the first prototype. 131

4.9 Lamp distribution on the rear face of the lamp box and the two circuits proposed in [34]. 132

4.10 Schematic view of the second prototype. 132

4.11 Real view of the second prototype [84]. 133

4.12 (left) h-measurement element and (right) measured data used in h-computation. 134

4.13 Calculated internal convective heat transfer coefficient with the measured data in Figure 4.12. 134

4.14 (left) Radiative heat flux meter position during thermal excitation calibration and (right) measured radiative flux of two tested thermal excitation power levels. 135

4.15 Thermal image of the tested surface with horizontal and vertical temperature profiles taken during the measurement with the second prototype. 136

4.16 Measurement on the IWI wall under constant condition (internal/external air temperature = 20°C/0°C) and its estimation result when using the second prototype with the excitation heat flux of 272 W/m^2. 136

4.17 (left) Sensors distribution on the rear side of the aluminum plate and (right) its real view. 137

4.18 Schematic view of the third prototype. 138

4.19 (left) Rear face of the aluminum plate with the lamp box and (right) real view of the third prototype. 139

4.20 Horizontal and vertical profiles of wall surface temperature measured by thermocouples on the aluminum plate during measurement. 139

4.21 Measurement on the IWI wall under constant condition (internal/external air temperature = 20°C/0°C) and its estimation result when using the third prototype. 140

4.22 Validation test configuration with the third prototype in the laboratory. 141

4.23 Measurement data during the prototype validation with two different heating level (240 W and 120 W or 100% and 50% of heating power) and the insulation guard thickness of 50 mm. 141

4.24 Ratio between theoretical and estimated thermal resistances for the insulated panel under two levels of heating power and an insulation guard thickness of 50 mm. 142

4.25 Ratio between theoretical and estimated thermal resistances for the entire wall under two levels of heating power and an insulation guard thickness of 50 mm. 143

4.26 Measurement data during the prototype validation with two different insulation guard thickness (5 mm and 50 mm) and the heating power of 240 W. 143

4.27 Ratio between theoretical and estimated thermal resistances for the insulated panel using two different insulation guard thicknesses (5 mm and 50 mm) and the heating power of 240 W. 144

4.28 Real view of the front and rear faces of the fourth prototype. 145

4.29 (left) Schematic view of the fourth prototype and (right) its real view in the measurement site. 146

4.30 Measurement on the IWI wall under constant condition (internal/external air temperature = 20°C/0°C) and its estimation result when using the fourth prototype. 146

5.1 General layout of the tested IWI wall. 150

5.2 Tested IWI wall: (left) Real views of the building block layer and (right) of the complete wall. 150

5.3 General layout of the tested EWI wall. 150

5.4 Tested EWI wall: (left) Real view of building block layer and metal frame, (middle) of the wall without BA13 from interior view and (right) of the metal cladding of the complete wall. 151

5.5 General layout of the tested WFW wall. 151

5.6 Tested WFW wall: (left) Rear and (right) front views of the insulation layer of the wall. 152

5.7 Tested SW wall: (left) Interior and (right) exterior views of the wall. 152

5.8 Guarded Hot Box device at CSTB [87]. 154

5.9 Thermal sensors on the internal surface of the tested SW wall used to apply the Heat Flux Meter method. 156

5.10 (up) Passive measurement data obtained on the tested SW wall in Sense-City and (down) wall thermal resistances computed from four series of data. 157

5.11 General representation of the climatic chamber at LNE [88]. 158

5.12 (left) Interior and (right) exterior views of the climatic chamber at LNE. 158

5.13 General representation of the climatic chamber at CEREMA. 159

5.14 (left) Interior and (right) exterior views of the climatic chamber at CEREMA. . 159

5.15 Exterior view of studied wall when testing under natural condition at CEREMA. 160

5.16 Regulation systems used in the climatic chamber Sense-City. 160

5.17 Roof of investigated building when testing under natural condition (outside the climatic chamber Sense-City) at IFSTTAR. 161

5.18 Prototype setup on (left) the metal cladding and (right) the external surface of insulation layer of the EWI wall. 162

5.19 Measurement zones on the WFW wall (dash-dotted line) with the thermal bridges and (solid line) without. 162

5.20 Environmental temperatures measured by Météo France. 164

5.21 (upper) External air temperature (or T_{aE} for the tested walls) profiles and (lower) solar radiation generated by the climatic chamber during measurements with the third prototype under variable conditions. 166

5.22 Solar protection used for the IWI tests at CEREMA. 166

5.23 (Upper) External air temperature (or T_{aE} for the tested walls) and (lower) solar radiation measured during measurements with the third prototype under natural conditions. 167

5.24 (upper) External air temperature (or T_{aE} for the tested walls) profiles and (lower) internal air temperature variation generated by the climatic chamber during measurements with the fourth prototype under variable conditions. 169

6.1 Measurement data of the IWI tests 1 to 6 under constant environmental conditions. 172

6.2 Estimated thermal resistances normalized by the reference value for the IWI tests with the third prototype under constant environmental conditions. 173

6.3 Measurement data of the IWI tests 48 to 50 under constant environmental conditions. 175

6.4 Estimated thermal resistances normalized by the reference value for the IWI tests with the fourth prototype under constant environmental conditions. 176

6.5 Measurement data of the EWI tests 7 to 9 under constant environmental conditions. 177

6.6 Measurement data of the EWI tests 10 to 17 under constant environmental conditions. 178

6.7 Estimated thermal resistances for the EWI tests with the third prototype under constant environmental conditions. 179

6.8 Measurement data of the SW tests 18 to 21 under constant environmental conditions. 180

6.9 Estimated thermal resistances normalized by the reference value for the SW tests with the third prototype under constant environmental conditions. 181

6.10 Measurement data for the WFW tests 22 to 26 under constant environmental conditions. 183

6.11 Estimated thermal resistances normalized by the reference value for the WFW tests under constant environmental conditions. 184

6.12 Measurement data of the thermal sensors installed inside the WFW wall during test 24. 185

6.13 Measurement data for the IWI tests 27 to 36 with the third prototype under variable environmental conditions. 186

6.14 Estimated thermal resistances normalized by the reference value for the IWI tests with the third prototype under variable environmental conditions. 187

6.15 Measurement data for the IWI tests 51 to 59 with the fourth prototype under variable environmental conditions. 188

6.16 Estimated thermal resistances normalized by the reference value for the IWI tests with the fourth prototype under variable environmental conditions. 189

6.17 Estimated thermal resistance according to the heating time for IWI tests 56 to 59. 190

6.18 Measurement data for the SW tests 37 to 40 under variable environmental conditions. 191

6.19 Estimated thermal resistances normalized by the reference value for the SW tests with the third prototype under variable environmental conditions. 192

6.20 Estimated thermal resistance according to the heating time for SW tests 39 and 40. 193

6.21 Measurement data for the IWI tests under natural environmental conditions. . . 194

6.22 Estimated thermal resistances normalized by the reference value for the IWI tests with the third prototype under natural environmental conditions. 195

6.23 Measurement data for the SW tests under natural environmental conditions. . . 196

6.24 Estimated thermal resistance according to the heating time for SW tests 46 and 47. 197

A3.1 Sensors in use during noise measurement. 218

A3.2 Raw measurement signal (a) and filtered signal (b). 219

A4.1 Estimated thermal resistance and residuals between measured and estimated minimization parameter for the six tests on the IWI wall under constant conditions with the third prototype. 221

A4.2 Estimated thermal resistance and residuals between measured and estimated minimization parameter for the eleven tests on the EWI wall under constant conditions with the third prototype. 223

A4.3 Estimated thermal resistance and residuals between measured and estimated minimization parameter for the four tests on the SW wall under constant conditions with the third prototype. 223

A4.4 Estimated thermal resistance and residuals between measured and estimated minimization parameter during for the five tests on the WFW wall under constant conditions with the third prototype. 224

A4.5 Estimated thermal resistance and residuals between measured and estimated minimization parameter during for the ten tests on the IWI wall under variable conditions with the third prototype. 226

A4.6 Estimated thermal resistance and residuals between measured and estimated minimization parameter for the four tests on the SW wall under variable conditions with the third prototype. 226

A4.7 Estimated thermal resistance and residuals between measured and estimated minimization parameter during for the five tests on the IWI wall under natural conditions with the third prototype. 227

A4.8 Estimated thermal resistance and residuals between measured and estimated minimization parameter for the two tests on the SW wall under natural conditions with the third prototype. 228

A4.9 Estimated thermal resistance and residuals between measured and estimated minimization parameter for the three tests on the IWI wall under constant conditions with the fourth prototype. 228

A4.10 Estimated thermal resistance and residuals between measured and estimated minimization parameter for the nine tests on the IWI wall under variable conditions with the fourth prototype. 230

List of Tables

1.1 Nomenclature of parameters used in [12]. 6

1.2 Results obtained for the equivalent thermal resistance and thermal capacitance from passive and active measurements in [33]. 20

1.3 Results obtained during an *in situ* study of a building: ISO 9869-1 (14 days of measurement) and EPM (1.5 hour of measurement) [35]. 24

1.4 Summarised review of five methods on U-value assessment of building wall in [41]. 28

1.5 Wall thermal resistance values and uncertainties obtained by four methods used in [42]. 28

1.6 Comparative table of the advantages and disadvantages of the passive and active approaches for several comparison criteria [44]. 29

1.7 Results of the numerical cases studied in [46]. 32

2.1 Input and output parameters of numerical simulation. 38

2.2 Nature of layers of tested wall. 40

2.3 Physical characteristics of each layer of the five studied walls. 41

2.4 Inputs and outputs of EWC and AbF models. 50

3.1 Power prior distribution parameter [65]. 80

3.2 Input parameters and estimated results obtained by five different estimation methods in the cases of analytic examples without and with noise (colors for the relative error between estimated parameter and input value: out of 20%, 10-20%, 5-10%, <5%). 90

3.3 Estimated thermal resistance obtained by three different estimation algorithms (colors for the relative error between estimated and theoretical values: out of 20%, 10-20%, 5-10%, <5%). 94

3.4 Theoretical and estimated thermal resistances (in $m^2.K.W^{-1}$) with corresponding uncertainties obtained with the 1D EWC model for the five studied walls under constant conditions (colors for the relative resistance error between $R_{estimated}$ and R_{ref}: out of 20%, 10-20%, 5-10%, <5%). 112

3.5 Time constants of the insulation layer of three tested IWI walls 113

3.6 Theoretical and estimated thermal resistances (in $m^2.K.W^{-1}$) with corresponding uncertainties obtained with the 1D EWC model for the five studied walls under two variable conditions (colors for the relative resistance error between $R_{estimated}$ and R_{ref}: out of 20%, 10-20%, 5-10%, <5%). 114

3.7 Theoretical and estimated thermal resistances (in $m^2.K.W^{-1}$) with corresponding uncertainties obtained with the 1D AbF model for the five studied walls under constant condition (colors for the relative error between $R_{estimated}$ and R_{ref}: out of 20%, 10-20%, 5-10%, <5%). 117

3.8 Theoretical and estimated thermal resistances (in $m^2.K.W^{-1}$) with corresponding uncertainties obtained with the 1D AbF model for the five studied walls under two variable conditions (colors for the relative error between $R_{estimated}$ and R_{ref}: out of 20%, 10-20%, 5-10%, <5%). 118

4.1 Advantages and disadvantages of three different heating ways. 126

4.2 Comparison between four measurement prototype proposed in this study (1 = the worst, 4 = the best). 147

5.1 Thickness and thermal conductivity of each element of the four tested walls. . . 153

5.2 Theoretical thermal resistance of the four tested walls according to Table 5.1. . 153

5.3 Thermal resistances of the first three tested walls obtained with the Guarded Hot Box device at CSTB under three different operating temperatures. 155

5.4 Measurement configurations for the four tested walls (IWI, EWI, SW and WFW) with the third prototype under constant conditions. 163

5.5 Measurement configurations for the two tested walls (IWI and SW) with the third prototype under variable conditions. 165

5.6 Measurement configurations for the two tested walls (IWI and SW) with the third prototype under natural conditions. 167

5.7 Measurement configurations for the four tested walls (IWI, EWI, SW and WFW) with the fourth prototype under constant and variable conditions. 168

6.1 Estimated thermal resistances and corresponding uncertainties (in $m^2 \cdot K/W$) for the IWI tests with the third prototype under constant environmental conditions (colors for the relative errors between $R_{estimated}$ and R_{ref}: out of 20%, 10-20%, 5-10%, <5%). 172

6.2 Estimated thermal resistances and corresponding uncertainties (in $m^2 \cdot K/W$) for the IWI tests with the fourth prototype under constant environmental conditions (colors for the relative errors between $R_{estimated}$ and R_{ref}: out of 20%, 10-20%, 5-10%, <5%). 175

6.3 Estimated thermal resistances and corresponding uncertainties (in $m^2 \cdot K/W$) for the EWI tests under constant environmental conditions. 177

6.4 Estimated thermal resistances and corresponding uncertainties (in $m^2 \cdot K/W$) for the SW tests under constant environmental conditions (colors for the relative errors between $R_{estimated}$ and R_{ref}: out of 20%, 10-20%, 5-10%, <5%). 182

6.5 Estimated thermal resistances and corresponding uncertainties (in $m^2 \cdot K/W$) for the WFW tests under constant environmental conditions. 182

6.6 Estimated thermal resistances and corresponding uncertainties (in $m^2 \cdot K/W$) for the IWI tests with the third prototype under variable environmental conditions (colors for the relative errors between $R_{estimated}$ and R_{ref}: out of 20%, 10-20%, 5-10%, <5%). 186

6.7 Estimated thermal resistances and corresponding uncertainties (in m^2·K/W) for the IWI tests with the fourth prototype under variable environmental conditions (colors for the relative errors between $R_{estimated}$ and R_{ref}: out of 20%, 10-20%, 5-10%, <5%). 189

6.8 Estimated thermal resistances and corresponding uncertainties (in m^2·K/W) for the SW tests with the third prototype under variable environmental conditions (colors for the relative errors between $R_{estimated}$ and R_{ref}: out of 20%, 10-20%, 5-10%, <5%). 191

6.9 Estimated thermal resistances and corresponding uncertainties (in m^2·K/W) for the IWI tests with the third prototype under natural environmental conditions (colors for the relative errors between $R_{estimated}$ and R_{ref}: out of 20%, 10-20%, 5-10%, <5%). 194

6.10 Estimated thermal resistances and corresponding uncertainties (in m^2·K/W) for the SW tests with the third prototype under natural environmental conditions. . 196

A2.1 Analytical Laplace transform functions, where $n = 1, 2, 3, \cdots$, $\Gamma(x)$, $u_c(t)$, and $\delta(t)$ are the Gamma, Heaviside, and Dirac delta functions, respectively [89]. . . 216

A2.2 Integral transforms in rectangular geometry [90]. 217

A3.1 Noise values of five thermal sensors obtained by measurement in the thermal oven.219

1 Literature studies

1.1 Introduction

This chapter focuses on the literature review of the existing studies on the wall's thermal resistance (or U-value) determination. The first section shows the definition and several studies of passive technique. Then, the second section concerns active technique with some advantages in comparison to the passive one. Various comparisons between these methods are shown in the third section. At the end of this chapter, a summary of both techniques, and the detailed objective of this study will be presented.

1.2 Passive methods for measuring wall thermal resistance

1.2.1 Definition

A passive method is a way of monitoring a thermal system without changing its thermal state (temperatures and heat fluxes) artificially. The thermal system which is mentioned here can be a building or a particular wall. With this method, the tested system reacts naturally with the environmental conditions during measurement. Then, its temperature variation is collected by using the thermal sensors (for instance, thermocouple or infrared (noted IR) camera) for further qualitative or quantitative studies.

Infrared thermography is now widely used as a passive approach for qualitative analysis of buildings. Using an infrared camera allows observing directly over large areas temperature differences related to the presence of irregularities. The detectable irregularities are thermal bridges [4], air leakage [5] or presence of mold [6]. However, its applications are quite limited because this method depends strongly on the environmental conditions.

As this Ph.D. work concerns the estimation of the wall thermal resistance, the quantitative analysis of a building wall which is based on passive technique is focused on in this section. By using thermal sensors (such as an IR camera or thermocouple), it is possible to obtain surface temperature but not the heat flux. However, these two quantities are necessary to determine thermal resistance, noted R-value, (or heat transfer coefficient, noted U-value) of the studied system. Two solutions are available to determine the heat flux. The first is direct and consists in measuring the heat flux by using a heat flux meter. The second is indirect and consists in computing the heat flux by using theoretical or empirical formulas (described in Section 1.2.5).

In many studies concerning the thermal resistance estimation in passive mode, two standards are commonly tested at first because of their precision, easy usage, and robustness: ISO 8990-1994 and ISO 9869-1-2014 (with extension ISO 9869-2). The first standard is intended for laboratory use (climatic chamber) and the second one for *in situ* measurement under specific environmental conditions. Both of them use a heat flux meter to measure the heat flux through the wall.

1.2.2 ISO 8990-1994 method

The complete name of the ISO 8990-1994 standard is "Thermal insulation - Determination of steady-state heat transfer properties - Calibrated and guarded hot box" [7]. This standard describes the experimental protocol (set-up structure, equipment, criteria, environmental conditions, etc.) to determine the heat transfer properties of a wall in the steady-state regime by using a calibrated and guarded hot box.

The guarded hot box contains two chambers (warm and cold chambers), as shown in Figure 1.1. The temperature in the warm chamber can vary between 10°C and 30°C. The cold chamber can be controlled from -10°C to 5°C [7, 8]. The analyzed wall is placed between these two chambers, and the whole system is guarded by insulation to maintain the system being adiabatic.

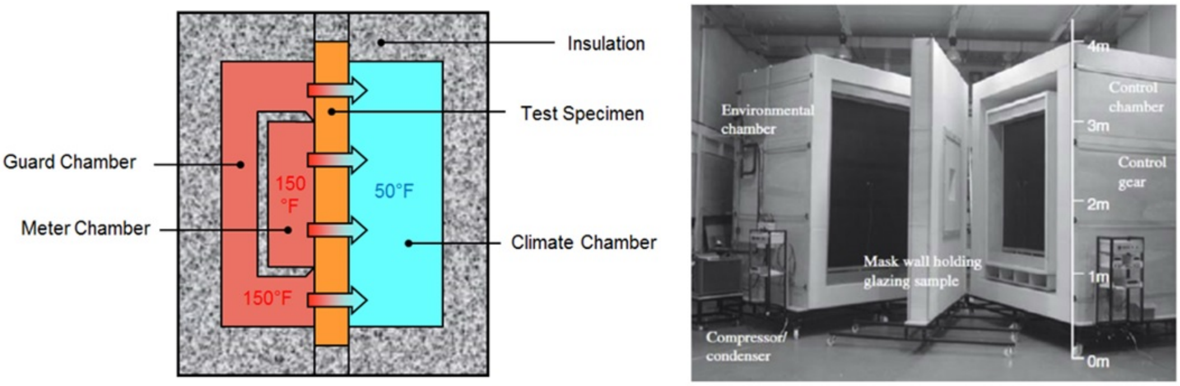

Figure 1.1: ISO 8990 standard [8]: (left) Schematic view of the experimental set-up and (right) Guarded hot box equipment.

At both sides of the tested wall, a heat flux meter and a thermocouple with a diameter less than 0.2 mm are used to measure the heat flux density (noted q) and the wall surface temperatures to deduce the temperature gradient between warm and cold sides (noted ΔT). Then, the heat transfer coefficient (or the thermal transmittance) of the tested wall, noted U, can be calculated as follows:

$$U = \frac{q}{\Delta T} = \frac{1}{R + R_{SI} + R_{SE}} \tag{1.1}$$

where:

R thermal resistance of the tested wall;

R_{SI} internal thermal surface resistance;

R_{SE} external thermal surface resistance.

Two thermal surface resistances R_{SI} and R_{SE} are determined by running equipment calibration. With this method, the measurement errors can be limited as much as possible. However, it is only available under laboratory conditions. The required test duration can vary between 24 hours and 72 hours, depending on the wall thermal inertia and the measurement precision required.

1.2.3 ISO 9869-1 method

The ISO 9869-1 standard entitled "Thermal insulation - Building elements - *in situ* measurement of thermal resistance and thermal transmittance - Part 1: Heat flow meter method" was proposed in 1967 and then revised and expanded in 2014 [9].

The temperatures and heat flux of both surfaces of the tested wall are measured by using two thermocouples and two heat flux meters, as in Figure 1.2. This method requires the temperature gradient of both sides and the heat flux going through the wall. The wall thermal resistance can be obtained by one of two equations below:

$$R = \frac{T_1 - T_2}{q_1} \tag{1.2}$$

or

$$R = \frac{T_2 - T_1}{q_2} \tag{1.3}$$

After several days of measurement, both equations return the same value because, in the steady-state regime, $q_1 = -q_2$. According to this standard, equation 1.2 is recommended because the heat flux measurement in the interior contains less noise than the one in the exterior, and the internal environment is controlled more easily than the external one. Since the measurement

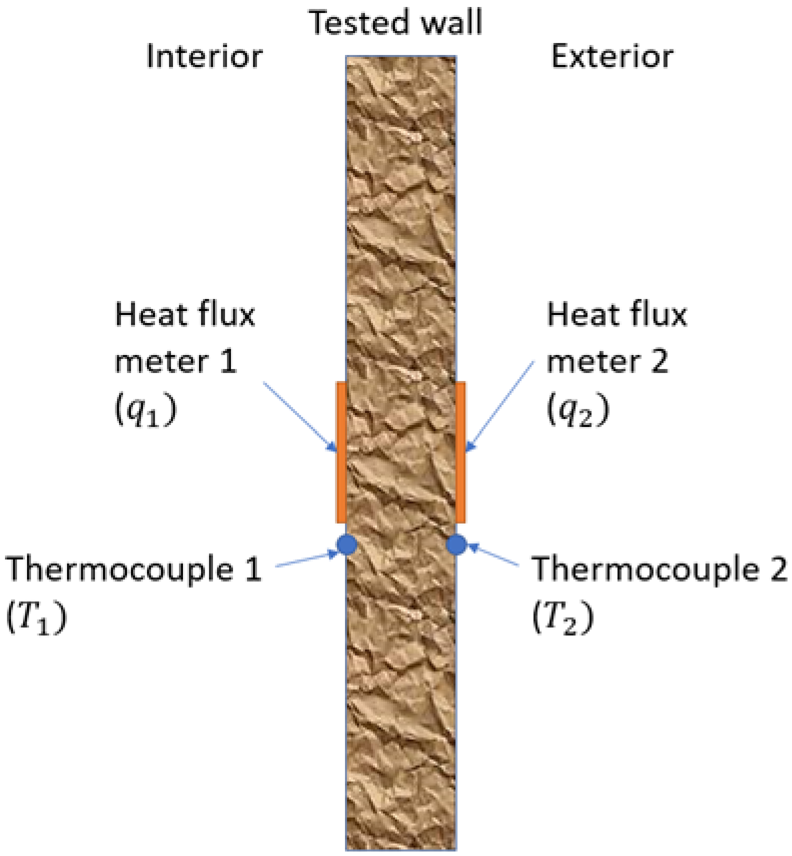

Figure 1.2: Schematic view of the experimental set-up of ISO 9869-1 standard.

noise may be high, an average formula is proposed in the standard:

$$R(t) = \frac{\sum_{i=0}^{i=t} T_1(i) - T_2(i)}{\sum_{i=0}^{i=t} q_1(i)} \tag{1.4}$$

However, this standard requires several specific conditions to be applicable *in situ*:

- the wall must be uniform (no thermal bridge, no junction) to make sure that the heat flux is one-dimensional;

- the wall must be north-facing because the sensors used cannot be in direct contact with solar radiation (it is possible to use a plastic film to protect them);

- the test duration depends on the climate conditions and on the nature of the walls (in general at least 72 hours).

Moreover, Desogus *et al.* [10] showed that the result obtained by this standard depends strongly on environmental conditions, particularly the temperature difference between indoor and outdoor. The authors concluded that a small temperature difference could lead to an imprecise result.

Because ISO 9869-1 standard is available for *in situ* measurement, it is used more widely than the first standard. Hence, some studies have been carried out to improve this standard in several ways (enhancing precision, using a model for environmental condition variations, etc.). The next section will detail these studies.

1.2.4 Studies based on ISO 9869-1 standard

Cesaratto *et al.* presented a series of *in situ* U-value measurements of the wall using ISO 9869-1 standard [11]. There were 29 different measurements on various walls during various periods. Several tests were launched on the same wall after and before renovation. Besides ISO 9869-1 standard, another method was used in this study: identification by a grey box model (LORD (LOgical R-Determinations) approach).

According to measurement results, the authors observed that the measured U-values were greater than theoretical ones. The grey box method was the most robust and less impacted by dynamic effects (variability of climate conditions, heavy inertia). The deviations of the U-value could reach nearly 20% for walls of the same design. The minimum test duration of 72 hours required by ISO 9869-1 standard was very restrictive, as climate conditions must be invariable during the steady-state regime. Therefore, to reduce the test duration of the standard. some research teams have proposed some improvements to this standard.

A long measurement time is required for ISO 9869-1 method because data must be averaged over a duration long enough to minimize climate variation influence. Therefore, a solution consists in applying a moving average that considers the wall's thermal inertia and thermophysical properties. Naveros *et al.* presented a proposition of a non-linear model to take these various phenomena into account [12]. The authors introduced all possible factors (see Table 1.1) to add to the modeling presented in Figure 1.3.

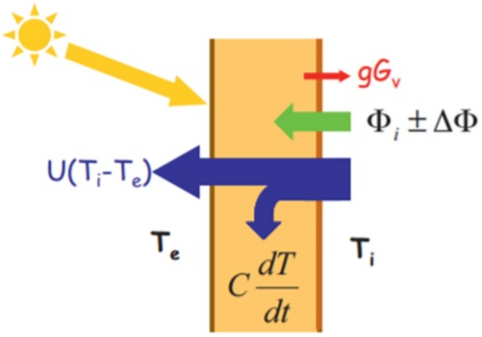

Figure 1.3: Diagram representing the various thermal phenomena in [12].

Type	Symbol	Description	Unit
Measurement quantity	G_v	Global solar radiation	W.m^{-2}
	T_i	Interior air temperature	K
	T_e	Exterior air temperature	K
	T_{si}	Temperature of interior surface	K
	T_{se}	Temperature of exterior surface	K
	ϕ	Heat flux density through the wall	W.m^{-2}
	W	Wind speed	m.s^{-1}
	G_{lw}	Long wave radiation	W.m^{-2}
Parameter	U	Heat transmission coefficient	W.m^{-2}.K^{-1}
	g	Solar energy transmittance	
	C	Effective heat capacity of wall	J.m^{-2}.K^{-1}
	σ	Stefan-Boltzmann constant	W.m^{-2}K^{-4}

Table 1.1: Nomenclature of parameters used in [12].

Depending on the complexity of the model, the expression of average heat flux density $\bar{\phi}$ as a function of U-value and the others factors could be written. Taking into account the energy balance between intervals $k-1$ and k (called integration time), the formula of $\bar{\phi}$ was expressed as follows (all measurement data in this expression are average values):

$$\bar{\phi} = U_0(\overline{T_i} - \overline{T_e}) - g\overline{G_v} + U_w\overline{W(T_i - T_e)} + a_4\overline{(\sigma T_{se}^4 - G_{lw})} + a_5(\overline{T_{si}(k)} - \overline{T_{si}(k-1)}) + b \quad (1.5)$$

where a_4, a_5 and b were constants for fitting data but their role in U-value determination was not important. Moreover, there were two terms of U-value which represent different factors, U_0 for the steady-state regime and U_wW for wind influence. By running parameter estimation to fit average heat flux, these two values were obtained and the global U-value of the investigated wall could be found as:

$$U = U_0 + U_wW \quad (1.6)$$

Authors launched a series of measurements from March 2009 to October 2010 to validate this method. A homogeneous opaque wall was made with integrated sensors according to the recommendations of ISO 9869-1 standard. Results suggested the following remarks:

- the minimum integration time to obtain acceptable results is five days;

- if only night-time period is analyzed, final results do not change;

- the variations of solar radiation and convection with the wind speed must be taken into account in the model used; otherwise, the results are not correct.

Another approach for taking into account these unstable fluxes by using storage effect was proposed by Bienvenido-Huertas *et al.* [13]. Two external and internal thermal mass factors of the kth layer of a wall were introduced as:

$$F_{out,k} = C_k\left(\frac{R_k}{R}\left(\frac{1}{6} + \frac{R_{in,k} + R_{out,k}}{3R}\right) + \frac{R_{in,k}R_{out,k}}{R^2}\right) \tag{1.7}$$

$$F_{in,k} = C_k\left(\frac{R_{out,k}}{R} + \frac{R_k^2}{3R^2} - \frac{R_{in,k}R_{out,k}}{R^2}\right) \tag{1.8}$$

where:

$R_{out,k}$	sum of thermal resistances from k+1th layer to external air;
$R_{in,k}$	sum of thermal resistances from k-1th layer to internal air;
C_k	thermal capacity of the kth layer per unit surface area;
R_k	thermal resistance of the kth layer;
R	total thermal resistance of the wall.

For a wall of N layers, the total heat flux q_{stor} which represented the energy storage during a duration of Δt could be expressed by:

$$q_{stor} = \frac{\delta T_{in}\sum_{k=1}^{N} F_{in,k} + \delta T_{out}\sum_{k=1}^{N} F_{out,k}}{\Delta t} \tag{1.9}$$

where δT_{in} (or δT_{out}) is the difference between the average internal (or external) air temperature for the 24 hours before measurement and for the 24 hours of the test. Then, the expression of U-value of equation 1.4 became:

$$U = \frac{\sum_{i=0}^{t} q(i) - q_{stor}}{\sum_{i=0}^{t} \Delta T(i)} \tag{1.10}$$

During this study, a good estimation of thickness, thermal conductivity, and thermal capacity of each layer of the wall was required to obtain the thermal mass factors. However, this estimation is quite difficult and expensive, so that the authors proposed to use artificial neural networks (ANNs) and the multilayer perceptron (MLP). These methods transfer each layer's thermal state information through the wall without calculating and making transformations in input variables. The authors concluded that the representation of storage effect helped reduce the deviation of measured U-value and the required test duration compared to existing methods (from more than three days to 2-3 days).

1.2.5 Studies using heat flux computation approaches

Instead of using a heat flux meter, some approaches were proposed to compute the heat flux across the wall from the temperature captured by an IR camera or a thermocouple. These approaches came from theoretical formulas of heat transfer fluxes: radiation flux q_{rad} and convection flux q_{conv}, which are computed from the wall surface temperature T_S, the surrounding environment temperature T_{surr} and several parameters of the environment. The radiation flux coming on the wall surface is obtained by applying the Stefan–Boltzmann law:

$$q_{rad} = \sigma\epsilon(T_{surr}^4 - T_S^4) \tag{1.11}$$

where ϵ is the emissivity of the wall surface and σ the Stefan–Boltzmann constant. Then, the convection flux can be obtained by the difference between wall surface temperature and air temperature T_a:

$$q_{conv} = h_{conv}(T_a - T_S) \tag{1.12}$$

where h_{conv} is the convective heat transfer coefficient.

The conduction flux transferred through the wall (q_{cond}) is computed by the conservation of heat flux, which can be expressed similarly as Kirchhoff's law in electricity: *The algebraic sum of currents in a network of conductors meeting at a point is zero.* It means that this conduction flux will be equal to the sum of the irradiation and convection fluxes:

$$q_{cond} = q_{rad} + q_{conv} \tag{1.13}$$

A thermocouple sensor can measure the air temperature, and the wall surface temperature can be obtained by an IR camera (or by a thermocouple). In this approach, the determination of h_{conv} is a challenge because this parameter is very sensitive to environmental conditions (humidity, geometry, air temperature, wind speed, etc.) and contributes a major part in the heat flux computation. Several additional measurements, theoretical hypotheses, and experimental correlations were proposed in order to estimate this coefficient.

Danielski *et al.* [14] used heat flux sensors to estimate h_{conv}. First, they did a separate measurement of the conduction heat flux by using heat flux sensors located close to the zone observed by IR thermography (left-hand side in Figure 1.4). Equation 1.11 provided the radiation flux, and the convection heat flux was calculated using equation 1.13. Then, the coefficient h_{conv} was estimated using the convection flux, the air and surface temperatures measured by thermocouple sensors in equation 1.12.

The obtained value of h_{conv} was used in the rest of the study, and the overall heat transfer coefficient U-value was computed as follows:

$$U = \frac{q_{cond}}{T_{SI} - T_{SE}} \tag{1.14}$$

where T_{SI} and T_{SE} were the temperatures of the internal and external wall surfaces.

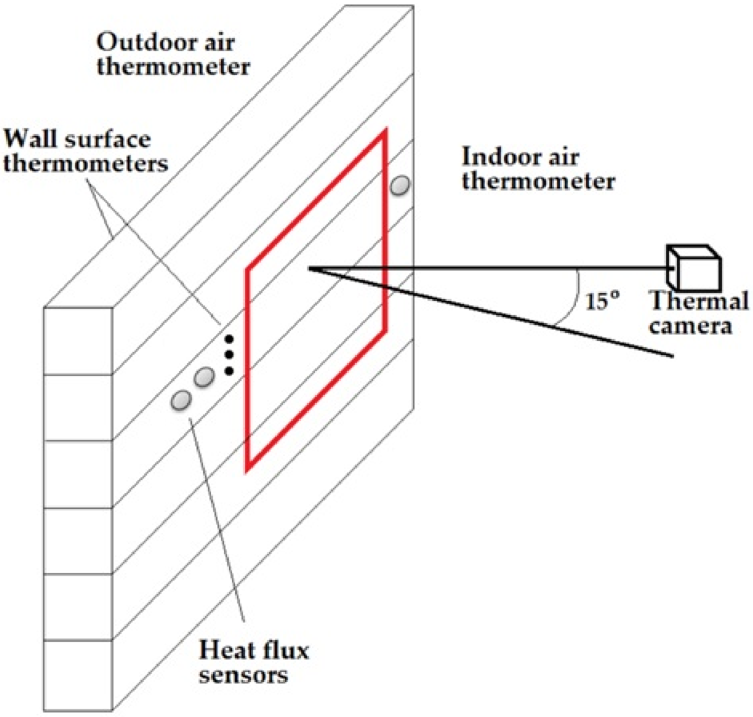

Figure 1.4: Measurement configuration in [14].

The second part of this paper presented a comparison between heat flux meter (HFM) measurement and IR thermography in U estimation by fitting the conduction heat flux (Cf. Figure 1.5). Sixty-five measurements were carried out during January and February in Sweden. The final results were found with small differences of 4% and 3%, respectively, for the conductivity and U-value, which suggested that thermography could be as accurate as heat flux meter measurement.

The U estimation in this study depended strongly on h_{conv}, which was very sensitive

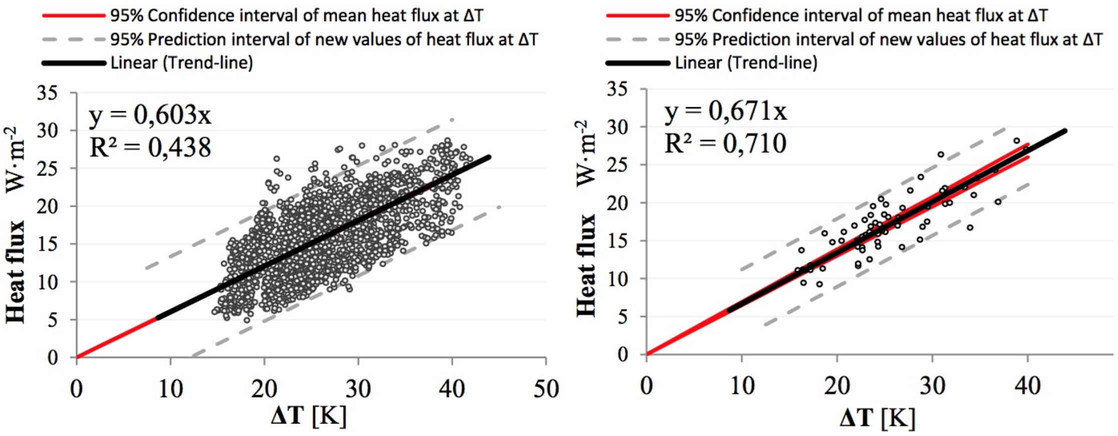

Figure 1.5: Conduction heat flux transferred on the surface of the wall: (left) heat flux meter measurements and (right) thermography measurements [14].

during the *in situ* experiments. An error on this value could lead to a serious wrong answer for the final result. Of course, in this case, if the authors could evaluate the correct value of h_{conv}, this study would be successful in U-value estimation by using only an IR camera.

In 1924, Jürges proposed an approach to calculate the convection coefficient via a linear function of wind speed v [15]. For each wind speed range, this parameter's expression must be modified to be adapted to the air flux situation. Datcu [16] made a literature study on the variation of h_{conv} in the function of wind speed with different conditions and positions in the building. After all, the authors agreed that it was too difficult to choose only one formula for all cases.

Albatici *et al.* [17, 18, 19] supposed that $h_{conv} = 3.8054v$ in case of low wind speed ($v <$ 5 m.s^{-1}) then applied this correlation to obtain U-value as in equation 1.14. In this case, the authors had to use a hot-wire anemometer positioned 0.1 m from the facade to determine v. The view of measurement arrangement is presented in Figure 1.6.

After several measurement campaigns, the authors observed the relative error of the estimation results from 8% to 23% compared to the theoretical ones, while the HFM method showed an error interval between 0% and 43%. On the other hand, all these values were found to be larger than theoretical ones. The authors explained this strange observation for several reasons, such as the difference between thermal properties of materials announced by the builders and the actual value or poor measurement repeatability of high insulating materials. Moreover, the authors highlighted the rapidity of their approach compared to the HFM (from two and ten hours depending on the stability of the climatic conditions). However, the method's application

Figure 1.6: View of the experimental arrangement from inside the building in [19].

appears very dependent on the on-site conditions (meteorological conditions, age of the building) and measurement conditions (use of the building, renovation work carried out or not).

A similar study as [19] was repeated by Nardi *et al.* [20] but with different meteorological conditions (cloudy day, sunny day) during 24 hours. Here, the authors ran U-value computation on the studied zone's thermogram to obtain a 2D U-value field (see Figure 1.7). The differences between the thermography method's results, the flux meter method, and the theoretical values, varied from 1% to 12%. Moreover, to obtain good results, two conditions must be satisfied: a high difference between the internal and external environmental temperatures. The wall surface temperature is higher than the environment one (at least 2°C). The measurement of the wall surface's spectral emissivity should be accurate and stable weather conditions were recommended.

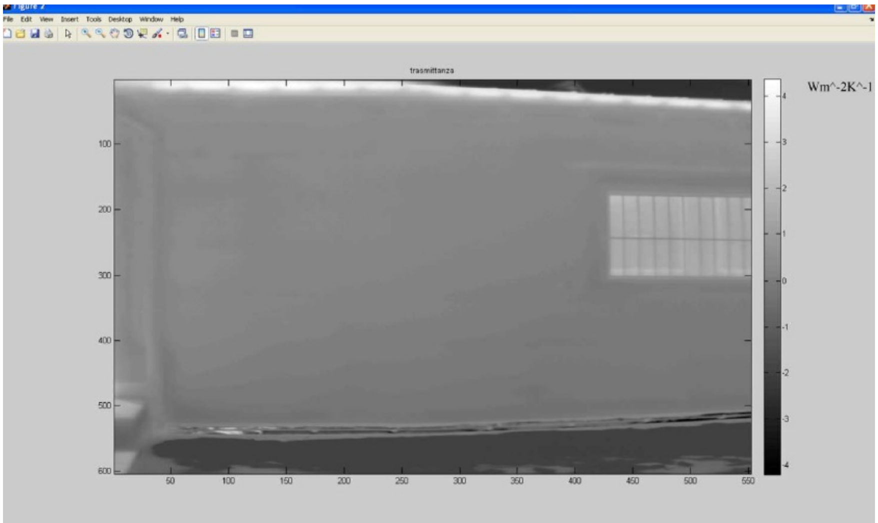

Figure 1.7: 2D U-value field obtained on the whole wall in [20].

Instead of using the classic equation of Stefan-Boltzmann, Fokaides *et al.* [21] expressed the radiative heat flux by supposing that the surface temperature T_S was close to the surrounding temperature T_{surr} as follows:

$$q_{rad} = 4\epsilon\sigma T_S^3(T_{surr} - T_S) \tag{1.15}$$

In this study, the emissivity and reflected temperature were determined by using the standard methods (ASTM E1862 97-2002 [22] and ISO 18434-1:2008 [23]). The measurements were launched from August 2009 to February 2010 (two different seasons) in five dwellings. The absolute deviations in percentage between the theoretical and the measured U-values measured by IR thermography were at an acceptable level (10-20%). However, some weaknesses of this measurement were mentioned by the sensibility test. A 10% of surface temperature variation captured by IR camera could lead to a 100% of variation for U-value. Moreover, the final results were very sensitive to the reflected temperature T_{surr} as shown in Figure 1.8.

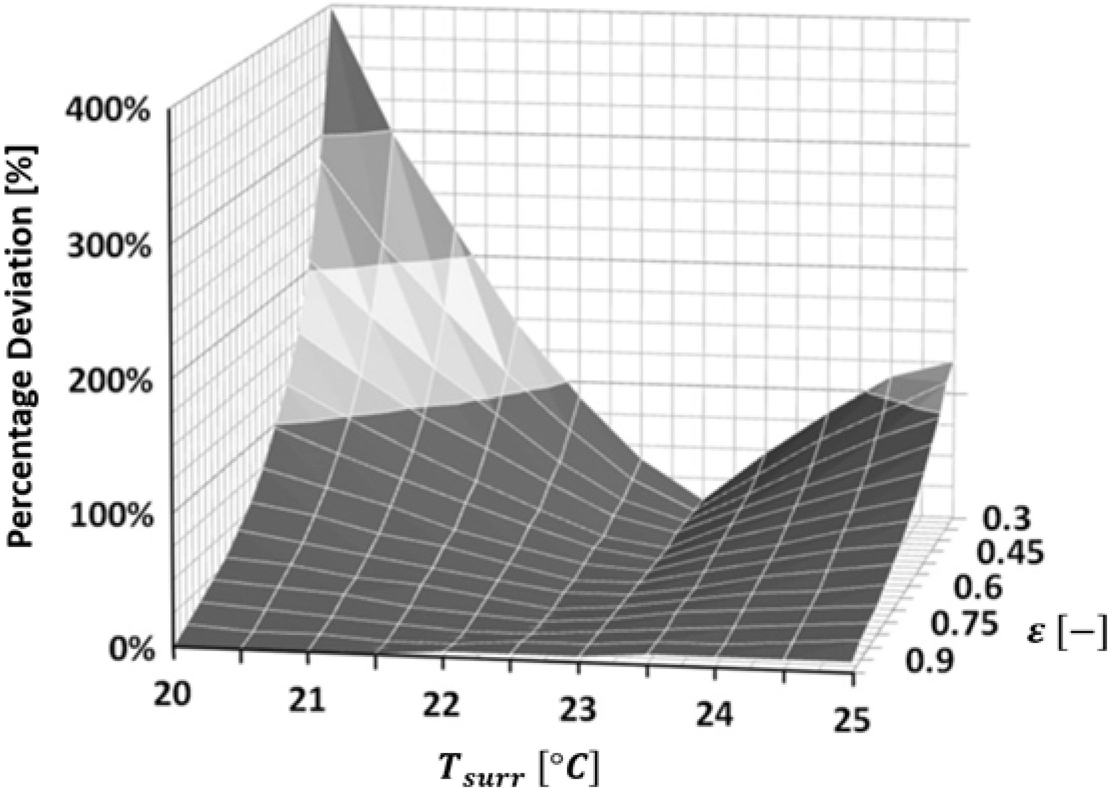

Figure 1.8: Variation of the U-value depending on the reflected temperature and the emissivity of the wall [21].

Nowoświat *et al.* proposed a mean computation of U-value on the whole surface by using internal surface resistance, which was evaluated by approximating the internal surface heat transfer coefficient in [24]. Several computations of U-value on separate areas of tested wall were carried out. Then the final value was obtained by the mean of the aforementioned results. Depending on the type of wall, a list of correcting coefficients and noises coming from surrounding conditions and physical characteristics of the tested wall was introduced to consider all possible influences in computing. Three walls of different thermal resistance were studied for 360 hours. The results obtained showed absolute error less than 10% compared to ISO 9869-1 method in all cases.

There are two approaches for U-value estimation by using additional elements to facilitate measurement. The first approached was proposed by Kato *et al.* in their paper [25] as a part of an extension of the standard ISO 9869-1 [9], which is published in [26]. The authors used two additional elements in this study. The first was a device that allowed measuring the heat exchange coefficient on the internal wall surface. A thin copper plate covered with high-emissivity paint was fixed on a thick plate of insulation whose thickness is more than 5 cm. This metal plate was heated by using a heating film to obtain a higher temperature (3-10°C) on the copper plate surface than the room air temperature. A heat flux meter and a thermocouple were sandwiched between the copper plate and insulation material to measure heat flux crossing this element.

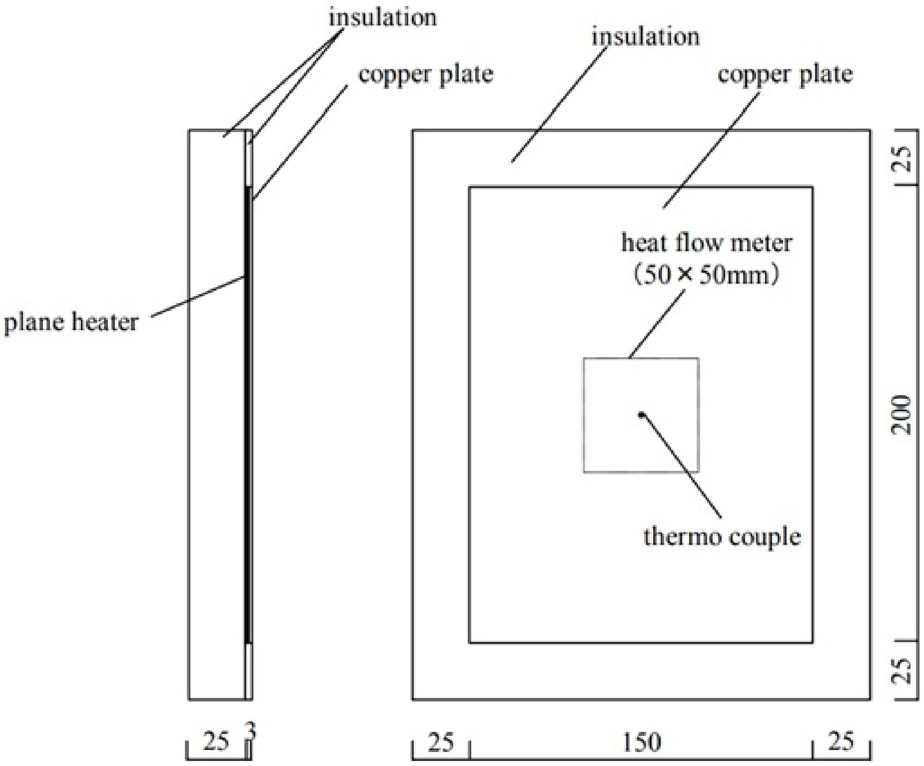

Figure 1.9: Outline of first additional element in [25].

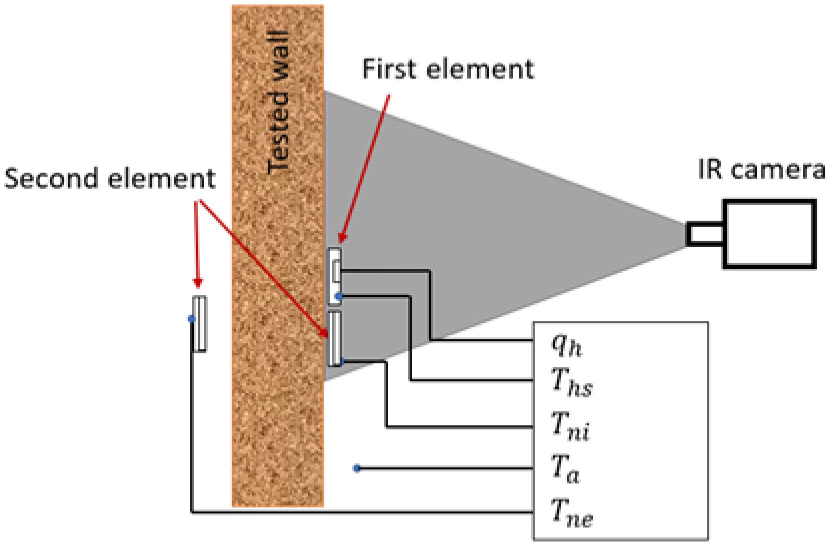

Figure 1.10: Diagram of the experimental device used in [25].

The second element was used to measure the interior and exterior environmental temperatures (by using the thermocouples). The configuration of this element was similar to the first one but without the heating film. The temperature was recorded by a thermocouple between copper and insulation plates. Both additional elements were fixed directly on the wall surface. Figures 1.9 and 1.10 present the general structure of this measurement protocol and devices.

According to the authors, the first additional element helped them to estimate the convective and radiative heat transfer coefficients by measuring incoming flux, environment, and wall surface temperatures. Then, this coefficient gave a possibility to compute global heat flux dissipated across a selected section of the wall by its surface temperature. Then, the wall U-value was estimated via equation 1.14.

In [25], this method was validated in laboratory for a wall made of wood whose U-value was equal to 0.75 W.m^{-2}.K^{-1} (value measured by the guarded hot box method [7]). A difference of 3.8$\%$ between the two methods was found. Then, an *in situ* test for a wooden wall insulated with 75 mm of stone wool was carried out for five days from midnight to 6 a.m. The average of measurement gave a U-value of 0.413 W.m^{-2}.K^{-1} instead of its theoretical value of 0.437 W.m^{-2}.K^{-1}.

The second approach is called SEID (Surface Equivalente d'Irrégularité ou de Défaut in French, or Equivalent Surface of Irregularity or Defect in English), which was proposed by

Pajani [27]. The additional element required here was an insulation plate of known thermal resistance R_{ref}, which was fixed on the wall surface and of emissivity close to the one of the wall surface. An infrared camera was used to observe temperature difference between wall (noted $T_{SI,app}$) and insulation surfaces (noted $T_{SRef,app}$) at the same time with environment temperature measurement (noted T_{NI}) (Cf. Figure 1.11).

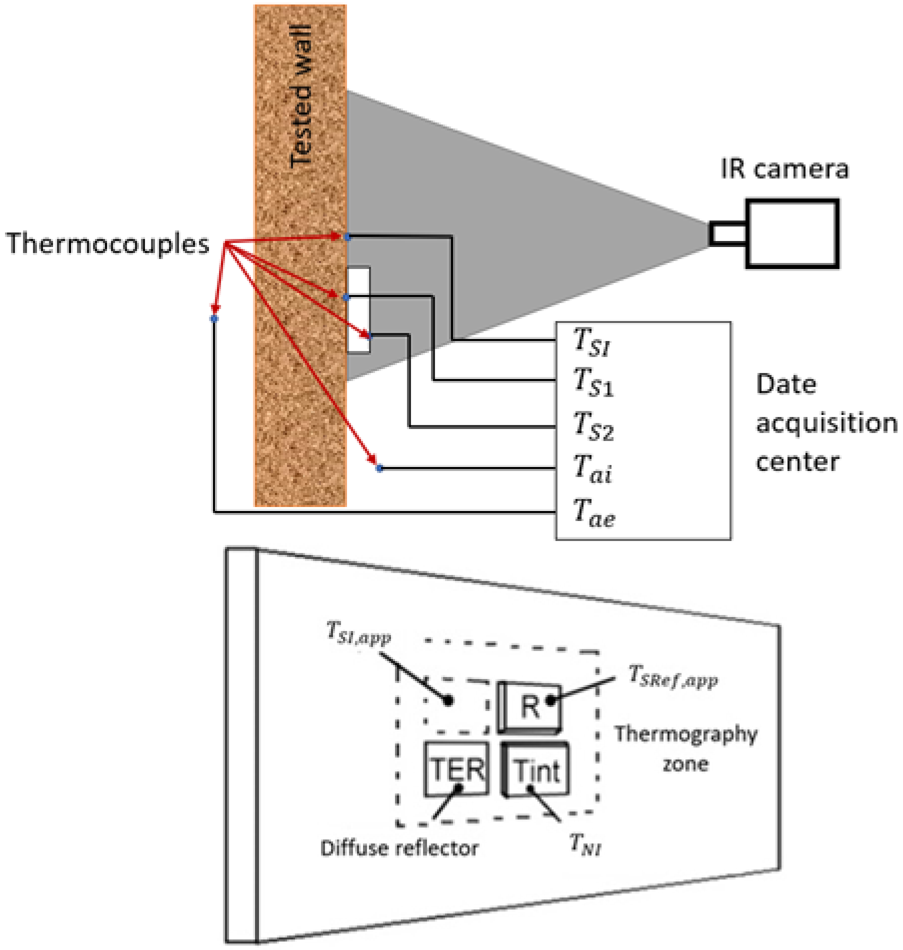

Figure 1.11: Diagrams of the experimental device used in the SEID method [27].

By using these three measured temperatures, the author could express the difference in thermal resistance between two zones with and without insulation plate to find out the U-value of the wall as:

$$U = \frac{1}{R_{ref}} \frac{T_{NI} - T_{SRef,app}}{T_{SRef,app} - T_{SI,app}} \tag{1.16}$$

The author suggested to install this plate a day before the testing day so that the whole system can reach the equilibrium when launching the measurement. Moreover, the thermal resistance of the additional insulation should be equivalent in value to wall resistance.

1.2.6 Passive studies using a physical model for thermal resistance estimation

Instead of using a classic steady-state computation of thermal resistance as in equation 1.14, several research groups prefer to integrate physical models into their thermal resistance estimation in order to reduce measurement time. Instead of waiting for a long duration, a dynamic physical model can represent correctly the temporal variation of the observed wall due to environmental conditions, then the physical characteristics of the wall can be estimated by using optimization algorithms.

A study, which was presented by Youcef *et al.* [28], tried to estimate a wall thermal resistance by using a COMSOL Multiphysics® simulation as the direct model and Levenberg-Marquardt optimization algorithm. Two week-long measurement campaigns were launched during two different seasons (autumn and winter) to estimate the thermal resistance of a real wall of a school. Two infrared cameras were used for monitoring both inside and outside of the building. Several additional parameters (interior and exterior air temperatures, solar irradiation, wall emissivity, etc.) were also recorded (Cf. Figure 1.12).

The authors supposed that the thermophysical properties of the insulation were known, then the estimation objectives were the insulation thickness, the interior and exterior exchange coefficients, and the solar radiation absorption coefficient. The temperature difference between the internal and external surfaces was minimized during the estimation process (see Figure 1.13). Finally, the authors found 1.33 $m^2.K.W^{-1}$ for the wall thermal resistance, instead of a theoretical value of 1.4 $m^2.K.W^{-1}$. This result showed that the estimated variables tended to converge to the stable values after at least three consecutive days of measurement.

Another model for passive measurement was proposed by Petojević *et al.* [29]. The authors used the thermal impulse response (TIR) as model and Tikhonov regularization technique for estimating parameters of the wall. The TIR model expressed the heat transfer inside the wall by a transfer box with two inputs and two outputs. In this study, the authors calculated heat fluxes on the two sides of the wall from surface temperatures as follows:

$$q_{SI} = \int_0^\infty g_{11}(\tau) T_{SI}(t-\tau) d\tau + \int_0^\infty g_{12}(\tau) T_{SE}(t-\tau) d\tau \tag{1.17}$$

$$q_{SE} = \int_0^\infty g_{21}(\tau) T_{SI}(t-\tau) d\tau + \int_0^\infty g_{22}(\tau) T_{SE}(t-\tau) d\tau \tag{1.18}$$

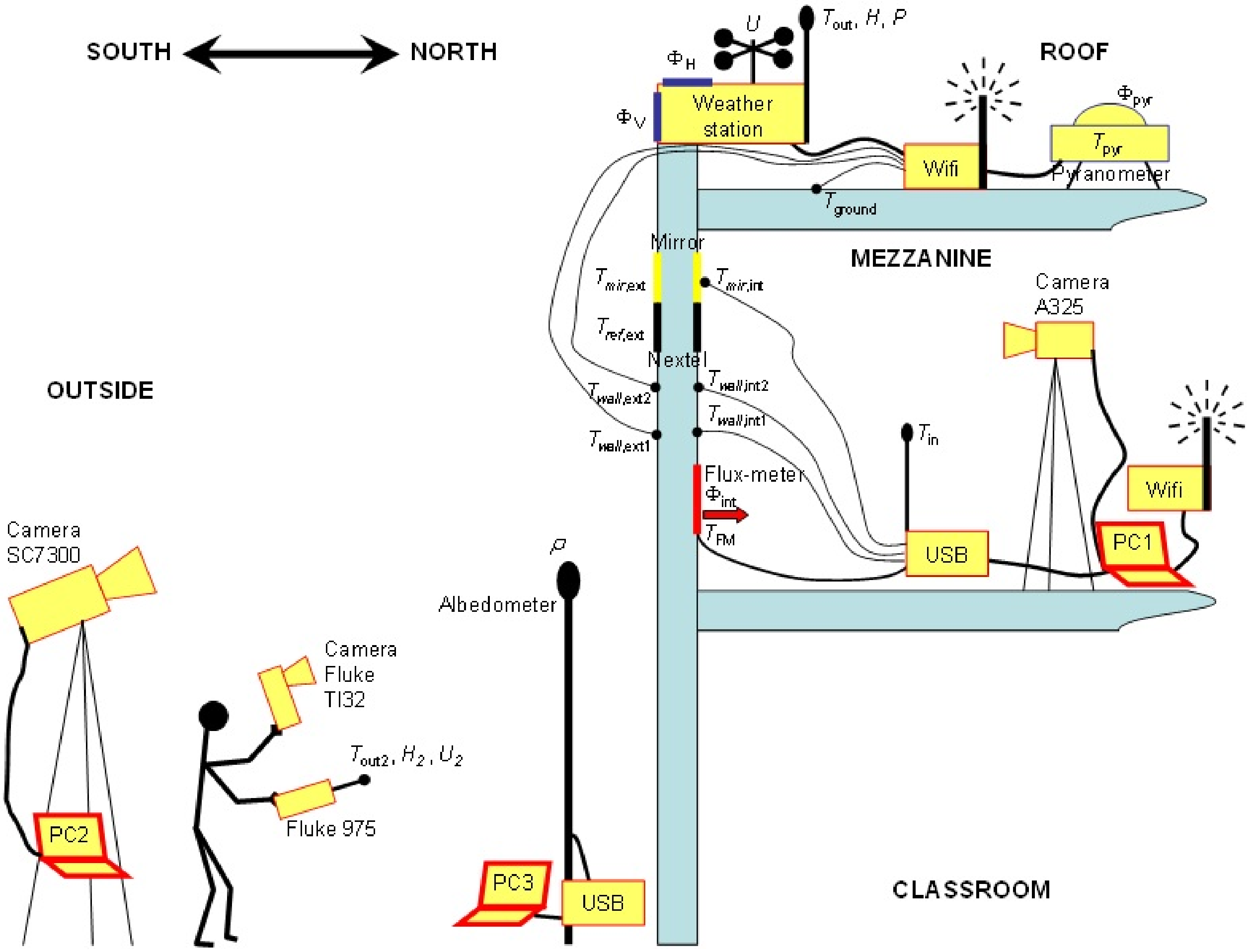

Figure 1.12: *In situ* experimental test bench in [28].

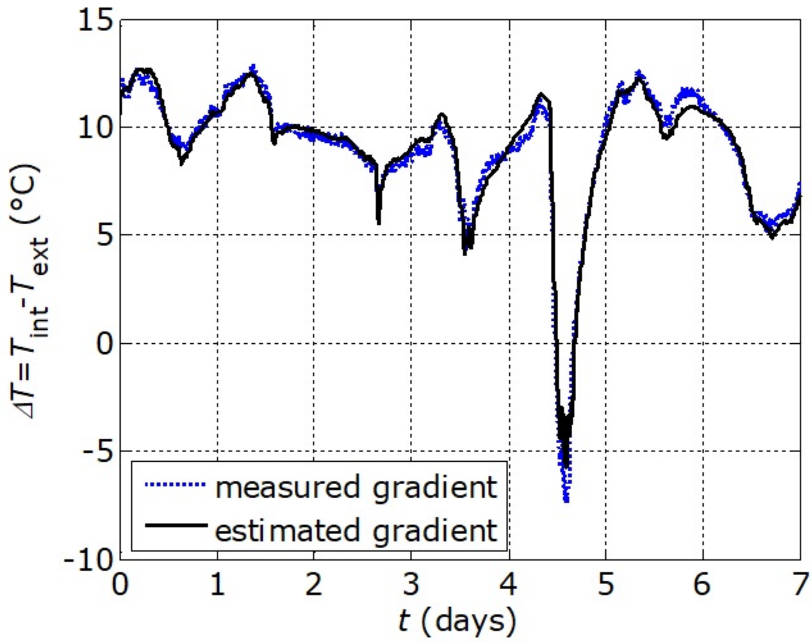

Figure 1.13: Measured and estimated interior-exterior temperature difference in [28].

where $g_{nm}(n, m = 1, 2)$ were the Green or TIR functions (more details in [29]). By applying time discretization on the equations above, the authors transformed the integral forms of q_1 and q_2 to a linear representation between inputs and outputs:

$$q_{SI} = \frac{t_{11}}{2} \sum_{i=1}^{N_{11}} w_{11,i} g_{11}(\tau_{11,i} T_{SI}(t - \tau_{11,i})) + \frac{t_{12}}{2} \sum_{i=1}^{N_{12}} w_{12,i} g_{12}(\tau_{12,i} T_{SE}(t - \tau_{12,i})) \tag{1.19}$$

$$q_{SE} = \frac{t_{21}}{2} \sum_{i=1}^{N_{21}} w_{21,i} g_{21}(\tau_{21,i} T_{SI}(t - \tau_{21,i})) + \frac{t_{22}}{2} \sum_{i=1}^{N_{22}} w_{22,i} g_{22}(\tau_{22,i} T_{SE}(t - \tau_{22,i})) \tag{1.20}$$

where $\tau_{nm,i} = t_{nm}(x_{nm,i} + 1)/2$ and τ_{nm} was the time at which function $g_{nm}(t)$ approximately vanish. Moreover, $w_{nm,i}$, $x_{nm,i}$, and N_{nm} were respectively the Gauss weights factors, interpolation points and number of interpolation points for the function g_{nm}. By minimizing least squares of heat fluxes, the TIR functions g_{nm} would be estimated, then the U-value of tested wall could be expressed by:

$$U = \int_0^{+\infty} g(\tau) d\tau \tag{1.21}$$

With 104 hours of measurement, the authors showed the capability of the proposed model to predict the dynamic thermal characteristics, the cumulative heat losses, the heat accumulation, the conductive pat of thermal transmittance, and the surface heat fluxes. According to the final results, the estimated U-value (0.4821 W.m^{-2}.K^{-1}) was close to the theoretical one (0.4787 W.m^{-2}.K^{-1}).

1.3 Active methods for measuring wall thermal resistance

1.3.1 Definition

The previous section showed the potential of the passive approach to measure a wall thermal resistance. However, this method requires a long time and, in most cases, suitable environmental conditions. That is why active methods are developed. These methods propose to use an artificial thermal source (for example heater or halogen spot) to create an artificial controlled heat flux through the wall. Therefore, the qualitative analysis by this type of method can be done faster than using the passive techniques. Besides, active methods allow detecting more irregularities than passive ones such as the detailed form of defects [30, 31] or air infiltration in house [32].

Using a passive technique, R-value (or U-value) can be computed by directly applying the static equation. However, with active methods or in the transient regime, this equation is no longer valid. Temperature and heat flux vary as a function of time and wall properties, then the statistic computation becomes wrong. In another way, only thermal resistance is involved in the passive mode while the active approach requires to take into account also the thermal capacitance. Then, the linear equation in passive mode becomes a differential equation in active mode. Therefore, to find out R-value (or U-value) of a wall, an inverse problem for fitting the dynamic evolution of measurement data with a theoretical model must be solved (more details will be in Chapter 3).

1.3.2 Studies based on the active approach for measuring wall thermal resistance

In 2016, Sassine *et al.* [33] proposed an experimental set-up for *in situ* measurements on real walls to estimate thermal resistance from a thermal quadrupoles approach. The artificial heat source of this study was a regulator fixed on a facade of a box (called "heating" box). The tested wall was installed in this box in front of the heater. The heat flux meter and thermocouples were equipped on the front face of the wall. The whole box was protected by an insulation to maintain adiabatic condition on its edges (Cf. Figure 1.14). The real view of the heating box and tested wall are presented in Figure 1.15.

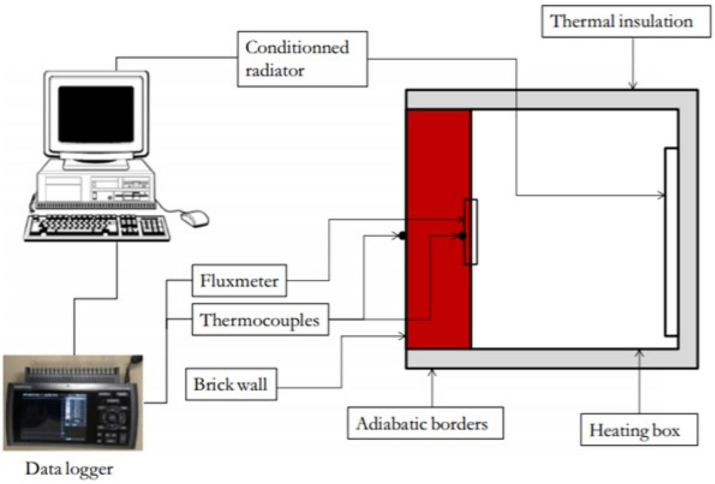

Figure 1.14: General diagram of experimental set-up in [33].

Figure 1.15: The real view of (left) the heating box and of (right) the experimental setup on the front face of the wall in [33].

By using Laplace transform (noted LT), the differential equation could be transformed to become linear. Then, a transfer matrix to express the relation between temperature and heat flux density on the front and rear faces by using equivalent thermal resistance R and equivalent thermal capacitance C is obtained (see equation 1.22). To determine the value of thermal resistance, the authors applied the ordinary least squares method and used the gradient descent method to minimize the difference between theoretical and measured heat flux on the front face.

$$\frac{\partial^2 T}{\partial x^2}(x,t) = \frac{\rho C_p}{\lambda}\frac{\partial T}{\partial t}(x,t) \xrightarrow{LT} \begin{pmatrix} \theta(p)_{SE} \\ \phi(p)_{SE} \end{pmatrix} = \begin{pmatrix} ch(\sqrt{pRC}) & \sqrt{\frac{R}{pC}}sh(\sqrt{pRC}) \\ \sqrt{\frac{pC}{R}}sh(\sqrt{pRC}) & ch(\sqrt{pRC}) \end{pmatrix} \begin{pmatrix} \theta(p)_{SI} \\ \phi(p)_{SI} \end{pmatrix} \tag{1.22}$$

where, $R = e/\lambda$ and $C = \rho C_p e$.

Parameter	Passive measurement	Active measurement	Relative deviation
R	0.384 m^2.K.W^{-1}	0.4 m^2.K.W^{-1}	3.9$\%$
C	129.7 W.h.m^{-2}.K^{-1}	125.5 W.h.m^{-2}.K^{-1}	3.2$\%$

Table 1.2: Results obtained for the equivalent thermal resistance and thermal capacitance from passive and active measurements in [33].

A series of measurements on a brick wall of weak thermal resistance was conducted during this study. The estimated thermal resistance and heat capacity were quite close to theoretical values (Cf. Figure 1.16 and Table 1.2). However, it required a long time for measurement (around 90 hours) which was similar to passive tests. Moreover, in this study, the targeted wall contained only one layer so that if this wall was a multi-layer sample, the model would have been more complex.

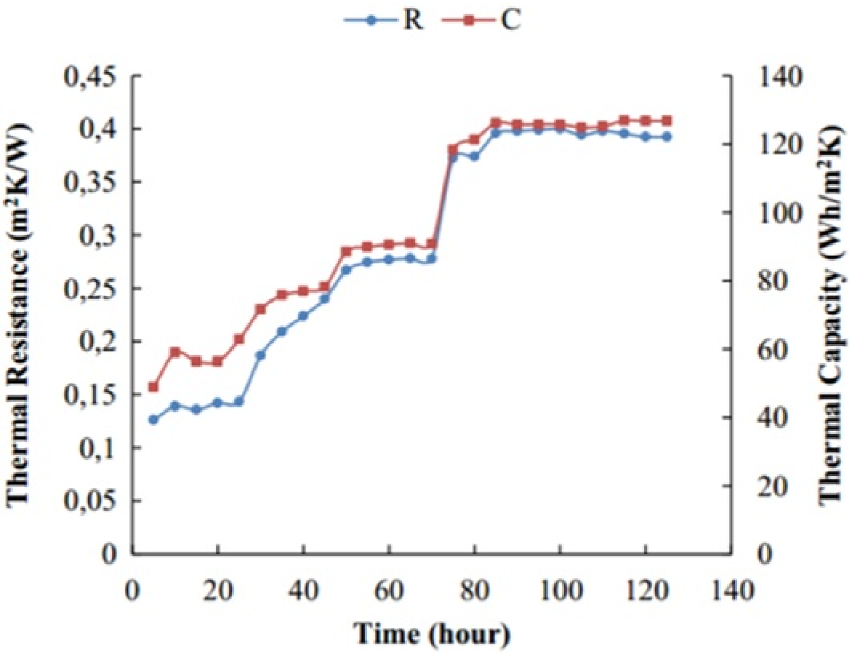

Figure 1.16: Results obtained for the values of R and C optimised from active experiment in [33].

A laboratory device developed by Youcef *et al.* allowed estimating wall thermal resistance in active mode by using the thermal quadrupoles model [34]. This device was a cubic box whose front face was open and facing the investigated wall and rear face contained halogen spotlights. The configuration of the spotlights assured the uniformity of heating flux coming to the front face. There was a hole on the rear face of the box so that an infrared camera could be used to observe the temperature field of the wall surface. Several walls with internal insulation were studied in laboratory. The schematic view of the experimental setup is presented in Figure 1.17.

To estimate the wall thermal resistance, the authors used the thermal quadrupoles computation as the direct model into the estimation code. In this study, there were four parameters to be estimated: absorbed heat density of excitation, internal convective heat transfer coefficient and time constants of the two first layers of the wall (plaster and insulation) by supposing that their thermal effusivity was known. Several types of insulation were tested (expanded polystyrene, polyurethane foam, stone wool). The internal surface of the walls was painted with black and high emissivity paint. According to the results in Figure 1.18, 90% of tests returned an estimated value with a margin of error within ± 20% in comparison to the theoretical value. The authors mentioned also that a measurement time of at least 1.5 hours was necessary.

Rasooli *et al.* proposed an active method in order to reduce measurement duration of ISO

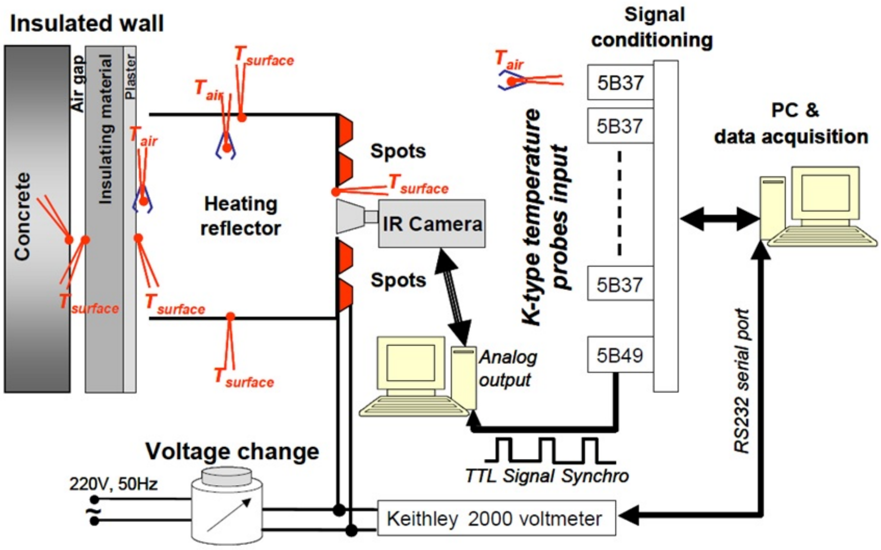

Figure 1.17: Active thermography experimental device in [34].

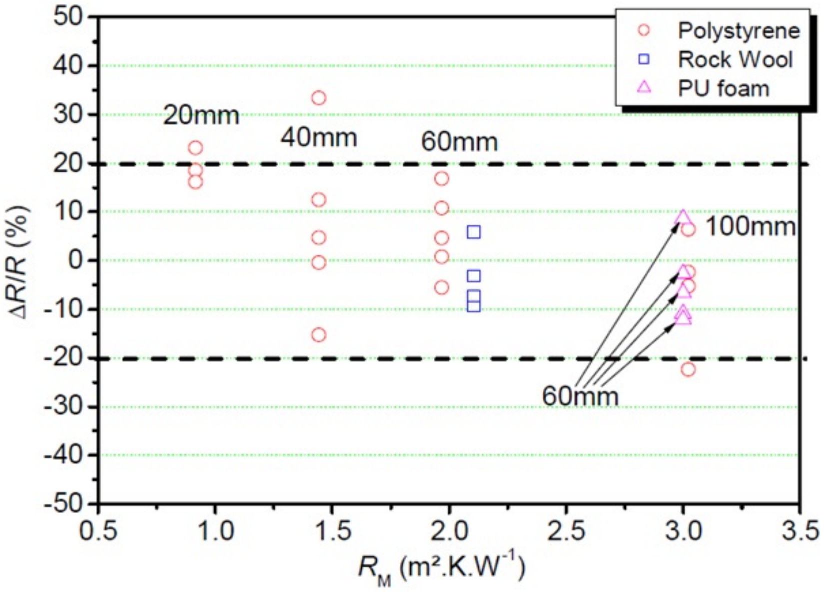

Figure 1.18: Results of thermal resistance estimation in [34].

9869-1 standard [35]. This method is called "Excitation Pulse Method" (noted EPM) and is based on the theory of thermal Response Factors (RFs) [36] (see Figure 1.19).

Here, the interior side of the wall was under a surface temperature regulation whose shape was triangular and magnitude (noted δ) was at least 1°C. Then, both heat flux densities on both surfaces were measured (Q_1 for the excitation side and Q_2 for the opposite side). Two response factors X_1 and X_2 were calculated using the following equations:

$$X_1 = \frac{Q_1}{\delta} \tag{1.23}$$

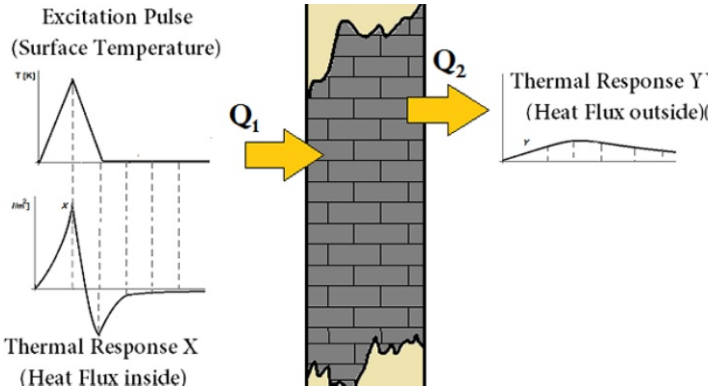

Figure 1.19: Basic diagram of the EPM method [35].

$$X_2 = \frac{Q_2}{\delta} \tag{1.24}$$

Finally, the thermal resistance was expressed by:

$$R = 2\left(\sum_{i=0}^{n}(X_i + Y_i)\right)^{-1} \tag{1.25}$$

According to the requirement of ISO 9869-1 standard, the thermal bridges should also be avoided in this method. Therefore, an IR camera was used to determine the favorable zone for measurement. Then, heat flux meters and thermocouples were installed on the surface of both sides and covered by a film of the same color as the wall. To lower as much as possible the unwilling fluctuations from outside, the exterior sensors were protected by insulation (see Figure 1.20). For regulating the temperature of the wall surface, a fan (for cooling) and a heater (for heating) were equipped to deliver the thermal excitation every ten seconds.

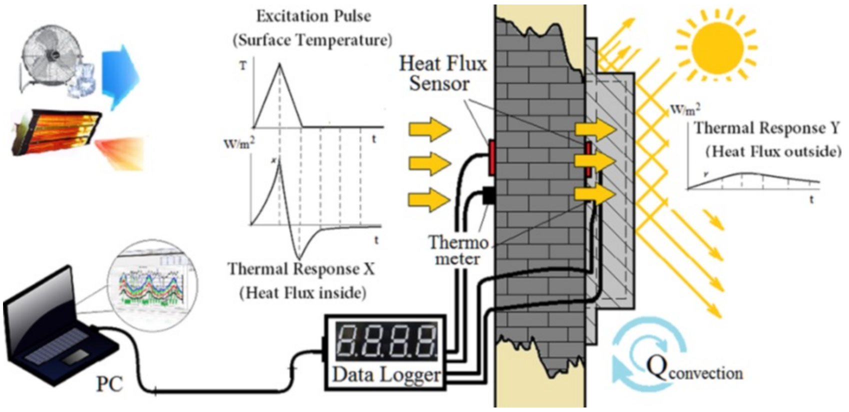

Figure 1.20: Experimental device developed in [35].

Table 1.3 presents a comparison of the thermal resistances measured with the standard and EPM methods. A difference of less than 2% was found for 14 days of measurement for standard method and 1.5 hours for the EPM method.

In 2019, the authors presented another study based on EPM to evaluate the thermal conductivity, the volumetric heat capacity and the thickness of a homogeneous wall by solving an inverse problem [37]. Several aspects were considered during this work: time interval, thermal response time, and excitation pulse magnitude. The thermal resistance was determined by minimizing the thermal response time of the wall by measurement and COMSOL simulation used as direct model.

Case study	R by ISO 9869-1	R by EPM	Relative difference
1	0.17 $m^2.K.W^{-1}$	0.17 $m^2.K.W^{-1}$	-0.58%
2	0.77 $m^2.K.W^{-1}$	0.78 $m^2.K.W^{-1}$	1.2%
3	1.57 $m^2.K.W^{-1}$	1.6 $m^2.K.W^{-1}$	2%

Table 1.3: Results obtained during an *in situ* study of a building: ISO 9869-1 (14 days of measurement) and EPM (1.5 hour of measurement) [35].

The authors highlighted that the required test duration must be at least twice the total response time of the wall. In the case of the unknown wall, X and Y Response Factors were observed as stopping criteria of this technique. According to the authors, their proposed method did not work well with heavily insulated walls (because of lateral effect) and the cavity walls (because of its thermal dissipation in the air).

Another approach applied in U-value determination by active method was proposed by Meulemans [38]. This approach called Quick U-building (or QUB/e) method allowed measuring the total heat loss coefficient and local U-value of a building in a night without occupancy. There were two phases in a QUB/e test: heating and cooling (see Figure 1.21). The author heated the inside environment of the tested room by several heaters then, by using thermal sensors (IR camera, thermocouples and heat flux meter), the measurement data were collected to compute directly U-value of a particular wall of the tested room as:

$$U = \frac{T_2^{'}q_1 - T_1^{'}q_2}{T_2^{'}\Delta T_1 - T_1^{'}\Delta T_2} \tag{1.26}$$

where q_i, $T_i^{'}$ and ΔT_i were respectively the mean heat flux density, the slope of the inside air temperature and the inside/outside air temperature difference at the "end" of the phase i. Besides, a 15-day passive measurement by ISO 9869-1 method was carried out to compare with proposed method.

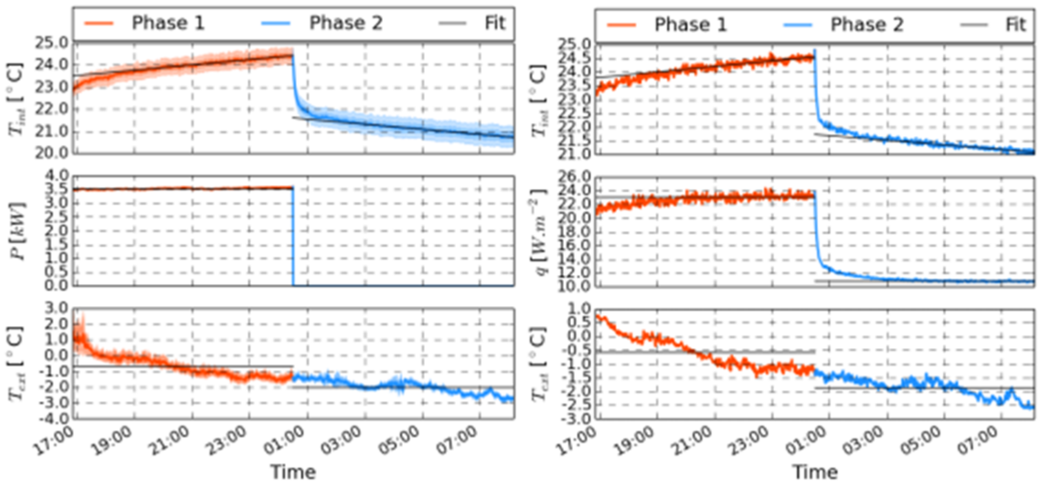

Figure 1.21: Evolution of measurement data during a QUB/e test with 8 hours of heating phase (red line) and 8 hours of cooling phase (blue line) in [38].

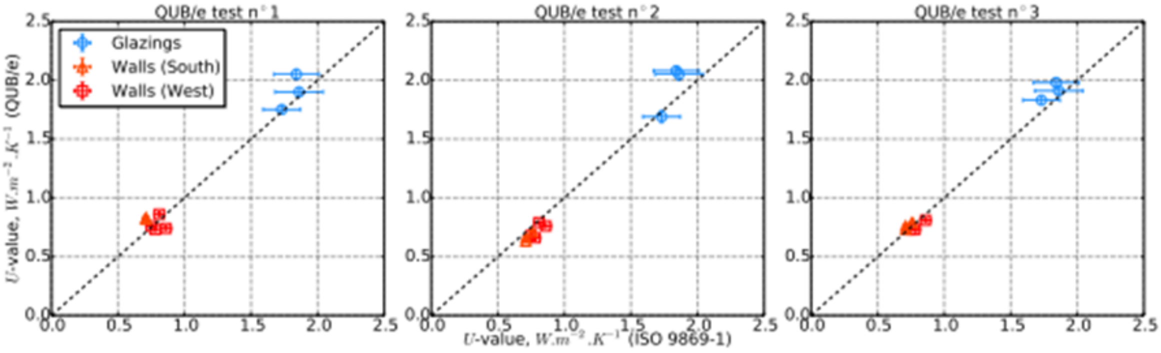

Figure 1.22: Comparison between ISO 9869-1 and QUB/e methods in [38].

An apartment in Sweden was used during this study and the author tried to evaluate the U-value of several positions in this apartment. Following results (Cf. Figure 1.22), the author concluded a good agreement between ISO 9869-1 and QUB/e methods. Moreover, the QUB/e method required only a single night for measurement which was shorter than 15 days of ISO 9869-1. However, the author launched the measurements only in a room without occupancy.

1.4 Comparison of methods for measuring wall thermal resistance

A comparison of U-value computation approaches was performed by Nardi *et al.* [39]. Four equations were proposed to calculate U-value of a wall tested in a controlled environment (guarded hot box):

- U-value computation based on a linearization of the Stefan-Boltzmann law as:

$$U = \frac{4\epsilon\sigma T_m^3(T_{SI} - T_{surr}) + h_I(T_{SI} - T_{aI})}{T_{aI} - T_{aE}} \tag{1.27}$$

where $T_m = (T_{SI} + T_{surr})/2$ and T_{surr} is the temperature of the surrounding environment.

- A similar approach as the first one but T_m was replaced by T_{SI} as:

$$U = \frac{4\epsilon\sigma T_{SI}^3(T_{SI} - T_{surr}) + h_I(T_{SI} - T_{aI})}{T_{aI} - T_{aE}} \tag{1.28}$$

- U-value computation based on the equivalence between the total absorbed flux and the convective heat flux (Temperature-based method) as:

$$U = \frac{h_E(T_{SE} - TaE)}{T_{aI} - T_{aE}} \tag{1.29}$$

where $h_E =$ 5.8+3.8054v,

- U-value computation in [17, 18, 19] from Albatici *et al.* which supposed $h_E =$ 3.8054v:

$$U = \frac{\epsilon\sigma(T_{SE}^4 - T_{aE}^4) + 3.8054v(T_{SE} - T_{aE})}{T_{aI} - T_{aE}} \tag{1.30}$$

The authors used an IR camera to observe the whole surface of the wall (see Figure 1.23). 24 tests of 72 hours under different environmental conditions were carried out in order to observe the relation between computed results by the four approaches above and the environmental conditions.

The results showed that the U-values computed with equations 1.27 and 1.28 were very similar. Moreover, the computed U-value was more stable with the higher temperature difference between indoor and outdoor, lower reflected temperature and the lower temperature difference between reflected and outdoor temperatures.

Soares *et al.* recently presented a summary of five popular passive measurement methods for obtaining overall thermal transmittance of a house or a part of the house: heat flow meter, guarded hot plate, guarded hot box, calibrated hot box, and infrared thermography technique (IRT) [40]. Different types of the tested element were mentioned in this study: homogeneous elements, moderately-homogeneous and non-homogeneous walls, windows, and construction

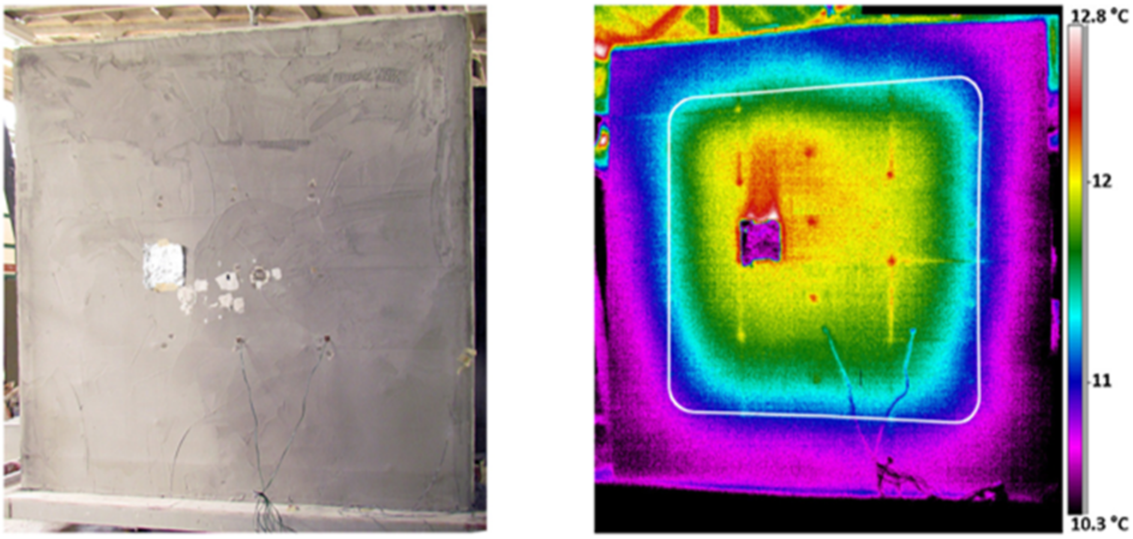

Figure 1.23: (left) Visible and (right) infrared image of the observed wall [39].

elements with innovative materials (aerogel, phase change materials, and vacuum insulation panels). The *in situ* and laboratory tests were carried out by the authors.

According to final results, the IRT technique was considered as the most commonly used method for building analysis but the influence of environment and surface characteristics should be quantified. Moreover, the authors showed that IRT could be used as a support for other techniques in the case of non-homogeneous structures. The effect of the thermal bridge was shown as one of the most important factors in the evaluation of non-homogeneous wall and there is a need for deeper research and experimental approaches to develop suitable methodologies for simulating the influence of this factor in the overall thermal transmittance measurement of building envelop.

Another review method was done by Teni *et al.* [41]. This review focused on existing experimental *in situ* non-destructive approaches for U-value determination: the heat flow meter method (HFM), infrared thermography (IRT), temperature-based method (TBM), natural convection and radiation method (NCaR), and simple hot box-heat flow meter method (SHB-HFM). To well visualize the comparison between these methods, an exhaustive comparison of all existing methods is detailed in this paper, including the test conditions, the test duration, and the accuracy of U-value determination for each of them. Table 1.4 presents a summary of this review.

A comparative study in real conditions between four measurement methods for determining

Method	Deviation range	Test duration	Remarks
HFM	0%-163%	Min. 3 days	This method has limitations for certain type of building and obviously the test duration.
IRT	0%-162%	Min. 3 nights	The result quality by this method depends on several factors which are not easily controlled during *in situ* measurement, especially the convective heat transfer coefficient.
TBM	4%-37%	$<$ 1 days	There are few researches studying the actual behaviour of walls in real conditions using this method.
NCaR	0.5%-26%	Min. 3 days	This method requires more studies on different types of building under several conditions in order to evaluate limitations and negative impacts.
SHB-HFM	4%-7%	n.a.	This method is still new and lacks to prove its applicability and accuracy.

Table 1.4: Summarised review of five methods on U-value assessment of building wall in [41].

a wall thermal resistance was presented by Monchau *et al.* [42]. The four methods under study were:

- Heat flux meter method from the ISO 9869-1 standard;
- IR thermography method from the ISO 9869-2 standard;
- SEID method;
- Passive infrared method developed in [43].

Two IR cameras were used to observe both interior and exterior surfaces simultaneously. The tested building was occupied and its walls had an external insulation. By the knowledge of the properties of the wall materials, the expected value was equal to 3.8 $m^2.K.W^{-1}$. Table 1.5 summarizes the measurement results and their details.

	ISO 9869-1	ISO 9869-2	SEID method	Passive IR method
Thermal resistance ($m^2.K.W^{-1}$)	2.8	2.1	1.6	4.5
Uncertainty ($m^2.K.W^{-1}$)	1	1.3	0.7	0.7
Measurement time (days)	5	3	1	7
Relative deviation with expected value (%)	-26	-45	-58	18

Table 1.5: Wall thermal resistance values and uncertainties obtained by four methods used in [42].

The ISO 9869-1 method which is a non-IR thermography method gave a mean value of 2.8 $m^2.K.W^{-1}$ with an uncertainty of 1 $m^2.K.W^{-1}$ which was greater than indicated by the standard. The second method (ISO 9869-2) which could analyze the resistance of the entire surface presented a final result quite far from the expected one. This bias of results obtained by the two standard methods could be explained by insufficient temperature gradient. The SEID method required the shortest duration but it needed to be developed more to obtain a better result. The passive method needed longer time and heavier instrumentation than the others but provided more adequate results.

Another comparison study of active and passive IR thermography methods was summarised by Ibos *et al.* [44]. The results presented in this paper showed that the estimation of thermal resistance was possible in some situations. Each passive or active method had its pros and cons. The authors also observed that the sensitivity of the estimation decreased as the level of insulation increased so that it was increasingly difficult to distinguish similar thermal resistance values when the insulation quality increased. Table 1.6 presents a short comparison between passive and active approaches considering several criteria.

Comparison criteria	**Passive thermography**	**Active thermography**
Spatial extent	Large (wall, facade)	Small, limited measurement (around 1 m^2)
Measurement time	Long (3-4 days)	Short (several hours)
Influencing factors	Many with great influences: weather data, radiation environment, emissivity	Little influence (emissivity, absorptivity)
Measurement positions	Exterior and interior	Insulation side only
Period of use	When there is a sufficient temperature gradient between the interior and exterior	Year-round
Preferential wall orientation	Difficulties correcting for façades in the sun	Any
Uncertainty in thermal resistance estimations	Unknown at present (only some situations studied)	Around 20$\%$

Table 1.6: Comparative table of the advantages and disadvantages of the passive and active approaches for several comparison criteria [44].

Ficco *et al.* perform a study of experimental aspects of *in situ* diagnosis via heat flux meter (HFM) [45]. In this paper, several methods for evaluating the U-value of seven different walls were presented along with their pros and cons:

- Method 1: Estimation based on data obtained by historical analysis of the building or analogies with similar buildings of the same age using specific technical databases: high uncertainty, lack of reliable data;

- Method 2: Estimation based on the nominal design data: better accuracy, but the materials used can be different from those in the design, and the properties can change over time;

- Method 3: Estimation based on the actual data obtained by structure identification (sampling or endoscope method): good accuracy but very invasive;

- Method 4: In situ measurements using HFMs: simple and precise in theory. In practice, it is sensitive to exterior climate variations (solar radiation, wind), interior and exterior temperature variations, and substantial flux variations during the test. It is not suitable for great inertia walls, and it could lead to high error and uncertainty. The ISO 9868-1 standard for in *in situ* heat flux measurement recommends that the measurement surface be representative of the wall. Therefore, it is important to be aware of the wall's uniformity and stay away from thermal bridges. It requires the test duration to be a multiple of 24 hours, lasting at least 72 hours.

Seven walls were tested by methods 2, 3, and 4. This work led to the following conclusions:

- The U-values estimated by methods 2 (based on initial design parameters) and 3 (based on updated parameters via sampling) are "compatible" with the values from method 4 (heat flux meter with steady-state processing), but their uncertainties depend on the degree of knowledge of the wall (variation from 10% to 30%);

- The temperature and humidity conditions greatly influence the conductance of porous materials and can increase the uncertainty or create measurement bias;

- The shape and area of the flux meter plates do not significantly influence the measurement (a debatable conclusion, given the results presented with a deviation of 10% for the coefficient U);

- Small temperature gradient (< 10°C), low heat flux, or inversion of flux during the test lead to very high uncertainty.

- In the event of non-optimal measurement conditions (low heat flux), the duration of the trial greatly impacts the uncertainty of the measurement of the U-value.

- Heavy walls present the highest uncertainty and require a longer test duration to obtain a reasonable level of uncertainty.

Another comparison between several methods for determining the thermal resistance of a wall from *in situ* measurement was presented by Deconinck *et al.* [46], with steady-state and dynamic conditions. The methods mentioned in this paper were:

- **Average method**: from the ISO 9869-1 standard, it expresses the thermal resistance of a wall as equal to the ratio of the heat flux over the temperature gradient on both sides of the wall in steady-state conditions. The data are averaged, under certain conditions, to obtain the steady-state conditions;

- **Average method with correction for the storage effect**: the ISO 9869-1 standard proposes a correction taking into account the effect of heat storage (inertia) for high-inertia walls and measurements in spring and summer conditions. The correction factor to be applied requires a good theoretical knowledge of the wall inertia;

- **Anderlind regression**: a dynamic method inspired by the one described in Appendix B of ISO 9869-1 was studied. The principle of this method is computing the total heat flux crossing the wall by three separate parts: a static part and two dynamic parts, one corresponding to the variations of the interior temperature and the other to the variations of the exterior temperature. The method is simple to use and does not require any complex calculations. It provides a standard deviation of the estimated resistance value, but its interpretation should be used with caution;

- **Black-box model** or **ARX modelling**: a more or less complex model to represent the relation between the input/output of observed system is proposed. The model is general, and the identified parameters do not necessarily have physical significance. Nevertheless, it is possible to determine the thermal resistance of the model representing the steady-state part. This method provides an estimation of the uncertainty;

- **Grey-box model** or **stochastic state-space modelling**: it builds a model based on the physics of the wall being studied by writing stochastic differential equations. The method makes it possible to identify the heat capacity and thermal resistance and provides uncertainty. The tool used for the simulation is CTSM-R [47].

Both numerical and experimental cases were analyzed by these five methods. The considered case is a double wall in full brick (fairly heavy), in which the cavity was filled with insulation, tested in winter and summer conditions. The air temperature was maintained at 20°C on the interior in winter and evolved freely or semi-controlled ($\geq$ 20°C) in summer. The data measured were the interior heat flux and the interior and exterior surface temperatures.

Table 1.7 shows the results obtained by five considered methods considering numerical data. By using data simulated in winter, both average and dynamic methods could estimate similar results. Moreover, the dynamic ones converged faster, and their estimated values were slightly more accurate than the two others. On the other hand, only the dynamic techniques could lead to reliable estimation results with spring and summer data.

	Measurement duration required to achieve a relative error of 10% or 5%					
	Winter		**Spring**		**Summer**	
Method	10%	5%	10%	5%	10%	5%
Average method	8 days	20 days	12-14 days	-	-	-
With storage effect	3-4 days	6 days	8 days	14 days	-	-
Anderlind	4 days	5 days	4-5 days	6 days	11 days	22 days
Black box	5 days	5 days	5 days	6 days	11 days	22 days
Grey box	4 days	5 days	4 days	5 days	11 days	20 days

Table 1.7: Results of the numerical cases studied in [46].

1.5 Conclusions

According to the studies described above, the passive or active approach can estimate a wall's thermal resistance (or wall's heat transfer coefficient). Each of them has its pros and cons.

The passive method can be launched without any interaction with the observed wall. The calculation of the thermal resistance is quite simple and fast. However, it requires a long duration for measurement to avoid unwilling noises. Moreover, this method is available only under some specific environmental conditions (cloudy sky, weak weather condition variation, etc.).

The active method shows a better qualitative analysis than the passive one. Moreover, quantitative active analysis allows reducing measurement time significantly and improving result accuracy. However, the estimation of thermal resistance with this kind of method is not as simple as the passive one. A physical model must be well defined, and it takes time to estimate the final result. Because of their complexity, studies based on an active method are much less common than those based on the passive approach.

The convective heat transfer coefficient plays an important role in determining the wall's thermal resistance in both methods. With the passive method, this parameter is used to compute R-value (or U-value) without using a heat flux meter [14], and, in some techniques, R-value (or U-value) can be determined directly from its value and the temperature gradient (for example, temperature-based method [48] and air–surface temperature ratio method [49]). However, it is challenging to evaluate this coefficient correctly by measurement because it depends on several environmental conditions and measurement positions. There are several different approximations for calculating the convective heat transfer coefficient by using wind speed, but none of them can guarantee the exactitude of obtained value in all cases. Besides, this coefficient becomes more difficult to determine in dynamic regime (active method) than in steady-state regime (passive method). The heat flux supplied by thermal source perturbs strongly the considered system (accelerating wind speed, changing air temperature and humidity, etc.). Until now, the number of studies that work on the convective heat transfer coefficient determination (by measurement or by parameter estimation) in the active configuration is quite limited.

Therefore, the objective of this research is to develop a new *in situ* measurement prototype based on the active technique for evaluating the thermal resistance of an opaque and homogeneous wall (no irregularity, no thermal bridge). This prototype has to be more robust, faster (less than 12 hours), and less affected by environmental conditions (temperature variation, air convection, etc.) than existing ones. Moreover, it should be applicable to occupied buildings (residential houses, offices, schools, etc.). The installation of the prototype has to be simple and fast so that everyone can use it.

2 Theory of heat transfer modelling

2.1 Introduction

This chapter presents the numerical tools developed to model heat transfer in the building wall to be characterized. These are based on the thermal quadrupole method (noted QUAD), which is perfectly suited to the geometry of a wall and allows detailed modeling of heat transfer while guaranteeing moderate calculation times. One of the main objectives here is to test the model's robustness in the context of the planned active method with real *in situ* conditions. Moreover, to estimate the thermal resistance, a direct model is required. This model should be correct and fast. According to the literature review chapter, the 1D model is preferred to be the direct model because of the short computation time. Then, in this study, the 1D QUAD model is chosen to be used as the direct model of the parameter estimation process and the 3D QUAD model for generating numerical data which is used to validate the proposed estimation process.

The first section clarifies the simulation configuration, including the boundary conditions, types of wall, thermal excitation, etc. Then, QUAD's theory and its computation steps in 1D and 3D configurations are detailed in the second section. Two computation approaches are discussed: **Excitation With Convection** (noted **EWC**) and **Absorbed Flux** (noted **AbF**). In the last section, a series of comparisons between QUAD and a commercial simulation software named COMSOL Multiphysics® will be presented to validate the proposed method for simulating heat transfer in the wall.

2.2 Simulation configuration and considered walls

The context of the modeling to be implemented is a building wall on-site submitted to external weather conditions and an artificial thermal excitation on the building's interior side. The solar radiation, the convective, and radiative heat fluxes are considered boundary conditions on the wall's external side. On the other side, the heat flux from an artificial heat source (radiator, lamp spot, heating resistance, etc.), the convective, and radiative heat fluxes describe the internal boundary conditions. The wall's internal side is chosen to be heated because it is easier to control its surrounding conditions. Moreover, it is always easier to install heavy equipment (for example, thermal heat source) inside the building. Different data of interest that can be measured will be considered output in this numerical study: the external and internal surface temperatures and the absorbed heat fluxes by the wall's internal and external surfaces. However, the role of the absorbed heat flux on the external side is not necessary because its role can be replaced by the external air temperature and the solar radiation. Among the four output variables, the internal surface temperature is the most important because it will be used as minimization data in parameter estimation, as seen later. The global diagram for simulation configuration, input parameters of boundary conditions, and data of interest are presented in Figure 2.1. Following the research objective, this study focuses on estimation capability for 24 hours; therefore, the simulation duration is 24 hours.

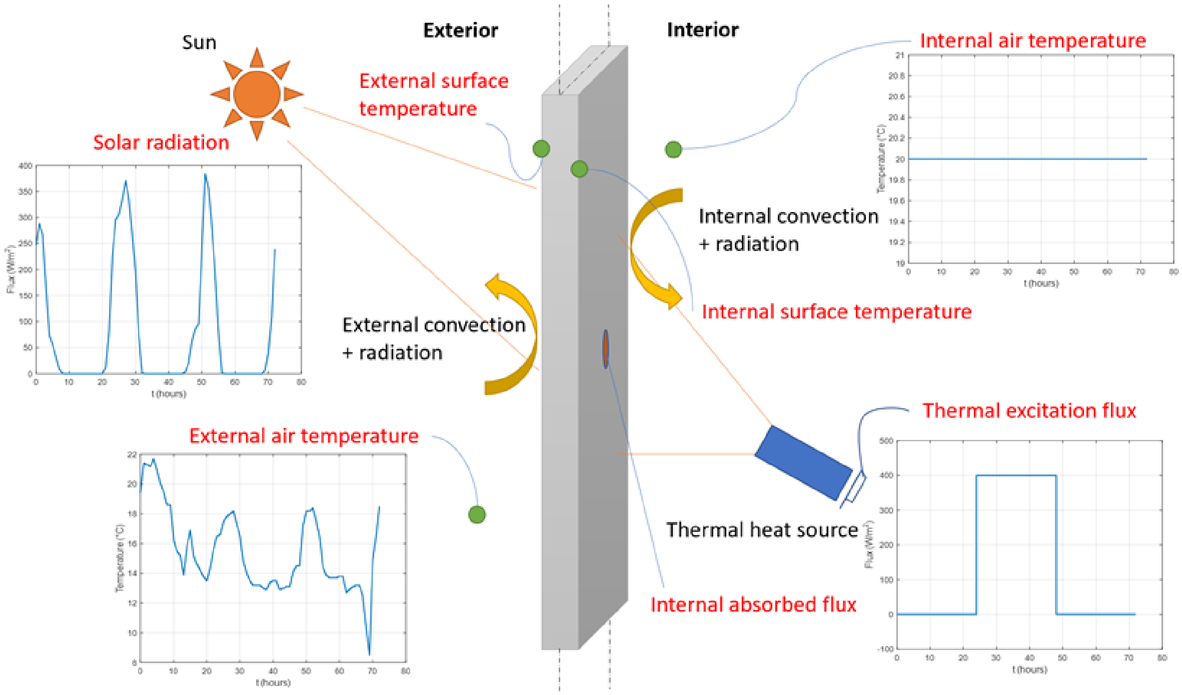

Figure 2.1: Global diagram for simulating heat transfer in a building wall on-site subject to an active excitation on the interior side of the building.

In the numerical study, the thermal heat source supplies a constant flux of 400 W.m^{-2} to the tested wall. Because the solar radiation coming to the external side is around 300 W.m^{-2} then the excitation heat flux must be stronger than outdoor influence. Besides, due to the security requirement, the temperature augmentation lower than 60°C is recommended. Therefore, 400 W.m^{-2} is a good value and possible for real measurement. Moreover, to calculate the convective and radiative heat fluxes on the boundary, the global heat exchange coefficient, including convection and radiation, must be known. According to ISO-6946 standard [50], the values for indoor and outdoor vertical surface are 7.7 W.m^{-2}.K^{-1} and 25 W.m^{-2}.K^{-1} respectively.

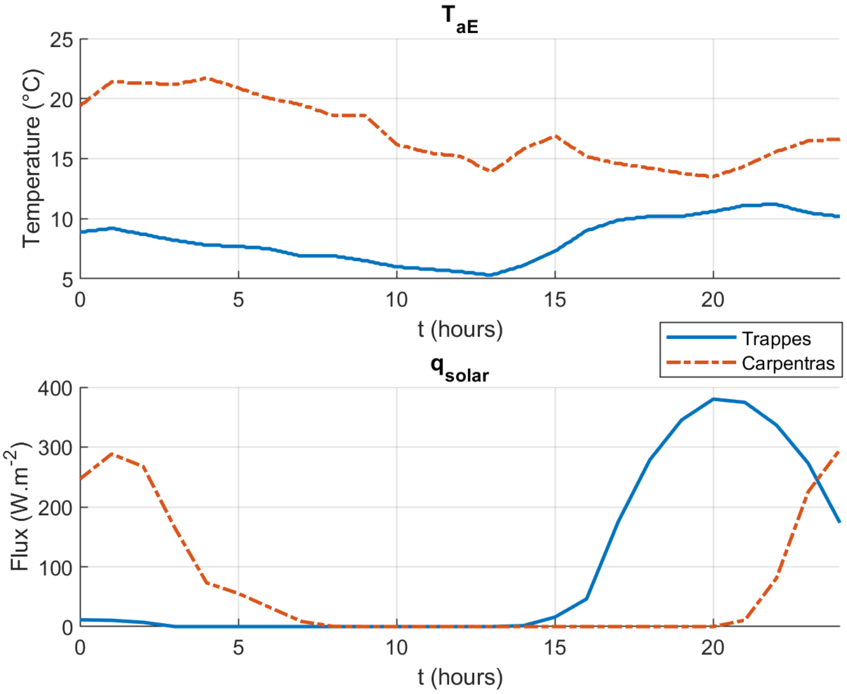

Figure 2.2: External air temperature and solar radiation in Trappes and Carpentras measured by Météo France.

Two variables of external boundary conditions, which are the external air temperature (noted T_{aE}) and the solar radiation (noted q_{solar}), are measured. In the case of the laboratory test, these values are controlled and usually constant. However, in an *in-situ* measurement, they are never constant. Therefore, to simulate an *in-situ* case, the real measurement data from Météo France database and recorded in two regions of France (Trappes and Carpentras) are used. Figure 2.2 shows these measurement data for three days, so at least six different real outdoor conditions are possible for the numerical study. Note that these environmental conditions are supposed homogeneous on the whole surface of the wall. All parameters are detailed in Table 2.1.

In this work, a wall of 2x2 m^2 is studied, and the thermal excitation will be placed on a zone at the center of this wall to create a symmetrical configuration. Then, it leads to a question of how big this zone is. Suppose the excitation heat flux is applied on the wall's whole surface (or limited but big enough). In that case, there is no difference between 1D and 3D simulations (or measurement data), so it is perfect for parameter estimation, but it is impossible in real measurement. If it is too small, differences between 1D and 3D simulations become more important because of thermal diffusion in the lateral direction. It can then lead to a bad

Parameter	Nomenclature	Remarks
Input		
Internal air temperature	T_{aI}	Constant at 20 °C
Internal heat transfer coefficient	h_I	Constant at 7.7 W.m^{-2}.K^{-1}
Thermal excitation flux	q_{exci}	Constant at 400 W.m^{-2}
External air temperature	T_{aE}	Variable
External heat transfer coefficient	h_E	Constant at 25 W.m^{-2}.K^{-1}
Incident solar radiation	q_{solar}	Variable
Output		
Internal surface temperature	T_{SI}	Minimization variable in parameter estimation
Absorbed flux by internal surface	q_{SI}	
External surface temperature	T_{SE}	
Absorbed flux by external surface	q_{SE}	Not necessary in measurement

Table 2.1: Input and output parameters of numerical simulation.

parameter estimation.

A small test is launched to find a suitable size of the heating zone. Several simulations in 3D COMSOL of a wall (IWI 1 wall in Table 2.3) in using different heating zone sizes are done. A 1D simulation with the same wall configuration is also generated then its T_{SI} is compared to the internal surface temperature at the center of 3D cases. Figure 2.3 shows the evolution of the difference between 1D and 3D cases as a function of the heating surface. According to this profile, there is not much variation of this difference between 0.25, 0.36, and 0.49 m^2. This difference drops close to 0 with a surface larger than 0.64 m^2. However, a larger heating zone means a heavier and more complicated system of thermal excitation. The surface of 0.36 m^2 (or 0.6×0.6 m^2) is chosen for applying thermal excitation. Moreover, 0.6 m is a common distance between wood (or metal) frames inside the wall. To characterize the thermal resistance of the studied wall well, these thermal bridges should be avoided. So, 0.6×0.6 m^2 is chosen for the heating zone area in this study.

This limited heating area will, therefore, be taken into account in 3D simulation for generating numerical data. The measurement data of interest (surface temperature and absorbed flux) will be collected at the center of the wall by averaging values in a smaller zone of 0.2x0.2 m^2 to be used as input data for estimating the thermal resistance (more details will be given in Chapter 3) as shown in Figure 2.4. The other sides of the wall are considered adiabatic because they are sufficiently far from the thermal excitation zone.

Three different wall typologies are used during the whole study: Internal Wall Insulation

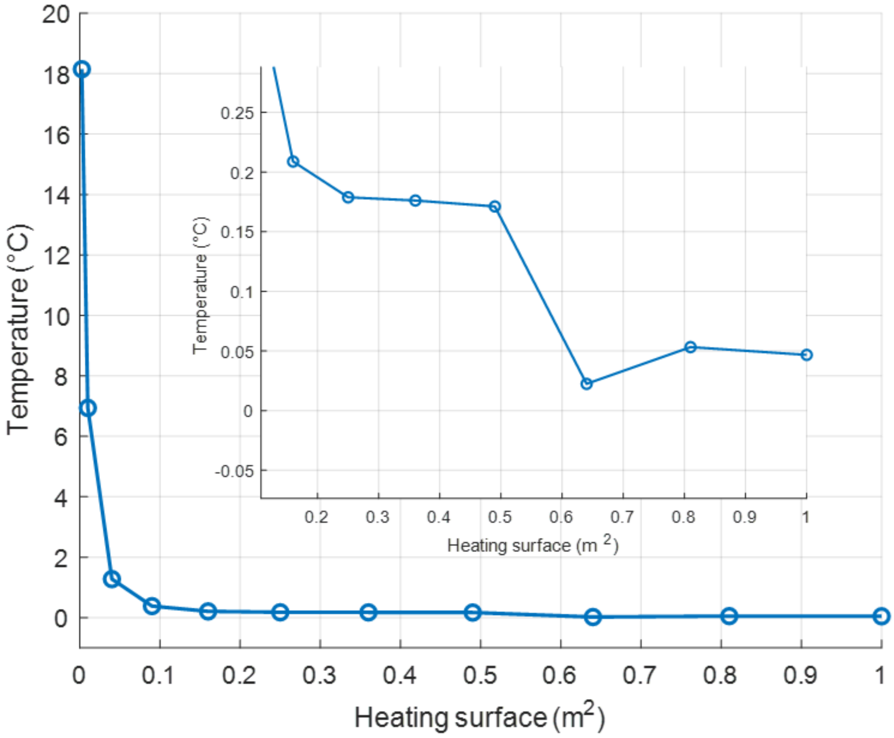

Figure 2.3: The difference of 1D-3D data as a function of heating surface.

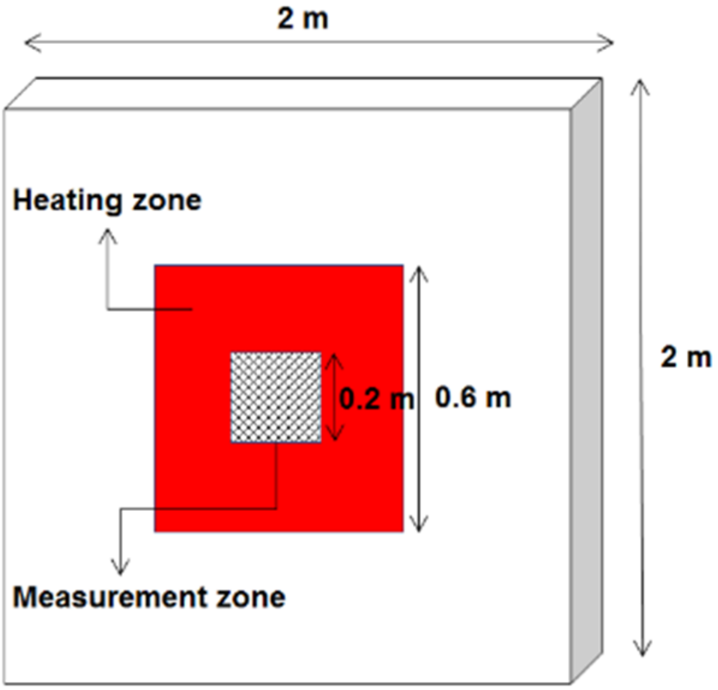

Figure 2.4: Schematic view of the indoor thermal excitation.

(namely IWI), External Wall Insulation (namely EWI) and Single Wall (namely SW) because of their popularity in France, especially IWI wall (around 70% of existing walls). Because of the lack of insulation, the SW wall is classified as a poorly insulated type, and it will represent the case that needs to be renovated. On the other hand, the IWI and EWI walls, which have an insulation layer, present high thermal resistance. Moreover, because the thermal excitation is applied on the internal wall surface, the IWI type, whose insulation layer is close to the internal surface, is expected to be suitable for the proposed configuration. Then, during the numerical study, including data simulation and parameter estimation, five wall configurations are analyzed: 3 IWI walls, 1 EWI wall, and 1 SW wall. The material and physical characteristics of these three walls are presented in Tables 2.2 and 2.3. These physical properties are derived from professional knowledge and are mainly extracted from French thermal regulation default values [3].

Layer	IWI	EWI	SW
1^{st}(interior)	Internal panel	Internal panel	Internal coating
2^{nd}	Insulation	Support wall	Concrete wall
3^{rd}	Support wall	Insulation	External coating
4^{th}(exterior)	External coating	External cladding	

Table 2.2: Nature of layers of tested wall.

2.3 Thermal quadrupole computation

Quadrupole method is an exact and explicit method for representing linear operation or system, such as in electronics or process control. Instead of using time discretization, this method uses some particular transforms in time and space and variable separations to simplify differential equations until obtaining another representation of these equations, which are simple enough to solve.

Thermal quadrupole computation (noted QUAD) was firstly presented in 1921 by Carslaw [51]. By using the Laplace transform, Carslaw *et al.* converted the heat transfer equation to an "equivalent" electrical circuit by considering temperature as electric potential and heat flux as current [52]. After decades, these notations are still efficient in the representation of thermal systems.

This calculation approach is sometimes considered "semi-analytic" because it requires a numerical inverse Laplace transform due to the complexity of the computation of theoretical inverse transform required to come back time-space. Because of its linearity of matrix computing, the QUAD method may reduce computation time and skip some unnecessary calculation steps.

	Thickness (m)	Thermal conductivity (W.m^{-1}.K^{-1})	Density (kg.m^{-3})	Heat capacity (J.kg^{-1}.K^{-1})
IWI 1	Thermal resistance: 5.66 m^2.K.W^{-1}			
$1^{st}layer$	0.01	0.7	1000	1000
$2^{nd}layer$	0.2	0.036	35	950
$3^{rd}layer$	0.15	2	2300	1000
$4^{th}layer$	0.02	1.2	1100	1000
IWI 2	Thermal resistance: 4.72 m^2.K.W^{-1}			
$1^{st}layer$	0.013	0.25	750	1000
$2^{nd}layer$	0.14	0.032	40	1030
$3^{rd}layer$	0.2	0.7	800	1000
$4^{th}layer$	0.01	1.3	1500	1000
IWI 3	Thermal resistance: 2.34 m^2.K.W^{-1}			
$1^{st}layer$	0.013	0.3	750	1000
$2^{nd}layer$	0.08	0.04	90	1000
$3^{rd}layer$	0.2	0.7	1300	1000
$4^{th}layer$	0.01	1.5	1100	1000
SW	Thermal resistance: 0.19 m^2.K.W^{-1}			
$1^{st}layer$	0.01	0.4	800	1000
$2^{nd}layer$	0.2	1.5	700	1000
$3^{rd}layer$	0.05	1.6	650	1000
EWI	Thermal resistance: 4.14 m^2.K.W^{-1}			
$1^{st}layer$	0.02	0.5	1200	1000
$2^{nd}layer$	0.2	2.3	2000	1000
$3^{rd}layer$	0.2	0.05	150	1200
$4^{th}layer$	0.02	1.8	2000	1000

Table 2.3: Physical characteristics of each layer of the five studied walls.

The following parts will present the theory, the computation steps, and some required transforms of this method (from 1D to 3D) and the integration of boundary conditions into the computation.

2.3.1 Thermal quadrupoles in unidirectional (1D) model

A simple homogeneous wall of isotropic material which has infinite lateral dimensions (Cf. Figure 2.5) is considered. Its thermal conductivity, thermal diffusivity and thickness are noted λ, a and e respectively. In this case, the lateral heat flux is ignored and only longitudinal flow is considered, then the geometry for computation is one dimension (noted 1D).

According to the law of heat conduction, also known as Fourier's law, the rate of heat transfer flow through a material is proportional to the negative gradient in the temperature and to the area. There are two different forms of this law, the integral form (2.1) which presents the total amount of energy flow $Q(x,t)$ and the differential form (2.2) which looks at the local flow

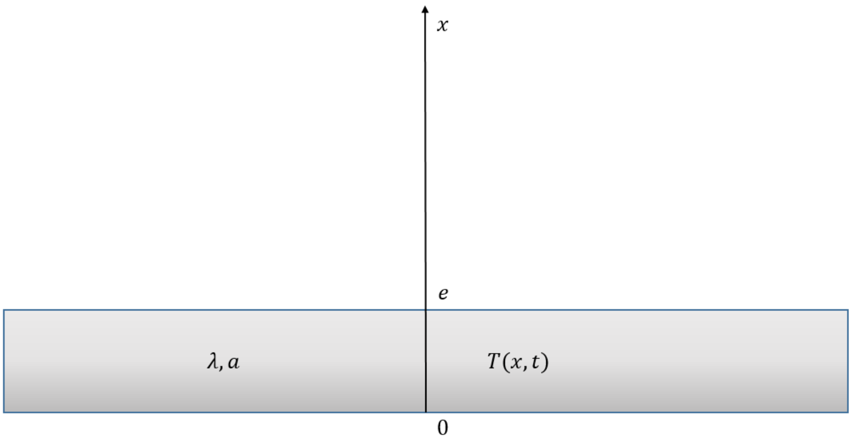

Figure 2.5: Homogeneous and isotropic wall considered in 1D computation.

rate $\vec{q}(x,t)$ (or heat flux):

$$\frac{\partial Q}{\partial t}(x,t) = -\lambda \nabla T(x,t) dS \tag{2.1}$$

$$q(x,t) = -\lambda \vec{\nabla} T(x,t) \vec{n}_x \tag{2.2}$$

If a small layer whose thickness and section are dx and dS inside the wall at x is focused on, a second relation between heat fluxes, which comes in at x and out at $x + dx$ during dt, and temperature variation $dT(x,t) = T(x,t+dt) - T(x,t)$ at this position x will be obtained as follows:

$$(q(x+dx,t) - q(x,t))dtdS = -\rho C_p (T(x,t+dt) - T(x,t))dxdS \tag{2.3}$$

or, if dx and dt are small enough,

$$\frac{\partial q}{\partial x}(x,t) = -\rho C_p \frac{\partial T}{\partial t}(x,t) \tag{2.4}$$

where ρC_p is the volumetric heat capacity of considered wall. By putting equation (2.2) into (2.4), heat transfer equation that describes temperature field in function of x and t can be expressed as:

$$\frac{\partial^2 T}{\partial x^2}(x,t) = \frac{1}{a} \frac{\partial T}{\partial t}(x,t) \tag{2.5}$$

where $a = \lambda/(\rho C_p)$. The classic computation ways as Finite element method will launch space and time discretisations for x and t respectively. However, QUAD method is based on another approach to solve this equation.

The Laplace transform (noted LT) is applied to $T(x,t)$ function to eliminate the time derivative of $T(x,t)$ in equation (2.5). The expression of Laplace transformed function $F(p)$ of a function $f(t)$ is:

$$F(p) = \int_0^\infty e^{-pt} f(t) dt = LT(f(t)) \tag{2.6}$$

where p is the Laplace variable. The advantage of this transform is that it can transforms a derivative to a linear function. It means that the transformed expression of temporal derivative of $T(x,t)$ can be rewritten as:

$$LT\left(\frac{\partial T}{\partial t}(x,t)\right) = p\theta(x,p) - T(t=0) \tag{2.7}$$

where $\theta(x,p)$ is the Laplace transformed function of $T(x,t)$. By supposing $T(x,0) = 0$, then new equation of transformed temperature $\theta(x,p)$ that contains only partial derivative in the direction x is:

$$\frac{\partial^2 \theta}{\partial x^2}(x,p) = \frac{p}{a}\theta(x,p) \tag{2.8}$$

Now, equation (2.8) contains only the second spatial derivative of transformed temperature in Laplace space $\theta(x,p)$. This equation can be easily solved and its solution is composed by 2 hyperbolic functions with 2 constants K_1 and K_1 as follows:

$$\theta(x,p) = K_1 ch(x\sqrt{\frac{p}{a}}) + K_2 sh(x\sqrt{\frac{p}{a}}) \tag{2.9}$$

Furthermore, using relation (2.2) above, transformed heat flux density $\phi(x,p)$ can be expressed as:

$$\phi(x,p) = -\lambda\frac{\partial\theta}{\partial x}(x,p) = -\lambda K_1\sqrt{\frac{p}{a}} sh(x\sqrt{\frac{p}{a}}) - \lambda K_2\sqrt{\frac{p}{a}} ch(x\sqrt{\frac{p}{a}}) \tag{2.10}$$

Equations (2.9) and (2.10) can be grouped in a matrix expression to describe both temperature and heat flux at any position x in the wall:

$$\begin{pmatrix}\theta(x,p)\\ \phi(x,p)\end{pmatrix} = \begin{pmatrix} ch(x\sqrt{p/a}) & sh(x\sqrt{p/a}) \\ -\lambda\sqrt{p/a}\, sh(x\sqrt{p/a}) & -\lambda\sqrt{p/a}\, ch(x\sqrt{p/a})\end{pmatrix}\begin{pmatrix}K_1\\ K_2\end{pmatrix} \tag{2.11}$$

In fact, the two coefficients K_1 and K_2 can be found by using boundary condition at

$x = e$:

$$\begin{pmatrix} K_1 \\ K_2 \end{pmatrix} = \begin{pmatrix} ch(e\sqrt{p/a}) & sh(e\sqrt{p/a}) \\ -\lambda\sqrt{p/a}\, sh(e\sqrt{p/a}) & -\lambda\sqrt{p/a}\, ch(e\sqrt{p/a}) \end{pmatrix}^{-1} \begin{pmatrix} \theta(e,p) \\ \phi(e,p) \end{pmatrix} \tag{2.12}$$

These equations allow writing a direct relation between thermal states on the front ($x = 0$) and rear faces ($x = e$) of the wall:

$$\begin{pmatrix} \theta(0,p) \\ \phi(0,p) \end{pmatrix} = \begin{pmatrix} 1 & 0 \\ 0 & -\lambda\sqrt{p/a} \end{pmatrix} \begin{pmatrix} ch(e\sqrt{p/a}) & sh(e\sqrt{p/a}) \\ -\lambda\sqrt{p/a}\, ch(e\sqrt{p/a}) & -\lambda\sqrt{p/a}\, sh(e\sqrt{p/a}) \end{pmatrix}^{-1} \begin{pmatrix} \theta(e,p) \\ \phi(e,p) \end{pmatrix} \tag{2.13}$$

By doing some matrix computation, this equation can be reformed as:

$$\begin{pmatrix} \theta(0,p) \\ \phi(0,p) \end{pmatrix} = \begin{pmatrix} ch(e\sqrt{p/a}) & (\lambda\sqrt{p/a})^{-1}\, sh(e\sqrt{p/a}) \\ \lambda\sqrt{p/a}\, sh(e\sqrt{p/a}) & ch(e\sqrt{p/a}) \end{pmatrix} \begin{pmatrix} \theta(e,p) \\ \phi(e,p) \end{pmatrix} \tag{2.14}$$

or a shorter expression as

$$\begin{pmatrix} \theta(0,p) \\ \phi(0,p) \end{pmatrix} = \begin{pmatrix} A & B \\ C & A \end{pmatrix} \begin{pmatrix} \theta(e,p) \\ \phi(e,p) \end{pmatrix} = \mathbf{M} \begin{pmatrix} \theta(e,p) \\ \phi(e,p) \end{pmatrix} \tag{2.15}$$

Here, **M** is called the transfer matrix from $x = 0$ to $x = e$ of a unidirectional structure of an isotropic wall. The explicit calculation of this matrix will be presented in Appendix A1.

If the considered wall has n different layers where the transfer matrix of i^{th} layer is M_i (Cf. Figure 2.6), global transfer matrix of the whole wall is the product of all its layer matrices:

$$\begin{pmatrix} \theta(0,p) \\ \phi(0,p) \end{pmatrix} = M_1 M_2 \dots M_i \dots M_n \begin{pmatrix} \theta(e,p) \\ \phi(e,p) \end{pmatrix} \tag{2.16}$$

This flexibility of calculation for multilayer walls is one of the great advantages of the QUAD method compared to other methods in heat transfer simulation. This relation means that if the thermal state (θ and ϕ or T and q) of front face is known, it is always possible to calculate the thermal state on the rear face, and inversely. Moreover, there is no need to calculate for each node between two different layer as other types of computation so that it will take less time than other methods. However, this computation is valid if and only if $T(x, 0) = 0$ and $q(x, 0) = 0$. Otherwise, non-zero terms $T(x, 0)$ and $q(x, 0)$ must be added into the expressions of $\theta(x, p)$

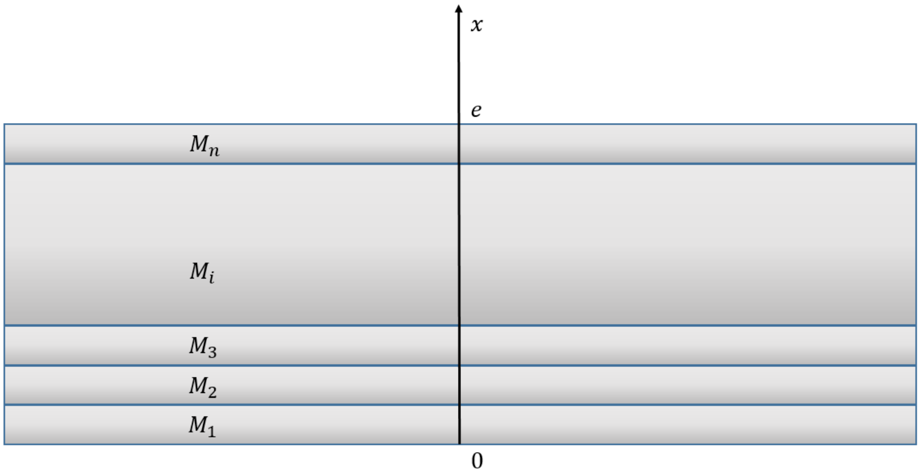

Figure 2.6: Multi-layer wall.

and $\phi(x,p)$. Therefore, the QUAD method considers only the temporal variation (or transient regime) of thermal states of the considered system, including the tested wall and environment. So that, a steady-state computation is required to complete the output of model.

2.3.2 Steady-state computation

Steady-state regime of a system represents the thermal equilibrium of the considered system. It means that there is no change in thermal state. In principle, there is a distribution of temperature of observed object (inside and on the boundary) which satisfies that the algebraic sum of heat flux flowing into the considered wall in the steady-state regime is always zero. In the case of a building wall, we can calculate rapidly these values by using thermal-electrical equivalence.

General idea of thermal-electrical equivalence is that a thermal system is converted into an electrical circuit by switching roles of temperature to voltage and heat flux to current. Let us consider a wall whose thermal resistance is $R = R_i + R_{-i}$ (R_i and R_{-i} are the thermal resistance of two parts of the wall from a particular point i inside the wall to internal and external surfaces respectively). Internal and external heat transfer coefficients (h_I, h_E) which represent both radiative and convective transfers are supposed known. An equivalent electrical circuit is presented in Figure 2.7.

Thus, T_{SE} and T_{SI} can be calculated by:

$$T_{SE} = T_{aE} + (T_{aI} - T_{aE})\frac{1/h_E}{R + 1/h_I + 1/h_E} \tag{2.17}$$

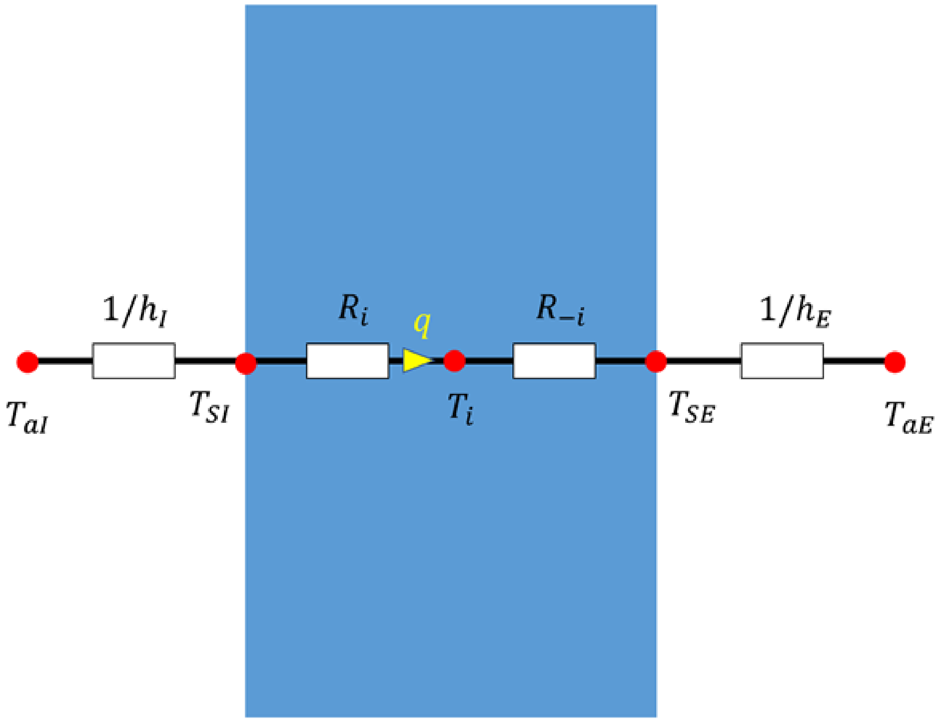

Figure 2.7: Equivalent electrical circuit of a wall in steady-state regime.

$$T_{SI} = T_{aI} - (T_{aI} - T_{aE})\frac{1/h_I}{R + 1/h_I + 1/h_E} \tag{2.18}$$

Then, the steady-state heat flux q which travels through the wall is obtained by:

$$q = \frac{T_{SI} - T_{SE}}{R} \tag{2.19}$$

Moreover, for a point i inside the wall, the temperature at the steady-state regime can be expressed as:

$$T_i = T_{aI} - (T_{aI} - T_{aE})\frac{1/h_I + R_i}{R + 1/h_I + 1/h_E} \tag{2.20}$$

2.3.3 Thermal quadrupoles in high dimensional model (3D)

Unidirectional (or 1D) case is the simplest simulation because there is no lateral heat diffusion, but this effect can not be ignored in higher dimension as 2D/3D. Thanks to Fourier series, the higher dimensional transfer equations can be solved in the same way as in 1D.

In 3D configuration, two other dimensions y and z are added into equation (2.5), as follows:

$$\lambda_x \frac{\partial^2 T}{\partial x^2}(x,y,z,t) + \lambda_y \frac{\partial^2 T}{\partial y^2}(x,y,z,t) + \lambda_z \frac{\partial^2 T}{\partial z^2}(x,y,z,t) = \rho C_p \frac{\partial T}{\partial t}(x,y,z,t) \tag{2.21}$$

where λ_x,λ_y and λ_z are the thermal conductivity of the wall in the direction x,y and z respectively. After applying Laplace transform, this equation becomes:

$$\lambda_x \frac{\partial^2 \theta}{\partial x^2}(x,y,z,p) + \lambda_y \frac{\partial^2 \theta}{\partial y^2}(x,y,z,p) + \lambda_z \frac{\partial^2 \theta}{\partial z^2}(x,y,z,p) = p\rho C_p \theta(x,y,z,p) \tag{2.22}$$

In this study, all materials are considered isotropic. Then, $\lambda_x = \lambda_y = \lambda_z = \lambda$. Then, equation 2.22 is presented as:

$$\frac{\partial^2 \theta}{\partial x^2}(x,y,z,p) + \frac{\partial^2 \theta}{\partial y^2}(x,y,z,p) + \frac{\partial^2 \theta}{\partial z^2}(x,y,z,p) = \frac{p}{a}\theta(x,y,z,p) \tag{2.23}$$

Instead of solving in the direction x as 1D case, 3D case must take into account the lateral directions (y and z). To simplify the differential element in y and z in equation 2.23, the integral transform (noted IT) is proposed to be used here. Based on Fourier series development, it is possible to present a function $f(x)$ by a sum of a series of periodic functions $g(\alpha_n, x)$ (sines and cosines) as:

$$f(x) = \sum_{n=0}^{\infty} \left(\hat{f}(\alpha_n) g(\alpha_n, x) \right) \tag{2.24}$$

where α_n and $\hat{f}(\alpha_n)$ are the eigenvalue of nth order and transformed function of $f(x)$ (or $IT(f(x))$) at this order (the detailed information of these notations will be described in Section 2.4.3). Thanks to periodic characteristics of $g(\alpha_n, x)$, the second derivative of $f(x)$ can be transformed as:

$$IT\left(\frac{\partial^2 f}{\partial x^2}(x) \right) = -\sum_{n=0}^{\infty} \alpha_n^2 \hat{f}(\alpha_n) g(\alpha_n, x) \tag{2.25}$$

If the integral transform is applied twice for y and z on both sides of equation 2.23, then only a particular order (n, m) is considered. Equation 2.23 becomes:

$$\frac{\partial^2 \hat{\theta}}{\partial x^2}(x, \alpha_n, \beta_m, p) = \left(\frac{p}{a} + \alpha_n^2 + \beta_m^2 \right) \hat{\theta}(x, \alpha_n, \beta_m, p) \tag{2.26}$$

Here, α_n and β_m are respectively eigenvalues for Fourier series development of $\theta(x, y, z, p)$ according to y and z and $\hat{\theta}(x, \alpha_n, \beta_m, p)$ is the transformed representation of $\theta(x, y, z, p)$. In fact, the choice of eigenvalues depends on boundary conditions of considered configuration and the Section 2.4.3 and Appendix A2 will show more details.

Equation (2.26) is similar to equation (2.8) in 1D. The term p/a in 1D is replaced by

$p/a + \alpha_n^2 + \beta_m^2$ in 3D and the computation steps to obtain transfer matrix **M** are the same, even for multilayer wall. However, the dimension of **M** is not the same. In 1D cases, θ and ϕ stay in a vector of two elements but, in 3D, they form a matrix whose each element represents an equation as 2.26 for a particular (n, m) order. So that, if this matrix of our 3D simulation has N elements, it will take N times longer than an 1D case. That is why 3D model is not suitable to be used for parameter estimation because of long computation time (see more in Section 2.5.2).

2.3.4 Boundary conditions in thermal quadrupole method

The previous section presented how to calculate thermal state of a wall by using the transfer matrix between two surfaces of the wall. This matrix leads to two equations so that at least two of four thermal states of the wall must be known in order to find out the others. This section will talk about how to create these two known states by using boundary conditions.

As mentioned at the beginning of this chapter, the boundary conditions considered in simulations are the solar radiation, the convective heat transfer on the internal and external surfaces and the thermal excitation flux.

The common thing between interior and exterior boundaries is the convective/radiative surface heat transfer. In both cases, this heat flux can be expressed by:

$$q_{conv/rad} = h(T_a - T_S) \tag{2.27}$$

where T_a and T_S are the air and surface temperature and h is the global heat transfer coefficient, including convection and radiation. Depending on the environment, the value of h can be varied as observed in the literature study. In case where there is only heat convection/radiation in considered system, this heat flux will be equal to the flux absorbed by the surface of wall q_S:

$$q_{conv/rad} = q_S \tag{2.28}$$

By replacing T and q by corresponding transformed parameters (θ and ϕ respectively), the quadrupole expression of heat convection/radiation boundary condition is expressed as:

$$\begin{pmatrix} \theta_S(p) \\ \phi_S(p) \end{pmatrix} = \begin{pmatrix} 1 & -1/h \\ 0 & 1 \end{pmatrix} \begin{pmatrix} \theta_a(p) \\ \phi_a(p) \end{pmatrix} \tag{2.29}$$

Besides, in the case of imposed heat flux such as thermal excitation or solar radiation, it is possible to place them directly to the position of absorbed flux, for instance for the solar radiation $\phi_{solar}(p)$:

$$\begin{pmatrix} \theta_S(p) \\ \phi_S(p) \end{pmatrix} = \begin{pmatrix} 0 \\ \phi_{solar}(p) \end{pmatrix} \tag{2.30}$$

Then, by using equations (2.29) and (2.30) for the four boundary conditions mentioned at the beginning, the set of thermal quadrupole equations associated with the considered wall are:

$$\begin{pmatrix} \theta_{SI} \\ \phi_{SI} \end{pmatrix} = \begin{pmatrix} 0 \\ \phi_{exci} \end{pmatrix} + \begin{pmatrix} 1 & -1/h_I \\ 0 & 1 \end{pmatrix} \begin{pmatrix} \theta_{aI} \\ \phi_{aI} \end{pmatrix} \tag{2.31}$$

$$\begin{pmatrix} \theta_{SE} \\ \phi_{SE} \end{pmatrix} = \begin{pmatrix} 1 & 1/h_E \\ 0 & 1 \end{pmatrix} \begin{pmatrix} \theta_{aE} \\ \phi_{aE} \end{pmatrix} + \begin{pmatrix} 0 \\ -\phi_{solar} \end{pmatrix} \tag{2.32}$$

$$\begin{pmatrix} \theta_{SI} \\ \phi_{SI} \end{pmatrix} = M \begin{pmatrix} \theta_{SE} \\ \phi_{SE} \end{pmatrix} \tag{2.33}$$

Equations (2.31),(2.32) and (2.33) represent respectively all thermal states on the internal and external surfaces of the wall. Here, to avoid confusing the direction of heat fluxes, the positive direction of flux is decided to come from interior to exterior. That is why a negative sign will be put before the solar radiation in equation (2.32). Thanks to linear characteristics of QUAD computation, the computations with the external environmental conditions and with the thermal excitation can be separated.

Supposing that the absorbed heat fluxes on the internal and external wall surfaces are composed by (ϕ_{aI-1},ϕ_{aI-2}) and (ϕ_{aE-1},ϕ_{aE-2}). By using equation 2.34 (or equation 2.35), the heat fluxes ϕ_{aI-1} and ϕ_{aE-1} (or ϕ_{aI-2} and ϕ_{aE-2}) can be determined when using only internal and external environmental conditions (or only the thermal excitation). This computation is useful for 3D QUAD computation because only thermal excitation which is applied on the limited zone is taken into account in the 3D model. The external conditions which are considered homogeneous on the whole surface can be computed by 1D model so that it costs less time than computing all conditions in 3D.

$$\begin{pmatrix} 1 & -1/h_I \\ 0 & 1 \end{pmatrix} \begin{pmatrix} \theta_{aI} \\ \phi_{aI-1} \end{pmatrix} = M \left(\begin{pmatrix} 1 & 1/h_E \\ 0 & 1 \end{pmatrix} \begin{pmatrix} \theta_{aE} \\ \phi_{aE-1} \end{pmatrix} + \begin{pmatrix} 0 \\ -\phi_{solar} \end{pmatrix} \right) \tag{2.34}$$

$$\begin{pmatrix} 0 \\ \phi_{exci} \end{pmatrix} + \begin{pmatrix} 1 & -1/h_I \\ 0 & 1 \end{pmatrix} \begin{pmatrix} 0 \\ \phi_{aI-2} \end{pmatrix} = M \begin{pmatrix} 1 & 1/h_E \\ 0 & 1 \end{pmatrix} \begin{pmatrix} 0 \\ \phi_{aE-2} \end{pmatrix} \tag{2.35}$$

Two different configurations of simulation are considered in this numerical study. The first configuration, which uses all three equations (2.31), (2.32) and (2.33), is called **EWC** (Excitation With Convection). This configuration requires the exact value of h_I. However, as shown in the literature review, it is the most difficult parameter to determine in experiments because it depends on a lot of factors (temperature, wind speed, nature of the wall, etc.). Moreover, the thermal resistance estimation is very sensitive to this parameter (see more in Section 3.7.1).

That is why the second configuration called **AbF** (Absorbed Flux) which uses the absorbed flux on the internal surface ϕ_{SI} instead of thermal excitation flux and internal convective heat flux is proposed. In this configuration, only equations (2.32) and (2.33) are used then h_I does not exist anymore in the computation.

Table 2.4 presents requires inputs (fixed and measured) and computed outputs of each model.

Model	Measured inputs	Fixed inputs	Outputs
EWC	q_{solar}, T_{aI}, T_{aE}	h_I, h_E, q_{exci}	T_{SI}, q_{SI}, T_{SE}, q_{SE}
AbF	q_{solar}, q_{SI}, T_{aE}	h_E	T_{SI}, T_{SE}, q_{SE}

Table 2.4: Inputs and outputs of EWC and AbF models.

2.4 Applied transforms in thermal quadrupole model

2.4.1 Laplace transform: continuous and discrete

As presented in Section 2.3.1, the Laplace transform helps us to simplify the temporal derivative and makes the heat transfer equation easier to solve. We do not have to calculate the Laplace transform of the thermal state of the wall because they are obtained from the transfer matrix and the boundary conditions. So, the Laplace transform computation will be applied on the boundary conditions. According to Table A2.1 in Appendix A2, a list of functions and their transformed functions is presented. However, all measured data are discrete and sometimes it is not easy to form a good enough analytic representation for them. Moreover, there are some special functions which can not be transformed analytically by Laplace transform (for example, the standard normal distribution). Therefore, an approximation for discrete Laplace transform is proposed by using linear calculation.

Firstly, several small sub-series which contain only 2 consecutive points are cut from the original series of measurement data. The original series can be expressed by a sum of these sub-series multiplied by a rectangular function $rect(t_i, t_{i+1})$ limited by the interval $[t_i, t_{i+1}]$ (Cf. Figure 2.8). For example, a series called $T(t)$ where the time step is $\Delta t = t_{i+1} - t_i$ can be written as:

$$T(t) = \sum_i \left(\frac{(T(t_{i+1}) - T(t_i))(t - t_i)}{\Delta t} + T(t_i) \right) * rect(t_i, t_{i+1}) \tag{2.36}$$

A bounded linear function is easily transformed by Laplace transform. According to the Table A2.1, the transformed representation of the equation (2.36) in Laplace space is:

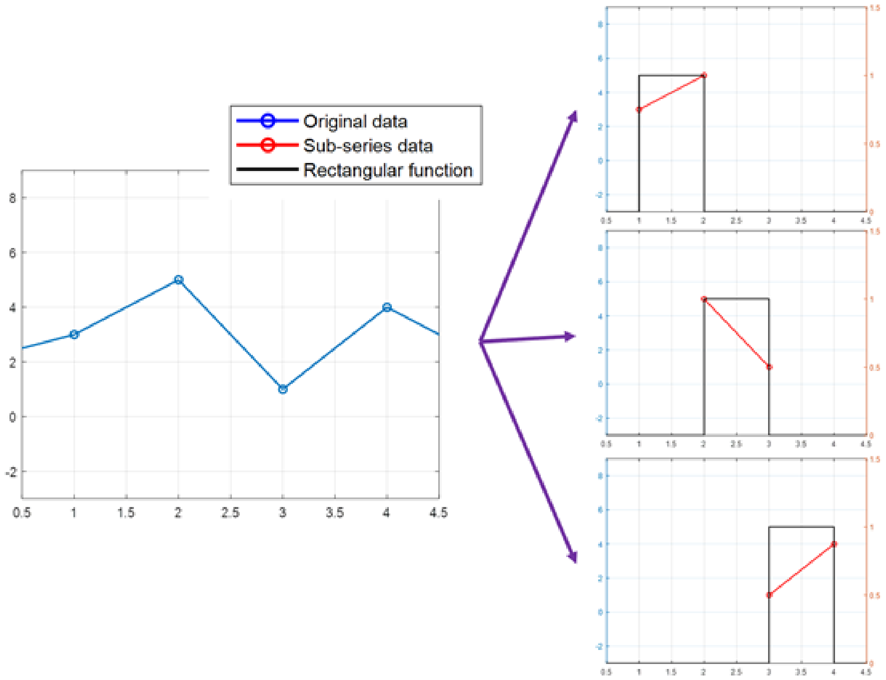

Figure 2.8: Original data (blue line) and sub-series data (red line).

$$\theta(p) = \sum_i (g_i(t_i, p) - g_i(t_{i+1}, p)) \tag{2.37}$$

where

$$g_i(t,p) = exp(-pt)\left(\frac{(T(t_{i+1}) - T(t_i))t}{p\Delta t} + \left(T(t_i) - t_i\frac{T(t_{i+1}) - T(t_i)}{\Delta t} + \frac{(T(t_{i+1}) - T(t_i))}{p\Delta t}\frac{1}{p}\right)\frac{1}{p}\right) \tag{2.38}$$

In addition, to avoid discontinuity at the end of series ($t = t_{end}$), a hypothesis that temporal signal after t_{end} remains constant and equals to final measurement value $T(t_{end})$ until infinite so that equation (2.37) has to include an additional term (called discontinuity correction term) as:

$$\theta(p) = \sum_i (g(t_i, p) - g(t_{i+1,p})) + \frac{T(t_{end}) * exp(-pt_{end})}{p} \tag{2.39}$$

To demonstrate the efficiency of this term, two transformed data of a temperature measurement are used, one with the additional term (noted DATA 1) and an other one without this term (DATA 2). By using the same inverse technique to return to time space, we obtain two different rebuilt data. As observed in Figure 2.9, both rebuilt data are quite close to original one but the case with DATA 1 seems better than with DATA 2 because it does not present any fluctuation at the end of the profile. Therefore, this hypothesis should be considered in discrete Laplace transform to avoid numerical error.

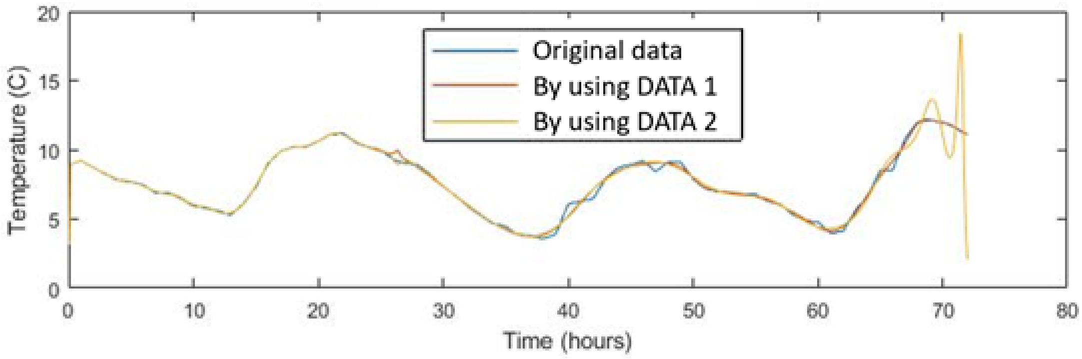

Figure 2.9: Comparison between original data (blue line) and the rebuilt data by using discontinuity correction term (DATA 1, red line) and not using (DATA 2, yellow line).

In fact, there is one thing which should be studied with discrete Laplace transform: the time step Δt. If this value is too big, it is possible to skip the important variation of measurement data (for example, in case of periodic data, if the time step is equal to its period, we observe only a constant all the time). On the other hand, if this parameter is too small, it will take time to compute and sometimes it is not necessary. Section 2.5.3 will detail the choice of this parameter value.

2.4.2 Inverse Laplace transform

After finishing QUAD computation and obtaining values of θ and ϕ, an inverse method for Laplace transform is required to come back to time-space. The theoretical computation of the inverse Laplace transform is:

$$f(t) = \frac{1}{2\pi j} \lim_{T \longrightarrow \infty} \int_{\gamma - jT}^{\gamma + jT} F(p) e^{pt} dp \tag{2.40}$$

where must be larger than the real part of all singularities of F(p)

This integral is very difficult to compute directly because it covers whole complex space. Then, if a numerical computation with a discretization method is used, it would take a huge time to calculate. Therefore, several approximations are proposed for computing this inverse transform.

Bromwich contour integral or the complex inversion formula gives us an integral representation of the inverse Laplace transform based on the Residue theorem (or Cauchy's residue theorem) [53] as:

$$f(t) = \frac{1}{2\pi j} \sum_{k=1}^{n} Res(e^{pt}F(p), p_k^0) \int_{\gamma - j\infty}^{\gamma + j\infty} \frac{dp}{p - p_k^0} \tag{2.41}$$

Here, $Res(e^{pt}F(p), p_k^0)$ is the residue of function $e^{pt}F(p)$ at its singularities (p_1^0, p_2^0, ..., p_n^0). This method presents the most analytic approach for inverse Laplace transform. However, it is not always applicable in any case because of difficulties of finding singularity values of $e^{pt}F(p)$, especially in discrete case.

Another theoretical approach for computing $f(x)$ in equation 2.40 was developed by Widder [54]:

$$f(t) = \lim_{n \longrightarrow \infty} \frac{(-1)^n}{n!} \left(\frac{n}{t}\right)^{n+1} F^{(n)}\left(\frac{n}{t}\right) \tag{2.42}$$

These two methods above come from theoretical calculation of equation (2.40). They are quite useful if we would like to inverse an analytic $F(p)$ which is differentiable or has at least one singularity. In this study, considering heat transfers within a multilayer wall, the analytic expression of transformed thermal states is quite complicated. Then, to obtain their singularities or nth derivative, it will be a costly work.

Therefore, numerical inverse of Laplace transform are interesting tools. There are two algorithms for inverse Laplace transform that are used commonly, Stehfest's [55] and de Hoog's algorithms [56].

Stehfest's algorithm can be expressed by:

$$f(t) = \frac{ln(2)}{t}\sum_{i=1}^{N} V_i F\left(\frac{iln(2)}{t}\right) \tag{2.43}$$

where N is a pair number and

$$V_i = (-1)^{N/2+i} \sum_{k=\left\lfloor \frac{i+1}{2} \right\rfloor}^{min(i,N/2)} \frac{k^{N/2}(2k)!}{(N/2-k)!k!(k-1)!(i-k)!(2k-i)!} \tag{2.44}$$

Here, $\lfloor \cdot \rfloor$ means entire part.

On the other hand, de Hoog's algorithm presents three different forms which are based on Fourier series for inverse Laplace transform in the following way:

$$f_1(t) = \frac{2}{T}exp(\gamma t)\left(\frac{F(\gamma)}{2} + \sum_{k=1}^{\infty} Re\left(F\left(\gamma + \frac{jk\pi}{T}\right)\right)cos\left(\frac{k\pi t}{T}\right)\right) \tag{2.45}$$

$$f_2(t) = -\frac{2}{T}exp(\gamma t)\sum_{k=1}^{\infty} Im\left(F\left(\gamma + \frac{jk\pi}{T}\right)\right)sin\left(\frac{k\pi t}{T}\right) \tag{2.46}$$

$$f_3(t) = \frac{1}{T}exp(\gamma t)\left(\frac{F(\gamma)}{2} + \sum_{k=1}^{\infty} Re\left(F\left(\gamma + \frac{jk\pi}{T}\right)exp\left(\frac{jk\pi t}{T}\right)\right)\right) \tag{2.47}$$

In [56], de Hoog showed that the discretization error for f_3 was lower than f_1 and f_2. For this reason, in this study, the third form is used for all tests of de Hoog's method.

A small comparison by using these two numerical methods was carried out to find which one is the best. In Figure 2.10, both methods return the same results but de Hoog's method takes less time than Stehfest's (more than 10 times). Therefore, considering computation time and output precision, de Hoog's approach for inverse Laplace transform will be used in this work.

Karl Hollenbeck [57] in Technical University of Denmark created a Matlab code called "invlap.m" which is based on equation (2.47) and his code helps to accelerate the convergence of de Hoog inversion with better overall accuracy. This code is integrated directly into the model developed in this work.

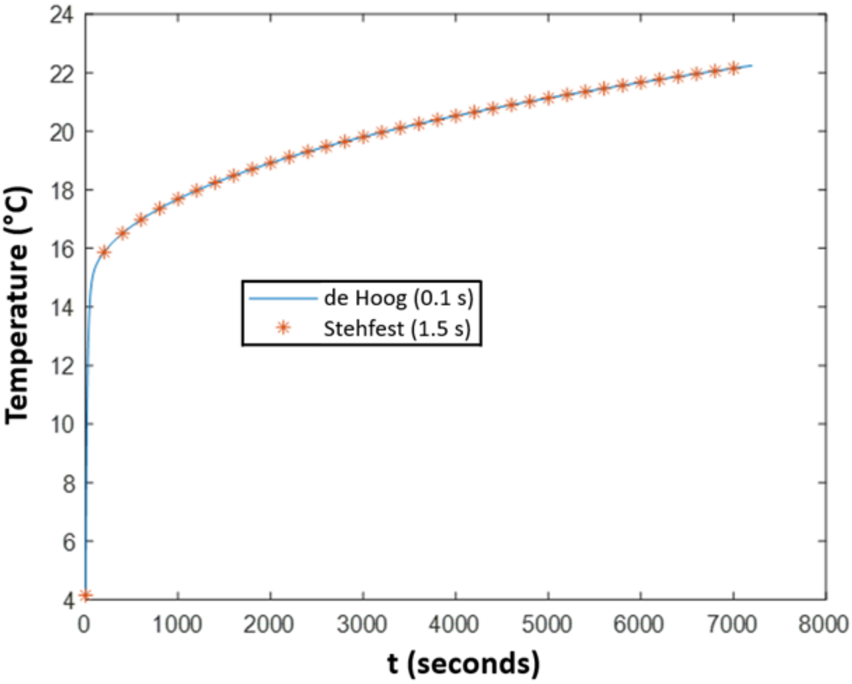

Figure 2.10: An example of two simulations using Stehfest's and de Hoog's algorithms and their computation time (in seconds).

2.4.3 Integral transform

In order to form the transfer matrix in 3D configurations as mentioned in Section 2.3.3, the integral transform which is based on Fourier series is used to handle lateral direction. In fact, by using Fourier series development, every functions $f(x)$ where $x \in [0, L]$ can be written as a sum of cosine and sine terms as:

$$f(x) = \sum_{n=0}^{\infty} \Big(A_n cos(\alpha_n x) + B_n sin(\alpha_n x) \Big) \tag{2.48}$$

where

$$A_n = \frac{2}{L} \int_0^L f(x) cos(\alpha_n x) dx \tag{2.49}$$

$$B_n = \frac{2}{L} \int_0^L f(x) sin(\alpha_n x) dx \tag{2.50}$$

Note that α_n and ($cos(\alpha_n x)$,$sin(\alpha_n x)$) are eigenvalue and eigenfunctions of Fourier series development of $f(x)$. Moreover, equations (2.48), (2.49), and (2.50) can be rewritten with no specific form of eigenfunctions as:

$$f(x) = \sum_{n=0}^{\infty} \Big(\hat{f}(\alpha_n) eigfunc(\alpha_n, x) / N(\alpha_n) \Big) \tag{2.51}$$

$$\hat{f}(\alpha_n) = \int_0^L f(x) eigfunc(\alpha_n, x) dx = IT(f(x)) \tag{2.52}$$

Here, we note $\hat{f}(\alpha_n)$ the transformed function of $f(x)$ at nth order by using the integral transform (noted IT). The cosine and sine functions are replaced by a general form $eigfunc(\alpha_n, x)$ which can be composed by cosine and sine functions. Moreover, a factor $N(\alpha_n)$ is called a transform norm of n^{th} order which is calculated as:

$$N(\alpha_n) = \int_0^{L_x} (eigfunc(\alpha_n, x))^2 dx \tag{2.53}$$

In case of three dimensions (3D), the final eigenfunction is the product of all eigenfunctions of each dimension, idem for the norm. The advantage of this development is that the second derivative of $f(x)$ in x can be simplified by periodic characteristics of cosine and sine functions as:

$$\frac{\partial^2 f}{\partial x^2} = \sum_{n=0}^{\infty} \hat{f}(\alpha_n) \frac{\partial^2 eigfunc(\alpha_n, x)}{\partial x^2} = \sum_{n=0}^{\infty} -\alpha_n \hat{f}(\alpha_n) eigfunc(\alpha_n, x) \tag{2.54}$$

After applying this transformed on $\theta(x, y, z, p)$ in equation (2.22) for y and z, this equation becomes:

$$\begin{aligned} &\textstyle\sum_{n=0}^{\infty}\sum_{m=0}^{\infty} \frac{\partial^2 \hat{\theta}}{\partial x^2}(x, \alpha_n, \beta_m, p) eigfunc(\alpha_n, \beta_m)/N(\alpha_n, \beta_m) \\ &+ \textstyle\sum_{n=0}^{\infty}\sum_{m=0}^{\infty} -\alpha_n^2 \hat{\theta}(x, \alpha_n, \beta_m, p) eigfunc(\alpha_n, \beta_m)/N(\alpha_n, \beta_m) \\ &+ \textstyle\sum_{n=0}^{\infty}\sum_{m=0}^{\infty} -\beta_m^2 \hat{\theta}(x, \alpha_n, \beta_m, p) eigfunc(\alpha_n, \beta_m)/N(\alpha_n, \beta_m) \\ &= \textstyle\frac{p}{a} \sum_{n=0}^{\infty}\sum_{m=0}^{\infty} \hat{\theta}(x, \alpha_n, \beta_m, p) eigfunc(\alpha_n, \beta_m)/N(\alpha_n, \beta_m) \end{aligned} \tag{2.55}$$

where $\hat{\theta}(x, \alpha_n, \beta_m, p) = IT(LT(T(x, y, z, t)))$. Then, if only the coefficients attached to $eigfunc(\alpha_n, \beta_m)$ are selected, the same equation as (2.26) will be obtained. In fact, the eigenfunction and eigenvalue are defined by using boundary conditions and must be chosen wisely in order to simplify computation. Table A2.2 in Appendix A2 presents all possible boundary conditions in the lateral direction and the corresponding eigenvalues and eigenfunctions.

In this study, the adiabatic condition is applied on the surrounding surfaces. Then, according to Table A2.2 in Appendix A2, the eigenfunctions are $cos(\alpha_n y)$ and $cos(\beta_m z)$ (case 5 in Table A2.2) then $\hat{\theta}(x, \alpha_n, \beta_m, p)$ can be expressed as:

$$\hat{\theta}(x, \alpha_n, \beta_m, p) = \int_0^{L_y} \int_0^{L_z} \theta(x, y, z, p) cos(\alpha_n y) cos(\beta_m z) dydz \tag{2.56}$$

A similar computation is applied to $\phi(x, y, z, p)$ to obtain $\hat{\phi}(x, \alpha_n, \beta_m, p)$. After solving equation (2.26), the solutions require an inverse transform to come back to Cartesian coordinates. Equation (2.51) already presents how to inverse it. As observed, the precision of output θ strongly depends on the number of developed order (or called truncated number). The choice of this number will be detailed in Section 2.5.2.

The external environmental conditions and internal heat convection are considered homogeneous on the whole external surface then their computation is similar in 1D and 3D simulations. On the other hand, the thermal excitation is imposed on a limited surface in 3D then its transformed function must be calculated before running QUAD computation. Supposing that the constant thermal excitation P_{exci} stays in the space interval [y_1,y_2;z_1,z_2], the expression of transformed thermal excitation flux $\hat{\phi}_{exci}(x, \alpha_n, \beta_m, p)$ is:

$$\hat{\phi}_{exci}(x, \alpha_n, \beta_m, p) = \begin{cases} (P_{exci}/p)(y_2 - y_1)(z_2 - z_1) \text{ if } n = m = 0 \\ (P_{exci}/p)(y_2 - y_1)sin(\beta_m z)/(\beta_m)\Big|_{z_1}^{z_2} \text{ if } n = 0, m > 0 \\ (P_{exci}/p)(z_2 - z_1)sin(\alpha_n y)/(\alpha_n)\Big|_{y_1}^{y_2} \text{ if } n > 0, m = 0 \\ (P_{exci}/p)sin(\alpha_n y)/(\alpha_n)\Big|_{y_1}^{y_2} sin(\beta_n z)/(\beta_n)\Big|_{z_1}^{z_2} \text{ if } n > 0, m > 0 \end{cases} \tag{2.57}$$

where $f(x)\Big|_{x_1}^{x_2} = f(x_2) - f(x_1)$.

2.5 Model validation

A series of validation studies is carried out to test the robustness of the model. The commercial simulation software called COMSOL Multiphysics® is chosen as the reference to be compared with the proposed model. This validation step contains two parts corresponding to the two model configurations: EWC (in 1D/3D) and AbF (in 1D).

The main difference between 1D and 3D models is the lateral diffusion computation. Then, it is better to choose the wall presenting the strongest lateral diffusion for validating the 3D model. To find this type among three types mentioned in Table 2.2, several COMSOL simulations were launched on these walls. Figure 2.11 shows the internal temperature horizontal profiles at the center for each wall after 24 hours of heating. The surrounding zone of the IWI 1 wall raises less than the two others. It means that lateral heat flux (or lateral diffusion) is smaller in this case. On the other hand, the EWI wall shows the strongest lateral diffusion. Therefore, the EWI wall is chosen for 3D model validation.

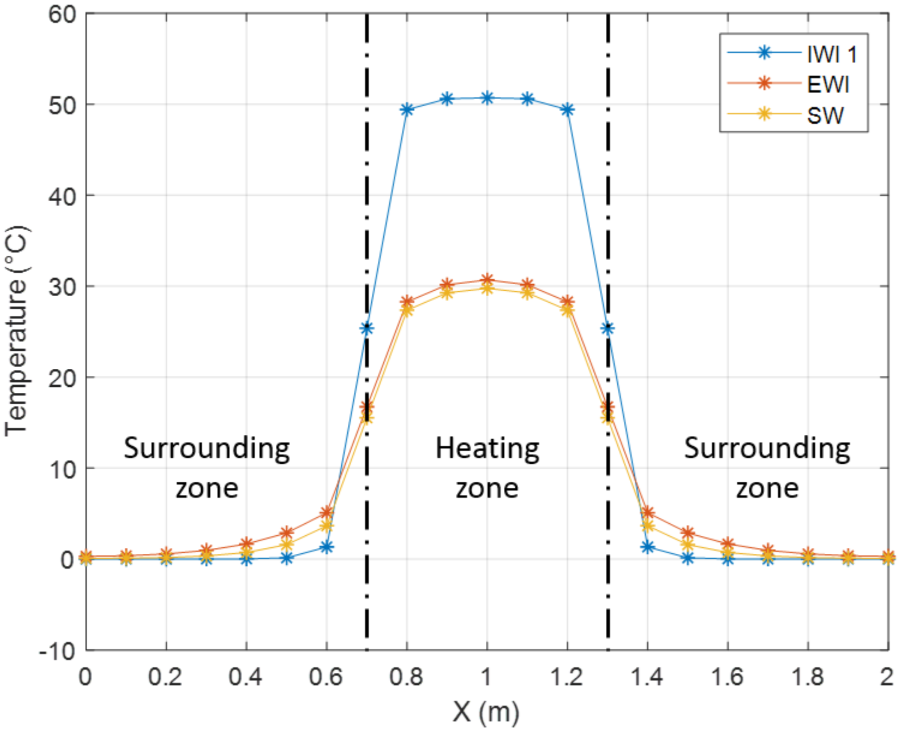

Figure 2.11: Internal temperature horizontal profiles at the center of the wall surface after 24 hours of heating computed by 3D COMSOL for 3 different walls: IWI 1, EWI and SW.

Besides, the IWI 1 wall is chosen for 1D model validation because this model does not concern the lateral computation. The physical properties of these two walls are found in Table 2.3. This section considers a 24-hour simulation under the environmental conditions of Trappes and Carpentras (Cf. Figure 2.2).

2.5.1 Comparison of 1D EWC model with COMSOL simulation

Figures 2.12 presents internal and external temperature profiles for the IWI 1 wall under 24 hours of environmental conditions of Trappes computed by 1D QUAD and 1D COMSOL. Figure 2.13 presents analogue results for absorbed heat flux. According to these figures, the internal surface of the 1D QUAD shows a very small difference in comparison to 1D COMSOL results. However, both profiles have a slight difference during the first minutes of the simulation (see Figure 2.14). This difference may come from the theoretical approaches of time discretization in simulation in each case. These differences are smaller than the measurement noise of thermal sensors (described in Appendix A3) so that these errors are acceptable.

However, these differences become more important in the profiles of thermal state on the

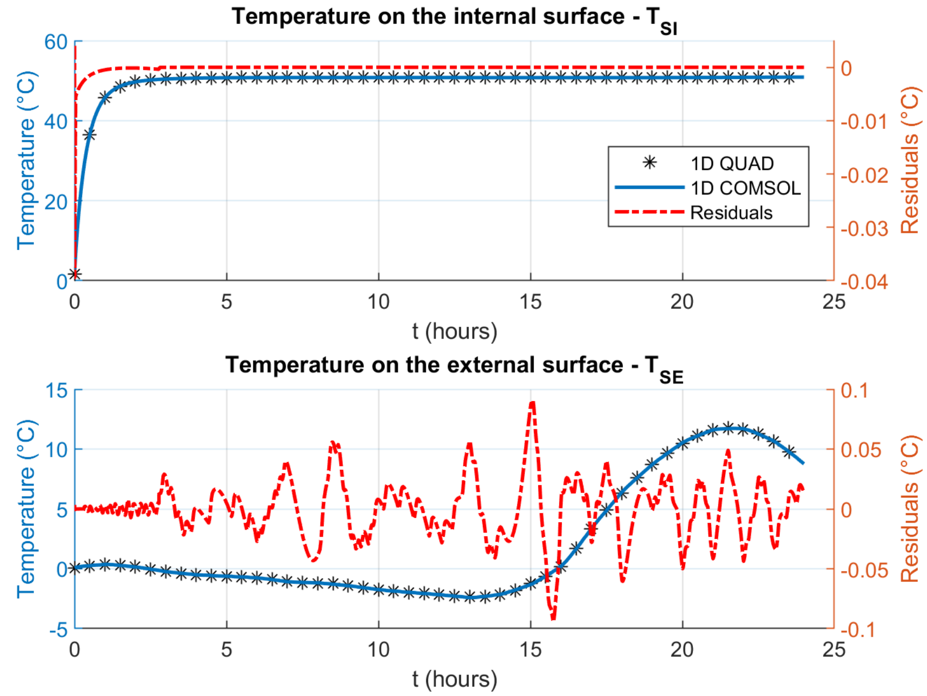

Figure 2.12: Temperature profiles of internal and external surfaces of the IWI 1 wall with the external environmental condition of Trappes simulated by 1D QUAD and 1D COMSOL and their differences.

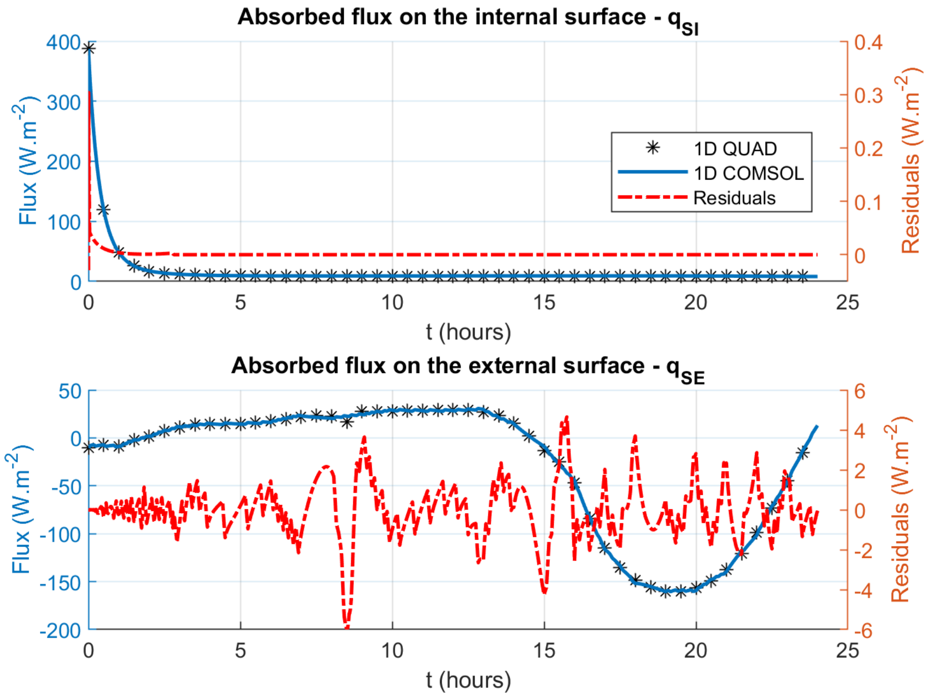

Figure 2.13: Absorbed heat flux profiles of internal and external surfaces of the IWI 1 wall with external environmental condition of Trappes simulated by 1D QUAD and 1D COMSOL and their differences.

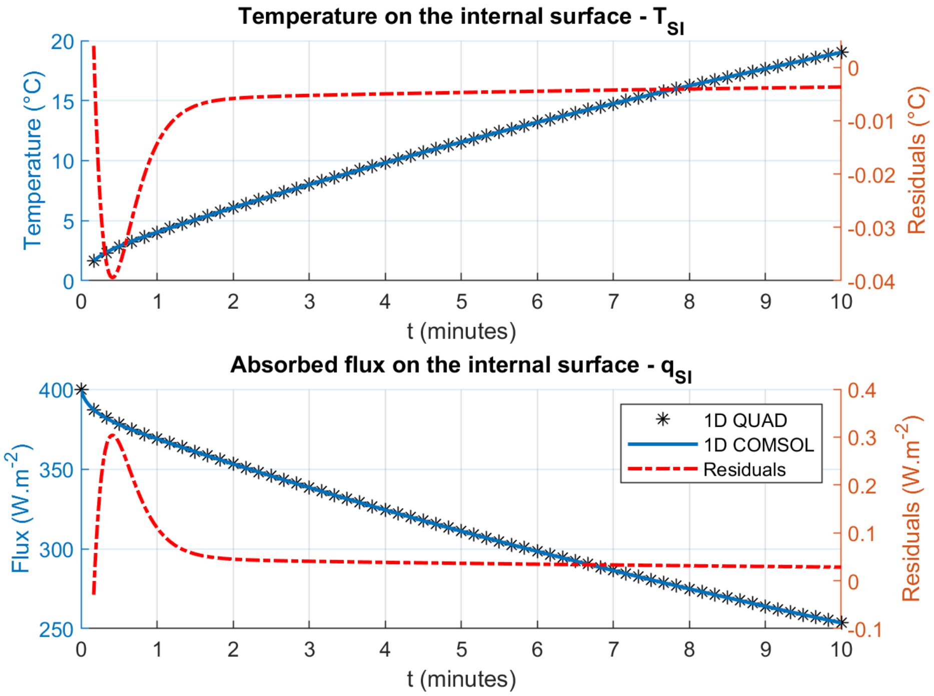

Figure 2.14: Temperature and absorbed flux on the internal surface of the IWI 1 wall with external environmental condition of Trappes simulated by 1D QUAD and 1D COMSOL and their differences during first ten minutes of heating.

external surface. The different interpolation methods for discrete Laplace transform on boundary condition in QUAD and COMSOL can explain this observation. The value of these errors is less than 3% of actual value so that it can be neglected. In the case using the condition of Carpentras, similar observations are obtained (see Figures 2.15, 2.16 and 2.17).

Following the observations above, the 1D QUAD computation can provide values on the interior surface very close to those provided by COMSOL. Although having some minor differences for the external side, the quadruples method can be considered correct for 1D simulation of heat transfer in the considered wall.

The introduction of this chapter mentioned that the 1D model was chosen to be used as the direct model for the estimation process. Then, another aspect that needs to be considered here is the computation time of the two models. The best compromise between accuracy and calculation time must be found. By running a similar case, 1D COMSOL needs approximately 22 seconds for finishing one simulation. On the other hand, 1D QUAD takes around 0.2 second or less to compute the same case. In fact, in a COMSOL simulation, there are more calculations than QUAD simulation does. However, in this work, a complex calculation is not necessary

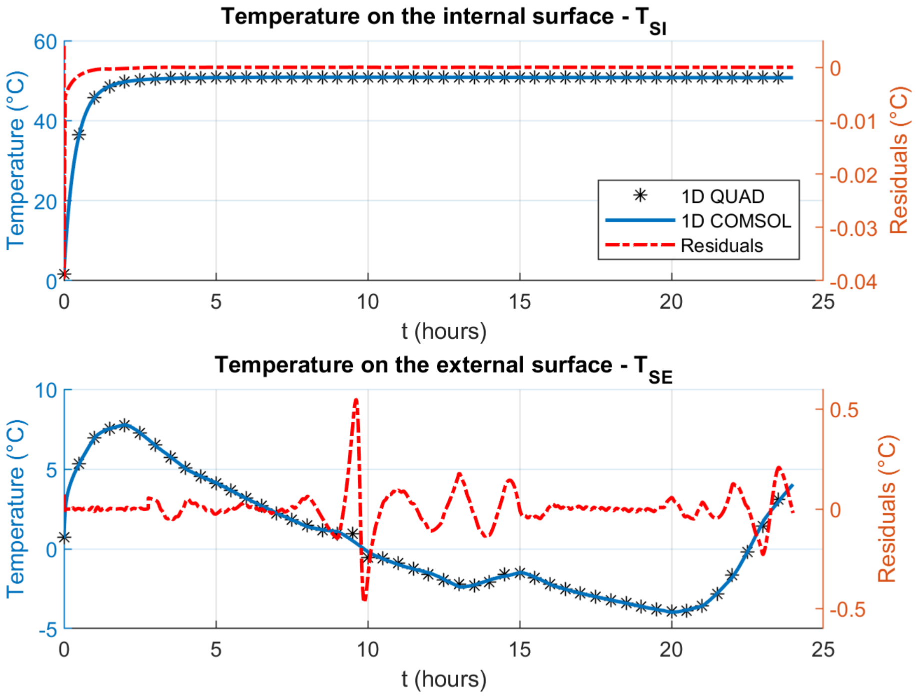

Figure 2.15: Temperature profiles of internal and external surfaces of the IWI 1 wall with the external environmental condition of Carpentras simulated by 1D QUAD and 1D COMSOL and their differences.

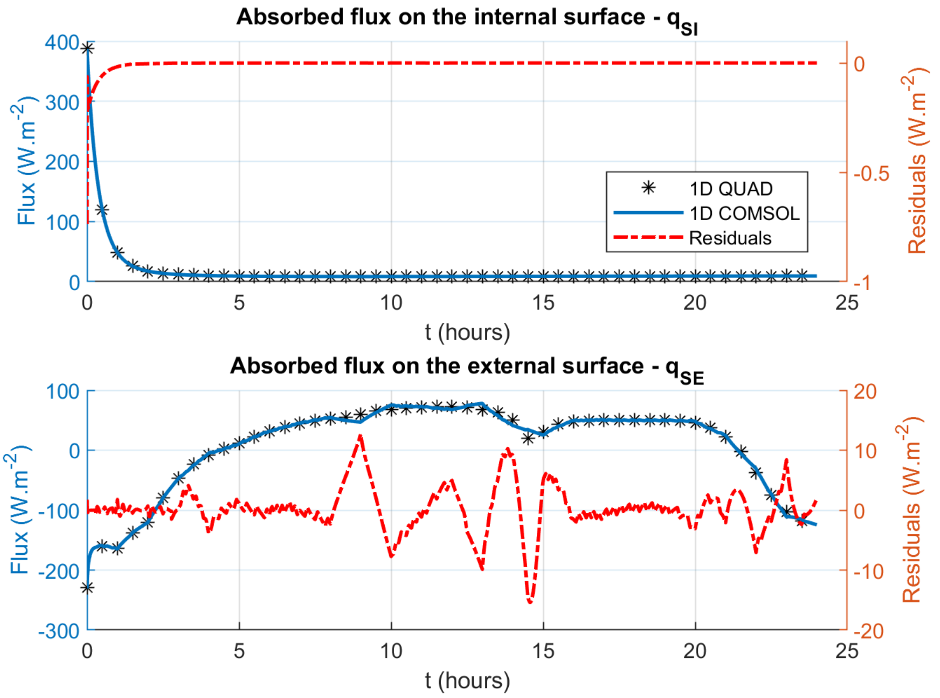

Figure 2.16: Absorbed heat flux profiles of internal and external surfaces of the IWI 1 wall with external environmental condition of Carpentras simulated by 1D QUAD and 1D COMSOL and their differences.

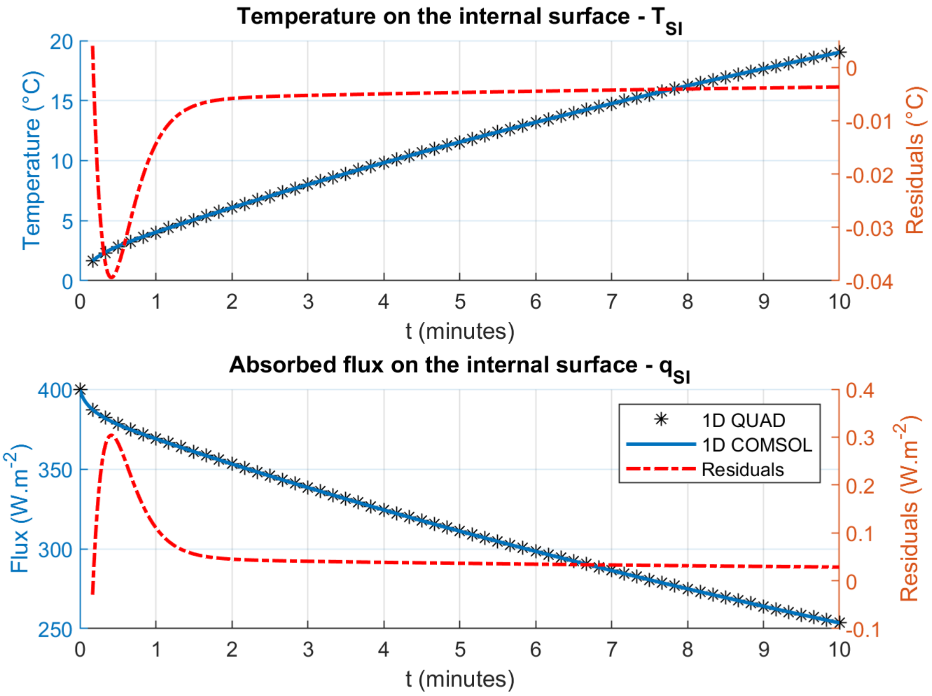

Figure 2.17: Temperature and absorbed flux on the internal surface of the IWI 1 wall with external environmental condition of Carpentras simulated by 1D QUAD and 1D COMSOL and their differences during first ten minutes of heating.

and the 1D QUAD model seems to be the most suitable to be used as the direct model in the parameter estimation process.

2.5.2 Comparison of 3D EWC model with COMSOL simulation

The 3D configuration is the most complicated case. The equations of QUAD show that 3D computation will take a very long time, much more than 1D cases because of lateral diffusion computation, then it is impossible to use it as a direct model for parameter estimation. Therefore, in this study, the 3D model is used as a numerical data generator. Two profiles are considered, one is horizontal at the middle of the wall and another crosses the wall diagonally (see Figure 2.18). Moreover, the temporal evolution of the temperature at the center of the wall surface between two models is compared also.

As observed in Section 2.4.3, the precision of transformed data depends on the truncated number used in the integral transform. Then, four values of the truncated number (5, 100, 300, and 500) are considered to demonstrate the influence of this parameter. Figures 2.19, 2.20 present the internal surface temperature after 5 hours of heating on the horizontal and diagonal lines on the surface of the EWI wall computed by 3D QUAD and 3D COMSOL models. Moreover,

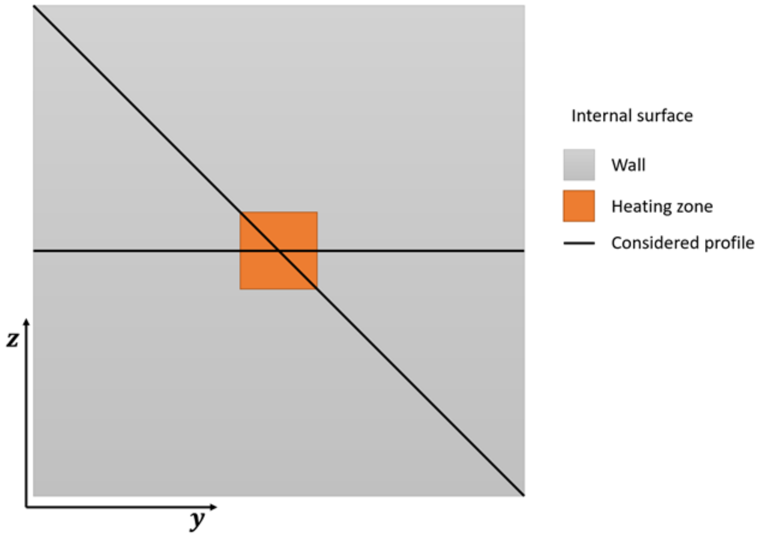

Figure 2.18: Two considered profiles in 3D comparison.

Figure 2.21 shows the temporal evolution of the temperature at the center of the studied wall by two considered models. According to these results, the influence of truncated number to output precision is well observed. A higher truncated number returns a more precise output. Moreover, 3D QUAD simulates correctly the lateral diffusion as 3D COMSOL. The same observation is obtained for the temperature at the center of the wall between two considered models with a small difference at the beginning of measurement as observed in 1D simulation before.

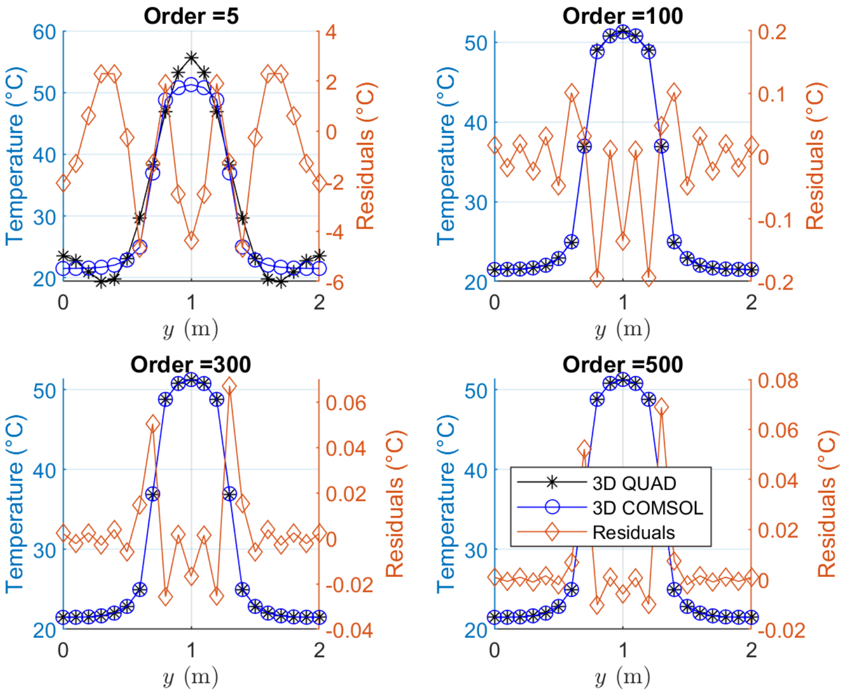

Figure 2.19: Internal temperature horizontal profiles of EWI wall computed by 3D QUAD and 3D COMSOL and their difference after 5 hours of heating with varied truncated orders.

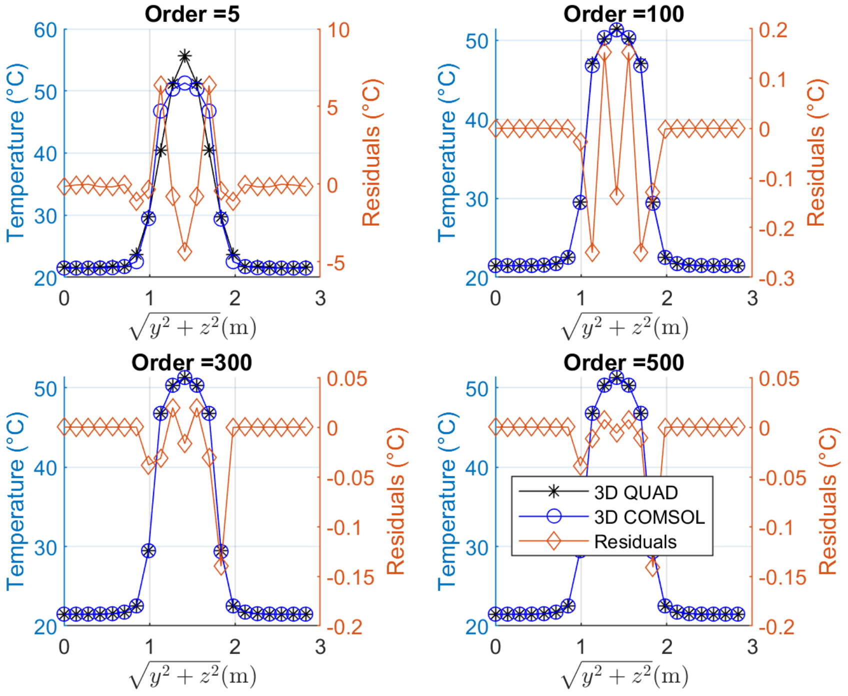

Figure 2.20: Internal temperature diagonal profiles of EWI wall computed by 3D QUAD and 3D COMSOL and their difference after 5 hours of heating with varied truncated orders.

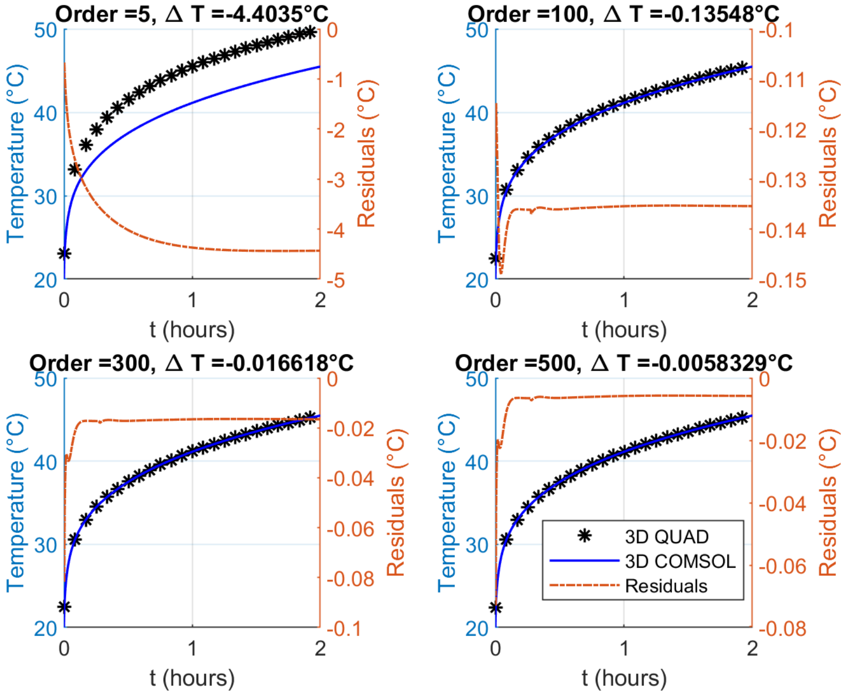

Figure 2.21: Temporal profiles of temperature at the center of the internal surface of EWI wall computed by 3D QUAD and 3D COMSOL and their difference with varied truncated orders.

Besides, the temperature difference on the boundary of the heating zone (y = 0.7 m and y = 1.3 m) presents the most important error compared to other points. The precision of computation

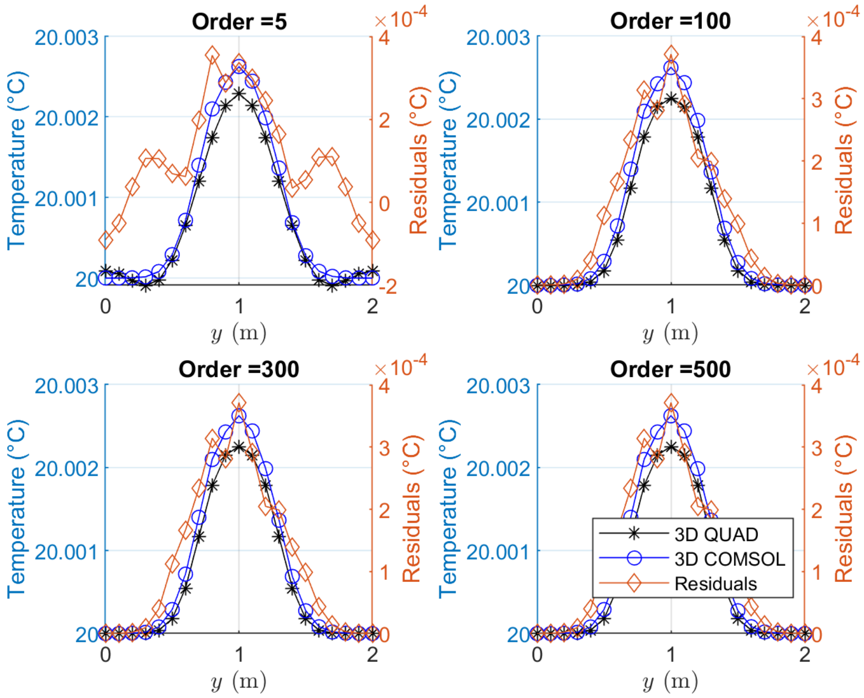

Figure 2.22: External temperature horizontal profiles of EWI wall computed by 3D QUAD and 3D COMSOL and their difference after 5 hours of heating with varied truncated orders.

at this point depends strongly on the boundary condition computation in the simulation. However, this error is quite small and it does not change a lot the final results. Because of the strong thermal resistance of the insulation layer, there is not much variation on the external side of this EWI wall. Figure 2.22 shows the external temperature profiles after 5 hours of heating with different truncated numbers. The shapes of both profiles do not look like the same but their difference is extremely small (around a few 10^{-4}°C).

According to this comparison, the 3D QUAD can simulate a similar numerical case as 3D COMSOL with a truncate number larger or equal to 300. Concerning the computation time, a 3D COMSOL simulation requires 6 days, 2 hours, and 31 minutes for a 5-hour simulation with a time step of 10 seconds, while only 1 hour and 30 minutes are needed for a 300 order 3D QUAD. Even with 500 orders, 3 hours are sufficient. As previously mentioned, 3D simulation is used as a numerical generator only. Thus, QUAD simulation will be used to generate numerical cases, which will be used in the next chapter, because of significant smaller computation time compared to COMSOL simulation for a similar precision.

2.5.3 Comparison of AbF model with EWC COMSOL simulation

Following definition of the AbF model in Section 2.3.4, EWC and AbF models are based on the same equations. Their difference is that AbF replaces thermal excitation q_{exci} and the internal convection/radiation heat flux of the EWC model by the net heat flux absorbed directly by the internal wall surface. Thus, they are theoretically equivalent. This absorbed flux is a measurement data so that it must be transformed by discrete Laplace transform to use in QUAD computation. According to Section 2.4.1, the time step of the discrete Laplace transform should be studied to be adapted to the considered case. Therefore, for validating AbF model, the EWC type will be used as the original (or reference) model.

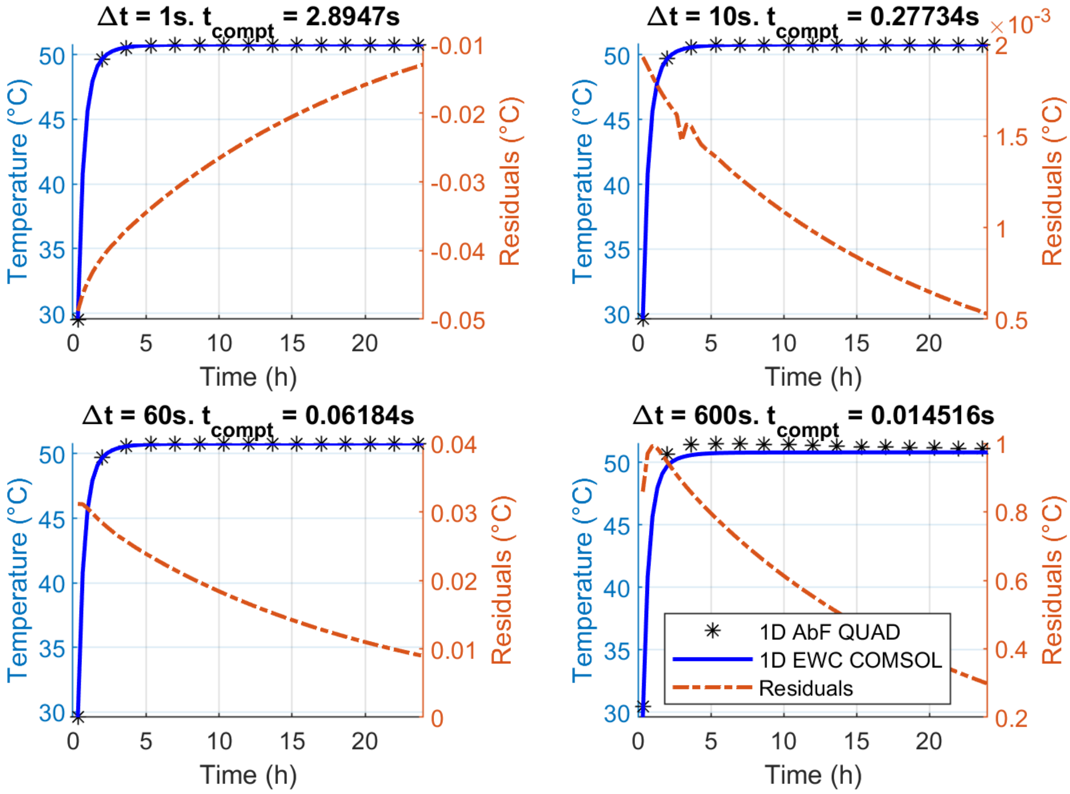

Figure 2.23: Comparison between the temporal internal surface temperature evolution computed by 1D AbF model in using different time steps for absorbed heat flux and 1D EWC model with the computation time corresponding.

To obtain an optimal time step for the absorbed flux, a data set of IWI 1 wall which is generated by 1D EWC COMSOL with the time step of 1 second is created. Then, a series of 1D AbF simulations with various Δt between 1 second and 600 seconds is launched. Figure 2.23 presents the residuals between 1D EWC and 1D AbF simulations and the computation time (noted t_{compt}) for each case. The higher Δt, the higher the residuals, especially at the beginning.

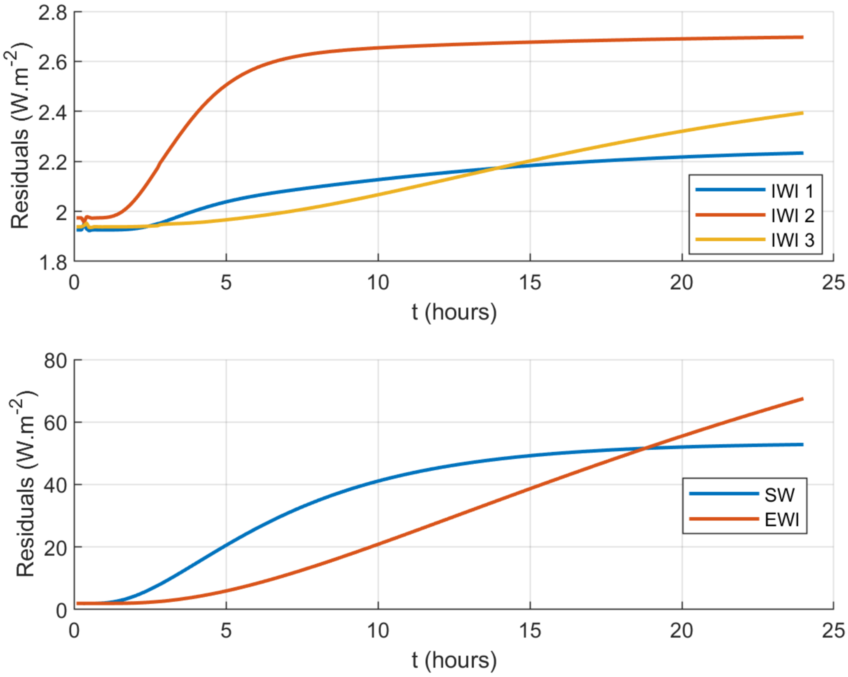

Figure 2.24: Internal absorbed flux residuals computed by 1D and 3D EWC models with 5 considered walls.

This error can be explained by the peak of absorbed flux at short times (see Figure 2.13). After several tests with different walls, a 10-second time step seems the best choice to use in AbF simulation.

Obviously, there is no way that the 1D AbF model using the absorbed flux of 3D computations can return the same temperature profile as a 3D case. Figure 2.24 presents the difference in absorbed flux between 1D and 3D EWC models. The three IWI walls show a weak difference (less than 3 W.m^{-2}) which corresponds to the lateral effects as presented before. On the other hand, SW and EWI walls present a huge difference which is 20 times larger than for IWI cases. Due to this difference, the 1D AbF model returns a completely different internal surface temperature for these cases compared to the 3D EWC one (see Figure 2.26).

This difference of absorbed flux can lead to an important difference in temperature computed by the 1D AbF model. Figure 2.25 presents the comparison with three considered IWI walls computed by the AbF model in using 3D absorbed flux and 3D EWC model. Each case in this figure shows a different profile and continuously increasing residuals as a function of time, even if a small difference of absorbed flux between 1D and 3D models is found for these walls. For IWI 2 and IWI 3 walls, compared to final temperature level (50°C), these differences are not too much. Then, the estimation with these walls could return good results.

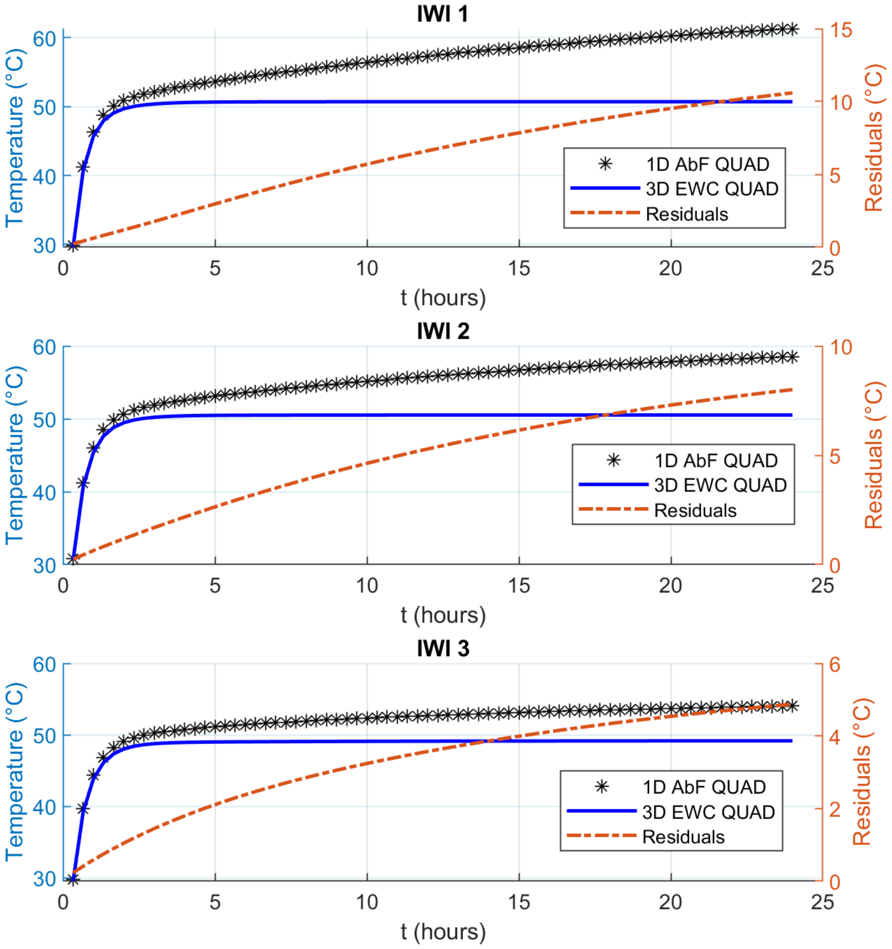

Figure 2.25: Comparison of the computed temperature profile of the internal surface of IWI configurations by using 3D EWC model and 1D AbF using 3D flux.

In this study, only 1D AbF model is mentioned. 2D/3D AbF models are quite complicated to simulate because of the complexity of 2D/3D absorbed flux. Figure 2.27 presents an example of the internal flux profile for the EWI wall after 5 hours of heating. It is not simple to form an analytical expression of this absorbed heat profile by using some data points of this profile. Moreover, supposing that it is possible to form this required analytical representation, a large number of heat flux measurement points is required, especially close to the boundary of the heating zone, to have enough data to rebuild it. However, for a numerical study, it is possible but not for a real measurement. Therefore, only 1D AbF model is used here.

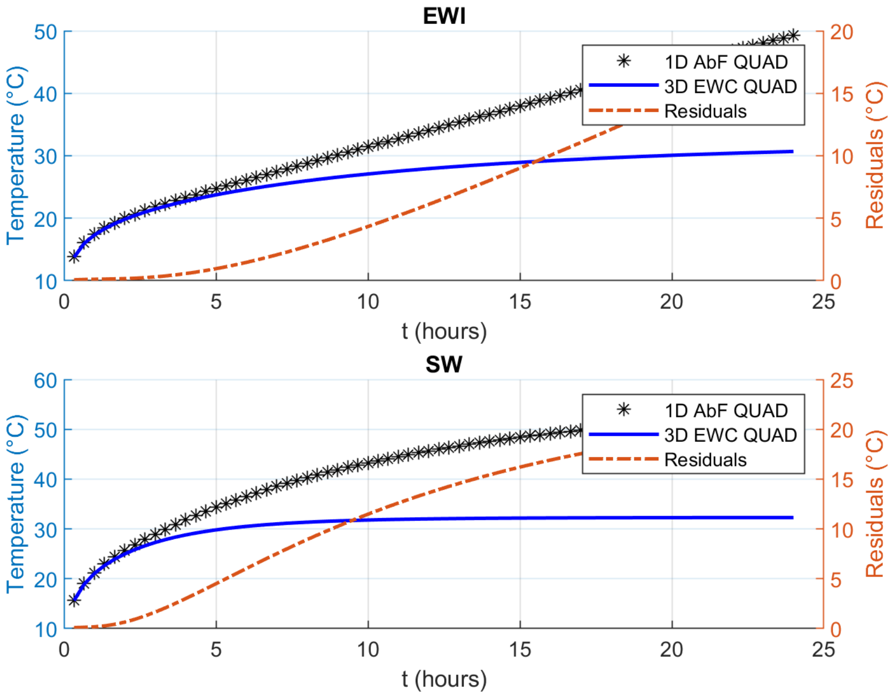

Figure 2.26: Comparison of computed temperature profile of internal surface of EWI and SW configurations by using 3D EWC model and 1D AbF using 3D flux.

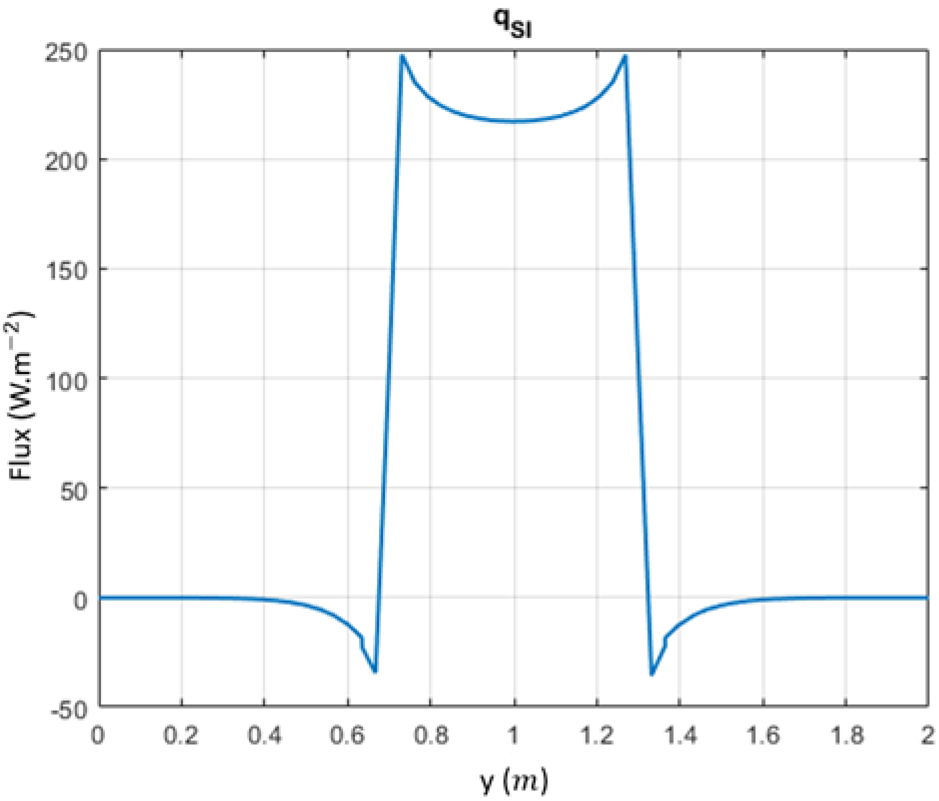

Figure 2.27: Internal absorbed flux horizontal profile for the EWI wall after 5 hours of heating computed by 3D QUAD model.

2.6 Conclusions

In this chapter, the theory of thermal quadrupole computation (QUAD) in the multi-dimensional case is presented for simulating heat transfer in a multilayer wall. By using the Laplace transform, the complex differential equation of heat transfer can be transformed into a simple matrix computation. This matrix computation allows calculating rapidly the transfer matrix of a multi-layer wall by using a direct matrix product. Because of the complexity of the analytic inverse Laplace transform, the numerical approach of de Hoog is used to obtain the final simulation output in time-space. For 2D/3D cases, the integral transform is required to be applied in the lateral direction of heat transfer. Two models, Excitation With Convection (EWC) and Absorbed Flux (AbF), are proposed. Each of them has pros and cons in numerical studies and experiments.

In numerical cases, the EWC model shows a strong capability of simulation in 1D/2D/3D cases with a very small error in comparison to COMSOL simulation. Moreover, QUAD simulation with this model leads to a significant reduction of computation time compared to COMSOL without losing accuracy. On the other hand, only the 1D structure is considered in the AbF model because of the complexity of lateral absorbed heat flux on the surface and of measurement difficulties in practice. Before using as model input, the absorbed flux must be transformed by discrete Laplace transform. Then the time step of two consecutive measurement data is an important parameter that can change the quality of model output. By balancing computation time and output precision, a time step of 10 seconds is chosen as the most optimal value for AbF model.

Instead of using a complicated data generator as COMSOL, the QUAD method is used also as a direct model of parameter estimation because of its rapidity of computation. Two models are chosen for being the direct model of parameter estimation, 1D EWC, and 1D AbF.

3 Theory of parameter estimation

3.1 Introduction: definition of an inverse problem

Physical theories give a base for making predictions in measurements. By providing a complete and exhaustive description of a physical system, it is possible to predict the outcomes/results of a measurement, which is sometimes difficult to achieve in reality. This action of predicting these results is normally called a modeling problem (or simulation problem or forward/direct problem) expressed by a direct model. Besides, the inverse problem consists in using real measurements to assess the values of certain parameters that characterize the considered system [58]. A short representation of these two types of problem is shown in Figure 3.1.

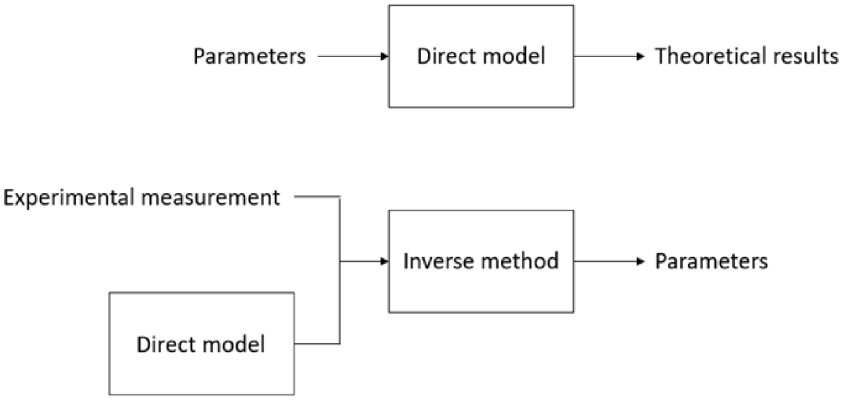

Figure 3.1: General representation of the direct and inverse problems.

An essential part of an inverse problem is the direct model. There are three typical types of models: white-box, black-box, and grey-box models.

A **white-box model** is based on the theory of physical phenomena or the knowledge of the studied subject. In thermal science, a white-box model involves calculations of conduction, convection, radiation, etc.. It means that this model should represent as much as possible the knowledge of the considered system. However, the researchers face several disadvantages when trying to use this type of model in parameter estimation such as:

- A large number of parameters may lead to identifiability conflicts (non-unique or non-physical solution, etc.);

- The required computation time can be very long because of the complexity of the model.

A **grey-box model** (or **semi-physical model**) proposes a simplified representation of a physical system. This type of model involves the theories about the studied system, but some factors can be simplified or removed to make it simpler than the original model (or the white-box model). The grey-box method's biggest strong points are the reduction of the required parameters and the computation time. On the other hand, because this model is simplified, it is possible to miss some important information so that the parameter estimation process may cause an error on estimated parameter values.

A **black-box model** does not use any knowledge or hypothesis about the studied system. It requires a large number of observations to deduce the model parameters to adapt to a relationship between inputs and outputs of the considered system. Most of them are constructed from polynomial series (non-linear regression) or convolution products between transfer functions and inputs/outputs. The algorithms for building a black-box model can be applied in any domain, whether in science or finance (no specific applications contrary to white and grey-box models), but a complex database is required.

Concerning the present study, which focuses on the heat transfer in a building wall, the theory of heat transfer was well established in Chapter 2 so that white-box and grey-box models are available for this case. Because of their short computation times, grey-box methods are considered as adequate models to use in parameter estimation. The most popular grey-box method for heat transfer modeling is the RC representation. Indeed, by using linear computation, the thermal quadrupole method, which is a white-box method, is frequently used in heat transfer analysis. Both methods are based on the partial differential equation of heat transfer, but the ways to solve this equation are different.

Figure 3.2 presents the global diagram of an inverse problem. A parameter proposal x, the output data $y_{i-theo}(x)$ computed by direct model and the measurement data y_{i-meas} (or called minimization data) at the moment i $(= 1, 2, ..., N)$ are inserted into an optimization/regularization model. The objective of this is to test if the proposal x can return a smaller least-square function $f(x)$ between the two groups of data than the previous iteration. The expression of the least-square function $f(x)$ can be written as:

$$f(x) = \sum_{i}^{N} \Big(y_{i-theo}(x) - y_{i-meas}\Big)^2 \tag{3.1}$$

If the accepted proposal value satisfies certain conditions (limiting iteration number, parameter precision, etc.), the process will stop and return the final estimated parameter. If it does not, the estimation model will generate a new proposal for the next iteration of the estimation process.

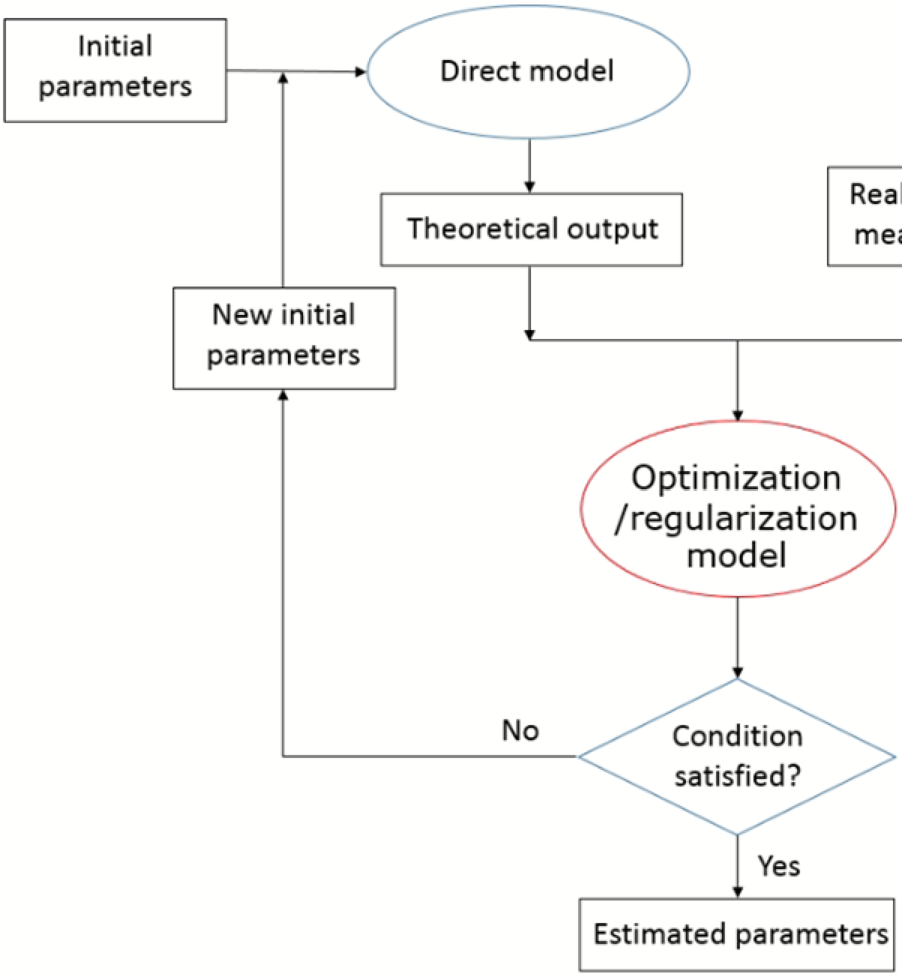

Figure 3.2: General diagram of inverse problem process.

In this study, the temperature of the internal wall surface is used as the minimization data, and the other measurements such as the air temperatures, the absorbed heat flux on the internal surface, the temperature of the external surface, and the solar radiation are inserted into the direct model as boundary conditions, depending on model requirements.

In the next sections, several methods for least-square minimization will be presented. The principle, computation steps, and advantages of each method will be detailed. A comparison between these methods in certain cases will be carried out to decide which one is the most suitable for the thermal resistance estimation. Next, a thermal resistance estimation process will be introduced to use in this study with a complete sensitivity analysis for all possible direct models with different types of studied walls. The last section will present some thermal resistance estimations using 3D simulation data as measurement data to validate the proposed process's estimation capability.

3.2 Least-squares minimization methods

3.2.1 Gradient Descent method

The Gradient Descent method (noted GD) is a first-order iterative optimization algorithm which uses the first derivative of $f(x)$ (or $y_{theo}(x)$), noted $G(x)$. If a minimum of $f(x)$ stays at $x = x_0$ in an observation zone $[x_1, x_2]$, the first derivative $\partial f(x)/\partial x$ will be larger (or smaller) than 0 if $x > x_0$ (or $x < x_0$). Therefore, according to these characteristics, if x_{k-1} at the (k-1)th iteration is still far from x_0, the new value x_k at the kth iteration which is closer to x_0 than the previous one can be calculated as:

$$x_k - x_{k-1} = h_{GD} = -\alpha G(x_{k-1}) = -\alpha \frac{\partial f}{\partial x}(x_{k-1}) \tag{3.2}$$

where α is a positive scalar called length of the step (or update step) in the steepest descent direction and h_{GD} is the parameter update whose matrix expression is given by:

$$h_{GD} = \alpha J^{\intercal}(y_{meas} - y_{theo}) \tag{3.3}$$

Here, J is the Jacobian matrix of $(y_{meas} - y_{theo})$ which is written as:

$$J = -\frac{\partial y_{theo}}{\partial x}(x) \tag{3.4}$$

The calculation of GD method is quite simple and easy to use. However, the gradient descent direction depends strongly on the update step α. If this step is too large, the estimated parameter will miss the true local minimum then it takes time to return. If it is too small, it will require an enormous number of steps to find out the willing value. Then, an approach for computing an efficient update step of gradient descent is proposed. This approach is called Conjugate Gradient Descent (noted CGD) method [59]. The proposal x_k of the CGD method is expressed by:

$$x_k = x_{k-1} + \alpha_k w_{k-1} \tag{3.5}$$

where

$$w_{k-1} = -G(x_{k-1}) + \gamma_{k-1} w_{k-2} \tag{3.6}$$

and

$$\gamma_k = \begin{cases} \frac{G(x_k)^\intercal G(x_k)}{G(x_{k-1})^\intercal G(x_{k-1})} & \text{if } k > 0 \\ 0 & \text{otherwise} \end{cases} \tag{3.7}$$

The value of α_k is obtained by minimizing the function $\hat{\phi}(r)$:

$$\hat{\phi}(r) = \frac{1}{2}\bigg(\|y_{meas} - y_{theo}(x_k + r w_k)\|^2 \bigg) \tag{3.8}$$

By using the linearization computation of equation 3.8, an approximation of α_k can be written as:

$$\alpha_k \approx \frac{G(x_k)^\intercal G(x_k)}{(J_k w_k)^\intercal J_k w_k} \tag{3.9}$$

This method allows calculating an optimized update step after each iteration compared to the Gradient Descent method before. However, it requires more calculations than the original method and in case of complex computation, more time is needed.

3.2.2 Gauss-Newton method

The Gauss-Newton method (noted GN) method uses another approach for computing parameter update step. Based on Taylor series, the theoretical value $y_{theo}(x + h_{GN})$ for the next parameter proposal $(x + h_{GN})$ can be developed as:

$$y_{theo}(x + h_{GN}) \approx y_{theo}(x) + \frac{\partial y_{theo}}{\partial x}(x) h_{GN} = y_{theo}(x) + J(x) h_{GN} \tag{3.10}$$

Then, $f(x + h_{GN})$ becomes

$$\begin{aligned} f(x + h_{GN}) \approx\ & y^\intercal_{theo}(x) y_{theo}(x) + y^\intercal_{meas} y_{meas} + h^\intercal_{GN} J^\intercal(x) J(x) h_{GN} \\ & -2 y^\intercal_{meas} y_{theo}(x) - 2(y_{meas} - y_{theo}(x))^\intercal J(x) h_{GN} \end{aligned} \tag{3.11}$$

The objective of this method is to find h_{GN} to minimize $f(x + h_{GN})$. It means that the derivative of $f(x + h_{GN})$ with respect to h_{GN} must be 0:

$$\frac{\partial f}{\partial h_{GN}}(x + h_{GN}) \approx -2(y_{meas} - y_{theo}(x))^\intercal J + 2 h^\intercal_{GN} J^\intercal(x) J(x) = 0 \tag{3.12}$$

Then, the Gauss-Newton update step h_{GN} is:

$$h_{GN} = (J^{\intercal}(x)J(x))^{-1}J^{\intercal}(x)(y_{meas} - y_{theo}(x)) \tag{3.13}$$

In fact, this method is a modification of Newton method with an approximation of the Hessian $H \approx J^T J$. Because $f(x)$ has a least-squared form, this method allows jumping directly to the minimum of the second order of Taylor-approximation at every step. The qualitative behavior in the neighborhood of the solution of this method is that its approximated second-order (curvature) information allows converging along a more direct path than the Gradient Descent method. Therefore, it converges faster than Newton method. On the other hand, this method is not recommended for a direct model y_{theo} whose parameters have strong correlations.

3.2.3 Levenberg-Marquardt method

The Levenberg-Marquardt method (noted LM), also known as the damped least-squares (DLS) method, is very well-known to solve non-linear least-square problems. This method is well integrated in MATLAB into *lsqnonlin* code [60].

The regularization factor of this method is composed of the update step of the Gradient Descent and Gauss-Newton methods [61]. The update step of the Levenberg-Marquardt method is expressed as follows:

$$(J^{\intercal}(x)J(x) + \gamma I)h_{LM} = J(x)^{\intercal}(y_{meas} - y_{theo}(x)) \tag{3.14}$$

where I is the identity matrix.

The parameter γ is the key parameter of this method which controls both magnitude and direction of h_{LM}. When γ is too small (or too big), h_{LM} becomes h_{GN} (or h_{GD}). In MATLAB, this parameter will be changed after each iteration. If the proposal parameter at the k^{th} iteration is accepted (it means $f(x_k) < f(x_{k-1})$), it will return $\gamma_{k+1} = \gamma_k/10$. Otherwise, $\gamma_{k+1} = 10\gamma_k$ is given. However, this method does not allow setting up bound constrains for estimated parameters.

3.2.4 Trust-region method

The trust-region method (noted TR) is defined as default method in *lsqnonlin* code in MATLAB. The objective of this method is to estimate a region (called trust region) where estimated parameter can be found under certain conditions [62].

With this method, another function $q(p_k)$ of update step p_k is proposed for minimization instead of $f(x)$. Its representation is written as:

$$q(p_k) = \frac{1}{2} p_k^\intercal f(x_k) p_k + (\bigtriangledown f(x_k))^\intercal p_k \tag{3.15}$$

Now, the objective is to minimize $q(p_k)$ so that $\|p_k\|_2 \leq \triangle_k$. Here, $\triangle_k$ is called trust region radius at the k^{th} iteration. A reduction ratio r_k must be calculated for each iteration because it decides if proposal value is accepted or not. Its expression for the k^{th} iteration is:

$$r_k = \frac{f(x_k) - f(x_k + p_k)}{q(0) - q(p_k)} \tag{3.16}$$

By using five regularization coefficients τ_i ($i = 0, ..., 4$), the trust region radius of the $(k+1)^{th}$ iteration will be determined. The computation process of TR method can be expressed by the 4 steps below:

Step 1: At $k = 1$, set the initial value x_1, $\triangle_1 > 0$, $\epsilon \geq 0$ (a well-threshold as stopping criterion), $0 < \tau_3 < \tau_4 < 1 < \tau_1$, $0 \leq \tau_0 \leq \tau_2 < 1$ (τ_2 must be bigger than 0);

Step 2: If $\| \bigtriangledown f(x_k)\|_2 \leq \epsilon$, stop and return x_k as final result. Otherwise, minimize $q(p_k)$ to obtain p_k;

Step 3: Compute r_k then update x_{k+1} and $\triangle_{k+1}$:

$$x_{k+1} = \begin{cases} x_k & \text{if } r_k \leq \tau_0 \\ x_k + p_k & \text{otherwise} \end{cases} \tag{3.17}$$

$$\triangle_{k+1} \in \begin{cases} [\, \tau_3 \|p_k\|_2, \tau_4 \triangle_k] & \text{if } r_k \leq \tau_2 \\ [\triangle_k, \tau_1 \triangle_k] & \text{otherwise} \end{cases} \tag{3.18}$$

Step 4: Return to step 2 with $k = k + 1$.

In numerical work, the regularization constants τ_i ($i = 0, ..., 4$) are equal to $[0.2; 0.25; 0.25; 0.5]$ respectively (typical values in common code).

This method can give a solution for handling bound constraints, which the LM method can not. Here, the upper and lower bounds for estimated parameters must be defined at the beginning. The parameter constraint is very necessary in the present study because the estimated targets are physical parameters that can not be negative and have to remain in realistic intervals (for example, the thermal conductivity of building material can not be higher than 10 W.m^{-1}.K^{-1}. However, its calculation duration is much longer than the LM algorithm, even when the same minimization parameters are set.

All of the four methods above are used widely for solving inverse problems. However, they have a common weakness. The uncertainty computation is unavailable for all of them. The result of estimation without uncertainty seems meaningless. Therefore, in the following section, the Bayesian approach is introduced as the fifth algorithm working on least-squares minimization and allows calculating both estimated parameters and their corresponding uncertainties.

3.3 Bayesian approach: Parameter and uncertainty estimation

Bayes' theorem (or Bayes' rule) describes a relation between 2 conditional event probabilities. It means that one happens if the other is true. Its expression can be written as:

$$P(A \mid B) = \frac{P(B \mid A)P(A)}{P(B)} \tag{3.19}$$

where A and B are two studied events. $P(A \mid B)$ is the conditional probability of A occurring given that B is true. The other name of this kind of probability is the likelihood. By the same definition, $P(B \mid A)$ is also a conditional probability (or likelihood) of B occurring given that A is true. $P(A)$ and $P(B)$ are called marginal probabilities of observing A and B separately.

If there is a series of exclusive and exhaustive events $A_1, A_2, \ldots, A_n$, $P(B)$ can be expressed as:

$$P(B) = \sum_{i=1}^{n} P(B \mid A_i)P(A_i) \tag{3.20}$$

Because $P(B)$ depends only on B when calculating $P(A_i \mid B)$, a simplified representation of equation 3.19 is:

$$P(A_i \mid B) \propto P(B \mid A_i)P(A_i) \tag{3.21}$$

This formula is the base of Bayesian inference, one of Bayes' theorem applications in statistics. In inverse problems, Bayes' theorem can be transformed to be used as a minimization algorithm by replacing A and B by x (model parameters) and y (observations), respectively. With this replacement, equation 3.19 becomes:

$$P(x \mid y) = \frac{P(y \mid x)P(x)}{P(y)} \propto P(y \mid x)P(x) \tag{3.22}$$

Using the same definition as in equation 3.20, we obtain:

$$P(y) = \int P(y \mid x_i)P(x_i)dx_i \tag{3.23}$$

$P(y)$ describes the marginal likelihood of observation (other name is "prior predictive distribution") [63, 64]. This distribution gives a prediction of how the observation looks like by using a theoretical model. It is not necessary to calculate this factor because it is constant and independent of parameters.

$P(y \mid x)$ is called likelihood function, which represents the link between the parameters and the observation data via a physical model. $P(x)$ is the prior distribution of parameter x that is considered a representation of the current state of the model parameter's knowledge. The choice of prior function is very important in Bayesian inference.

Depending on knowledge about studied parameters, different types of prior function can be used. There are four typical priors: informative, weakly informative, least informative, and uninformative.

By using previous studies in the past or available information on parameters, an **informative prior distribution** that describes explicitly knowledge about studied parameters can be constructed. Some prior functions allow taking into account data and results in the past to simplify the calculation, for example, the power prior distribution presented in equation 3.24 and Table 3.1 [65].

$$\pi(x \mid D_o, a_o) \propto L(x \mid D_o)^{a_o}\pi_o(x \mid c_o) \tag{3.24}$$

On the other hand, this prior is not simple to use because of its complexity. When working on a new parameter, it is impossible to formulate it by a single general equation.

Weakly informative prior distribution is used when there is not enough useful information for studied parameters. This prior is used to prevent problems such as an algorithmic

Notation	Definition
$\pi(x \mid D_o, a_o)$	Power prior distribution of parameter x for the current study
$L(x \mid D_o)$	Likelihood function for a regression model with the historical data D_o
$\pi_o(x \mid c_o)$	Prior distribution for x before D_o is observed
a_o	Hyper-parameter which controls the heaviness of the tails of prior for x
c_o	Hyper-parameter which weights the historical data relative to the likelihood of the current data

Table 3.1: Power prior distribution parameter [65].

failure to explore the state-space (stabilization, regularization) [63]. A popular prior of this type, according to [63], is a normal distribution $N(0, 10000)$. In [66], the authors show that the Student-t prior distribution is also a good choice. However, choosing a suitable weakly informative prior is not easy at all because there are always prior-data conflicts [67].

Moreover, if we prefer a prior, which contains the minimal amount of subjective information and which affects not much to the posterior distribution, the **least informative prior distribution** should be a good option. "To let the data speak for themselves" [63] is what is expected to see when choosing this kind of prior. A uniform distribution from negative infinity to positive infinity (or flat prior) is considered "least informative".

An **uninformative prior distribution** does not contain any information. However, this type does not truly exist [68]. Each prior has information in some ways. There are some priors associated with uninformative priors in use, like diffuse or vague priors [63].

In this work, the least informative prior distribution is used for parameter prior. It respects Gaussian form where the expectation μ_x and the variance σ_x are fixed or variable in certain cases (see more in Section 3.4.4). However, they must remain in the realistic interval of estimated parameter:

$$P(x) \propto exp\left(- \frac{(x - \mu_x)^{\intercal}(x - \mu_x)}{2\sigma_x^2} \right) \tag{3.25}$$

If the prior function is considered as parameter information without observing data, the likelihood function is the conditional density of the data given parameters. The likelihood function will reach its maximum if estimated parameters are equal to the correct parameters.

Before directly addressing the likelihood formula, we should understand what a likelihood function is. Firstly, the likelihood function is not a probability. While a probability is associated with possible results that are mutually exclusive and exhaustive, the likelihood relates to hypotheses that are neither exclusive nor exhaustive.

Moreover, there is another distinction between probability and likelihood. A probability allows predicting unknown outcomes based on known parameters, but likelihood allows estimating unknown parameters based on known outcomes.

In the present study, the measurement data $y_{measure}$ and the model simulation $y_{model}(x)$ with parameters x are compared to minimize the least-squares so that the likelihood function proposed here is:

$$L(y_{measure} - y_{model}(x) \mid x) = L(\Delta y(x) \mid x) \propto exp\bigg(- \frac{\Delta y^{\intercal}(x)\Delta y(x)}{2\sigma_y^2}\bigg) \tag{3.26}$$

where σ_y is the variance for minimization data. Finally, the posterior distribution, or the probability distribution of the parameters x once the data $y_{measure}$ is observed, can be written as:

$$P(x \mid \Delta y(x)) \propto exp\bigg(- \frac{\Delta y^{\intercal}(x)\Delta y(x)}{2\sigma_y^2}\bigg) exp\bigg(- \frac{(x-\mu_x)^{\intercal}(x-\mu_x)}{2\sigma_x^2}\bigg) \tag{3.27}$$

Monte Carlo Markov Chain method (MCMC) is a typical method for generating random sample from a probability distribution [69]. This method is the base of data modeling for Bayesian inference and numerical integration. Metropolis-Hasting (or Random Walk Metropolis-Hastings) algorithm [70] is the first and the most typical type of MCMC methods to generate Markov chains. There are other types, for instance Gibbs sampling or Hamiltonian MC, but they are special cases of Metropolis-Hasting algorithm. The next section shows four methods for generating Markov chain from the posterior distribution: Metropolis-Hasting, Gibbs sampling, Hamiltonian Monte Carlos, and Adaptive Metropolis methods.

3.4 Markov chain generation methods

3.4.1 Metropolis-Hastings method

Before applying the Metropolis-Hastings method with the posterior distribution $P(x)$, a random proposal density $q(x^i \mid x^{i-1})$ must be well defined to select a new parameter proposal given the previous one. A starting point x^0 is required for the first iteration. At the ith iteration, a sample x^* is generated from the proposal distribution above and is written as:

$$x^* \propto q(x^i \mid x^{i-1}) \tag{3.28}$$

Then, the acceptance probability α_i corresponding to step ith will be evaluated to decide if this candidate sample x^* is accepted or not. A ratio between two joint distributions $P(x)q(x)$ of the previous state and sample state is computed. If this ratio is smaller than 1, the acceptance probability will take its value. If not, it will be equal to 1.

$$\alpha_i = min\left\{1, \frac{P(x^*)q(x^{i-1} \mid x^*)}{P(x^{i-1})q(x^* \mid x^{i-1})}\right\} \tag{3.29}$$

This acceptance value is compared to a uniform random variable $u \sim U(0,1)$, then the new parameter sample for the ith iteration will be obtained from this comparison as:

$$\phi^i = \begin{cases} \phi^* & \text{if } u \leq \alpha_i \\ \phi^{i-1} & \text{otherwise} \end{cases} \tag{3.30}$$

Finally, a series of parameter sample evolving as a function of step number will be obtained. If plotting its histogram, a distribution form of parameter x will be observed (as in Figure 3.3).

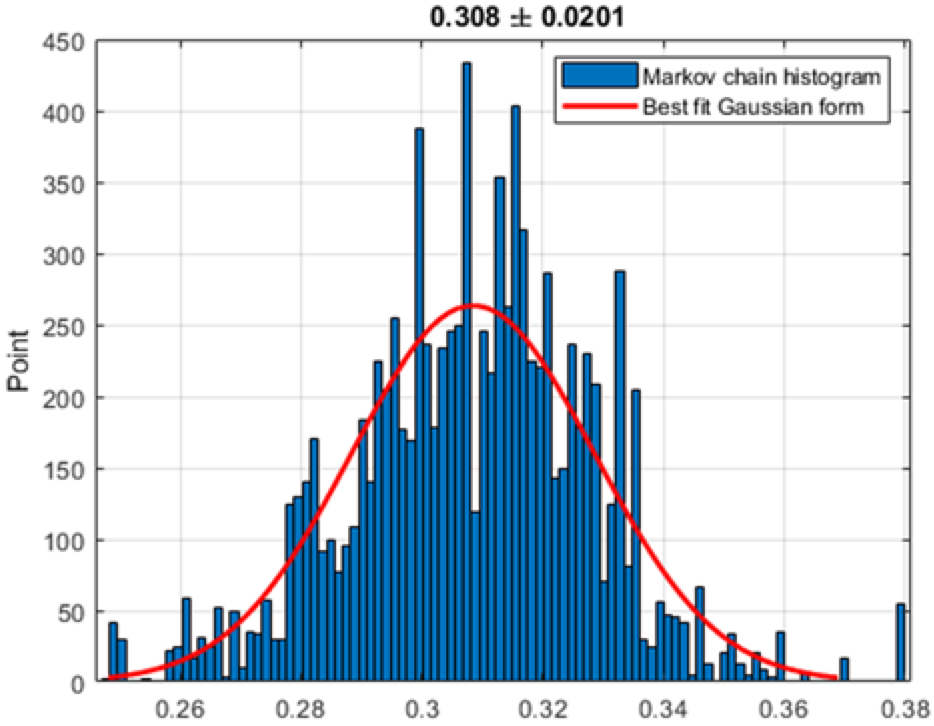

Figure 3.3: Histogram of parameter distribution generated by the Metropolis-Hastings method (blue line) and its fitted Gaussian form (red line).

In most cases, the symmetric proposal distribution ($q(\phi^*|\phi^{i-1}) = q(\phi^{i-1}|\phi^*)$) is used in order to simplify the expression of the acceptance probability (in that case, a normally distributed random distribution $N(0,1)$ is chosen). By using this type of distribution, the equation 3.29

becomes:

$$\alpha_i = min\left\{1, \frac{P(x^*)}{P(x^{i-1})}\right\} \tag{3.31}$$

This method is also called Random Walk Metropolis-Hastings (noted RWM) because it uses the random proposal distribution for generating a new sample. It is the most frequently used method in Markov chain generation. However, because of the lack of controlled conditions which help to accelerate the parameter convergence, this method requires a large number of iterations.

3.4.2 Gibbs sampling method

The Gibbs sampling method is considered the second most popular method after the RWM method for generating Markov chains, particularly in multi-dimensional cases. There are two important remarks about this method. Firstly, Gibbs sampling is applicable only with variables of more than two dimensions, whereas the RWM method can work with all types of variables. The other remark is that the acceptance rate of Gibbs sampling is always equal to 1. It means that it accepts all parameter proposals [71]. This point can be considered an advantage of the Gibbs sampling method compared to the classic RWM method.

Suppose that, at the ith iteration of a case of a *d*-dimension variable, $x^i = \{x_1^i, x_2^i, ..., x_d^i\}$ is obtained and $p(x)$ is the target distribution. Each element of x^{i+1} is calculated by using x^i and some previous elements of x^{i+1}. Starting with x_1^{i+1}, this element is computed by $p(x)$ given x^i but without x_1^i:

$$x_1^{i+1} \sim p(x_1 \mid x_2^i, x_3^i, ..., x_d^i) \tag{3.32}$$

After obtaining x_1^{i+1}, this element will be used to compute the next element. In general, at the *k*th element of x^{i+1}, the element x_k^{i+1} will be computed as follows:

$$x_k^{i+1} \sim p(x_k \mid x_1^{i+1}, x_2^{i+1}, ..., x_{k-1}^{i+1}, x_{k+1}^i, ..., x_d^i) \tag{3.33}$$

x_{-k}^i is the vector of all elements of x^i except x_k^i. Hence, the proposal distribution in this case can be expressed by:

$$q(x^* \mid x^i) = p(x_k^* \mid x_{-k}^i) IND(x_{-k}^* = x_{-k}^i) \tag{3.34}$$

where IND is an indicator function which enables that only k^{th} element is changed at the k^{th} iteration:

$$IND(x^*_{-k} = x^i_{-k}) = \begin{cases} 1 & \text{if } x^*_{-k} = x^i_{-k} \\ 0 & \text{otherwise} \end{cases} \tag{3.35}$$

Note that if x is true (or exists), x_k and x_{-k} are true (or exist) also at the same time, then the probability distribution can be developed as:

$$p(x) = p(x_k, x_{-k}) = p(x_k \mid x_{-k})p(x_{-k}) \tag{3.36}$$

Then, the actual acceptance rate in this case can be rewritten as:

$$\alpha_k = \frac{p(x^*)q(x^i \mid x^*)}{p(x^i)q(x^* \mid x^i)} = \frac{p(x^*_k \mid x^*_{-k})p(x^*_{-k})p(x^i_k \mid x^*_{-k})}{p(x^i_k \mid x^i_{-k})p(x^i_{-k})p(x^*_k \mid x^i_{-k})} \tag{3.37}$$

Moreover, x^*_{-k} and x^i_{-k} are the same so that α_k is always equal to 1 for all k and i. It means that this method accepts all parameter proposals at any iteration. Then, the acceptance rate comparison is no longer used and the choice of a suitable proposal distribution also becomes less important. However, the Gibbs sampling method takes more time to run. If Metropolis-Hastings method needs n iterations for a d-dimension variable, Gibbs sampling requires $d \times n$ iterations. The second weakness of this method is that $p(x)$ must be conditional so that equation 3.36 is valid. If not, all calculations above are wrong.

3.4.3 Hamiltonian Monte Carlo method

The Hamiltonian equations in classical mechanics express the movement of a particle of weight m under a potential field $U(q)$. The Hamiltonian function can be written as:

$$H(p,q) = U(q) + \frac{p^2}{2m} = U(q) + K(p) \tag{3.38}$$

where q and p are respectively the position and momentum of the considered particle and the two terms in equation 3.38 are respectively the potential energy and the kinetic energy of the particle. Then, if taking the partial derivative via each variable (q and p), the two famous Hamiltonian equations will be obtained as:

$$\frac{\delta q}{\delta t} = \frac{\delta H}{\delta p} = \frac{p}{m} \tag{3.39}$$

$$\frac{\delta p}{\delta t} = -\frac{\delta H}{\delta q} = -\frac{\delta U}{\delta q} \tag{3.40}$$

According to the two equations above, the position of studied particle at every moment t and its corresponding momentum can be calculated easily. If having N particles and their weights distributed into the diagonal of a NxN matrix M, equations 3.38, 3.39 and 3.40 can be transformed by considering q and p as two vectors of N elements:

$$(3.38) \longrightarrow H(p,q) = U(q) + \frac{p^T M^{-1} p}{2} \tag{3.41}$$

$$(3.39) \longrightarrow \frac{\delta q_i}{\delta t} = [M^{-1}p]_i \tag{3.42}$$

$$(3.40) \longrightarrow \frac{\delta p_i}{\delta t} = -\frac{\delta U}{\delta q_i} \tag{3.43}$$

The main idea of Hamiltonian Monte Carlo (or HMC) method comes from the similarity in expression of the target distribution (or prior) in posterior distribution and the potential energy in Hamiltonian function (Cf. equation 3.41) [72]. By introducing a “fake” momentum variable of a particle corresponding to actual value of interest, a Markov chain can be generated by using Hamiltonian approach. The joint distribution P of “position” q which represents estimated parameter x and “momentum” p can be defined as:

$$P(q,p) \propto exp(-H(q,p)) = exp(-U(q))exp(-K(p)) \tag{3.44}$$

Then, the posterior distribution is represented by $U(q)$ with prior $\pi(q)$ and likelihood $L(q \mid \Delta y))$. The expression of $U(q)$ is:

$$U(q) = -log(\pi(q)L(q \mid \Delta y)) \tag{3.45}$$

In the expression of $H(q,p)$ in equation 3.41, the second term expressed by p is equivalent to a Gaussian distribution with zero mean and covariance M. Because the choice of distribution of p is totally independent on q, the weight matrix M can be fixed equal to 1 in order to simplify its expression. Then, with this algorithm, we generate the Markov chain from the joint distribution $P(q,p)$, instead of the posterior distribution $U(q)$.

According to equations 3.42 and 3.43, the next values of p and q of the "fake" particle are calculated by partial time derivatives. By applying Euler’s method or Leapfrog method, which allows calculating numerically q and p by using a time step Δt small enough [72]. These methods also require to know how many time steps this particle moves (noted n). At the i^{th} iteration of Markov chain generation, the variable p_i is drawn from a random distribution (usually the independent standard normal multivariate) and is considered as momentum at the position q_i. Then, a computation loop of n times based on equations 3.42 and 3.43 is launched and returns a new position of particle q_{i+1} for the next iteration. This process replaces the role of proposal distribution in the classic Metropolis-Hastings algorithms.

The biggest advantage of the HMC method is that the acceptance rate is always equal to 1 so that, as for Gibbs sampling, it is not necessary to run the acceptance rate comparison between old and new positions. Because the Hamiltonian function conserves the energy then, at every moment t, $H(q, p)$ is always constant so that the ratio between current and proposal probabilities is always 1. Moreover, the HMC method can immediately generate all q whose dimension is higher than 1 at the same time. Then it costs less time than the Gibbs sampling method. Therefore, it is the fastest method among the three methods mentioned above.

However, the HMC method requires the partial derivative of the direct model with respect to all estimated parameters. For some models which can be expressed by an explicit analytical function, it seems possible. On the other hand, with complex models (like the present study, which involves non-linear heat transfer equation), the calculation of these partial derivatives can be difficult and costly in computation time.

3.4.4 Adaptive Metropolis method

In many cases of Metropolis-Hastings tests, the proposal distribution for the estimated parameter is always an important factor for the convergence of the algorithm. If choosing a large range of choices, the Markov chain may not converge to the willing value. However, if reducing this range, it will take more time to reach the willing value. Therefore, creating an effective proposal is the main objective of recent researches in MCMC techniques.

An adaptive way was introduced to update Gaussian proposal distribution by using the completed information in the previous tests and by monitoring the acceptance rate [73, 74]. Haario *at al.* introduced in their paper an algorithm called Adaptive Metropolis, which was based mostly on the Random Walk Metropolis-Hastings algorithm but with a small modification, which was the Adaptive Proposal algorithm (namely AP) [73]. In the AP algorithm, the proposal distribution in use is a Gaussian distribution centered at the current state, and its covariance is calculated from a fixed finite number of the previous states.

Suppose that at time t, there are already $t-1$ states of d dimensions $(X_0, X_1, ..., X_{t-1})$ where X_0 is the initial state. The proposal distribution for X_t is a Gaussian distribution using X_{t-1} as the expectation with covariance C_t which is defined as:

$$C_t = \begin{cases} C_0 & \text{if } t \leq t_0 \\ s_d \frac{1}{t-1}\left(\sum_{k=0}^{t-1} X_k X_k^\intercal - t\overline{X_{t-1}}\,\overline{X_{t-1}}^\intercal \right) + s_d \epsilon I_d & \text{if } t > t_0 \end{cases} \tag{3.46}$$

where $\overline{X_k} = \frac{1}{k+1}\sum_{j=0}^{k} X_j$.

C_0 is defined here as the covariance of the best priori knowledge about a considered state which can be good or not. The parameter s_d depends only on state dimension d and the authors in [73] recommended using $s_d = (2.4)^2/d$. The small constant $\epsilon > 0$ is just used to ensure that C_t will not become singular (see more details in [73]).

The computation of C_t requires all previous data until the considered moment. That is why the starting time t_0 must be defined. The choice of t_0 is free, but the bigger it is chosen, the slower the effect of the adaptation starts to take place.

In a simple expression, the proposal $\mathbb{R}^d$ vector of the estimated parameters in this method can be written as:

$$X_n = X_{n-1} + SU_n \tag{3.47}$$

where S is a $\mathbb{R}^{d\times d}$ non-singular matrix (constant or varied at every iteration) and $U_n \sim q$ is an independent random vector (sometimes, the multivariate Gaussian distribution is used for q).

Recently, there are some researches in adaptive MCMC methods that try to learn some properties of the target distribution and use this information to create a more efficient sampling than existing ones [73, 75, 76]. Some of them proposed a replacement of S by a random matrix S_{n-1} that depends on the past data. Haario *et al.* proposed the Adaptive Metropolis algorithm (noted AM) that uses $S_{n-1} = \theta L_{n-1}$ where L_{n-1} is the Cholesky factor [77] of empirical covariance matrix $C_{n-1} = Cov(X_1, \ldots, X_{n-1})$ and θ is a tuning parameter chosen by the user (the most widely used is $2.4/\sqrt{d}$) [73]. However, this tuning parameter is very sensitive when the user wants to obtain a desired mean acceptance rate (typically 23.4% in multi-dimensional settings [78]). For coercing the acceptance rate, the Adaptive Scaling Metropolis (namely ASM) proposed by Vihola [79] and the Adaptive Scaling Within Adaptive Metropolis (namely ASWAM) proposed by Andrieu [80] performed efficiently in generating Markov chains and coercing the desired acceptance rate. On the other hand, they also had difficulties (described in [81]).

Vihola in [81] proposed a new alternative to the ASWAM approach called Robust Adaptive Metropolis (noted RAM). This algorithm uses a matrix factor S that captures the shape of the target distribution and, at the same time, allows attaining a given mean acceptance rate. The RAM process can be represented by the following five steps:

Step 1: Defining a proposal density q which is spherically symmetric, a $\mathbb{R}^{d\times d}$ positive lower-diagonal matrix S_0, a step size sequence decaying to zero $\{\eta_n\}_{n\geq 1} \in (0,1]$, the target posterior distribution π, the initial point $X_0 \in \mathbb{R}^d$ and the target mean acceptance probability of the algorithm α_*.

Step 2: At the n^{th} iteration, computing $X_n^* = X_{n-1} + S_{n-1}U_n$, where $U_n \sim q$.

Step 3: Computing the probability $\alpha_n = \min\{1, \pi(X_n^*)/\pi(X_{n-1})\}$, if the proposal is accepted, $X_n = X_n^*$. Otherwise, $X_n = X_{n-1}$.

Step 5: Computing the positive lower-diagonal matrix S_n which satisfies:

$$S_n S_n^\intercal = S_{n-1}(I_d + \eta_n(\alpha_n - \alpha_*)\frac{U_n U_n^\intercal}{{U_n}^2})S_{n-1}^\intercal \tag{3.48}$$

where $I_d \in \mathbb{R}^{d\times d}$ stands for the identity matrix.

Step 5: Returning to step 2 with $(n+1)^{th}$ iteration.

The comparison between the AM, ASWAM, and RAM methods was carried out in [81], and the authors concluded that the RAM method allowed converging nicely to a limiting value with the same iteration number. However, it requires more time than the two others because more calculations are needed.

3.5 Comparison of estimation methods: from simple to complex cases

As mentioned above, several estimation algorithms allow estimating unknown parameters by a direct model and measured data. However, all of them have pros and cons. Therefore, this section will show a comparison of estimation capability between five different algorithms: Conjugate Gradient Descent (CGD), Levenberg-Marquardt (LM), Trust-region (TR), Random Walk Metropolis-Hastings (RWM), and Robust Adaptive Metropolis (RAM). In the case of the

CGD, RWM, and RAM methods, 10000 iterations are carried out in the investigated examples. By using some examples from simple to complex, this comparison will highlight which method is the most suitable for the proposed study. Four examples are studied here:

- Polynomial equation: $y = A + Bx + Cx^2$;

- Exponential equation: $y = A + B(1 - exp(-Cx))$;

- Periodic equation: $y = A + Bcos(Cx)$;

- A case of a four-layer wall generated by 1D QUAD computation with the EWC and AbF models (described in Section 2.3.4) used as the direct model of the parameter estimation.

This comparison concerns computing time and estimation result accuracy. These cases are studied with two data sets: one without noise and the other with a white noise of magnitude equal to 0.5 for the first three cases. For the last case, we use the measured noise of 0.1°C obtained in Appendix A3.

The first three cases are considered at the beginning because their analytic representation is available so that they are classified as simple examples. In Table 3.2, all inputs which are used to generate data and estimated values obtained by five considered methods for these cases are presented.

The polynomial example is the most simple case among three simple tests. The CGD, LM, and TR methods return the correct answers immediately after running (less than 0.1 second) in the cases without noise. The RWM and RAM methods, which have to generate a Markov chain of 10000 elements, need more time than the others and their estimated values are quite close to willing ones, but not absolutely exact as the three previous ones. Concerning data with noise, the first three methods do not return the exact value as the previous case, but the estimated values are very close to input values. However, their computation time is longer than the case without noise. The Bayesian techniques return good value for all parameters with the same computation time as for cases without noise.

The CGD method fails the second test with the exponential equation (without and with noise). The three coefficients estimated by this method are wrong. In Figures 3.4 and 3.5, the estimated data profile obtained by the CGD method does not look like the original data. The LM and TR methods perform again as the most rapid methods with under 0.1 second for the

Equation	Coefficient	Input	CGD	LM	TR	RWM	RAM
Polynomial without noise	A	5	5	5	5	4.9424	4.9686
	B	2	2	2	2	1.9898	2.0018
	C	0.5	0.5	0.5	0.5	0.5021	0.5027
Time (s)			<0.1	<0.1	<0.1	3.7	5.1
Polynomial with noise	A	5	5.0497	5.0497	5.0497	4.4846	4.7126
	B	2	2	2	2	1.9987	1.9988
	C	0.5	0.5	0.5	0.5	0.5096	0.506
Time (s)			31.5	1.48	<0.1	3.7	2.7
Exponential without noise	A	2	1.2562	2	2	2.0173	2.0002
	B	3	1.0518	3	3	3.0047	2.9869
	C	4	2.957	4	4	4.0038	3.9926
Time (s)			17.1	<0.1	<0.1	2.8	4.5
Exponential with noise	A	2	1.2704	2.0498	2.0498	2.0692	2.045
	B	3	1.0482	3	3	3.0042	2.977
	C	4	2.9556	4.0001	4.0001	4.0039	3.9876
Time (s)			53.3	<0.1	<0.1	7.7	8.3
Periodic without noise	A	5	4.9973	5	4.9964	5.0175	4.9819
	B	2	-0.1416	2	0.126	1.9621	1.9906
	C	5	1.0535	-5	0.953	4.9761	4.9741
Time (s)			17.7	<0.1	13.1	3.6	5.0
Periodic with noise	A	5	5.2477	5.2414	5.2477	5.2101	5.2269
	B	2	0.0658	0.1951	0.0659	1.9385	1.9768
	C	5	0.9759	2.3566	0.9756	4.9568	4.9759
Time (s)			68.3	<0.1	19.3	10.7	11.1

Table 3.2: Input parameters and estimated results obtained by five different estimation methods in the cases of analytic examples without and with noise (colors for the relative error between estimated parameter and input value: out of 20%, 10-20%, 5-10%, <5%).

computation time, and their estimated results are very close to input values. For this type of equation, 10000 iterations seem enough for the RWM and RAM methods to estimate acceptable results.

For the periodic example, two Bayesian techniques can return the acceptable results for both cases with noise and without. However, the RAM's results seem better than the RWM's ones. The first three methods succeed in estimating the first coefficient of the periodic equation. However, in the cases without noise, the LM method returns the negative third coefficient. In terms of output value y, it is correct, but its estimated parameters are not the correct answer (see Figure 3.6). That is the biggest problem of the non-constrained searching boundary of the LM method. On the other hand, this algorithm can not determine the third coefficient correctly. For the CGD and TR techniques, they can not find out the last two coefficients in both cases (Cf. Figures 3.6 and 3.7).

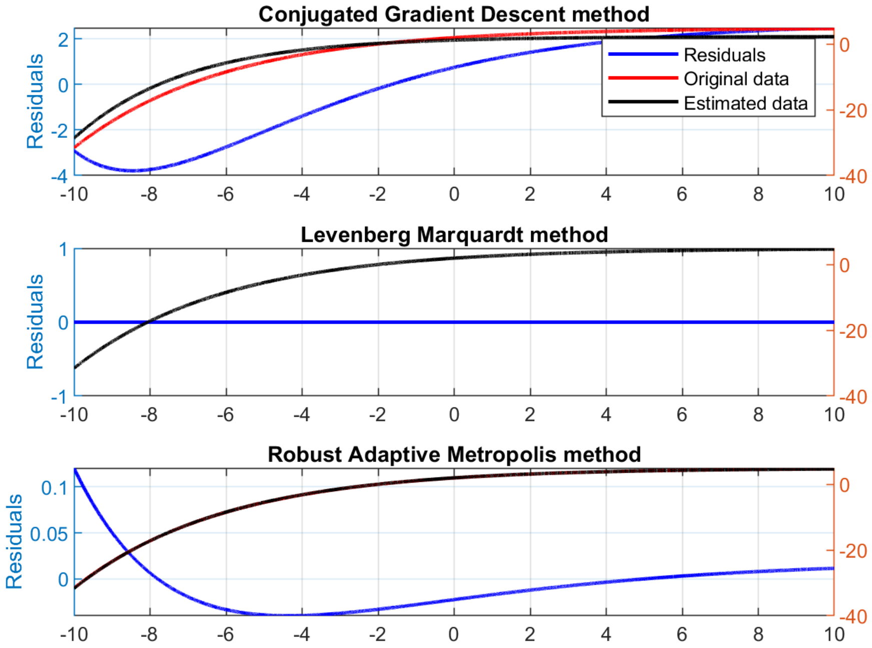

Figure 3.4: Exponential example without noise: original (blue) and estimated (black) profiles by using the Conjugate Gradient Descent, Levenberg-Marquardt, and Robust Adaptive Metropolis methods.

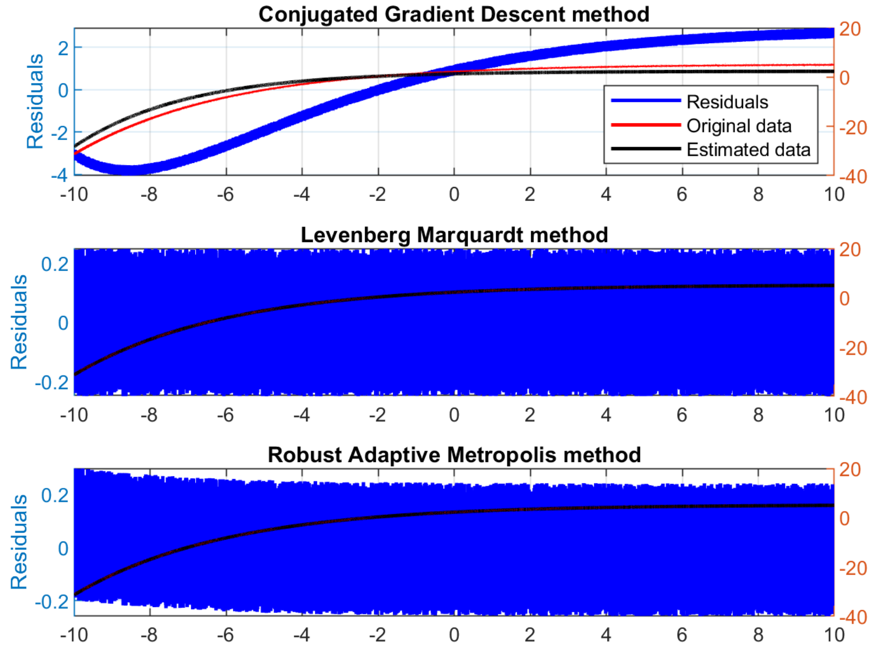

Figure 3.5: Exponential example with noise: original (blue) and estimated (black) profiles by using the Conjugate Gradient Descent, Levenberg-Marquardt and Robust Adaptive Metropolis methods.

The last case concerns the thermal resistance estimation of a 1D case by using the EWC

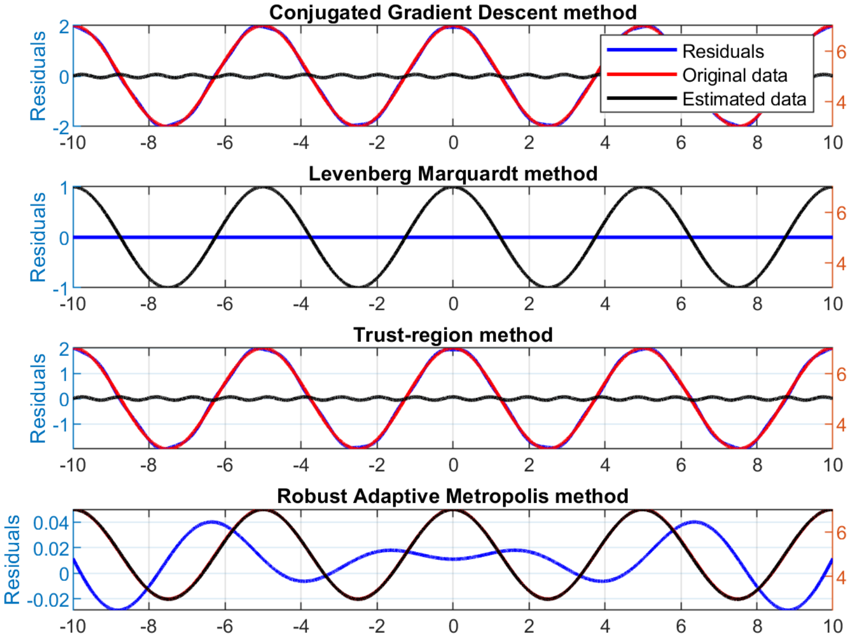

Figure 3.6: Periodic example without noise: original (blue) and estimated (black) profiles by using the Conjugated Gradient Descent, Levenberg-Marquardt, Trust-region and Robust Adaptive Metropolis methods.

and AbF models. According to the previous simple examples, only three out of five methods are chosen to be used in this part: **LM**, **TR** (because of their precision and rapidity), and **RAM** (which is more optimal than RWM). Because there is no particular definition or limitation for each layer of the tested wall in the estimation, there are several possible configurations of layer characteristics that provide the same temporal evolution of minimization data (in this case T_{SI}) and the same wall thermal resistance. Therefore, this comparison focuses only on estimated total thermal resistance.

The thermal resistance value of the considered wall is 4.37 m^2.K.W^{-1}. Here, we suppose that no information on the wall is available, including the number of layers. Then, for each estimation method, three configurations of the wall corresponding to three numbers of layers (2, 3, and 4 layers) are considered. Moreover, this part is based only on data with noise.

Table 3.3 presents the estimation results obtained in this comparative study. As observed in this table, the RAM method is the most robust method among the three considered methods because there is not much difference in estimated results obtained by the RAM method by

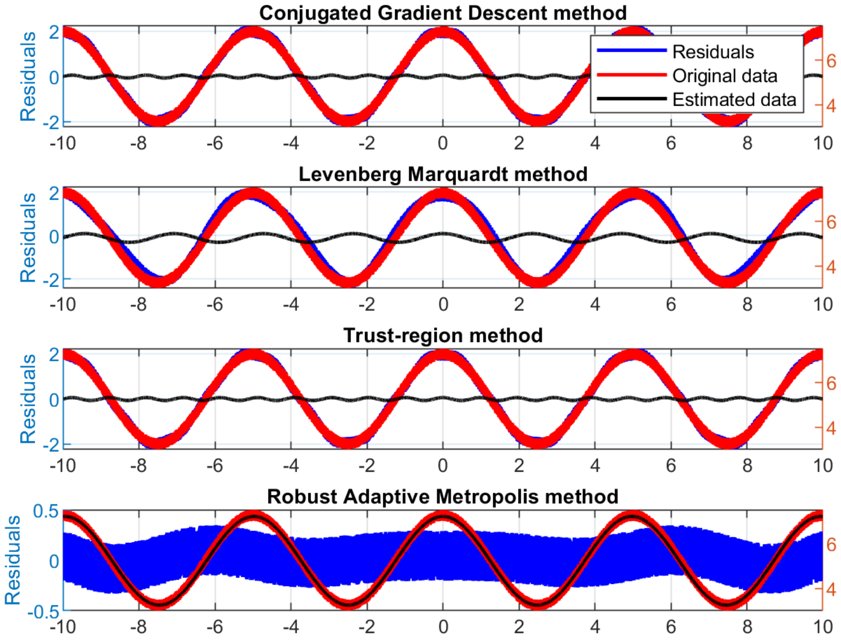

Figure 3.7: Periodic example with noise: original (blue) and estimated (black) profiles by using the Conjugated Gradient Descent, Levenberg-Marquardt, Trust-region and Robust Adaptive Metropolis methods.

using the EWC and AbF models with the three proposed configurations of the studied wall. If analyzing longer data, we will estimate a value closer to the willing one. The 2-layer one seems not enough to represent the studied wall, so that its final result is smaller than the two others.

The TR method shows a good estimation capability with both proposed models. Its results are quite similar to the RAM method with the EWC model, but it needs more time to reach the reference value than the RAM one in the cases of AbF model.

Besides, this comparison shows the problem of the non-constrained boundary of the LM algorithm again as in the previous examples. The four-layer result obtained by the LM method and the EWC model is far from the theoretical value. "Bad profile fit" and "not enough detailed configuration" do not explain this bad estimation because original and estimated profiles are well superimposed, and the number of layers is the same as the one used for the simulation of original data. A "negative" thermal resistance (more specifically, the thermal effusivity) for a layer is found by this method. By using the AbF model, only 3-layer and 4-layer models used in estimation lead to satisfactory results (2-layer model gives a negative value for thermal effusivity).

Method/Moment	No. of layers	6 hours	12 hours	24 hours
Theoretical value	$4.37\ m^2.K.W^{-1}$			
EWC model				
Levenberg-Marquardt Computation time: 4 seconds	2	4.03	4.47	4.48
	3	4.39	4.45	4.48
	4	1.63	1.78	1.85
Trust-region Computation time: 444 seconds	2	3.38	3.99	4.27
	3	4.68	4.49	4.49
	4	4.23	4.64	4.49
Robust Adaptive Metropolis Computation time: 746 seconds	2	3.45	4.13	4.41
	3	3.6	4.65	4.52
	4	4.27	4.49	4.49
AbF model				
Levenberg-Marquardt Computation time: 3 minutes	2	-4.16	-3.74	-3.99
	3	3.76	4.52	4.51
	4	3.75	4.48	4.5
Trust-region Computation time: 92 minutes	2	0.73	1.59	4.87
	3	1.01	4.26	4.22
	4	3.61	4.47	4.5
Robust Adaptive Metropolis Computation time: 107 minutes	2	3.43	4.08	4.24
	3	3.74	4.41	4.46
	4	3.98	4.29	4.46

Table 3.3: Estimated thermal resistance obtained by three different estimation algorithms (colors for the relative error between estimated and theoretical values: out of 20%, 10-20%, 5-10%, <5%).

Moreover, Table 3.3 shows that the estimation using the AbF model requires much more time to run than the EWC one because we have to calculate the discrete Laplace transform on the absorbed flux.

According to the comparative study carried out from simple to complex cases, the Robust Adaptive Metropolis method appears to be the most robust estimation method, even if it requires a longer calculation time. This method also makes it possible to calculate the uncertainty on estimated parameters, while other methods do not. Therefore, the RAM method is chosen in this work to be used as the main estimation algorithm.

3.6 Identification model in use

Following Chapter 2, the thermal quadrupole computation in 1D can provide results similar to those obtained with a commercial calculation code such as COMSOL but with shorter calculation times. Therefore, this computation method is chosen as the direct model for parameter estimation. This section will specify the parameters are estimated in each considered model and the way to estimate them.

According to Section 2.3, the 1D quadrupole representation for surface thermal states of a mono-layer wall is:

$$\begin{pmatrix} \theta(0,p) \\ \phi(0,p) \end{pmatrix} = \begin{pmatrix} ch(e\sqrt{p/a}) & (\lambda\sqrt{p/a})^{-1}\, sh(e\sqrt{p/a}) \\ \lambda\sqrt{p/a}\, sh(e\sqrt{p/a}) & ch(e\sqrt{p/a}) \end{pmatrix} \begin{pmatrix} \theta(e,p) \\ \phi(e,p) \end{pmatrix} \tag{3.49}$$

In this equation, there are three physical parameters of the layer which need to be estimated: e, a and λ (or e, ρC_p and λ). After estimating them, the thermal resistance of this mono-layer wall can be calculated as follows:

$$R = \frac{e}{\lambda} \tag{3.50}$$

and its uncertainty u_R:

$$u_R = \sqrt{\left(\frac{1}{\lambda}u_e\right)^2 + \left(\frac{e}{\lambda^2}u_\lambda\right)^2} \tag{3.51}$$

In the case of a multilayer wall, these equations become:

$$R = \sum_i \frac{e_i}{\lambda_i} \tag{3.52}$$

$$u_R = \sqrt{\sum_i \left(\left(\frac{1}{\lambda_i}u_{e_i}\right)^2 + \left(\frac{e_i}{\lambda_i^2}u_{\lambda_i}\right)^2\right)} \tag{3.53}$$

This representation is called $e - \lambda - \rho C_p$ so that three parameters are needed to estimated for each wall layer. However, this layer can be characterized using two parameters only if using the expression as follows:

$$\begin{pmatrix} \theta(0,p) \\ \phi(0,p) \end{pmatrix} = \begin{pmatrix} ch(\sqrt{p\tau}) & (b\sqrt{p})^{-1}\, sh(\sqrt{p\tau}) \\ b\sqrt{p}\, sh(\sqrt{p\tau}) & ch(\sqrt{p\tau}) \end{pmatrix} \begin{pmatrix} \theta(e,p) \\ \phi(e,p) \end{pmatrix} \tag{3.54}$$

where $b = \lambda/\sqrt{a}$ and $\tau = e^2/a$ are respectively the thermal effusivity and the time constant of the layer material. This representation is called $b - \tau$. In this case, the thermal resistance and its uncertainty can be computed as:

$$R = \frac{\sqrt{\tau}}{b} \tag{3.55}$$

$$u_R = \sqrt{\left(\frac{1}{2b\sqrt{\tau}}u_\tau\right)^2 + \left(\frac{\sqrt{\tau}}{b^2}u_b\right)^2} \tag{3.56}$$

In the case of a multilayer wall, these equations become:

$$R = \sum_i \frac{\sqrt{\tau_i}}{b_i} \tag{3.57}$$

$$u_R = \sqrt{\sum_i \left(\left(\frac{1}{2b_i\sqrt{\tau_1}}u_{\tau_1}\right)^2 + \left(\frac{\sqrt{\tau_i}}{b_i^2}u_{b_i}\right)^2\right)} \tag{3.58}$$

The advantage of this representation is that the terms $b-\tau$ are separated inside and outside the hyperbolic function, so that it is more efficient in estimation than the first representation. Moreover, there are only two unknown parameters to estimate for each layer, instead of three as the previous representation. However, this form can only be used in 1D case. It can not be used in 2D/3D cases because there is the eigenvalue of integral transform under square root (see equation 2.26). Then, only $e - \lambda - \rho C_p$ configuration is possible for 2D/3D estimation. In this study, a 1D model will be used as direct model for parameter estimation then the $b - \tau$ representation is highly recommended.

The choice of analyzed data is very important in our estimation because it affects directly the result accuracy and the computation time. There are two options: from the beginning to the considered moment $[0, t_i]$ and a particular interval $[t_{i-1}, t_i]$. The first option requires more time to compute than the second one. However, the second option may miss the dynamic evolution of our considered system which is observed at the beginning of the measurement. In this study, we focus on the dynamic characteristics of the wall then the first option is chosen. Moreover, the data length is also an important factor. If we use data of long duration, the number of Markov chain iterations should be increased to reach the willing value and it may return an imprecise value with large uncertainty. On the other hand, if using a data of short duration, we can "train" the estimated parameters to reduce the iteration number and optimize the search zone of proposal parameters for the next estimations. Therefore, this study will analyze data hour-by-hour to obtain an hourly evolution of estimated thermal resistance. It means that the k^{th} estimation will use the data of the first k hours of measurement from the beginning.

Because of the difference in parameter magnitude, terms called normalized parameters are used as estimated targets instead of real physical parameters. By directly estimating b and τ, their update steps are not the same, then it may be too large for one and too small for the other.

That is why normalized parameters are used. Before running an estimation, a typical value for each parameter supposed to be realistic is defined. A value of 1 is given to the normalized coefficients A_1^{1-in} (for b) and A_2^{1-in} (for τ) for initialization of the first estimation. The real parameters for direct model at the i^{th} estimation are:

$$\begin{pmatrix} b_i \\ \tau_i \end{pmatrix} = \begin{pmatrix} A_1^{i-in} & 0 \\ 0 & A_2^{i-in} \end{pmatrix} \begin{pmatrix} b_{typ} \\ \tau_{typ} \end{pmatrix} \tag{3.59}$$

For each estimation (for example the k^{th} estimation for data of k hours of heating), the histogram of the Markov chain of each estimated target will be fitted with Gaussian distribution $G(\mu, \sigma^2)$ to deduce the new normalized parameters $A_1^{k-out} = \mu_1$ and $A_2^{k-out} = \mu_2$. A new vector of real parameters is computed from these values and the typical parameters in equation 3.59. The next estimation will take results of the previous one as the starting point ($A_1^{k+1-in} = A_1^{k-out}$ and $A_2^{k+1-in} = A_2^{k-out}$). Moreover, to improve the estimation quality, the prior distribution which is used in the posterior probability will take the starting point as its expectation. This action helps limiting the optimal searching zone. Additionally, the uncertainty for the estimated normalized parameters are $uA_1^{k-out} = \sigma_1$ and $uA_2^{k-out} = \sigma_2$. Finally, according to equations 3.57 and 3.58, the estimated thermal resistance and its uncertainty will be obtained. Figure 3.8 shows the complete process of thermal resistance estimation used in this study.

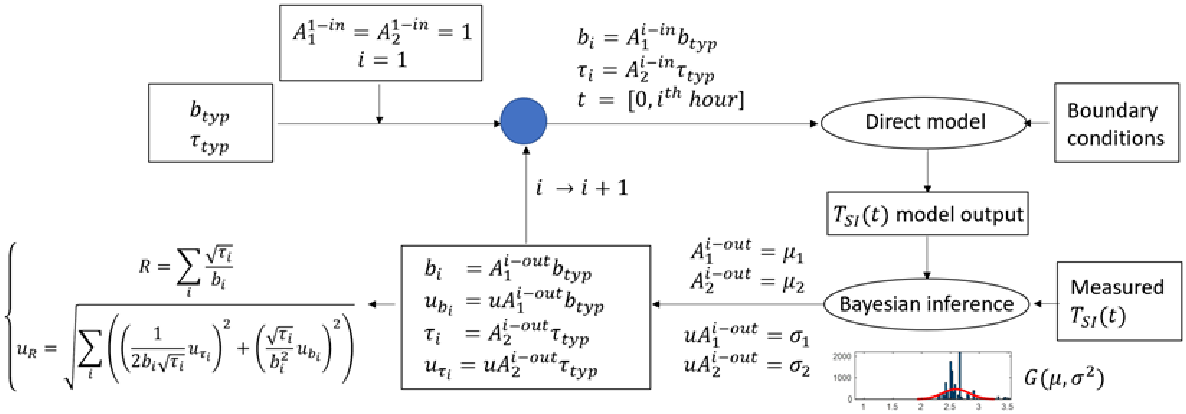

Figure 3.8: Thermal resistance estimation process used in this study.

An estimation example for a 6-hour real measurement data is shown in Figure 3.9. We observe clearly that the estimated value at the beginning has a large uncertainty because we do not have much information. Then, with more information, the next results converge rapidly to a stable value with small uncertainty.

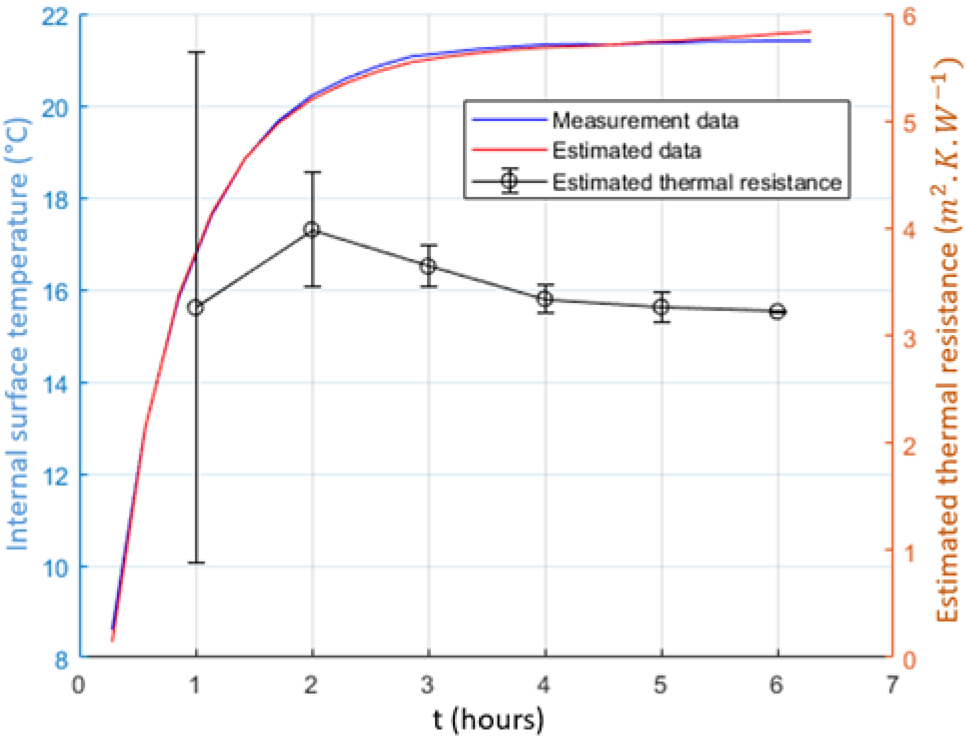

Figure 3.9: Example of an estimation case: (blue line) measurement data, (red line) estimated data and (black line) estimated thermal resistance with corresponding uncertainty.

3.7 Estimation capability validation with 3D numerical data

The final stage of the numerical study focuses on validating the proposed estimation algorithm on numerical data before testing on real data. As presented in Section 2.2, three types of walls are studied here: Internal Wall Insulation (IWI), Single Wall (SW), and External Wall Insulation (EWI). The physical properties of these walls are presented in Table 2.3.

The internal air temperature is fixed to 20°C. Three different external environmental conditions are considered: a constant condition at 20°C without solar flux and two 24-hour variable conditions from Trappes and Carpentras Météo France database (see Figure 2.2 in Section 2.5) . The difference between the two variable conditions is that solar radiation in Carpentras is very high at the beginning compared to Trappes case. The temperature and the absorbed heat flux on the internal surface are calculated by the 3D QUAD simulation. Moreover, a noise which is obtained experimentally is added on each computed data to generate numerical data close to real data (see Appendix A3).

Two direct models are tested here: 1D EWC and 1D AbF. For the EWC model, the correct values of applied thermal excitation q_{exci} and internal heat transfer coefficient h_I as used in the simulation are applied in the estimation. In addition, both EWC and AbF models use correct constant external heat transfer coefficient h_E.

The first two parts of this section present the sensitivity study and the heat flux study to predict the estimation capability. Then, two series of estimations using the 1D EWC and 1D AbF models are shown in the third and fourth parts.

3.7.1 Parameter sensitivity study

Before running estimation process, the sensitivity study is always launched to determine which parameters are the most important in the considered estimation. Here, two models and three types of walls are studied, then six sensitivity tests are carried out. Among the three IWI walls, the IWI 1 configuration is chosen to represent IWI type wall in this study.

This sensitivity study is based on the internal surface temperature T_{SI} which is chosen as minimization data for estimation. In order to compare the sensitivities of the parameters, the reduced sensitivity coefficient S_k of the parameter k is defined as follows:

$$S_k = k\frac{\delta T_{SI}}{\delta k} \tag{3.60}$$

Figure 3.10 presents the reduced sensitivity coefficients for EWC model and IWI 1 wall during the first three hours of simulation. The two highest sensitivity coefficients are clearly observed for q_{exci} and h_I. These important magnitudes are the reason why the EWC model is not preferred in this work. Indeed it is difficult to ensure the homogeneity of the incoming thermal excitation flux on the applied surface. Therefore, assuming that this flux is perfectly homogeneous on a surface of 0.6x0.6 m^2 in real measurement, the estimation could give seriously wrong results (the detailed discussion about the homogeneity of the thermal excitation flux will be presented in Section 4.2). In fact, this problem could be solved by a well-protected thermal source which allows homogenizing the imposed thermal excitation flux and calibrating its value. However, the most difficult factor here is h_I which is hardly controlled during an *in-situ* measurement. This parameter depends on the environmental conditions (temperature, air velocity, humidity, etc.). There are several measurement techniques to evaluate its value but none of them can be considered robust enough to be used *in-situ*, especially for an active measurement.

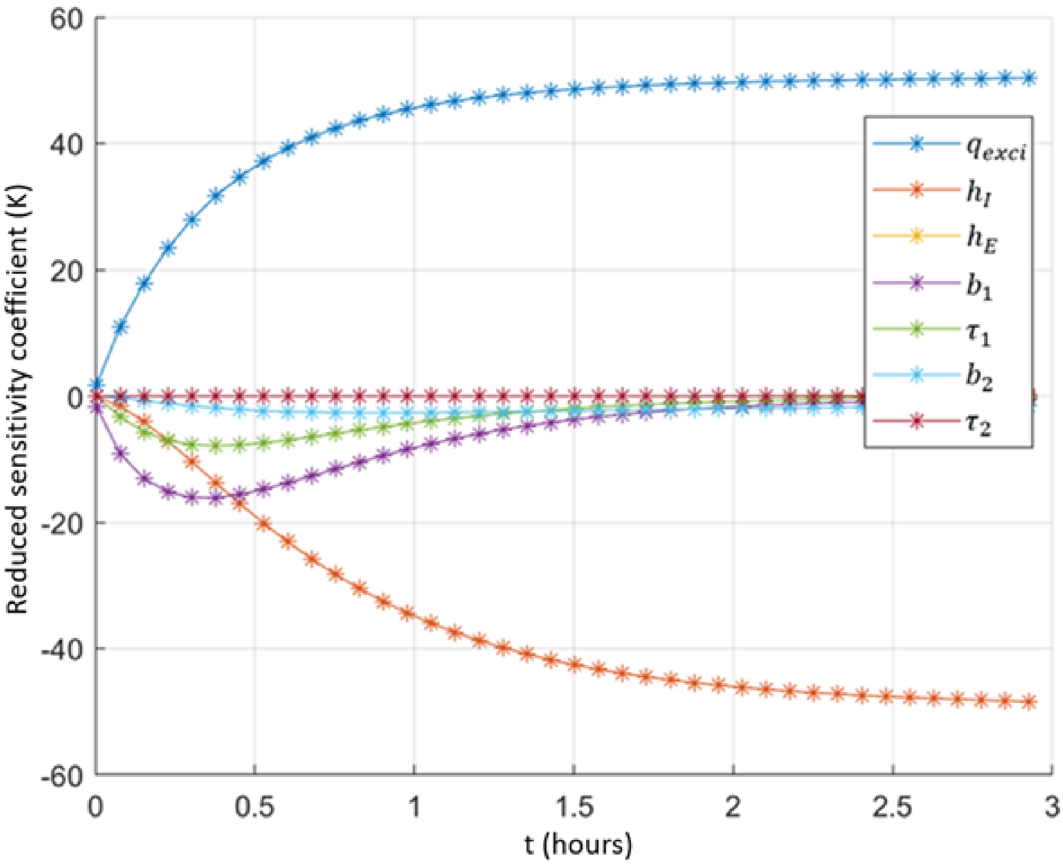

Figure 3.10: Reduced sensitivity coefficients of parameters computed with the EWC model for the IWI 1 wall.

In order to show the effect of h_I on thermal resistance estimation, a small test of estimation by varying h_I value is launched. The measured data is simulated by 3D thermal quadrupole computation with IWI 1 wall under the constant condition. Three estimations are carried out with 3 different fixed values of h_I corresponding to 100%, 99%, and 101% of h_I used in the simulation. These three values are very close to each other (only 0.077 W/m^2·K of difference). The objective of this test is determining how the estimated thermal resistance varies when we have a small variation of h_I, caused by measurement noise for instance.

Figure 3.11 shows three completely different estimation results. In the case of the correct value h_I (100%), the estimated value (5.23 m^2.K.W^{-1}) is very close to the reference one (5.66 m^2.K.W^{-1}). However, for the two other cases, the estimated thermal resistances are totally wrong. This example illustrates the important role of h_I in the EWC model. In the numerical studies, with a known and constant value of h_I, the thermal resistance estimation is performed without any problem but it is not so simple for experimental situations. That is why the AbF model was mentioned as a more preferred option for experimental works than EWC one.

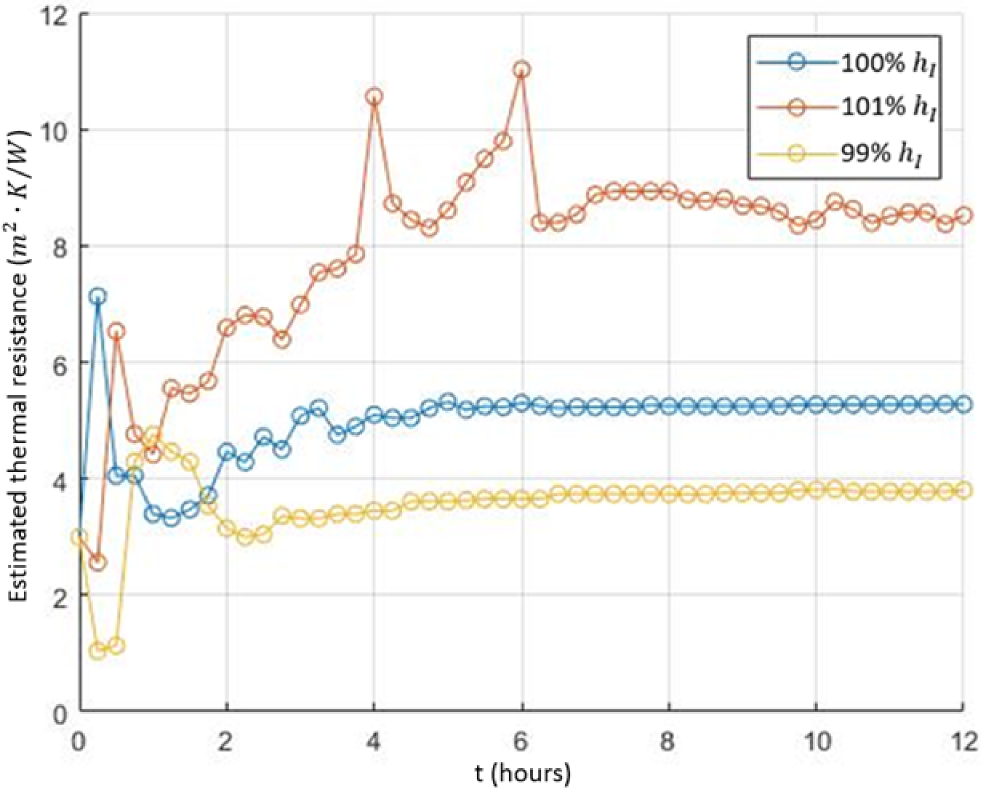

Figure 3.11: Temporal evolution of estimated thermal resistance by varying the internal global heat transfer coefficient.

If removing q_{exci} and h_I in Figure 3.10, only the physical characteristics of the wall are considered in the sensitivity test for both EWC and AbF models (there is also h_E coefficient but its sensitivity is very weak when considering the internal surface temperature). For each case, to verify the correlation of studied parameter sensitivity, a correlation matrix is calculated. For the sensitivity of parameters b_1 and τ_1 (noted S_{b_1} and S_{τ_1}, respectively), their correlation coefficient can be computed as:

$$corr(S_{b_1}, S_{\tau_1}) = \frac{cov(S_{b_1}, S_{\tau_1})}{\sigma_{b_1}\sigma_{\tau_1}} \tag{3.61}$$

where σ_{b_1} and σ_{τ_1} are the standard deviations of S_{b_1} and S_{τ_1} respectively.

The first study concerns the IWI type wall. Figure 3.12 presents the reduced sensitivity coefficients of the thermal effusivity (b) and the time constant (τ) for each layer calculated by using 1D EAC model. In the case of EWC model in Figure 3.12, the parameters of the first layer (b_1, τ_1) can be estimated at the beginning of the test but they are completely correlated (see Figure 3.13).

The thermal effusivity of second layer b_2 which depends only on the material physical

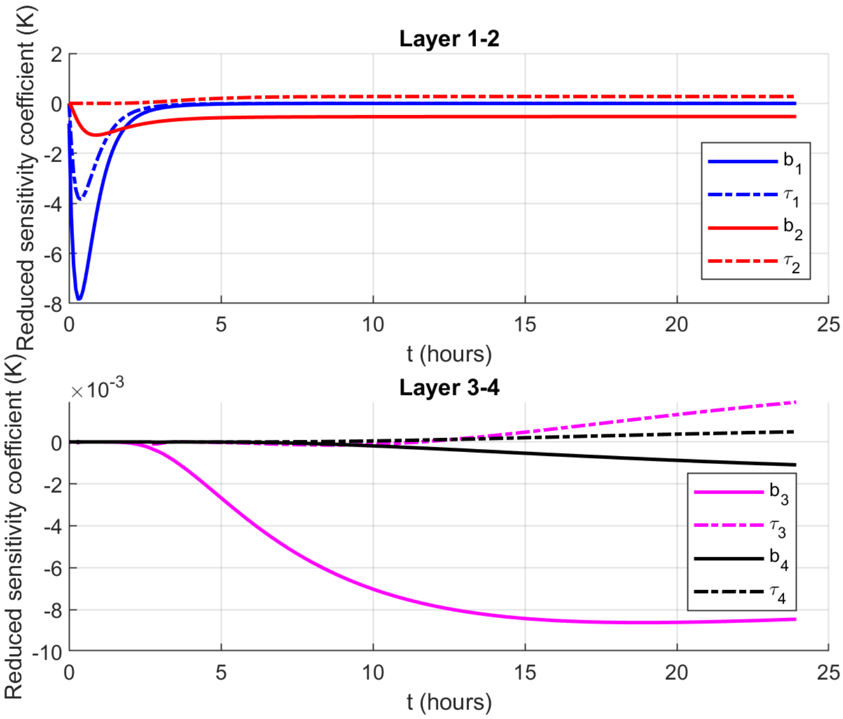

Figure 3.12: Reduced sensitivity coefficients computed with the 1D EWC model for the IWI 1 wall.

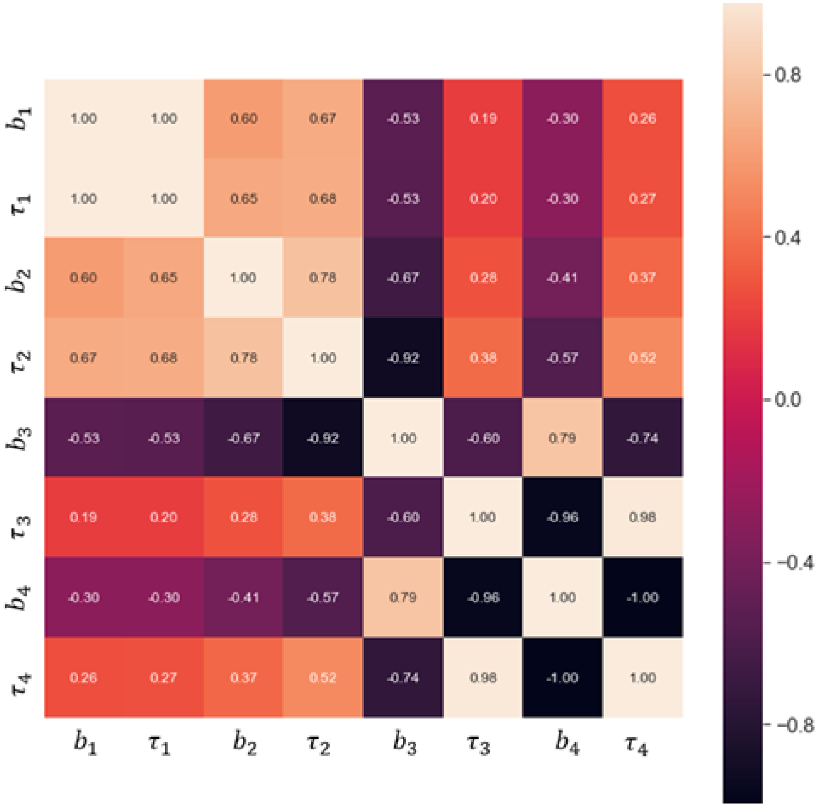

	b_1	τ_1	b_2	τ_2	b_3	τ_3	b_4	τ_4
b_1	1.00	1.00	0.60	0.67	-0.53	0.19	-0.30	0.26
τ_1	1.00	1.00	0.65	0.68	-0.53	0.20	-0.30	0.27
b_2	0.60	0.65	1.00	0.78	-0.67	0.28	-0.41	0.37
τ_2	0.67	0.68	0.78	1.00	-0.92	0.38	-0.57	0.52
b_3	-0.53	-0.53	-0.67	-0.92	1.00	-0.60	0.79	-0.74
τ_3	0.19	0.20	0.28	0.38	-0.60	1.00	-0.96	0.98
b_4	-0.30	-0.30	-0.41	-0.57	0.79	-0.96	1.00	-1.00
τ_4	0.26	0.27	0.37	0.52	-0.74	0.98	-1.00	1.00

Figure 3.13: Correlation coefficients of reduced sensitivity coefficients computed with the 1D EWC model for the IWI 1 wall.

properties increases immediately after the first few minutes of heating. Besides, its time constant τ_2 shows a weak sensitivity (but not zero) in comparison to the three other parameters of the layers 1 and 2. It is understandable because the second layer of IWI type wall is insulating then it takes time to diffuse the heat flux because of strong inertia. Additionally, the sensitivity coefficients of these two parameters have the weakest correlation compared to other (Cf. Figure 3.13). For the last two layers 3 and 4, the reduced sensitivity coefficients are very close to 0 so that these parameters seem to be difficult to detect.

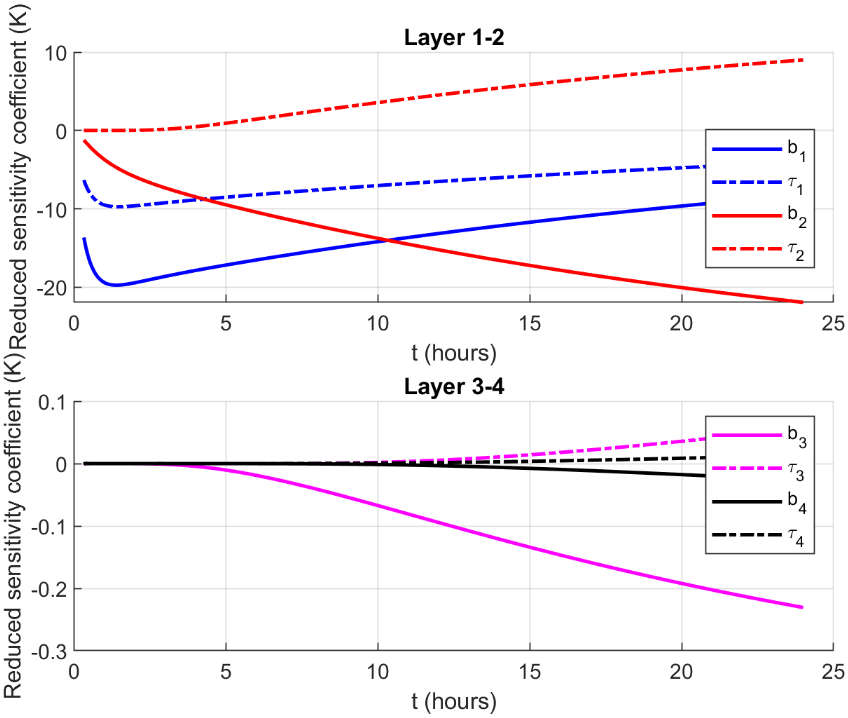

Figure 3.14: Reduced sensitivity coefficients computed with the 1D AbF model for the IWI 1 wall.

With the AbF model, high reduced sensitivity coefficients and their correlation are observed in Figures 3.14 and 3.15 for the parameters of the first two layers. It can be explained by the strong relation between the absorbed flux used as model input and the physical characteristics of tested wall. Indeed the absorbed flux contains already certain exclusive information of wall characteristics. With a same incident thermal excitation from the lamps, different walls will transfer different absorbed fluxes. Therefore, the AbF model presents more important sensitivity and stronger sensitivity correlation than EWC one with the same wall. Similar to the results obtained with the EWC model for IWI wall, sensitivities of the last two layers are quite weak compared to those of the first two layers, at least for a measurement time limited to 24 hours.

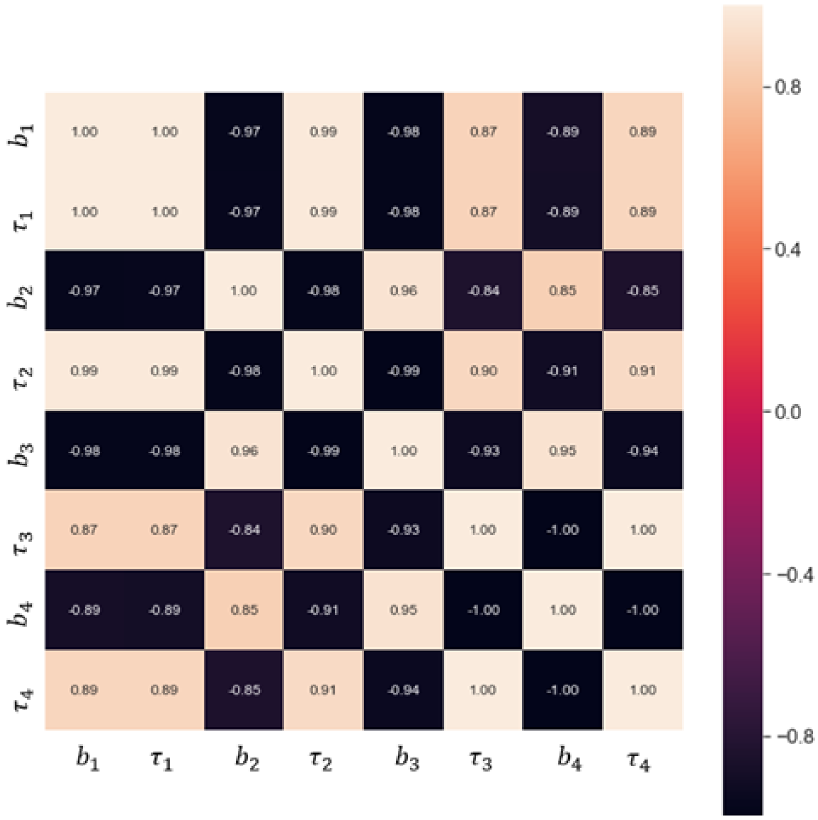

	b_1	τ_1	b_2	τ_2	b_3	τ_3	b_4	τ_4
b_1	1.00	1.00	-0.97	0.99	-0.98	0.87	-0.89	0.89
τ_1	1.00	1.00	-0.97	0.99	-0.98	0.87	-0.89	0.89
b_2	-0.97	-0.97	1.00	-0.98	0.96	-0.84	0.85	-0.85
τ_2	0.99	0.99	-0.98	1.00	-0.99	0.90	-0.91	0.91
b_3	-0.98	-0.98	0.96	-0.99	1.00	-0.93	0.95	-0.94
τ_3	0.87	0.87	-0.84	0.90	-0.93	1.00	-1.00	1.00
b_4	-0.89	-0.89	0.85	-0.91	0.95	-1.00	1.00	-1.00
τ_4	0.89	0.89	-0.85	0.91	-0.94	1.00	-1.00	1.00

Figure 3.15: Correlation coefficients of reduced sensitivity coefficients computed with the 1D AbF model for the IWI 1 wall.

According to these observations, it is possible to well estimate the thermal characteristics of the first two layers of the IWI wall which contribute mainly to the wall thermal resistance. The properties of the last two layers, which may not be estimated correctly, contribute only to 2-3% of the total thermal resistance. So, their estimated values could not significantly change the final result of the estimation. In the case where the initial values for these layers are realistic, their normalized coefficients do not change a lot because of a weak sensitivity.

The EWC model for EWI wall presents stronger reduced sensitivity coefficients and correlation for the first two layers than the last two ones (Cf. Figures 3.16 and 3.17). These layers of this wall are the coating and the concrete wall and react more quickly and strongly at the beginning of the test than the insulation layer in the case of the IWI wall. Weak reduced sensitivity coefficient values are found for the insulation layer (the third layer) so it seems difficult to estimate its properties.

There is not much difference between the sensitivity coefficients obtained with the EWC and AbF models (Cf. Figures 3.18 and 3.19). Therefore, we can estimate only the first two layers of the EWI wall, whose thermal resistance is only 3-4% of total resistance of the wall, so

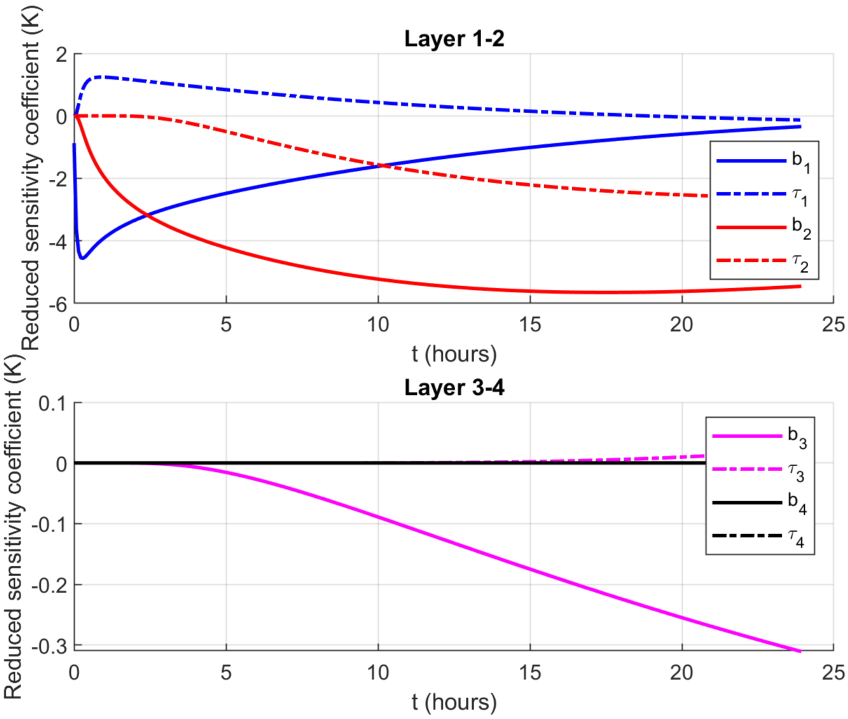

Figure 3.16: Reduced sensitivity coefficients computed with the 1D EWC model for the EWI wall.

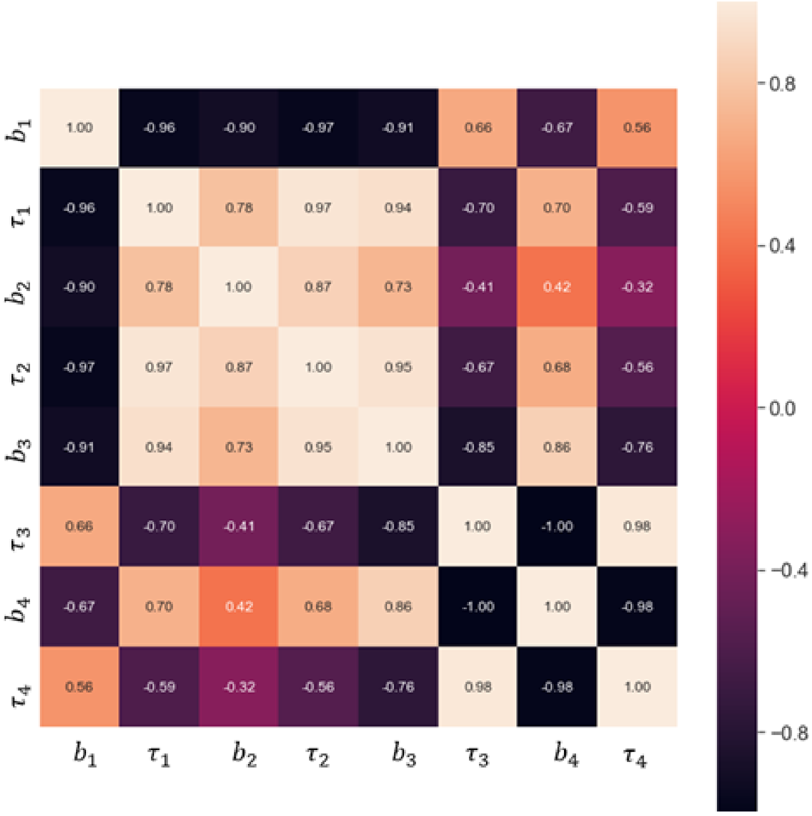

	b_1	τ_1	b_2	τ_2	b_3	τ_3	b_4	τ_4
b_1	1.00	-0.96	-0.90	-0.97	-0.91	0.66	-0.67	0.56
τ_1	-0.96	1.00	0.78	0.97	0.94	-0.70	0.70	-0.59
b_2	-0.90	0.78	1.00	0.87	0.73	-0.41	0.42	-0.32
τ_2	-0.97	0.97	0.87	1.00	0.95	-0.67	0.68	-0.56
b_3	-0.91	0.94	0.73	0.95	1.00	-0.85	0.86	-0.76
τ_3	0.66	-0.70	-0.41	-0.67	-0.85	1.00	-1.00	0.98
b_4	-0.67	0.70	0.42	0.68	0.86	-1.00	1.00	-0.98
τ_4	0.56	-0.59	-0.32	-0.56	-0.76	0.98	-0.98	1.00

Figure 3.17: Correlation coefficients of reduced sensitivity coefficients computed with the 1D EWC model for the EWI wall.

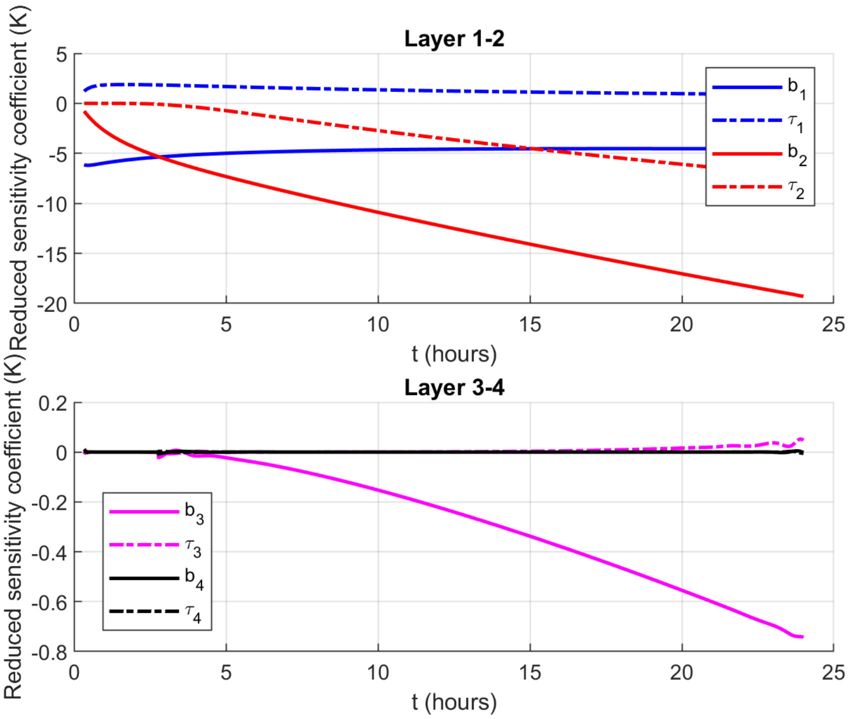

Figure 3.18: Reduced sensitivity coefficients computed with the 1D AbF model for the EWI wall.

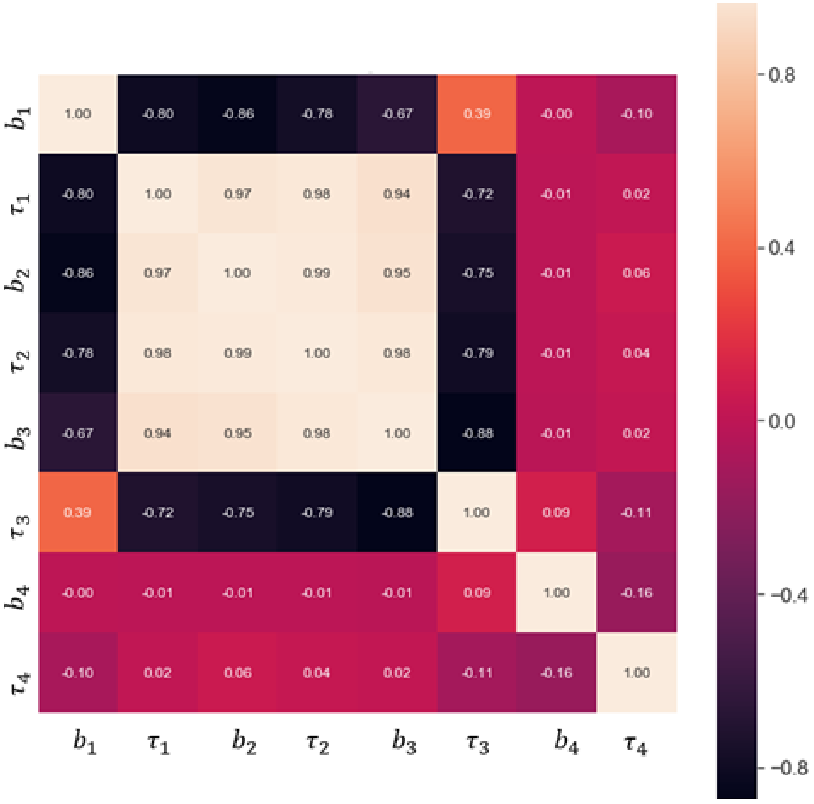

	b_1	τ_1	b_2	τ_2	b_3	τ_3	b_4	τ_4
b_1	1.00	-0.80	-0.86	-0.78	-0.67	0.39	-0.00	-0.10
τ_1	-0.80	1.00	0.97	0.98	0.94	-0.72	-0.01	0.02
b_2	-0.86	0.97	1.00	0.99	0.95	-0.75	-0.01	0.06
τ_2	-0.78	0.98	0.99	1.00	0.98	-0.79	-0.01	0.04
b_3	-0.67	0.94	0.95	0.98	1.00	-0.88	-0.01	0.02
τ_3	0.39	-0.72	-0.75	-0.79	-0.88	1.00	0.09	-0.11
b_4	-0.00	-0.01	-0.01	-0.01	-0.01	0.09	1.00	-0.16
τ_4	-0.10	0.02	0.06	0.04	0.02	-0.11	-0.16	1.00

Figure 3.19: Correlation coefficients of reduced sensitivity coefficients computed with the 1D AbF model for the EWI wall.

that our estimated result will be very small in compared to the willing value.

As observed in Figures from 3.20 to 3.23, SW type wall returns high reduced sensitivity coefficients for all parameters with both tested models. After 5 hours of heating, the parameters of its three layers have a high sensitivity. So, the wall thermal resistance could be completely estimated. By analyzing the sensitivity correlation, the thermal effusivity b_2 performs the weakest correlation among six studied parameters. However, with the AbF model, the time constant τ_2 is strongly correlated to both parameters of the third layer.

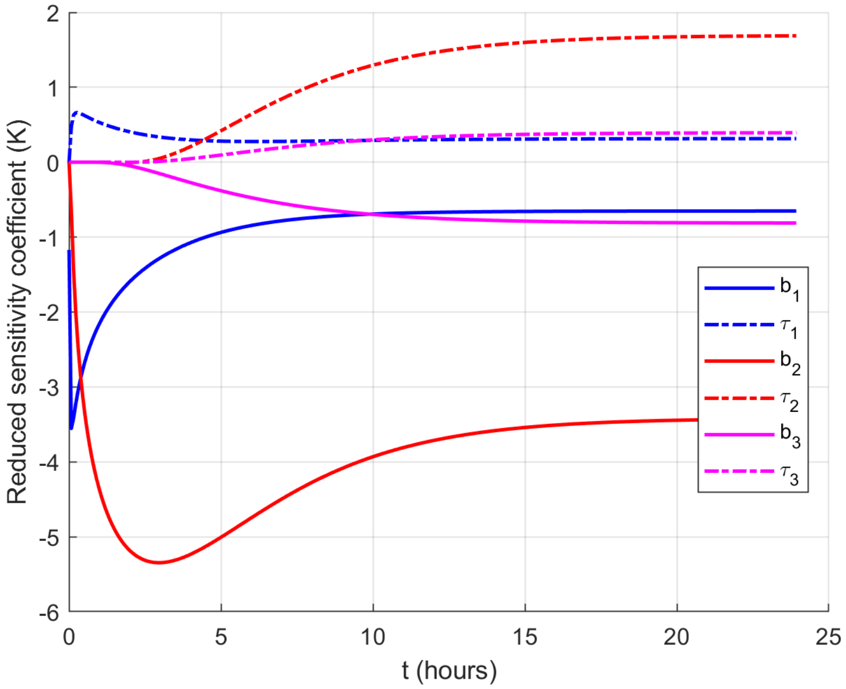

Figure 3.20: Reduced sensitivity coefficients computed with the 1D EWC model for the SW wall.

3.7.2 Prediction of estimation capability via numerical studies of heat flux

In addition to the sensitivity study, several numerical simulations computed by COMSOL in 3D are launched to observe heat flux distribution inside the three types of walls studied.

Figure 3.24 shows that for the case of IWI type wall, the heat flux does not vary a lot along the insulation layer. This is due to weak lateral effects. The longitudinal heat flux at the center of the front and rear faces of the insulation layer ($y = 0$) are 9.2 and 8.7 W.m^{-2} respectively. Then, A strong variation of color, which is observed in this layer in Figure 3.24 (more heat flux

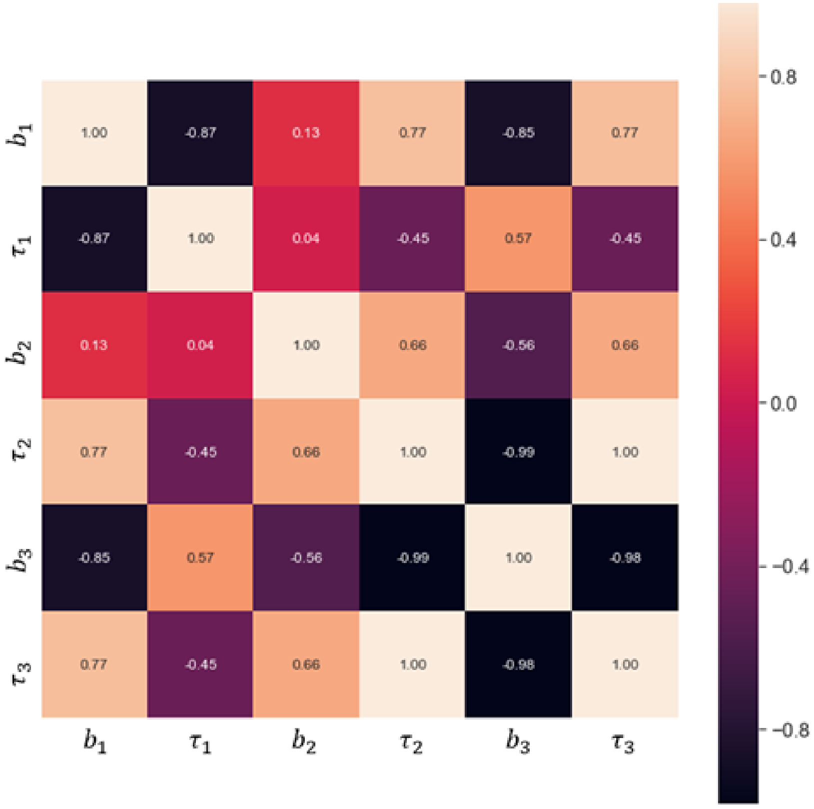

	b_1	τ_1	b_2	τ_2	b_3	τ_3
b_1	1.00	-0.87	0.13	0.77	-0.85	0.77
τ_1	-0.87	1.00	0.04	-0.45	0.57	-0.45
b_2	0.13	0.04	1.00	0.66	-0.56	0.66
τ_2	0.77	-0.45	0.66	1.00	-0.99	1.00
b_3	-0.85	0.57	-0.56	-0.99	1.00	-0.98
τ_3	0.77	-0.45	0.66	1.00	-0.98	1.00

Figure 3.21: Correlation coefficients of reduced sensitivity coefficients computed with the 1D EWC model for the SW wall.

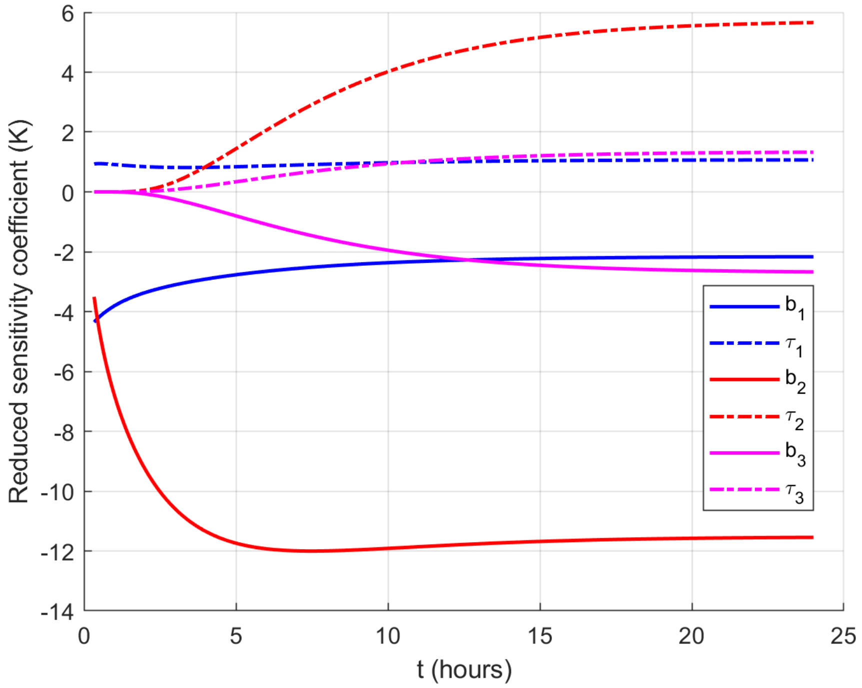

Figure 3.22: Reduced sensitivity coefficients computed with the 1D AbF model for the SW wall.

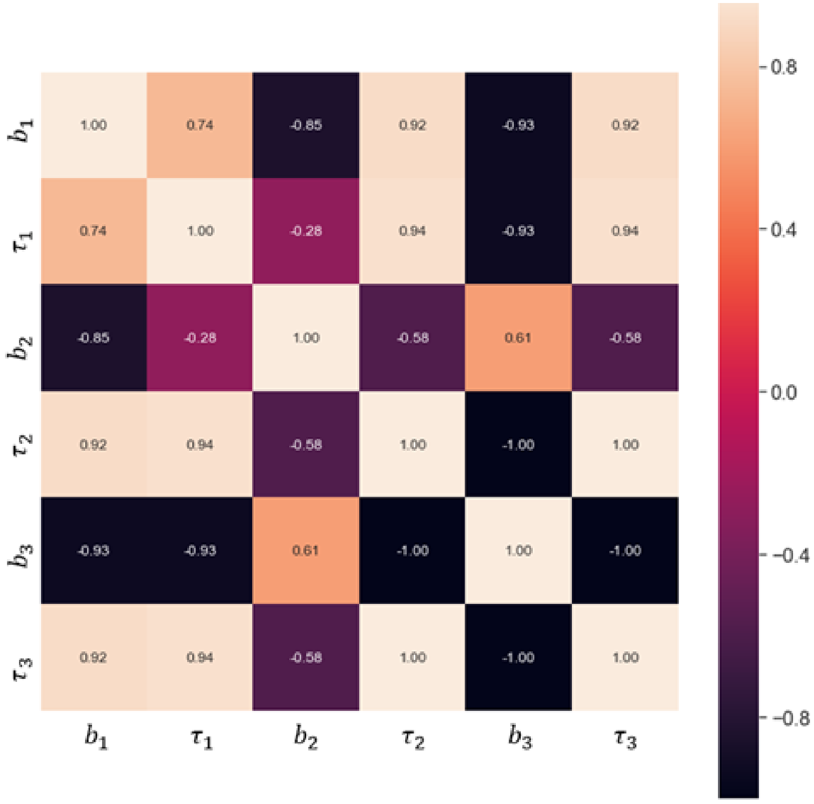

	b_1	τ_1	b_2	τ_2	b_3	τ_3
b_1	1.00	0.74	-0.85	0.92	-0.93	0.92
τ_1	0.74	1.00	-0.28	0.94	-0.93	0.94
b_2	-0.85	-0.28	1.00	-0.58	0.61	-0.58
τ_2	0.92	0.94	-0.58	1.00	-1.00	1.00
b_3	-0.93	-0.93	0.61	-1.00	1.00	-1.00
τ_3	0.92	0.94	-0.58	1.00	-1.00	1.00

Figure 3.23: Correlation coefficients of reduced sensitivity coefficients computed with the 1D AbF model for the SW wall.

isolines in the third layer than the second one), indicates that the heat diffuses laterally inside the third layer (support/concrete wall). This observation leads to the conclusion that the insulation layer of IWI wall, which contributes to 95% of the wall thermal resistance, can be correctly estimated because the heat flux passing this layer in 3D model behaves the same way as 1D model which is used in the thermal resistance estimation.

The heat flux between the two faces of the second layer of the EWI wall drops rapidly (from 134 W.m^{-2} on the front face to 7.7 W.m^{-2} on the rear face, see 3.25). It means that the majority of incoming heat flux diffuses laterally. So, the insulation layer receives less than 6% of the heat flux absorbed by the internal surface. As in the conclusion of Section 3.7.1, it is possible to estimate only the first two layers of the EWI wall which represent less than 5% of the wall thermal resistance.

The SW wall is the simplest configuration among the proposed walls. It does not have any insulation layer so that the heat flux can diffuse everywhere in this type of wall. The lateral diffusion seems more important than for the two other walls (see Figure 3.26) so that it may create difficulties if using the AbF model for the estimation of the thermal resistance.

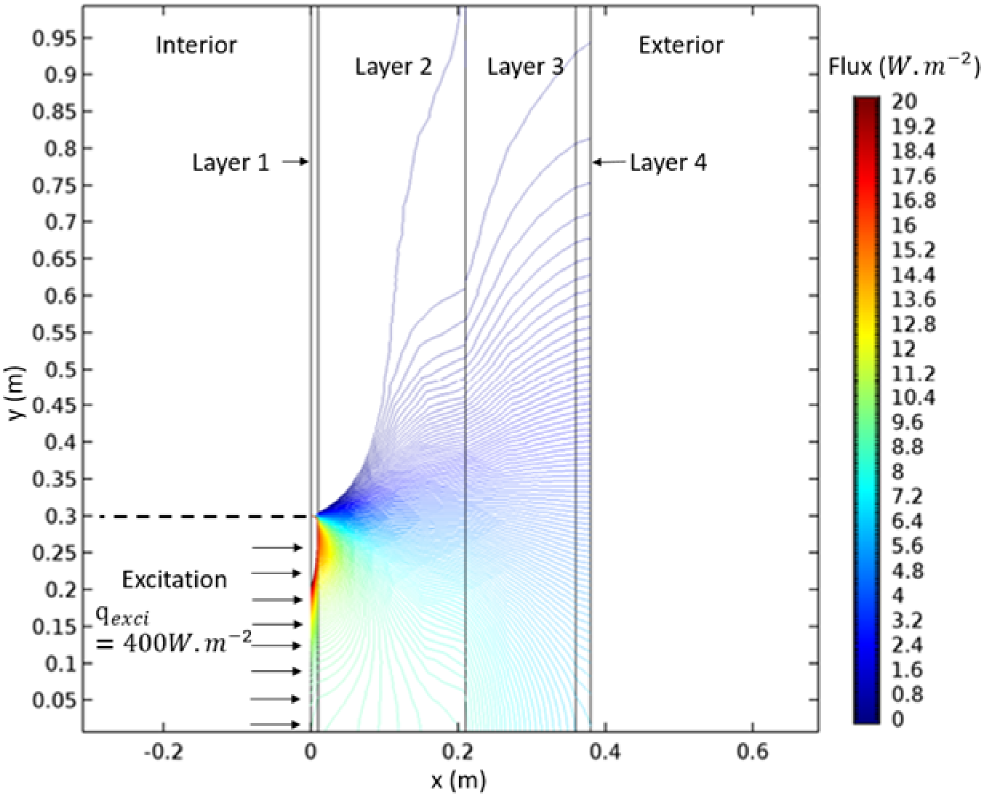

Figure 3.24: Longitudinal heat flux isolines in IWI wall after 24 hours of heating.

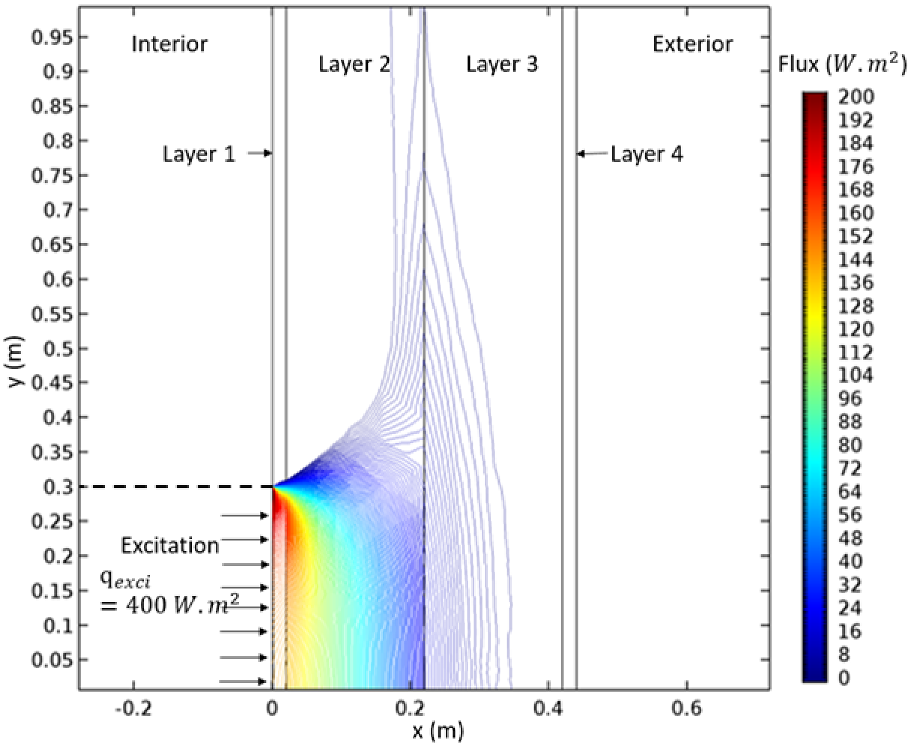

Figure 3.25: Longitudinal heat flux isolines in EWI wall after 24 hours of heating.

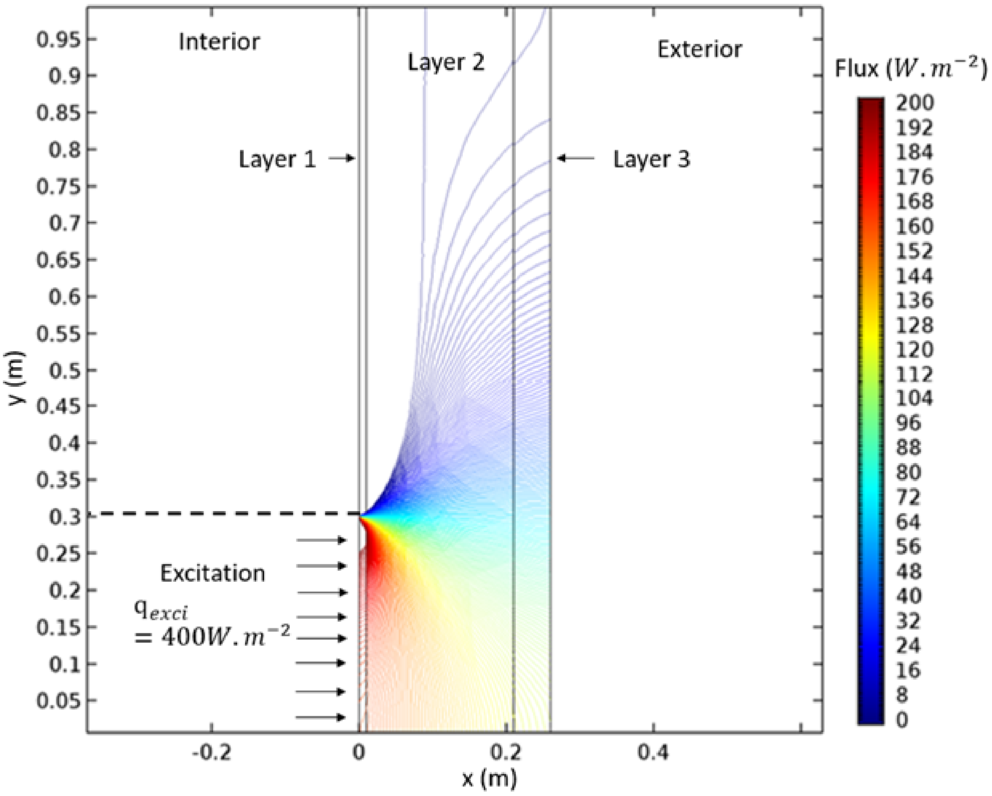

Figure 3.26: Longitudinal heat flux isolines in SW wall after 24 hours of heating.

3.7.3 Estimation results of the cases under constant conditions by using 1D EWC model

The first considered data set is the case under constant conditions (both internal and external air temperatures are constant and equal to 20°C without solar radiation). Figure 3.27 and Table 3.4 present the ratios between theoretical and estimated thermal resistances with corresponding uncertainties obtained by using the 1D EWC model for five considered walls during 24 hours of heating.

Globally, estimated values are quite close to theoretical ones in the case of the three IWI walls. As observed in Figure 3.27, for IWI 3 wall, a stable estimated value (2.21 $m^2.K.W^{-1}$) is obtained after 5 hours, whereas the estimated thermal resistance for IWI 2 wall needs a little longer duration (around 6-7 hours) to stabilize at 4.66 $m^2.K.W^{-1}$ because of a higher thermal resistance. For the last one (IWI 1 wall), which has the strongest resistance (5.66 $m^2.K.W^{-1}$), a quite good result (5.61 $m^2.K.W^{-1}$) is obtained after 8 hours. Then, we observe variation of the estimated thermal resistance and a stabilization at 5.22 $m^2.K.W^{-1}$ from 12-15 hours of measurement. To explain this difference of convergence time, we should focus on the insulation

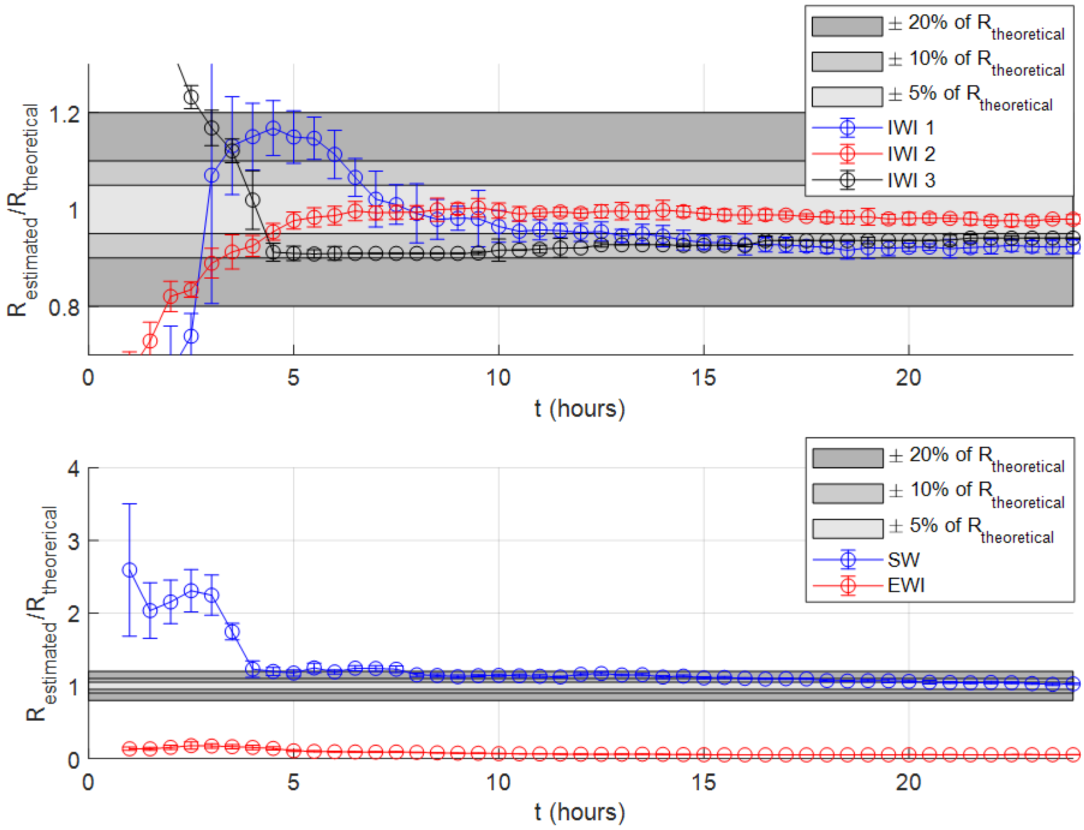

Figure 3.27: Ratio between the theoretical and estimated thermal resistances for the five considered walls under constant conditions according to the heating duration by using the EWC model.

	IWI 1	IWI 2	IWI 3	SW	EWI
R_{ref}	5.66	4.72	2.34	0.19	4.14
Measurement time	$R_{estimated}$ ($u_{R_{estimated}}$)				
6 hours	6.31 (0.28)	4.66 (0.09)	2.21 (0.03)	0.23 (0.01)	0.39 (0.03)
8 hours	5.61 (0.34)	4.69 (0.07)	2.12 (≈ 0)	0.22 (0.01)	0.35 (0.01)
12 hours	5.39 (0.11)	4.68 (0.04)	2.15 (≈ 0)	0.22 (0.01)	0.25 (0.01)
18 hours	5.22 (0.07)	4.64 (0.05)	2.19 (≈ 0)	0.2 (0.01)	0.21 (0.01)
24 hours	5.23 (0.08)	4.62 (0.04)	2.2 (≈ 0)	0.19 (0.01)	0.22 (0.01)

Table 3.4: Theoretical and estimated thermal resistances (in m^2.K.W^{-1}) with corresponding uncertainties obtained with the 1D EWC model for the five studied walls under constant conditions (colors for the relative resistance error between $R_{estimated}$ and R_{ref}: out of 20%, 10-20%, 5-10%, <5%).

layer thermal inertia. According to Table 3.5 and the previous observation, the wall with smaller time constant for the insulation layer converges faster to its stable value.

In the case of the EWI wall, a very small amount of the theoretical resistance is estimated (around 0.35 m^2.K.W^{-1} or 8-9% of total resistance) after the first few minutes of heating and this value does not change significantly during the 24 hours of measurement. This results can be

Wall	Time constant (s)
IWI 1	36944
IWI 2	25235
IWI 3	14400

Table 3.5: Time constants of the insulation layer of three tested IWI walls

explained by the strong lateral diffusion inside the second layer, as presented above.

The SW case leads to a better result than expected in the sensitivity study. 6-hour data can return a value quite close to the theoretical one (estimated and theoretical thermal resistances are respectively 0.23 and 0.19 $m^2.K.W^{-1}$). For a poorly insulated wall with a significant lateral effect such as the SW type, this error of 0.04 $m^2.K.W^{-1}$ is acceptable.

In addition, we observe that the estimated value is reduced when increasing heating duration. This tendency can be explained by the difference between 1D and 3D models. In the 1D model, used as direct model in the estimation algorithm, the applied thermal excitation flux will go straight to the rear end of the studied wall. However, in the 3D model used to generate simulated measurement data, this flux has to share a small amount for lateral diffusion. This amount becomes more important when the thermal excitation lasts longer. Therefore, the difference between surface temperature computed by 1D and 3D models for the same configuration becomes larger with longer heating duration (T_{SI} of 1D model is higher than that of 3D model). Moreover, as the thermal resistance is proportional to the surface temperature in steady state (long duration), this explains why we observe a lowering of estimated results.

3.7.4 Estimation results of the cases under variable conditions by using 1D EWC model

The cases under variable condition also provide interesting results. There are two variable conditions tested here. We recall that data from Carpentras present quite strong solar radiation at the beginning and high external air temperature (unfavorable condition as seen in the literature review) while data from Trappes correspond to more favorable condition. Table 3.6 shows the estimated results for these cases.

According to the results presented in Table 3.6 and Figure 3.28, only the thermal resistance of three IWI walls can be considered well characterized under Carpentras conditions. Their results converge to a stable value after 12 hours of measurement with a relative error less than

	IWI 1	IWI 2	IWI 3	SW	EWI
R_{ref}	5.66	4.72	2.34	0.19	4.14
Measurement time	$R_{estimated}$ ($u_{R_{estimated}}$)				
External condition: **Carpentras**					
6 hours	3.84 (0.12)	3.81 (0.03)	1.79 (0.05)	9.56 (13.1)	1.53 (0.42)
8 hours	4.8 (0.34)	4.17 (≈ 0)	1.98 (0.02)	2.11 (1.22)	1.16 (0.21)
12 hours	5.38 (0.15)	4.59 (0.08)	2.16 (0.04)	20.18 (14.4)	1.71 (1.32)
18 hours	5.54 (0.18)	4.83 (0.01)	2.3 (≈ 0)	23.84 (26.87)	13.4 (12.87)
24 hours	5.52 (0.04)	4.87 (0.06)	2.34 (≈ 0)	15.88 (13.21)	0.25 (0.01)
External condition: **Trappes**					
6 hours	5.29 (0.09)	4.94 (0.09)	2.16 (0.02)	0.21 (0.01)	0.38 (0.03)
8 hours	5.34 (0.12)	4.68 (≈ 0)	2.17 (0.01)	0.18 (0.01)	0.34 (0.02)
12 hours	5.35 (0.05)	4.64 (≈ 0)	2.21 (≈ 0)	0.14 (≈ 0)	0.26 (0.01)
18 hours	5.34 (0.07)	4.67 (≈ 0)	2.25 (≈ 0)	0.14 (0.01)	0.2 (0.01)
24 hours	5.35 (0.06)	4.47 (0.05)	2.13 (≈ 0)	0.14 (≈ 0)	0.23 (0.01)

Table 3.6: Theoretical and estimated thermal resistances (in m^2.K.W^{-1}) with corresponding uncertainties obtained with the 1D EWC model for the five studied walls under two variable conditions (colors for the relative resistance error between $R_{estimated}$ and R_{ref}: out of 20%, 10-20%, 5-10%, <5%).

10%. However, the SW and EWI's cases return a bad estimation (unstable estimation results, high relative error).

The strong solar radiation at be beginning of this conditions can explain this observation. This heat flux can be considered as a second thermal excitation from the exterior which make the heat flux in this investigated wall more complicated than the constant conditions. This flux will be composed by the thermal excitation limited on a specific zone of the internal surface (with 3D effects) and a solar radiation on the whole external surface (purely 1D) So, with the IWI walls, their estimated results start to converge when the thermal excitation becomes stronger then the solar radiation (after 6-7 hours of measurement). When the solar radiation raises again from the 15^{th}, the estimation model has already a good parameters of these wall and it can adapt to this variation so that the estimation results remain unchanged. However, for a non-isolated wall as the SW wall, the lateral effect combined with the mix of heat fluxed becomes more complicated then the 1D model of the estimation process is no longer valid. With the EWI wall, this heat flux combination helps to return a larger estimated thermal resistance but it is still far from the expected one. Moreover, the raise of the solar radiation from the 15^{th} hour of measurement affects directly to the estimation results of this wall (a strong variation of the estimated thermal resistance observed during this moment)

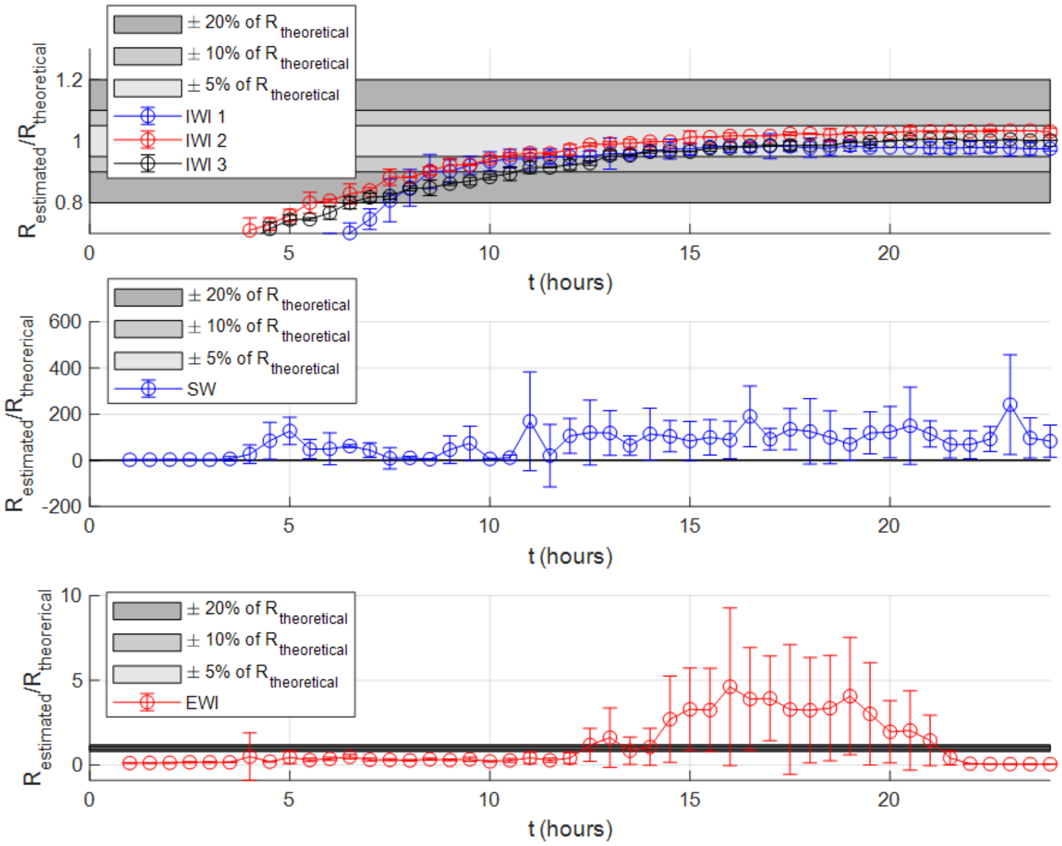

Figure 3.28: Ratio between the theoretical and estimated thermal resistances for the five considered walls under variable condition of Carpentras according to the heating duration by using the EWC model.

The second variable condition provides better results than the previous one (Cf. Figure 3.29). IWI results look similar than the cases under constant conditions. A faster convergence is observed compared to the use of the conditions of Carpentras. For the SW wall, the result is also more stable than in the previous case. The 6-hour data presents a good estimated thermal resistance but the estimation result goes down due to the external air temperature variations and to the increasing importance of lateral diffusion effects. Similarly to the test under constant conditions, the EWI wall returns a very small value for the thermal resistance (around 5% of the expected value).

For the results above, we can conclude that the IWI walls can be well characterized under any external condition (constant or variable) after 6-12 hours by using the EWC model. However, the SW wall requires an external condition as constant as possible in order to find out its thermal resistance and the solar radiation should be avoided. Besides, none of EWI cases can lead to a correct estimation of the thermal resistance. The only solution for this type of wall is to apply the excitation heat flux from exterior, which would be almost similar to the case of the IWI wall

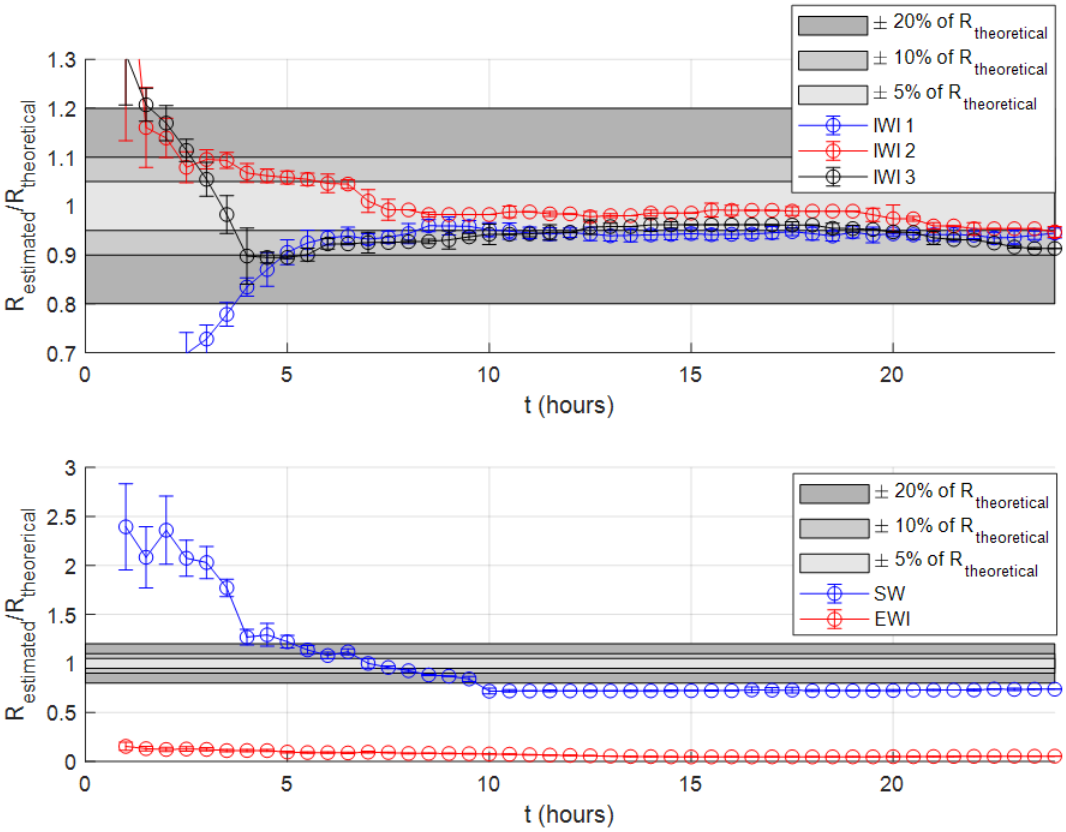

Figure 3.29: Ratio between the theoretical and estimated thermal resistances for the five considered walls under variable condition of Trappes according to the heating duration by using the EWC model.

heated from the interior.

3.7.5 Estimation results of the cases under constant conditions by using 1D AbF model

According to Figures 2.25 and 2.26 in Section 2.5.3, the difference between 1D AbF model and 3D data can not be ignored and becomes more important when the thermal excitation lasts longer. The results of the EWC model showed that only 12 hours of measurement are required to obtain a good estimated thermal resistance. So, this section concerning the AbF model will focus on the estimated results obtained with 12-hour data.

Tables 3.7 and Figure 3.30 present the estimated thermal resistances of the studied walls under constant external conditions by using the 1D AbF model. At first sight, we can observe that the estimation with the AbF model does not return as good results as with the previous model. The thermal resistances of all IWI walls are underestimated compared to EWC model results.

	IWI 1	IWI 2	IWI 3	SW	EWI
R_{ref}	5.66	4.72	2.34	0.19	4.14
Measurement time	$R_{estimated}$ ($u_{R_{estimated}}$)				
4 hours	4.63 (0.09)	4.01 (0.03)	2.03 (0.02)	0.19 ($\approx$ 0)	0.23 (0.05)
6 hours	4.41 (0.23)	4.12 ($\approx$ 0)	2.02 (0.02)	0.17 ($\approx$ 0)	0.15 (0.01)
8 hours	4.36 (0.21)	4.06 (0.01)	2.01 (0.01)	0.17 ($\approx$ 0)	0.16 (0.01)
12 hours	4.35 ($\approx$ 0)	4.04 ($\approx$ 0)	2.02 (0.03)	0.16 ($\approx$ 0)	0.17 (0.01)

Table 3.7: Theoretical and estimated thermal resistances (in $m^2.K.W^{-1}$) with corresponding uncertainties obtained with the 1D AbF model for the five studied walls under constant condition (colors for the relative error between $R_{estimated}$ and R_{ref}: out of 20%, 10-20%, 5-10%, <5%).

The case of highest theoretical thermal resistance (IWI 1 wall) presents the most important residuals between 1D and 3D models (Cf. Figure 2.25) and the highest difference between theoretical and estimated thermal resistance values. The strong dependence of the AbF model on the absorbed flux is the biggest problem in using this model. On the other hand, as observed in Figure 3.30, the estimation results for these three walls converge quite fast. The best estimation result is found between 5 and 6 hours of measurement for all IWI walls and it does not change much after 7 hours.

The results of the SW wall are quite good with only 0.02 $m^2.K.W^{-1}$ of difference from the theoretical value after 3 hours and varies a little bit around 0.17 $m^2.K.W^{-1}$ until the end of the measurement. As expected before, the EWI wall thermal resistance is still impossible to estimate.

3.7.6 Estimation results of the cases under variable conditions by using 1D AbF model

Concerning the cases under variable condition, similar observations as for EWC results can be made (see Table 3.8 and Figures 3.31 and 3.32). The use of Trappes conditions allows a better estimation of thermal resistances than the use of Carpentras conditions. The solar radiation contributes a very small amount to internal absorbed flux but the AbF model is very sensitive to this data. A change of 0.1 or 0.2 $W.m^{-2}$ can can significantly modify the computed model output. That is why we obtain a small and unstable estimated thermal resistance with all considered walls under the condition of Carpentras. Only the result of IWI 2 and 3 walls can be considered as good using this climate.

According to Figure 3.32, the estimated thermal resistances of the three IWI walls and

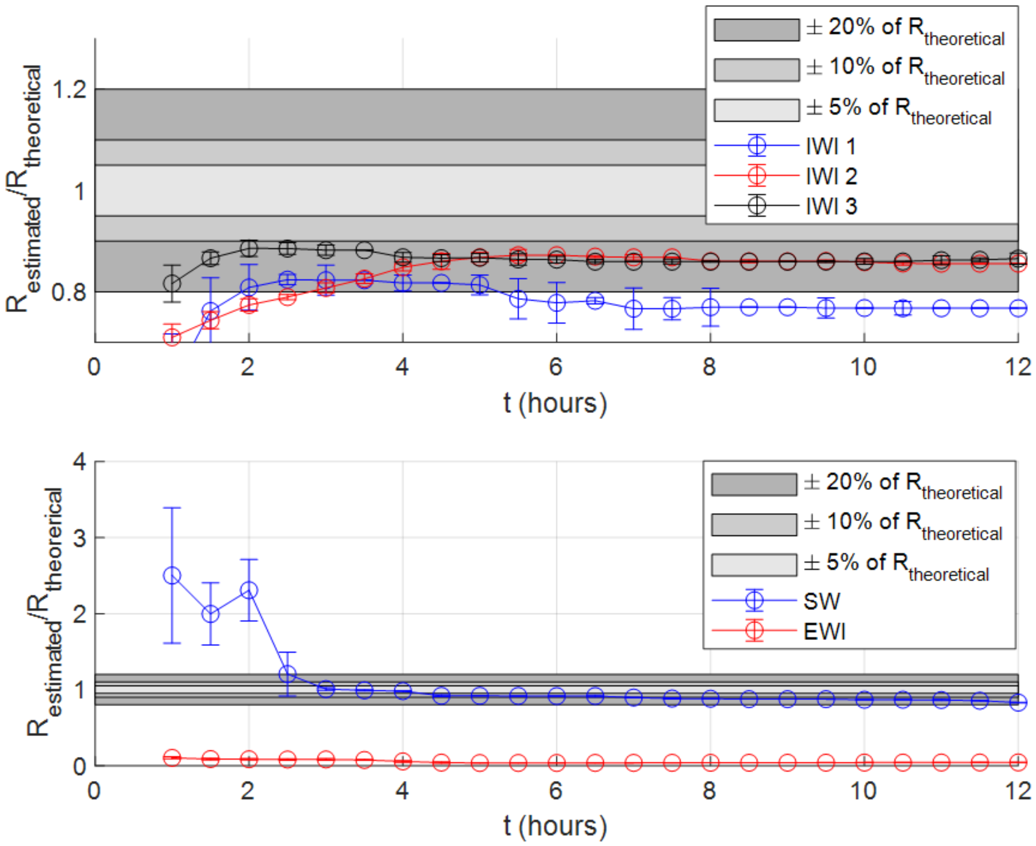

Figure 3.30: Ratio between the theoretical and estimated thermal resistances for the five considered walls under constant condition according to the heating duration by using the AbF model.

	IWI 1	IWI 2	IWI 3	SW	EWI
R_{ref}	5.66	4.72	2.34	0.19	4.14
Measurement time	$R_{estimated}$ ($u_{R_{estimated}}$)				
External condition: **Carpentras**					
4 hours	2.83 (≈ 0)	3.88 (0.03)	1.86 (0.01)	0.38 (0.05)	0.43 (0.02)
6 hours	3.36 (≈ 0)	3.89 (≈ 0)	1.71 (≈ 0)	3.87 (1.55)	0.46 (0.01)
8 hours	3.69 (≈ 0)	3.87 (0.02)	1.85 (0.02)	0.13 (0.01)	0.42 (0.01)
12 hours	4.16 (0.05)	3.86 (0.02)	2.12 (≈ 0)	0.14 (0.01)	0.41 (0.01)
External condition: **Trappes**					
4 hours	4.59 (≈ 0)	4.36 (0.01)	2.07 (0.06)	0.22 (0.01)	0.35 (0.01)
6 hours	4.57 (0.06)	4.17 (0.03)	1.98 (0.01)	0.19 (0.01)	0.15 (0.01)
8 hours	4.48 (≈ 0)	4.13 (0.01)	2 (0.02)	0.17 (0.01)	0.15 (0.001)
12 hours	4.43 (≈ 0)	4.08 (≈ 0)	2.05 (≈ 0)	0.18 (0.01)	0.17 (≈ 0)

Table 3.8: Theoretical and estimated thermal resistances (in m^2.K.W^{-1}) with corresponding uncertainties obtained with the 1D AbF model for the five studied walls under two variable conditions (colors for the relative error between $R_{estimated}$ and R_{ref}: out of 20%, 10-20%, 5-10%, <5%).

SW wall are acceptable when testing under Trappes condition. So, we can conclude that 6-hour data is enough to characterize the thermal resistance of these walls. Besides, the EWI wall is the only wall which can not be characterized in these cases.

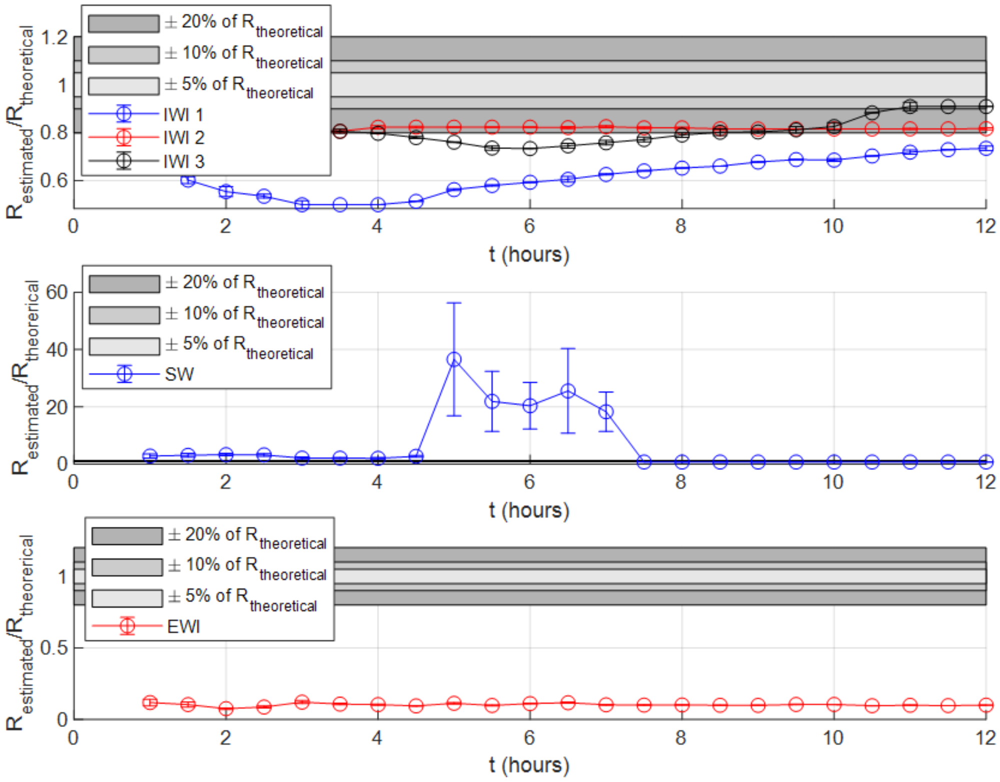

Figure 3.31: Ratio between the theoretical and estimated thermal resistances for the five considered walls under variable condition of Carpentras according to the heating duration by using the AbF model.

The strong point of the AbF model is that this model allows converging to a correct stable value faster than the EWC model. As mentioned in Section 3.7.1, the absorbed heat flux used as an input of the estimation model contains already some exclusive information of the wall (the absorbed heat flux contains already the thermal characteristics of the tested wall) so that it help our model searching faster a suitable result than the EWC model. Moreover, because of not using directly h_I and q_{exci}, this model is more robust and less dependent on measurement conditions than the EWC one.

3.8 Conclusions

This chapter presented the theory of inverse problems to estimate unknown parameters of a given physical system. The objective of the inverse problems is to find a set of parameters that minimizes a least-square criterion between measurement and model data.

Several minimization methods were presented such as Gradient Descent, Gauss-Newton,

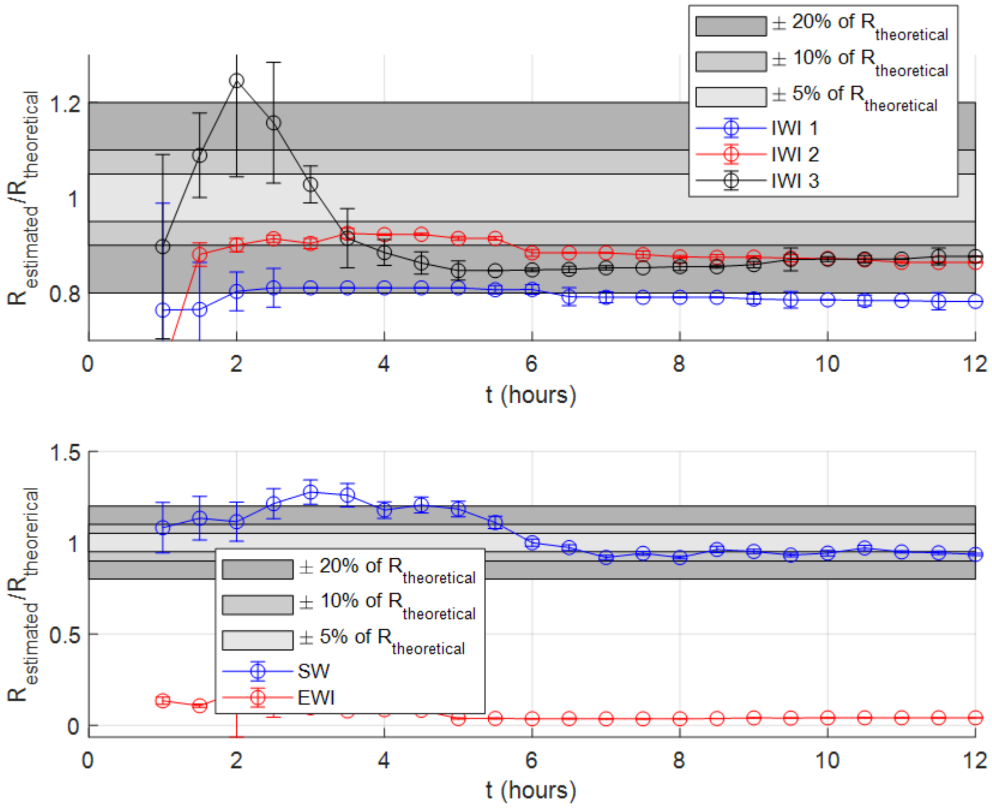

Figure 3.32: Ratio between the theoretical and estimated thermal resistances for the five considered walls under variable condition of Trappes according to the heating duration by using the AbF model.

Levenberg-Marquardt, Trust-region, and Bayesian methods. Each of them has advantages and disadvantages in terms of computation time and estimation accuracy. However, only the Bayesian method allows computing uncertainties of estimated parameters. For its better control of random choice of proposal parameters, the Robust Adaptive Metropolis method, one of the Bayesian methods, was chosen to be used in this study.

For estimating the thermal resistance of a building wall, two models were proposed as direct model of the estimation process: Excitation With Convection (EWC) and Absorbed Flux (AbF). Five different walls (3 IWI, 1 EWI, and 1 SW) were studied under three external conditions (1 constant and 2 variables). According to estimated results, the thermal resistance of IWI and SW walls could be estimated by the two proposed models under constant and variable conditions with weak solar radiation and EWC model led to better estimated values than AbF model.

The concrete layer of EWI wall is closer to thermal excitation source than the insulation layer. Thus, heat flux diffuses mainly laterally through this layer, so a very small value of thermal resistance was estimated in all cases of EWI wall. Another solution to estimate the EWI wall would be to apply the excitation heat flux from the exterior.

With the AbF model, the estimation results showed that 6 hours are required to get the best value of thermal resistance estimation in the estimatable cases. Moreover, the estimation became worse when analyzing data of longer duration because of the lateral effect which becomes more important if increasing the heating duration. However, when considering the parameter sensitivity, the AbF model seems more favorable for the real measurements than the EWC because it does not need the sensitive parameters, such as convective heat transfer coefficient.

In fact, our simulation used to generate the numerical data in this study is not complete. Several points which we did not take into account in the numerical simulation such as:

- The variation of the thermal conductivity as a function of the operating temperature;

- The relationship between the thermal conductivity and the the water content of the wall materials.

- The presence of the humidity, which can cause the condensation and evaporation inside the tested wall;

- The variation of the surrounding air temperature;

- The variation of the convective heat transfer coefficient in the interior and the exterior;

These factors influence directly to the heat flux absorbed by the wall surface. Therefore, the data used in this numerical study can not represent correctly what happens in real measurement conditions.

4 Measurement prototype development

4.1 Introduction of chapter

As mentioned in Chapter 1, the active method requires more measurements and a more complex measurement prototype than the passive one. Therefore, this chapter introduces the developed measurement prototypes based on the active method to estimate the wall thermal resistance during this study and the RESBATI project.

The first section of this chapter details the difficulties of using the active method to estimate the thermal resistance and existing prototypes' weaknesses. This section will help to determine important points for the development of the new prototype. The second section presents four measurement prototypes:

- The first uses a strong lamp to heat the tested wall and a big lens to create a heating zone of 60×60 cm^2 on the wall surface.

- The second prototype is presented in [34]. It contains a series of small halogen lamps fixed on the rear side of a wood box (called lamp box), which delivers the excitation heat flux to the tested wall on the front side.

-The third one uses the second prototype's lamp box but with an aluminum plate of 60×60 cm^2 fixed in front of this box to homogenize the imposed thermal excitation and improve the measurement quality.

- The last one uses the same idea as the third prototype but more compact. It replaces the lamp box by a heating resistance in order to simplify its design.

The detailed configuration of these prototypes (dimension, element, etc.) will be presented in the following sections.

4.2 Difficulties of existing active method prototypes

The first thing is how to choose a good thermal excitation source. As presented in Section 1.3.2, there are three options: using a lamp, using a heater (or ventilator), and using a contact heating element (for example, heating resistance). Each of them has their pros and cons.

The excitation by a lamp is the most common way found in research on the active method because it is possible to localize the heating zone. Moreover, it can be considered as a contactless way so that it is possible to heat a non-flat surface or in a high position. However, the lamp projection shape is a cone (Cf. Figure 4.1). Therefore, the light intensity received at the same height as the lamp drops significantly when moving away from the testing lamp axis.

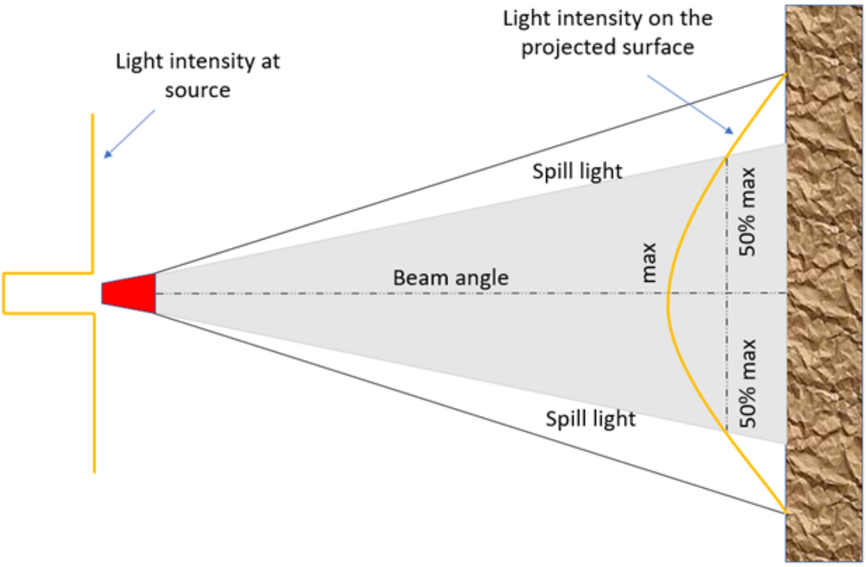

Figure 4.1: Light beam form of a lamp.

In [82], a series of light intensity measurement when increasing the distance between the lamp and the receiver is carried out and, as presented in Figure 4.2, a ratio of 3 is found when the receiver is installed at 10 cm and 20 cm away from the lamps.

Besides, as shown in Figure 4.1, the distribution of light intensity on the received surface is not homogeneous (it looks like a Gaussian form) so that the 2D/3D lateral diffusion should be taken into account in the estimation. Then, the 1D direct model is no longer valid.

The second type of excitation source is the heater. It is the simplest source because it does not require any adjustment as the lamps. On the other hand, this type allows global heating for the whole testing room, not for a specific surface. The global heating may be good for the thermal estimation using the 1D model because all surfaces are heated, and the lateral effect is weak, but it is available only when testing in a closed room. Moreover, global heating will create a very complicated thermal excitation on the wall surface. In this case, the heating process is that the heater heats the air in the testing room. The wall surface is heated by the convection with air so that the heat flux absorbed by the wall surface depends strongly on the convective/radiative

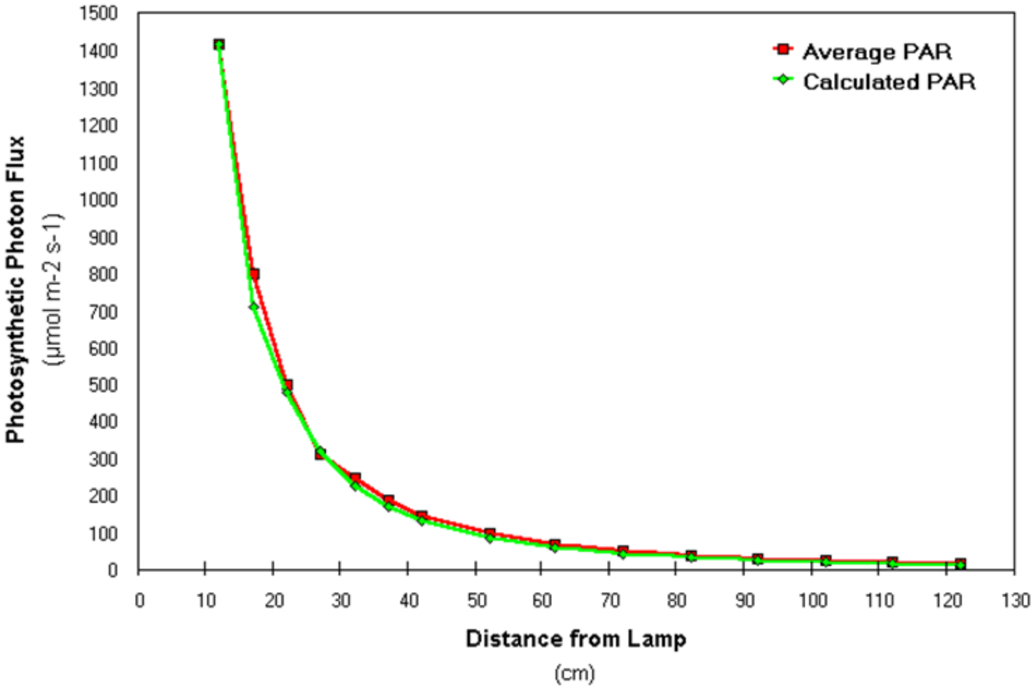

Figure 4.2: Distance from 150W Metal Halide light source versus light intensity (measured and calculated, PAR: Photosynthetically Active Radiation) [82].

heat transfer coefficient. As discussed in Chapter 1, the heat transfer coefficient depends on many variables, and it is rarely identical on the whole surface. Therefore, the absorbed heat flux on the tested surface is hardly homogeneous.

The last heating option is using a contact heating element. This type is different from the previous ones because it must be in contact with the tested surface. Therefore, it is available only for a flat wall surface. However, it can ensure a properly imposed heat flux in a willing limited zone so that there is no problem with homogeneity in this case. On the other hand, in this case, the heat flux will be distributed in two different directions, toward the wall surface and the surrounding air (Cf. Figure 4.3). Normally, the amount toward the air is stronger than toward the wall surface because of the weak thermal resistance of air. Therefore, backward insulation is recommended to improve the amount of heat flux absorbed by the wall surface (see Figure 4.3). Besides, the heat flux towards the wall depends strongly on the ratio between thermal resistances of the wall and the backward insulating layer, and sometimes it is not very easy to control.

Table 4.1 summaries all advantages and disadvantage of three heating options. All three heating methods can not insure a perfect homogeneous heating form, even with a heating plate. As presented in Section 3.7.1, the excitation heat flux is the most sensitive parameter in the thermal resistance estimation. So, we need another heating way which can assure the

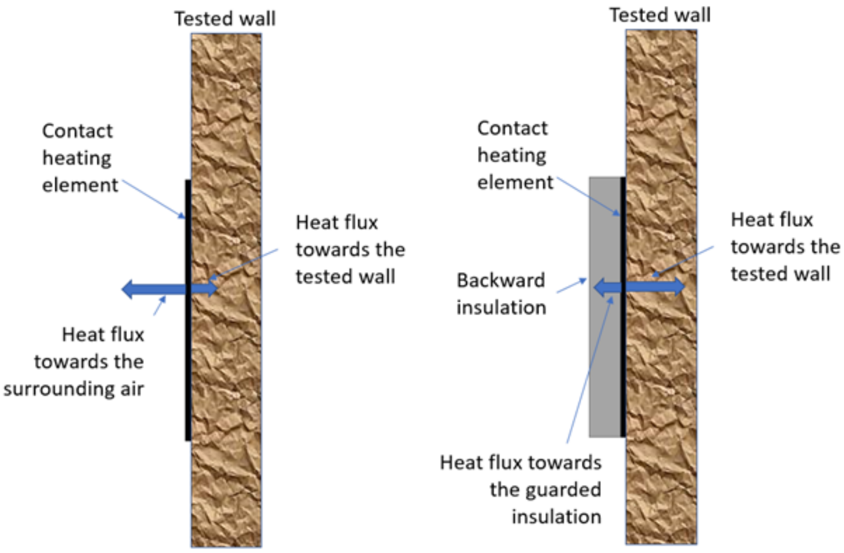

Figure 4.3: Heat flux distribution when using the contact heating element (left: without guarded insulation, right: with guarded insulation).

homogeneity of the imposed thermal excitation.

Heating type	Advantages	Disadvantages
By lamp	- Contactless heating way - Easy to localize the heating zone - Possible for all tested surface	- Non homogeneous imposed heat flux - Weak amount of heat flux received by tested surface
By heater	- Contactless heating way - Easy and fast installation - Possible for all tested surface - Easy to generate the global heating	- Strong dependence on the convective/ radiative heat transfer coefficient - Impossible to avoid the thermal bridges
By heating object	- Easiness to control heating uniformity	- Contact heating way - Possible only for flat surfaces - A backward insulation required to improve absorbed heat flux

Table 4.1: Advantages and disadvantages of three different heating ways.

The second issue lies in the difficulty of knowing the internal convective/radiative heat transfer coefficient h_I under experimental conditions. It can be evaluated by linear regression [15] or experimental approaches. However, none of these methods can ensure that the correct value is obtained, especially in an active measurement. The thermal excitation source heats the wall surface and the surrounding environment of the heating zone. It induces a variation of all environment parameters together (air velocity, humidity, air temperature, etc.). Therefore, the coefficient h_I behavior becomes more complicated than in the passive method. The convection is not the same on the whole wall surface. It may be similar at the same height but certainly not at different heights because of the up-and-down circulation of hot-cool air on the wall surface.

Therefore, the hypothesis of constant convection on the whole surface is not correct anymore. Moreover, the radiative/convective heat transfer coefficient, which is the second most sensitive parameter after the excitation heat flux in the thermal estimation (Cf. Section 3.7.1), is the most difficult factor to evaluate.

The last problem is the strong noise caused by the environment when using an active method. Figure 4.4 presents a heat flux measurement carried out by a heat flux meter fixed on the wall surface. The noise, in this case, is significant, with the signal-to-noise ratio around 5.4. Even using a noise filter, this noise is still remarkable.

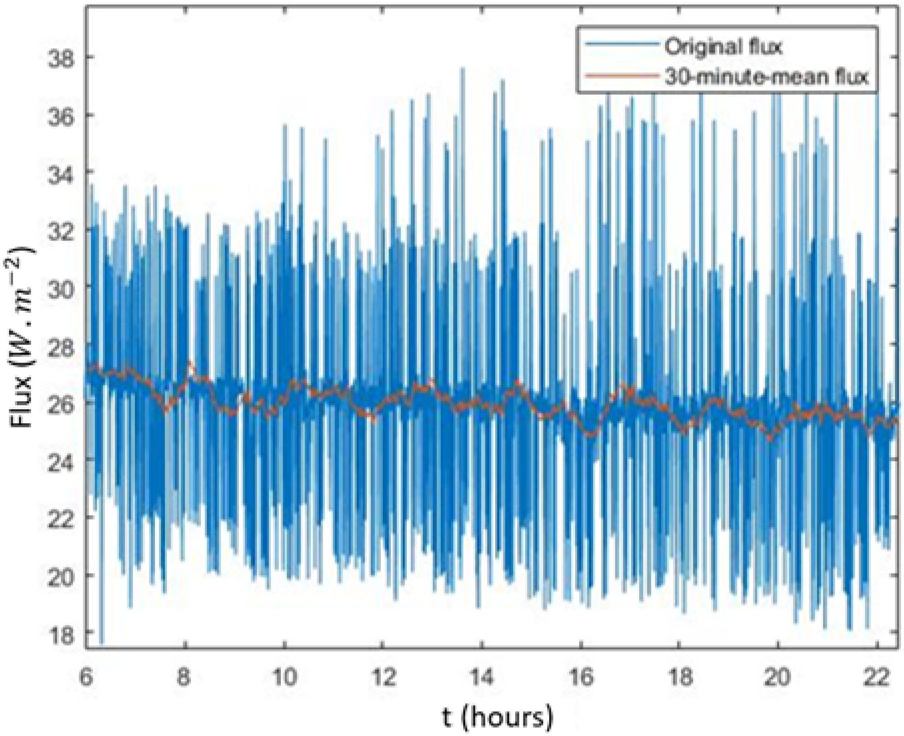

Figure 4.4: Measured heat flux on the wall surface by a heat flux meter fixed on the surface during an active measurement.

In this Ph.D. work and the RESBATI project, the objective is to develop a new measurement approach/prototype that can improve all three problems. The next section will present several proposals for this prototype.

4.3 Proposed measurement prototypes

4.3.1 Prototype 1: excitation with strong lamp

The prototype was proposed at the beginning of the RESBATI project. The IFSTTAR partner developed this prototype. It contains a strong halogen lamp and a big Fresnel lens, which is used to improve the incident light beam. The halogen lamp is installed close to the lens's focal point to create a parallel light beam toward the wall surface. If the lens is completely perfect (it means that the thickness of its edges is zero), the light source should stay at its focal point for obtaining a parallel beam. However, there is no perfect lens in reality, so that the optimal position for the light source may not be the lens's focal point but close to it.

Moreover, an IR camera is used to capture the surface temperature, and an aluminum foil is fixed in its visual field to correct the thermal image (as described in [83]). A reflective covering is installed to avoid the light dispersion between the Fresnel lens and the tested surface. Also, the internal coating color is usually white so that it reflects almost wavelengths of incident light and absorb less heat flux than the black coating. Therefore, instead of painting in black the tested surface, a black paper was used to cover the heating zone to improve the wall surface's heat absorption.

The schematic and real views of this prototype are shown in Figures 4.5 and 4.6. This configuration is considered as a contactless prototype.

With this prototype, two parameters must be known: q_{exci} (by calibration or using energy conversion efficiency between electrical power and thermal power) and h_I (by RT2012 or by measurement). As mentioned before, the computation of these parameters may not be totally correct. Besides, when analyzing the IR camera's thermal image in this case, a strong diminution of the surface temperature in the lateral direction is observed. Figure 4.7 presents the surface temperature on two directions (horizontal and vertical) when using this prototype on an IWI wall (see Chapter 5 for more details). According to the numerical study, this drop of surface temperature is too high, and it illustrates the non-homogeneity of the imposed thermal excitation on the wall surface.

To illustrate the estimation capability in using this prototype, a measurement on the same IWI wall as presented before is launched under constant condition (20°C for the interior and

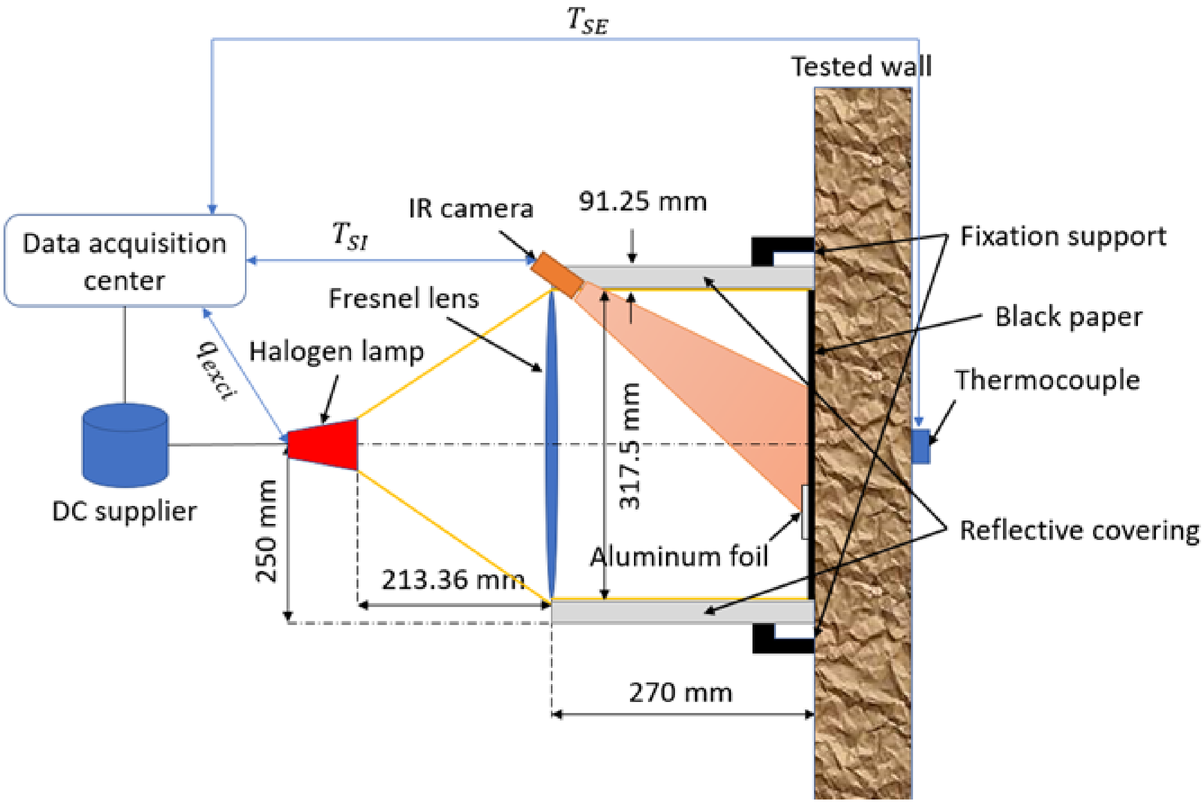

Figure 4.5: Schematic view of the first prototype.

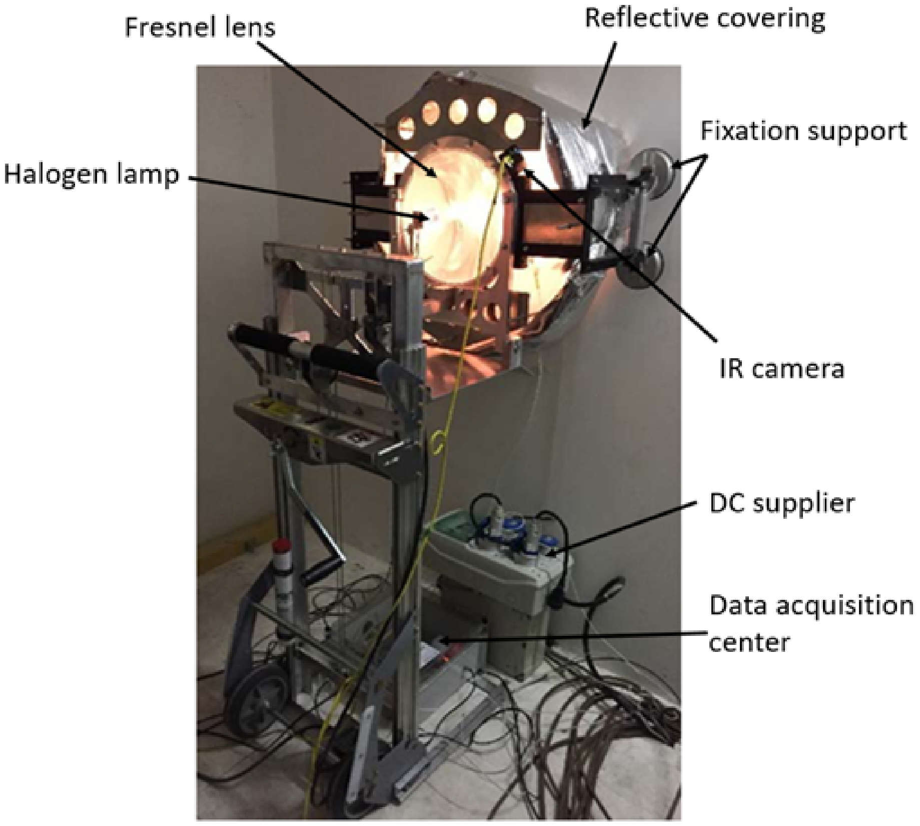

Figure 4.6: Real view of the first prototype.

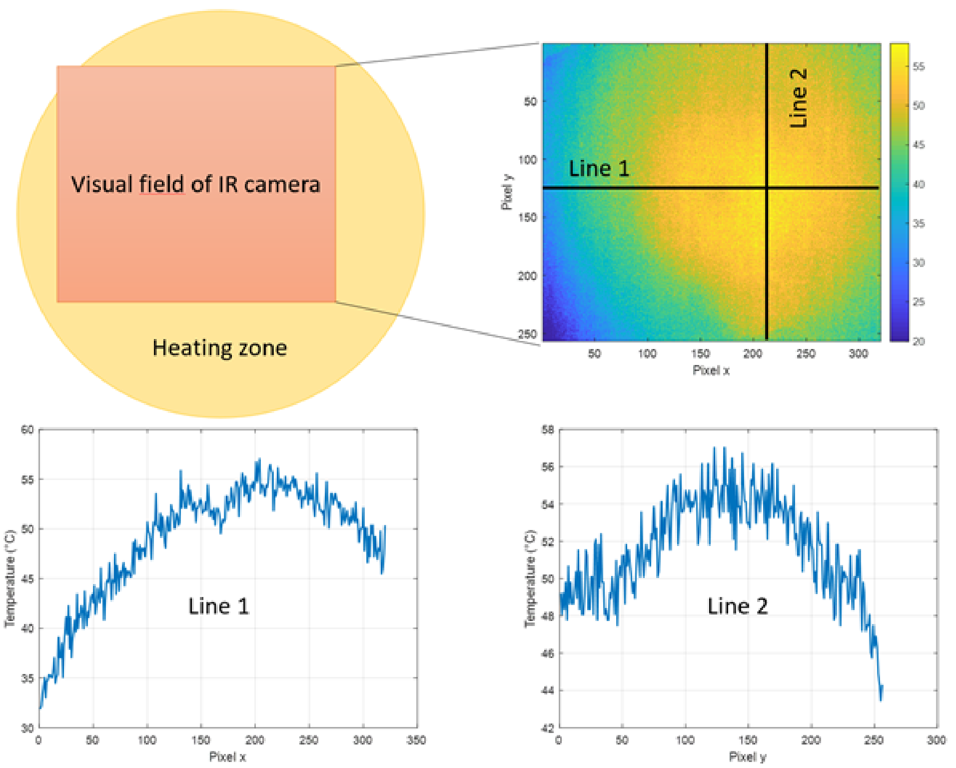

Figure 4.7: Thermal image of the tested surface with horizontal and vertical temperature profiles taken during the measurement with the first prototype.

0°C for the exterior). Here, there are some problems in determining the excitation heat flux q_{exci} so that a heat flux meter fixed at the center of the heating zone is used to evaluate this parameter. The objective is to find 3.8 $m^2.K.W^{-1}$ for the wall thermal resistance.

Figure 4.8 presents the measurement data and the estimated thermal resistance of this test. As observed in this figure, the surface temperature profile after 30 hours of heating has still the increasing tendency, not stable after several hours as seen in the numerical study with this type of wall. It means that the lateral effect in this test is quite strong. Moreover, with a temperature gradient of 26°C and the wall thermal resistance of 3.8 $m^2.K.W^{-1}$, the absorbed heat flux of 25 $W.m^{-2}$ seems too strong (the theoretical heat flux should be 6.8 $W.m^{-2}$).

After 5 hours of measurement, the estimated thermal resistance is around 4-4.2 $m^2.K.W^{-1}$, but it drops significantly to 2 $m^2.K.W^{-1}$ and stays around this value after that (see Figure 4.8). Therefore, the final estimation result in this test is 2 $m^2.K.W^{-1}$, which is far from the expected one. By observing the lateral effect in figure 4.7, this result is understandable.

This first measurement prototype has many disadvantages, such as :

- The Fresnel lens must be well-positioned in order to create the parallel light beam.

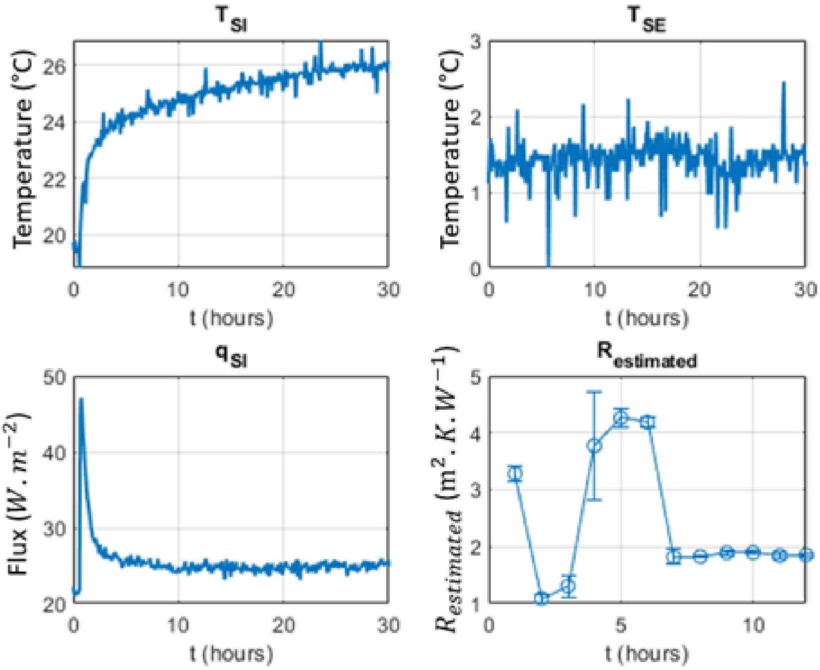

Figure 4.8: Measurement on the IWI wall under constant condition (internal/external air temperature = 20°C/0°C) and its estimation result when using the first prototype.

- This prototype can not ensure the homogeneous imposed heat flux as expected.

- Several calibrations should be carried out before launching measurement (for determining q_{exci} and h_I).

4.3.2 Prototype 2: excitation with a lamp box

The most serious problem of the first prototype is the adjustment of the Fresnel lens. It may take much time, and sometimes, with a small installation error, it can significantly change the projected light beam. Therefore, the second prototype proposed in this project tries to remove this element.

In fact, this prototype was developed during a previous project in the CERTES laboratory. This prototype is a wood box called the lamp box whose front face is open. Instead of using a strong halogen lamp, 24 small halogen spots are installed on the rear face (Cf. Figure 4.9). A reflective film covers its four other faces. This film reflects all light beams from the halogen spots and homogenizes the heat flux from the front face to the wall surface. An IR camera is equipped at the center of the rear face, and its visual field covers the whole surface of the front face. Figure 4.10 and 4.11 show the schematic and real views of this prototype.

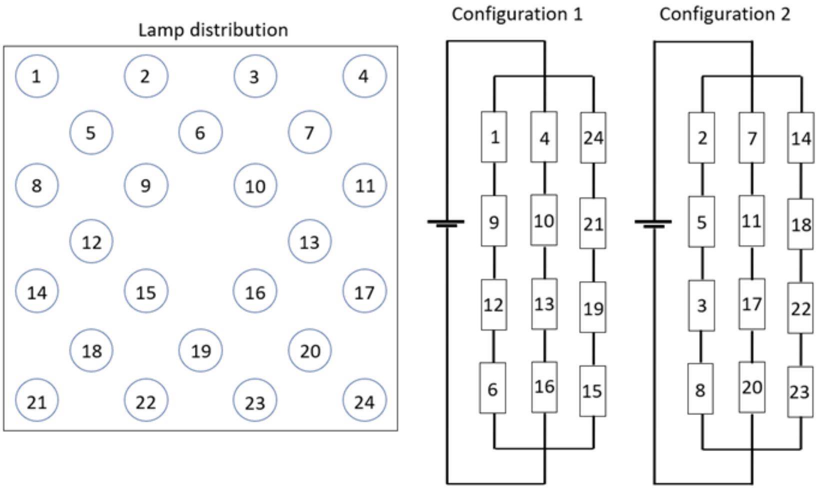

Figure 4.9: Lamp distribution on the rear face of the lamp box and the two circuits proposed in [34].

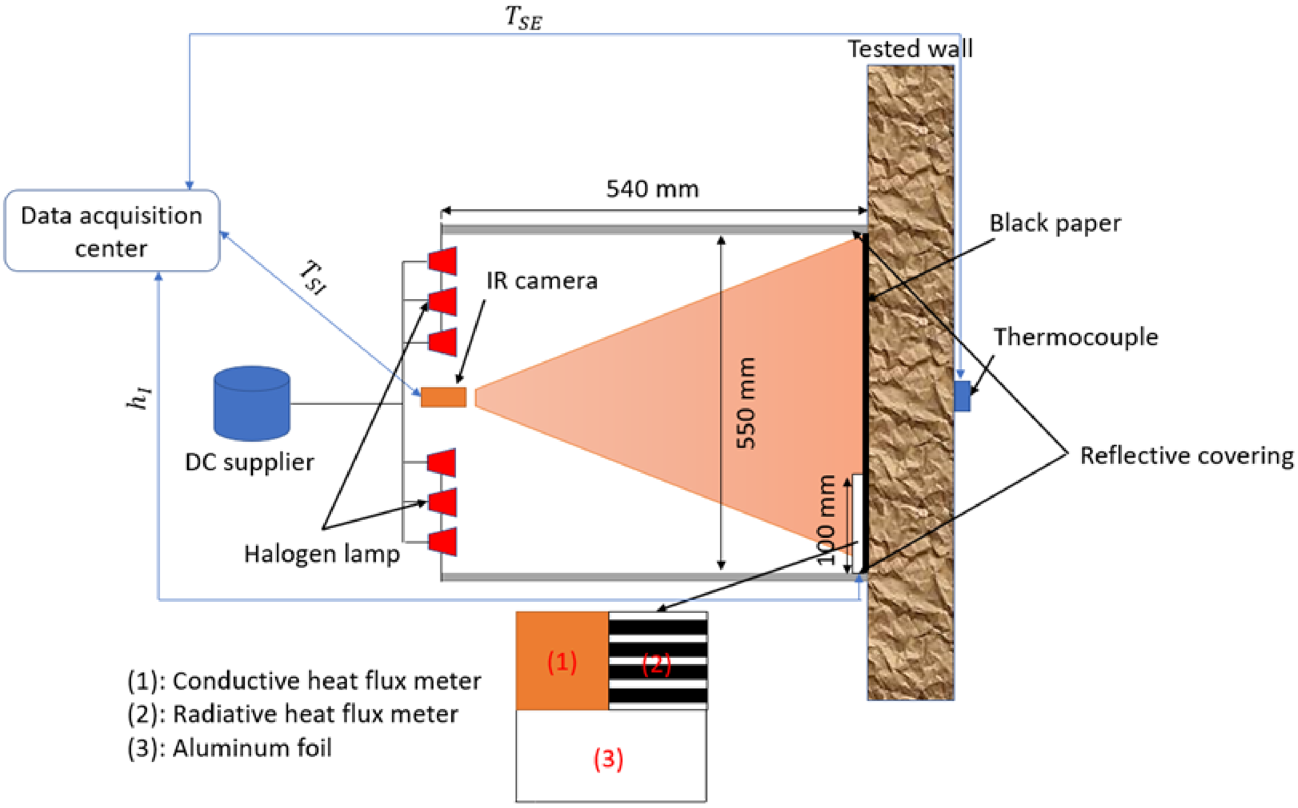

Figure 4.10: Schematic view of the second prototype.

In this configuration, the convective heat transfer coefficient will be measured by an additional element, as in Figure 4.10. It contains a conductive heat flux meter and a radiative heat flux meter. The temperatures of air T_a and the conductive heat flux meter surface T_S are

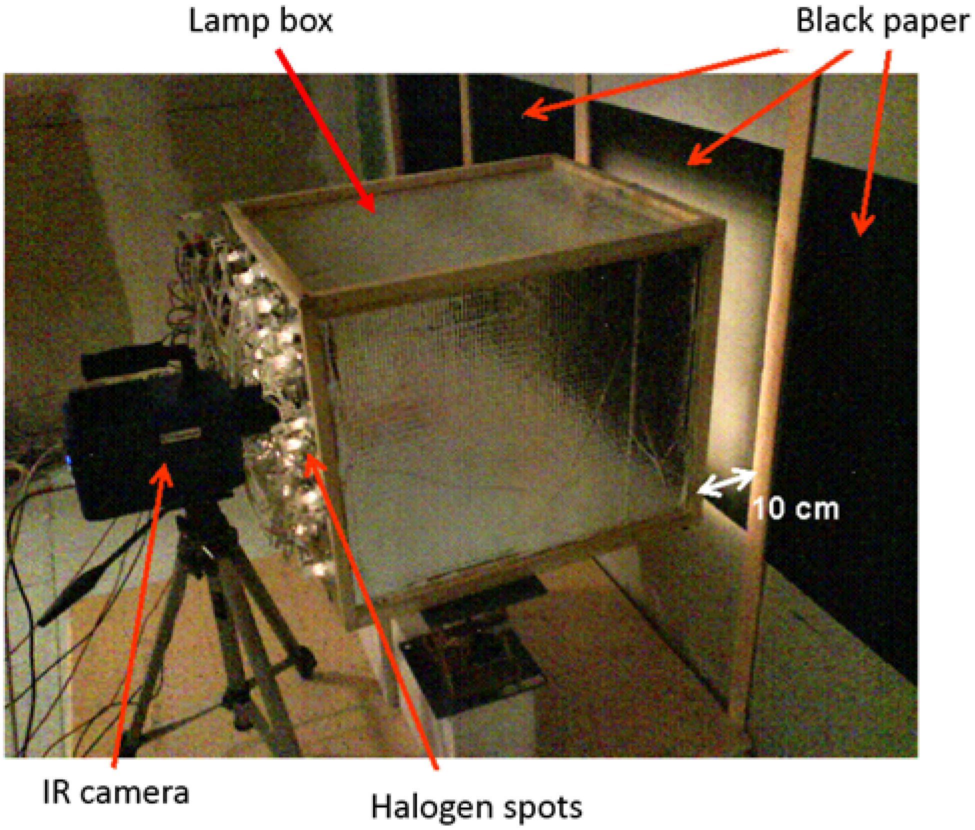

Figure 4.11: Real view of the second prototype [84].

also recorded. The expression of h_I can be written as:

$$h_I = \frac{q_{rad(cond.f)} - q_{cond(cond.f)}}{T_S - T_a} \tag{4.1}$$

where:

- $q_{rad(cond.f)}$: the amount of radiative flux absorbed by the conductive flux meter;

- $q_{cond(cond.f)}$: the amount of conductive flux measured by the conductive flux meter;

The incoming radiative flux (measured by the radiative heat flux meter) is very strong, but the real amount of this flux absorbed by the conductive flux meter is not much (around 3%). Figure 4.12 shows an example of measured h_i under two different heating powers. By using equation 4.1, the value of h_I can be evaluated directly.

In Figure 4.13, the profile of the calculated h_I, which contains much noise because of measured conductive heat flux. Therefore, a noise filter is applied to obtain a smoother profile of h_I than the original one. Under two different heating powers, the similar value of h_I (around 2 W.m^{-2}.K^{-1}) during heating phrase is determined.

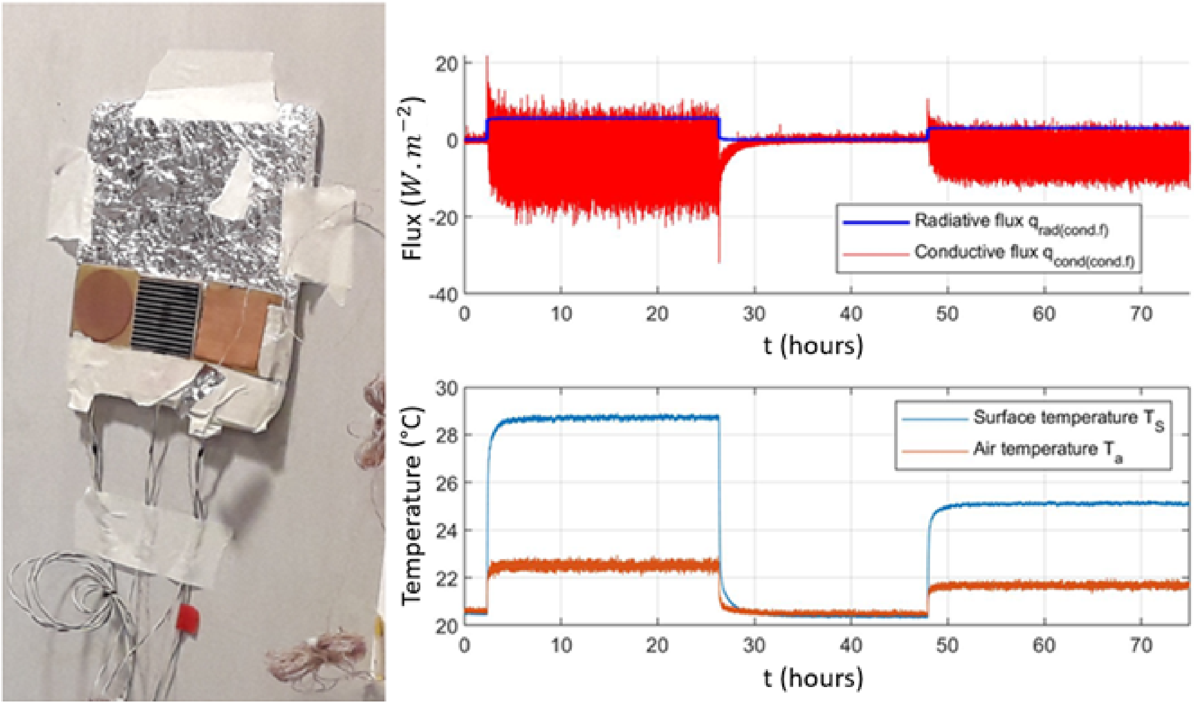

Figure 4.12: (left) h-measurement element and (right) measured data used in h-computation.

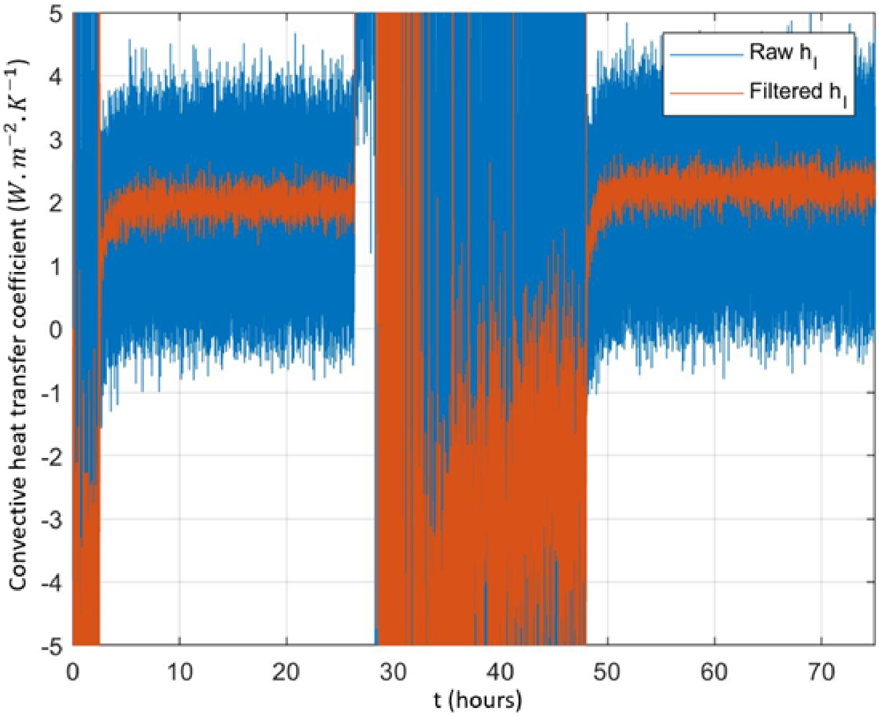

Figure 4.13: Calculated internal convective heat transfer coefficient with the measured data in Figure 4.12.

Before using this prototype, a calibration of the excitation heat flux is carried out. A radiative heat flux meter is fixed in the middle of the prototype's front face without touching the wall surface as Figure 4.14. In this figure, the maximal measured flux corresponds to q_{exci} when

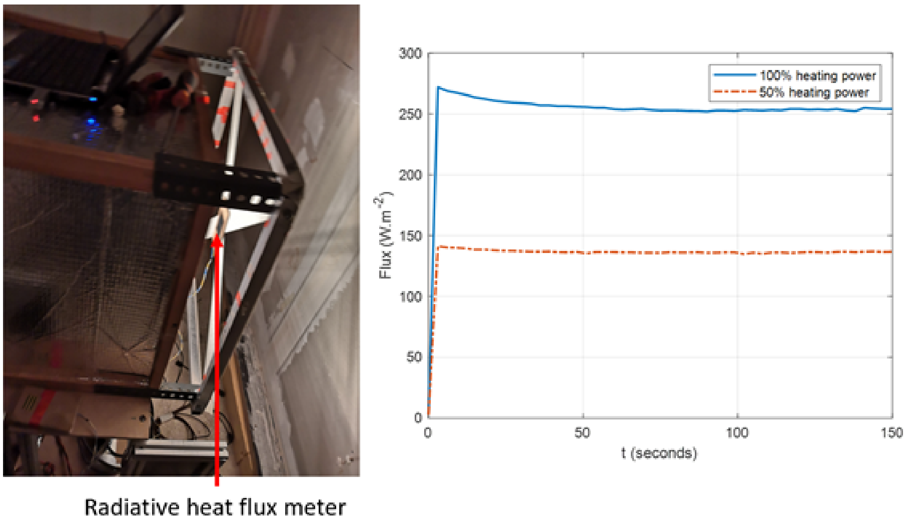

Figure 4.14: (left) Radiative heat flux meter position during thermal excitation calibration and (right) measured radiative flux of two tested thermal excitation power levels.

using two levels of heating power during this calibration.

This prototype does not touch the wall surface; then, it can be considered a contactless method. Several tests under constant condition (20°C and 0°C for the interior and exterior) were performed on the same IWI wall as for the first prototype.

First of all, the homogeneity of the surface temperature is examined. Figure 4.15 shows the thermal image and vertical and horizontal profiles of the surface temperature during the heating phase. In comparison with Figure 4.7, the second prototype can deliver a better surface temperature distribution than the previous one, but its lateral variation remains significant.

Secondly, a 24-hour measurement data is used in the estimation model to evaluate the wall thermal resistance. Figure 4.16 presents the measurement data and the estimation results of this test.

With this prototype, only a very small thermal resistance is found (around 0.1 m^2.K.W^{-1}). If considering the moment where T_{SI} and T_{aI} reach their stable value (47.5°C and 28.5°C respectively after 20 hours of heating), the absorbed heat flux computed by measured h_I at this moment is 234 W.m^{-2}, which is much more than the theoretical one (12.5 W.m^{-2}). Even if using the value of h_I as presented in RT2012 (7.7 W.m^{-2}.K^{-1}), the computed value of this value (125 W.m^{-2}) is still too much. Therefore, computing the absorbed heat flux by the convective heat transfer coefficient is not a good idea in this case. The only solution to determine this flux is using a conductive heat flux meter fixed on the investigated wall surface.

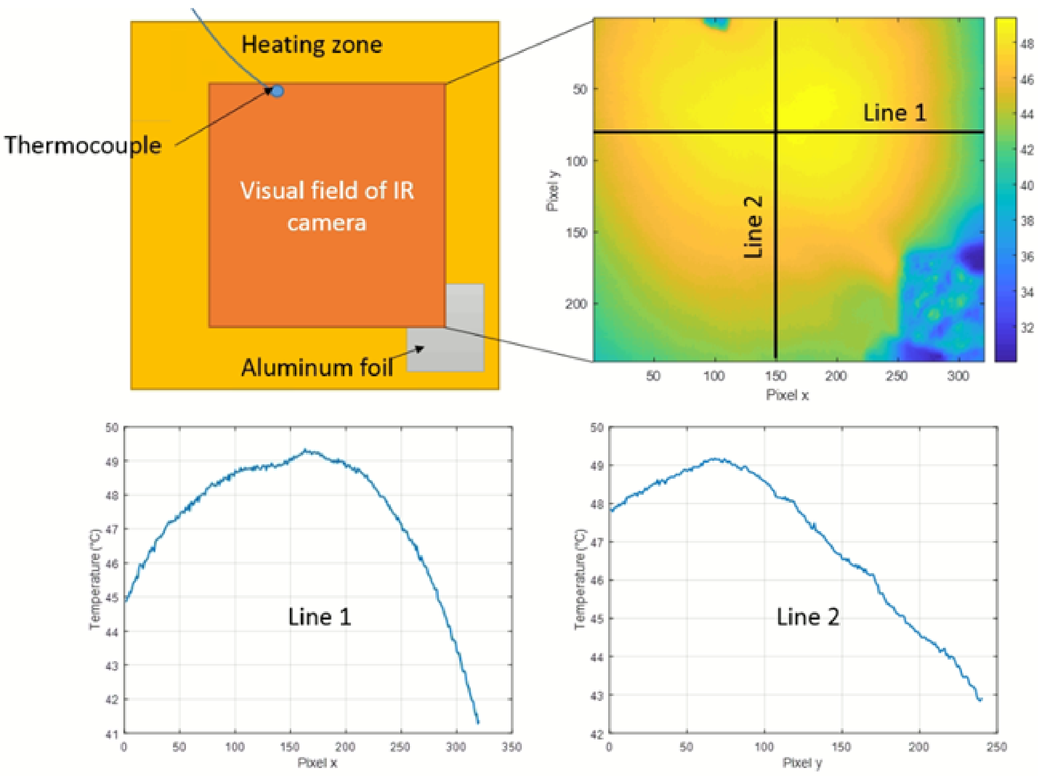

Figure 4.15: Thermal image of the tested surface with horizontal and vertical temperature profiles taken during the measurement with the second prototype.

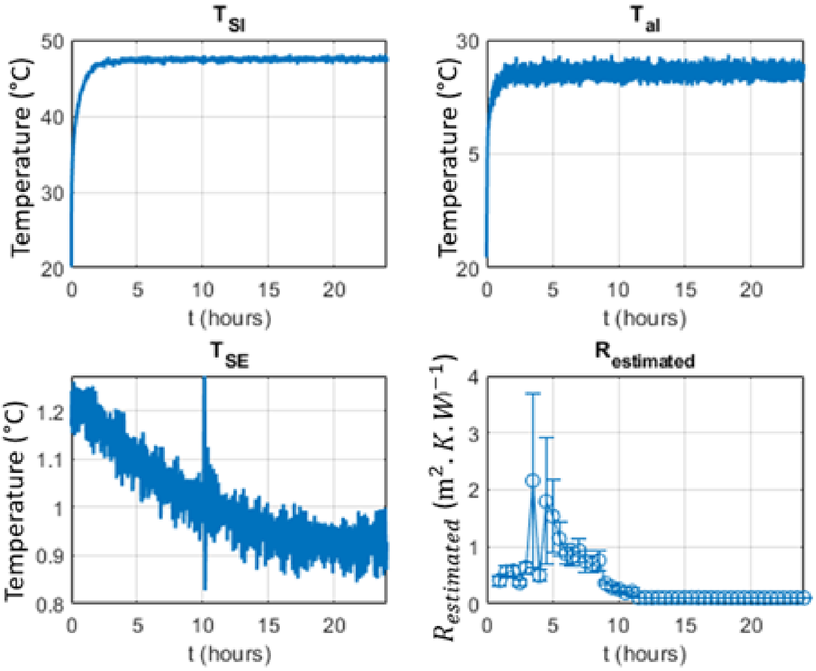

Figure 4.16: Measurement on the IWI wall under constant condition (internal/external air temperature = 20°C/0°C) and its estimation result when using the second prototype with the excitation heat flux of 272 W/m^2.

4.3.3 Prototype 3: excitation with a lamp box and an aluminum plate

After several tests with the first two prototypes, we showed the difficulty of controlling the homogeneity of imposed thermal excitation and evaluating the convective heat transfer coefficient (or the absorbed heat flux) when using a contactless method. Therefore, the third prototype is proposed with a different way of heating.

This prototype reuses the second one's lamp box, but an aluminum plate whose dimension is $600\times600\times5$ mm^3 is fixed in front of this box, with thermal sensors integrated. Using this plate allows homogenizing the tested wall's surface temperature because of the fast thermal diffusion effect on the metallic plate's surface.

The front face of this plate facing the lamp box is painted black to improve its radiative absorption. Besides, its rear face, which is in contact with the wall, contains several heat flux meters and thermocouples at the center and close to the plate edges (see Figure 4.17). With the proposed estimation based on the 1D model, only temperature and heat flux at the plate's center are needed. The other sensors are used to observe the lateral evolution of surface temperature and absorbed flux.

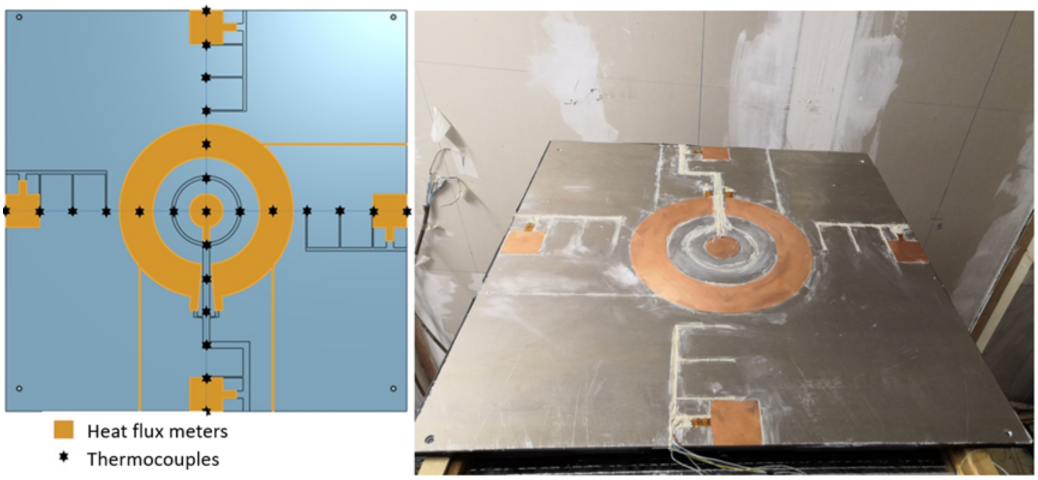

Figure 4.17: (left) Sensors distribution on the rear side of the aluminum plate and (right) its real view.

To make the tracks needed to place the sensors and their wires inside the plate, a numerical metal carving machine that allows a cutting precision of 1-2 mm was used. Different depth levels are designed to ensure that each sensor's upper surface is right on the plate surface to minimize the air gap between the plate and the wall. A metal-to-metal glue with a strong adhesion named SintoFer® is chosen to fix sensors onto the plate surface properly without any problem (removal at high temperature, disturbing thermal response because of thermal characteristics of glue, etc.).

To avoid thermal losses on the plate boundaries, a thick insulation guard is installed around the aluminum plate. This element helps to reduce the heat losses via convection on the edge of the plate. In this study, this guard's thickness and depth are 10 and 5 cm, respectively. The schematic and real views of this prototype are shown in Figures 4.18 and 4.19. This prototype is available only for the thermal resistance estimation using the 1D AbF model.

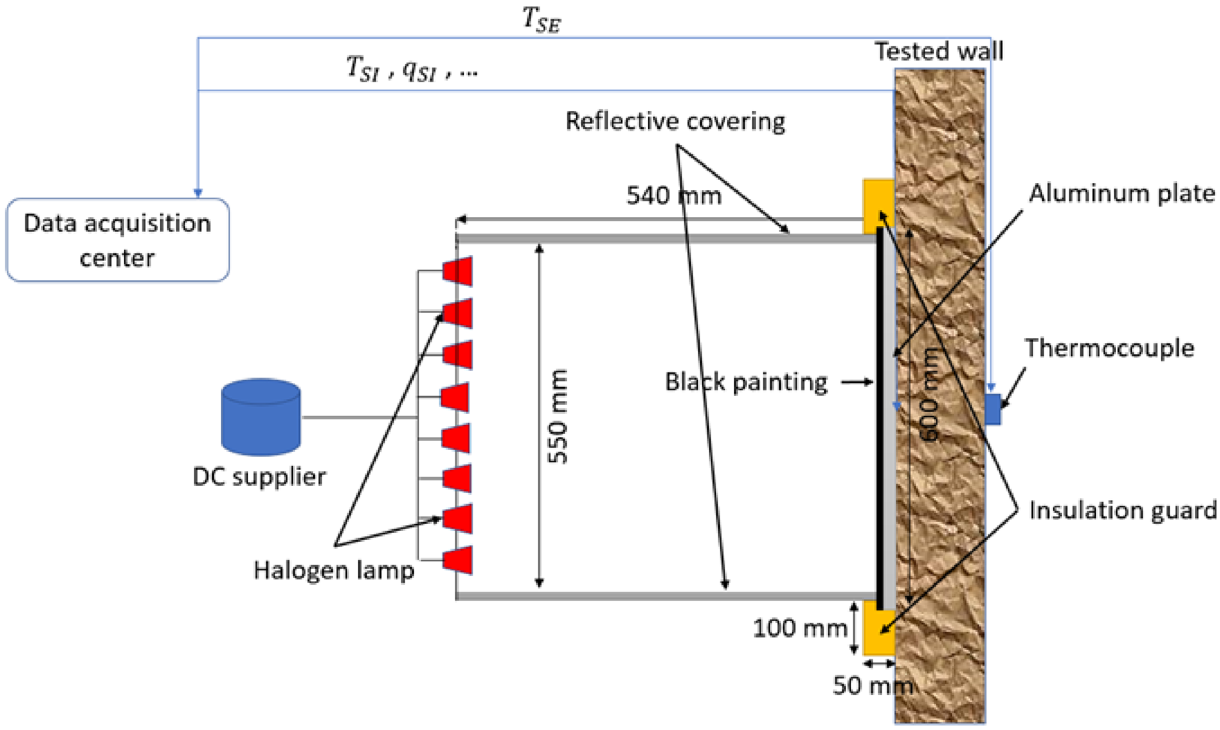

Figure 4.18: Schematic view of the third prototype.

As observed in Figure 4.15, a significant part of heat disperses laterally without the use of the aluminum plate, which leads to an important lateral temperature gradient in the heating zone. By using this prototype on the same IWI wall as before, a small lateral diminution of surface temperature is obtained (about 1-1.5°C in a radius of 20 cm from the center of the plate, see Figure 4.20). It can indicate that this wall's lateral effect is much weaker than testing with the first two prototypes. It is the biggest advantage of this prototype in comparing to the others.

Moreover, as observed in Figure 4.21, the internal surface temperature shows a quasi-constant evolution, which is different from the first prototype and which is quite similar to the numerical one as in Section 2.5. Besides, thanks to the aluminum plate's protection, the measurement data with this prototype are less noisy than with the first two ones and the thermal sensor noise evaluated in Appendix A3 (0.018°C for T_{SI} and 0.167 W.m^{-2} for q_{SI} in this case).

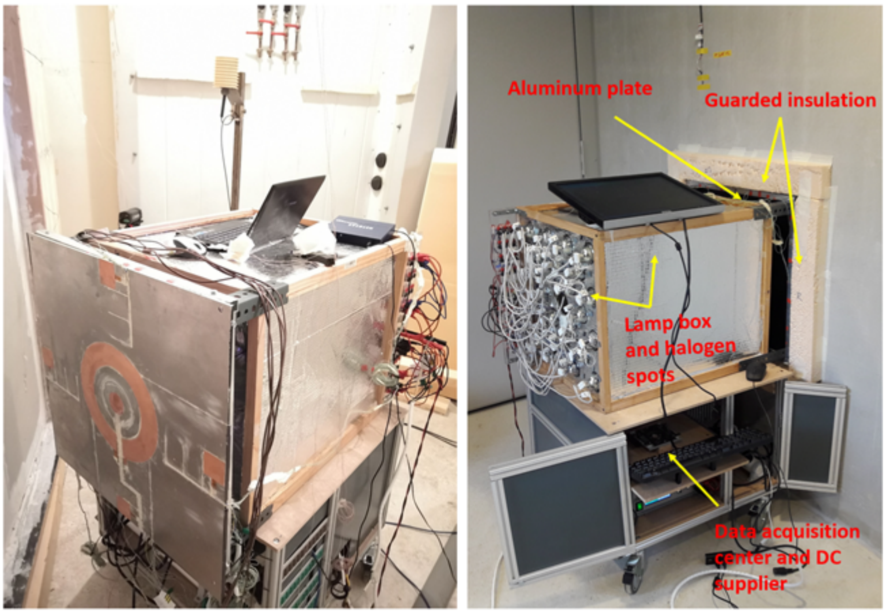

Figure 4.19: (left) Rear face of the aluminum plate with the lamp box and (right) real view of the third prototype.

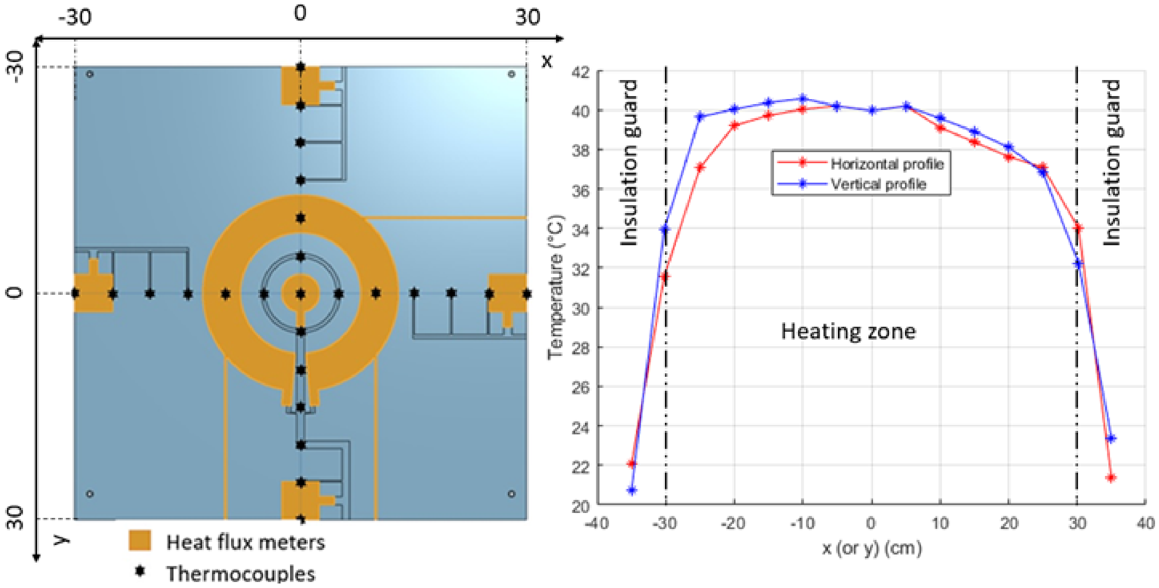

Figure 4.20: Horizontal and vertical profiles of wall surface temperature measured by thermocouples on the aluminum plate during measurement.

Therefore, no data filtering or data post-processing is required. After analyzing this data set, the estimated thermal resistance is around 3.56 $m^2.K.W^{-1}$ which is very close to the reference one (3.8 $m^2.K.W^{-1}$).

To validate this prototype, a measurement series is carried out on an insulated panel by varying two configuration parameters: the excitation heating power and the insulation guard's thickness. This 250×120 cm^2 wall includes two layers: a coating layer of BA13 (13 mm) and

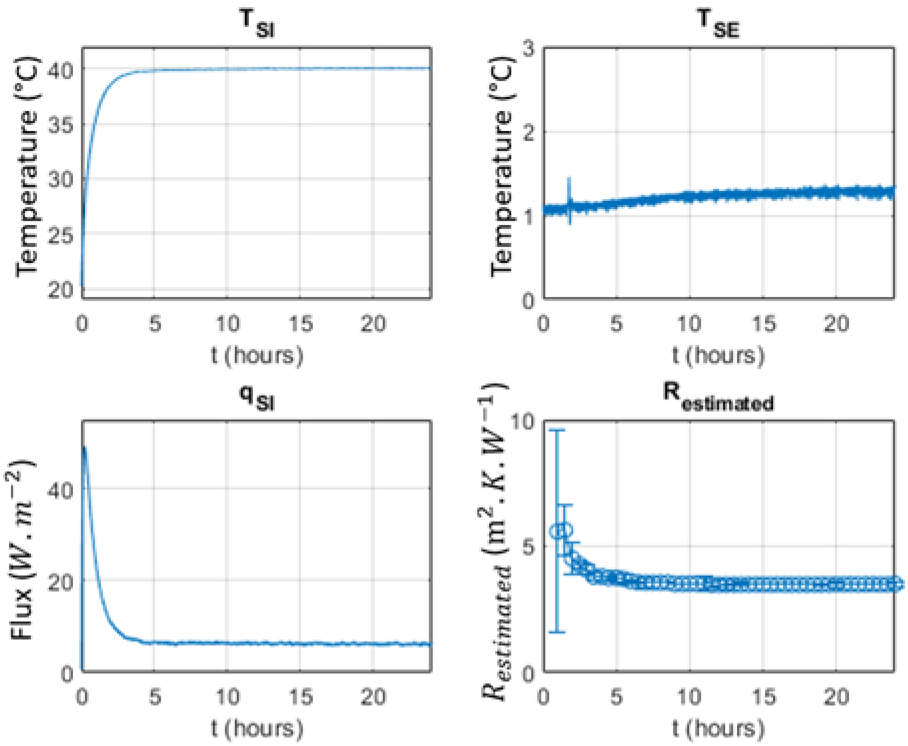

Figure 4.21: Measurement on the IWI wall under constant condition (internal/external air temperature = 20°C/0°C) and its estimation result when using the third prototype.

a thick layer of polystyrene or PSE (80 mm). Its thermal resistance is 2.55 $m^2.K.W^{-1}$. This insulated panel is fixed on the laboratory wall (Cf. Figure 4.22) whose thermal resistance is around 0.25-0.3 $m^2.K.W^{-1}$. There are two estimation objectives: the insulated panel's resistance only (2.55 $m^2.K.W^{-1}$) and of the entire wall (2.85 $m^2.K.W^{-1}$). Note that the studied wall is located inside a building and is therefore not submitted to external weather conditions. Moreover, there is no environmental control during the test.

To estimate the thermal resistance of the wall, the temperatures of the internal and external surfaces of the tested wall (one between the insulation layer and laboratory wall called T_{SE-1} and another on the external surface of the laboratory wall called T_{SE-2}) and the absorbed flux at the center of the tested wall are recording.

The first test is devoted to the study of heating power's influence in fixing the insulation guard thickness at 50 mm. The measurement data with two different heating powers (240 W and 120 W or 100% and 50% of heating power) are shown in Figure 4.23. The heating source's influence can be seen in the measurement data of T_{SE-1} but becomes invisible when observing T_{SE-2}. Moreover, during these tests, some people entered the testing room, but, as seen in Figure 4.23, this does not influence much measurement data.

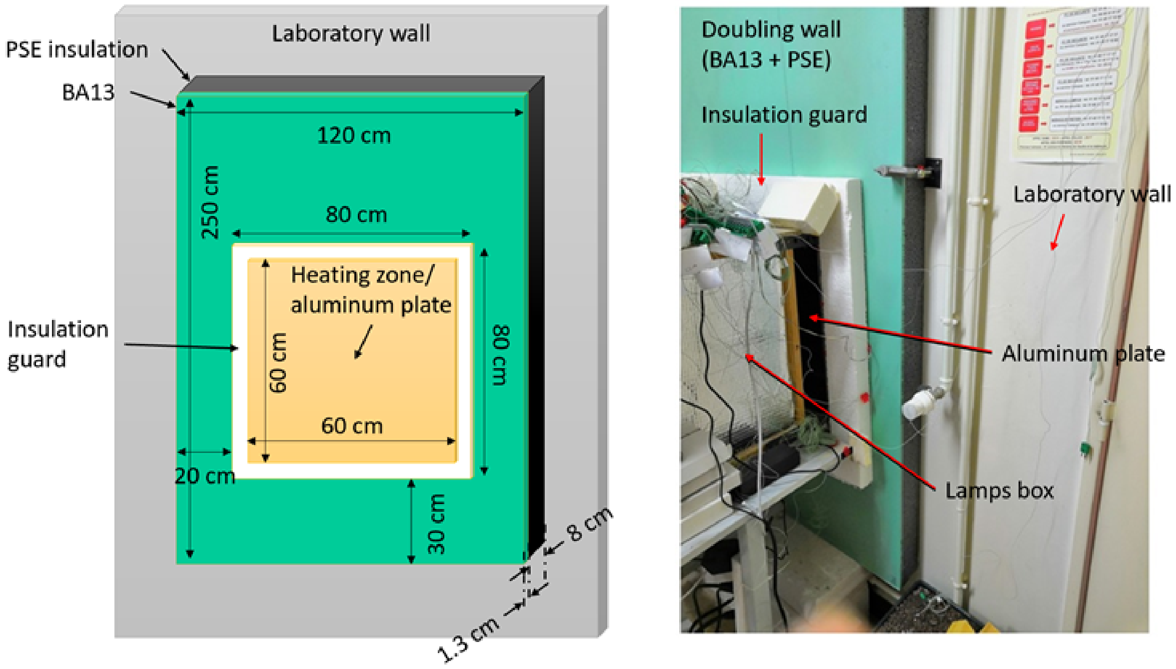

Figure 4.22: Validation test configuration with the third prototype in the laboratory.

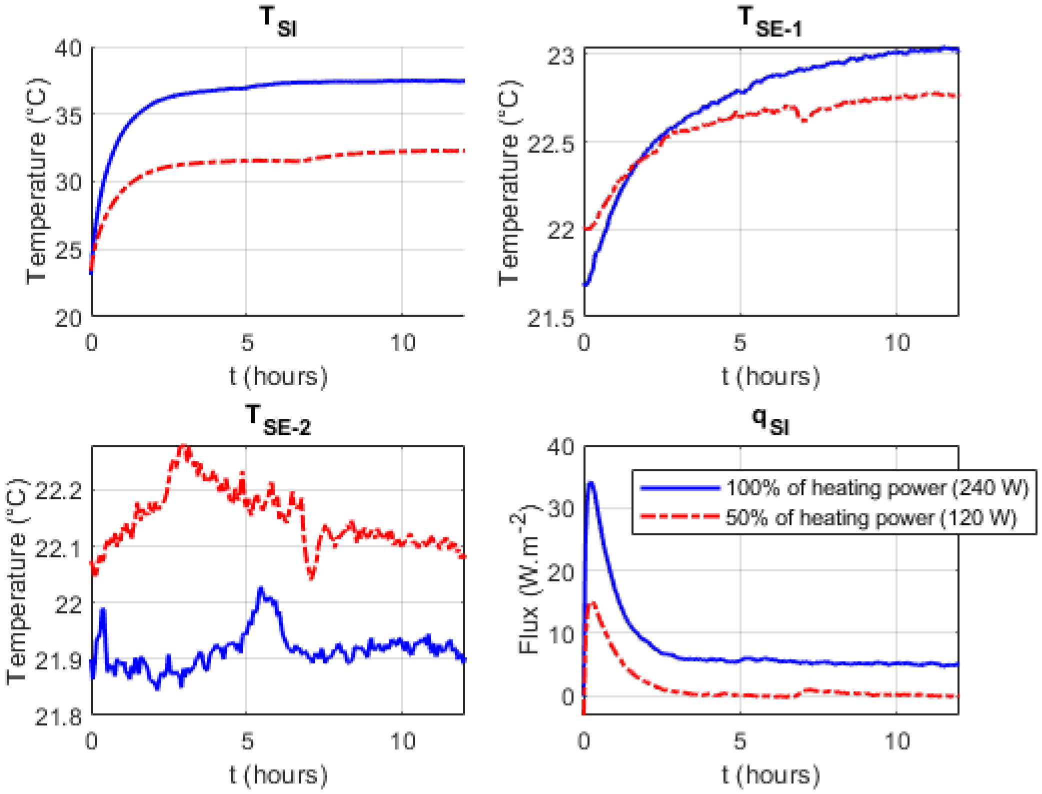

Figure 4.23: Measurement data during the prototype validation with two different heating level (240 W and 120 W or 100% and 50% of heating power) and the insulation guard thickness of 50 mm.

By using T_{SI} and T_{SE-1}, the estimated thermal resistance is very close to the expected one (as shown in Figure 4.24) with both levels (100$\%$ of power seems a little better than 50$\%$). If T_{SE-2} is used, there is not much difference in estimated thermal resistance of the tested wall by using 100$\%$ and 50$\%$ of power (see Figure 4.25). However, the higher heating power allows a faster convergence of the estimation results than the weaker ones, but both tests converge to a stable value after 6 hours of heating. As observed in Figure 4.23, the lower heating power shows a variation of 7°C only compared to 12°C with the higher one and, because of this weak evolution of input data, the estimation model must consider more data with this level in order to converge to a stable value than the other one.

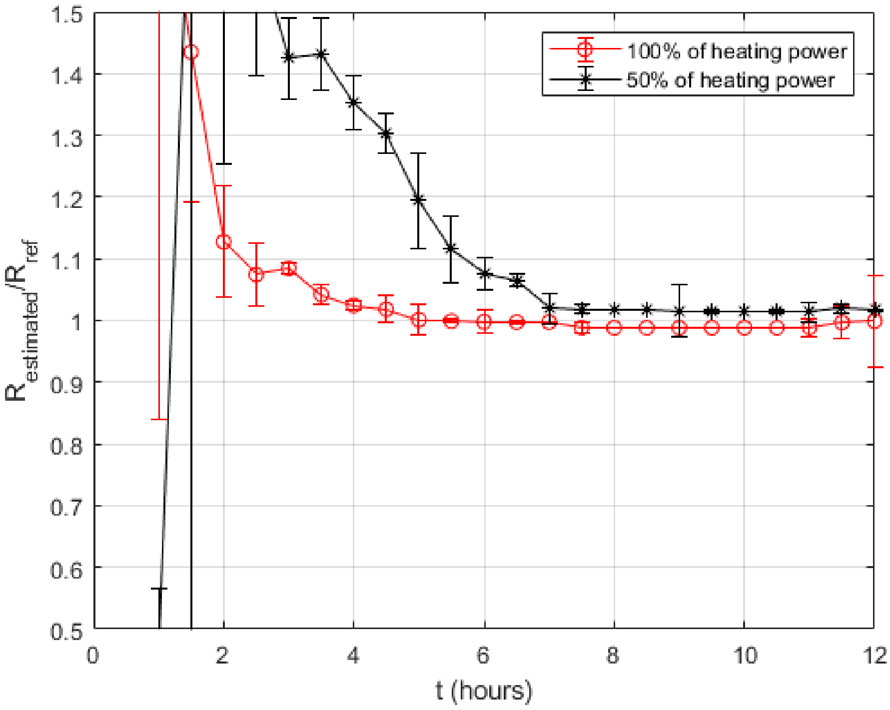

Figure 4.24: Ratio between theoretical and estimated thermal resistances for the insulated panel under two levels of heating power and an insulation guard thickness of 50 mm.

To highlight the important role of the insulation guard, another test using two different thicknesses (5 mm and 50 mm) of insulation with a fixed heating power of 240 W (or 100$\%$ of heating power) is carried out. This test evaluates the difference in estimated thermal resistance between a thick and thin insulation boundary. Figure 4.26 shows the three measurement data and the horizontal profile of the internal surface temperature after 10 hours of heating when using two different insulation guarded thickness. According to this image, the thinner insulation shows a weaker internal surface temperature evolution.

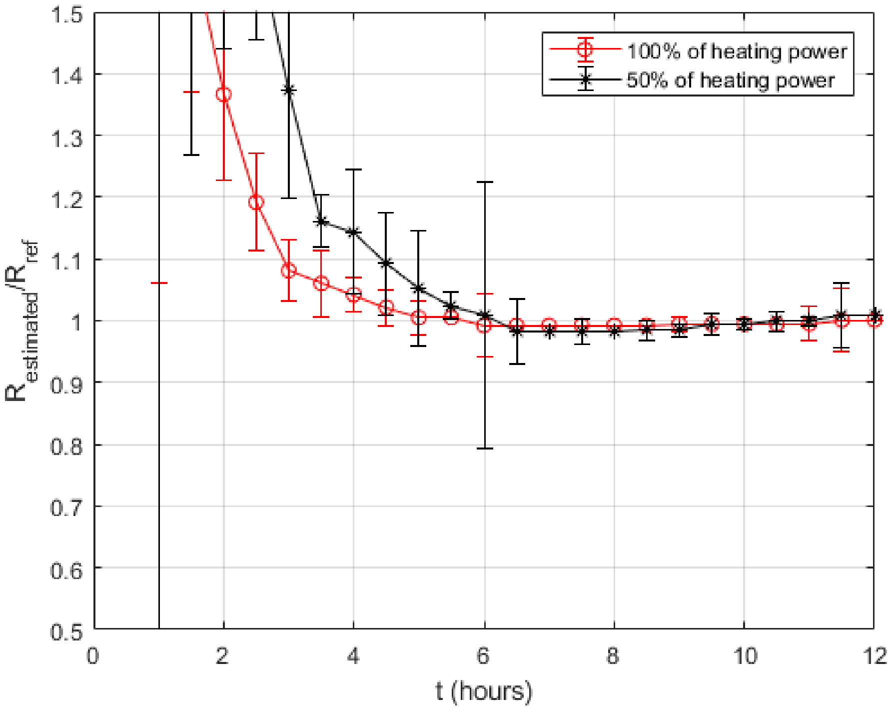

Figure 4.25: Ratio between theoretical and estimated thermal resistances for the entire wall under two levels of heating power and an insulation guard thickness of 50 mm.

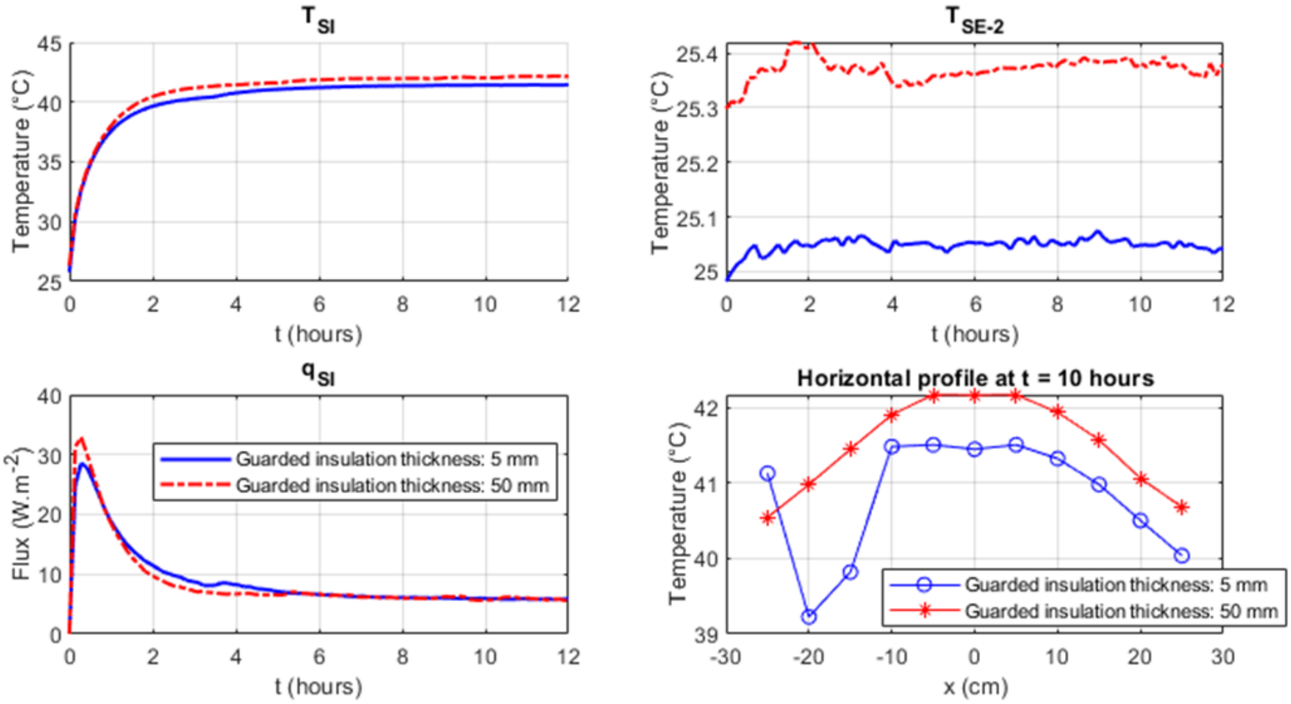

Figure 4.26: Measurement data during the prototype validation with two different insulation guard thickness (5 mm and 50 mm) and the heating power of 240 W.

As presented in Figure 4.27, the thickest insulation guard returns better results than the other one. Stronger heat losses and air leakage at the boundary can explain this observation. The thickest boundary can reduce more heat exchanges with the surrounding air on the aluminum plate edges and provide a better air tightness there than the thinnest one. As observed in Figure 4.26, a strong drop on the left-hand side of the surface temperature profile in the case with the thinnest guard is found and indicates a significant heat loss over there. Therefore, the use of the thickest insulation guard is highly recommended.

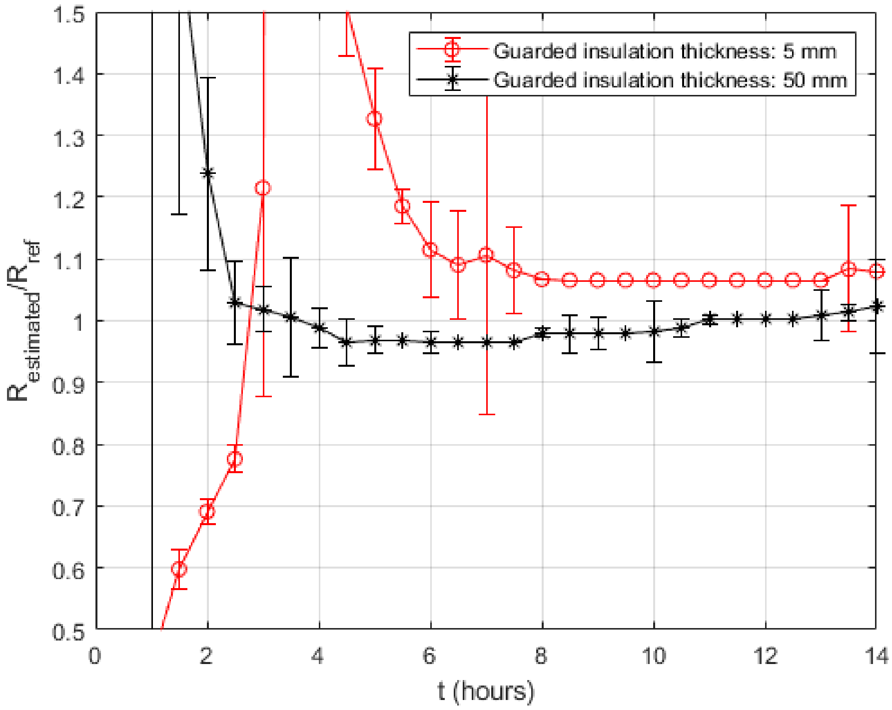

Figure 4.27: Ratio between theoretical and estimated thermal resistances for the insulated panel using two different insulation guard thicknesses (5 mm and 50 mm) and the heating power of 240 W.

The result of these tests validates the third measurement prototype's ability for estimating a wall thermal resistance, at least for an IWI wall. Moreover, this prototype can better homogenize the thermal excitation imposed on the wall surface and provide the measurement data less noisy than the existing ones. Besides, the installation time is around 5 minutes, much less than the other ones, because all thermal sensors are integrated on the aluminum plate.

4.3.4 Prototype 4: excitation with a heating resistance and an aluminum plate

Although the third prototype returns a good estimation capability, its elements seem too big and heavy (lamp box, data acquisition center ...). Therefore, based on the idea of the third one, a fourth measurement prototype was built for future use by professionals. Instead of using a lamp box, a heating resistance is fixed on the aluminum plate's front face. This prototype is for professionals to use on their wall, not for researchers, so that it contains only three thermal sensors: a thermocouple and a conductive heat flux meter on the center of the rear face, and a thermocouple for measuring the external surface temperature. Due to the reduction of sensor numbers, the data acquisition center can be miniaturized. With this configuration, holding support is required to maintain the aluminum plate in contact with the wall surface. Figure 4.28 and 4.29 show the schematic and real views of this prototype and its aluminum plate. This prototype was developed in collaboration with THEMACS Ingénierie company in the framework of the RESBATI project

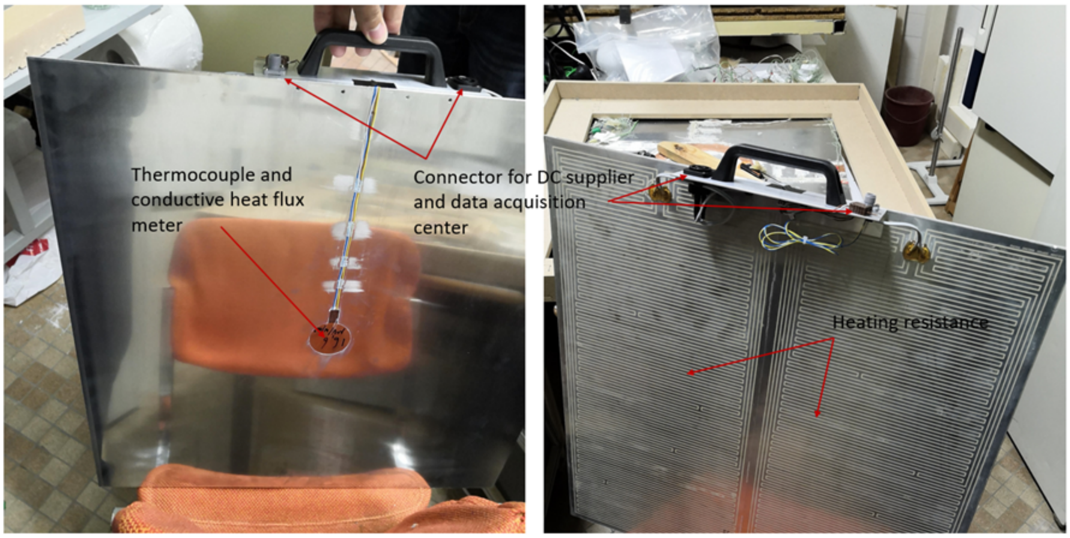

Figure 4.28: Real view of the front and rear faces of the fourth prototype.

To verify the estimation capability, the same measurement on the IWI wall as the first three ones were performed with this prototype. Figure 4.30 presents the measurement data obtained by this prototype and the estimated thermal resistance corresponding.

Similar measurement data (quasi-constant T_{SI} after several heating hours) are observed with this prototype as with the previous one. After 6 hours of heating, the estimation result is 3.76 m^2.K.W^{-1}, which is quite close to the willing value and even better than with the third

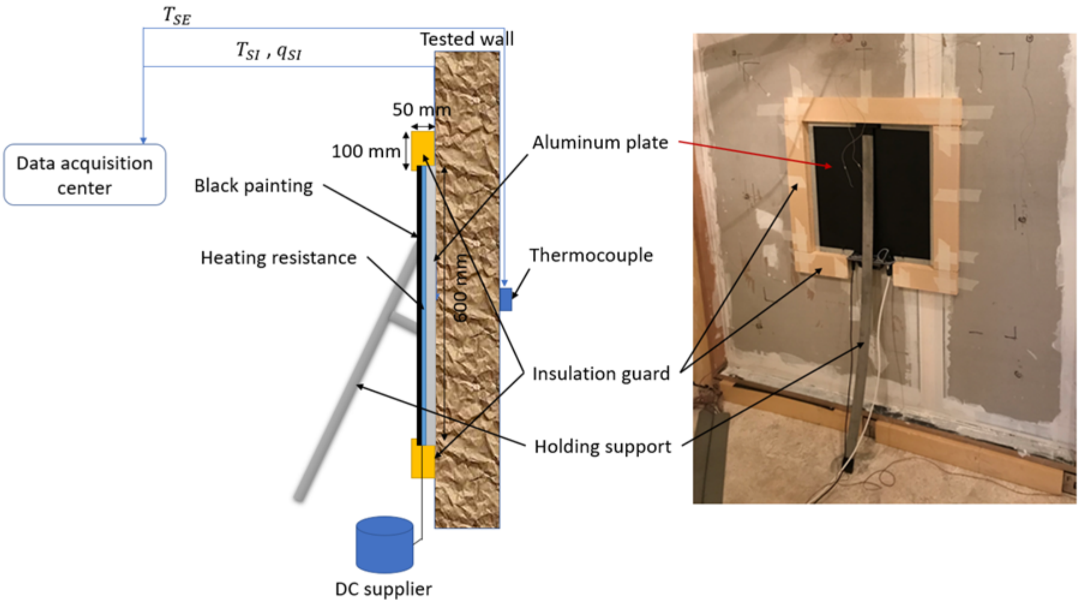

Figure 4.29: (left) Schematic view of the fourth prototype and (right) its real view in the measurement site.

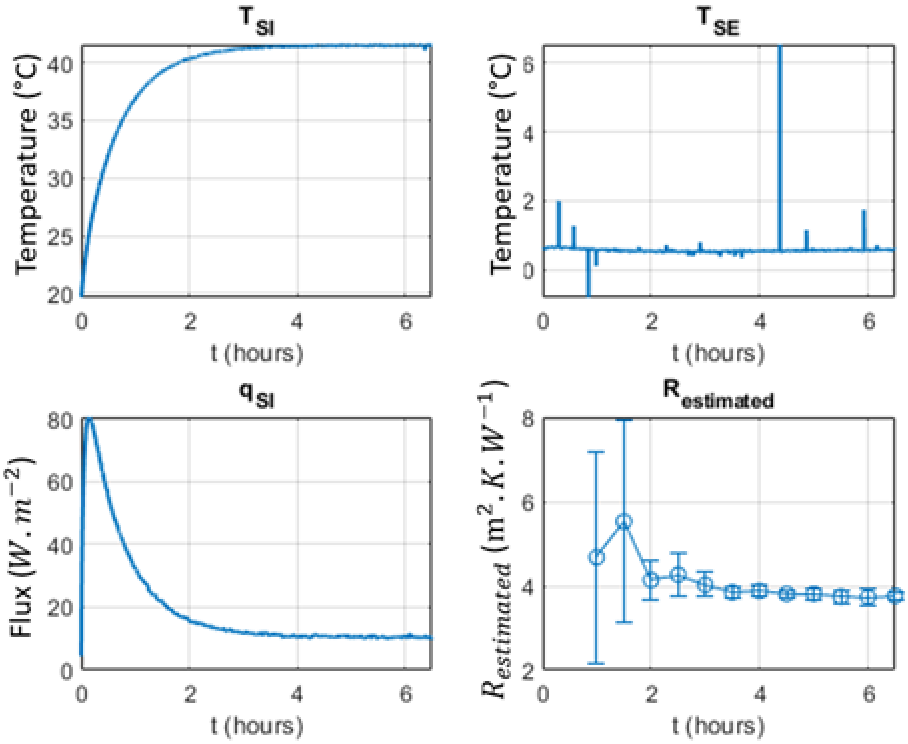

Figure 4.30: Measurement on the IWI wall under constant condition (internal/external air temperature = 20°C/0°C) and its estimation result when using the fourth prototype.

prototype.

However, sometimes the holding support used in this configuration does not provide a perfect contact with the wall surface as with the heavy lamp box, so this element must be optimized in the further studies. Briefly, this prototype configuration is less complicated than the third one, so that it requires less time to be installed (around 2-5 minutes).

4.3.5 Comparison between four measurement prototypes

Table 4.2 details the comparison between the four measurement prototypes mentioned in the previous sections. Here, the third prototype is considered the best one for evaluating the wall thermal resistance. The fourth one is also a good choice, but it requires some design optimizations to deliver a good measurement as the third one. Both of them require only a few minutes to be installed compared to the first two ones. However, the aluminum plate of these prototypes must perfectly touch the tested surface so that only flat wall surfaces are possible to be tested.

	Prototype 1	Prototype 2	Prototype 3	Prototype 4
Heating way	Contactless	Contactless	Contact	Contact
Thermal excitation source	Halogen lamp	Lamp box	Lamp box with aluminum plate	Heating resistance with aluminum plate
Tested surface	Flat and non-flat	Flat and non-flat	Flat	Flat
Surface temperature measurement	By IR camera	By IR camera	By thermocouple	By thermocouple
Heating power evaluation	By calibration	By calibration	By measurement	By measurement
Convective heat transfer coefficient determination	Yes	Yes	Not required	Not required
Homogeneity of surface temperature	1	2	4	3
Capability of thermal resistance estimation	1	2	4	4
Installation time	30 minutes	15-30 minutes	5-10 minutes	2-5 minutes
Compactness	1	3	2	4

Table 4.2: Comparison between four measurement prototype proposed in this study (1 = the worst, 4 = the best).

4.4 Conclusions

There are four measurement prototypes proposed in this chapter: two contactless ones and two contact ones. After several tests on the real wall in the laboratory, two contact prototypes exhibit a high thermal resistance estimation ability. With a quasi-flat lateral profile of surface temperature, these prototypes show higher performance in homogenizing imposed thermal excitation. Moreover, all measurement sensors are integrated into the plate, so it does not need much time to install these sensors manually compared to other methods. The required time for a full installation is around 5 minutes for both prototypes.

Another advantage that should be mentioned is that the aluminum plate helps to protect the measurement from the environment variation more efficiently than without this plate. According to the laboratory measurement, smooth profiles for both temperature and absorbed flux are observed even if someone is entering or working in the testing room. This point opens the possibility of running measurements in occupied spaces.

After several laboratory tests, the thermal resistance estimation ability by using these prototypes is confirmed, and they are ready to be tested on real walls on site.

5 Measurement setup

5.1 Introduction of chapter

This chapter presents all tested walls used in this study and configurations of each test performed. The first section shows the details (layout, thickness, thermal conductivity) of the four tested walls (Internal Wall Insulation, External Wall Insulation, Wood Frame Wall and Single Wall). Then, several measurements with standard methods to evaluate the thermal resistance of these walls are shown in the second section. The next section describes three climatic chambers at LNE, CEREMA and IFSTTAR where the measurements are carried out. The last two sections list all the tests with the third and fourth prototypes under different external environmental conditions (constant, variable and natural) with different test configurations (two heating power levels, heating position, with/without solar protection, etc.).

5.2 Presentation of the tested walls

Four different walls were tested experimentally in this study: Internal Wall Insulation (IWI), External Wall Insulation (EWI), Wood Frame Wall (WFW) which were made by the CSTB wih a surface dimension of 2×2 m^2 and a concrete wall of a real building (called Single Wall or SW) which is located in the mini city named Sense-City at the IFSTTAR.

Figures 5.1 presents the layout of the IWI wall. This type of wall does not contain any irregularity such as thermal bridge or support stub. There are four homogeneous layers: plasterboard (or BA13), insulation layer (Expanded polystyrene or EPS), building block and external coating layer. Figure 5.2 shows two real views of its building block surface and of the complete wall.

Figures 5.3 and 5.4 show the general layout and real views of the EWI wall. Its structure is more complex than that of the IWI wall and its insulation layer stays on the external side of the wall. Moreover, this wall requires several metal frames, wood stubs and plastic fixations to hold the stone wool insulation, which results in the presence of several thermal bridges. In addition, there is a ventilated air gap located between the metal cladding and the insulation layer.

Figure 5.5 and 5.6 present the structure and some real views of the WFW wall. Among

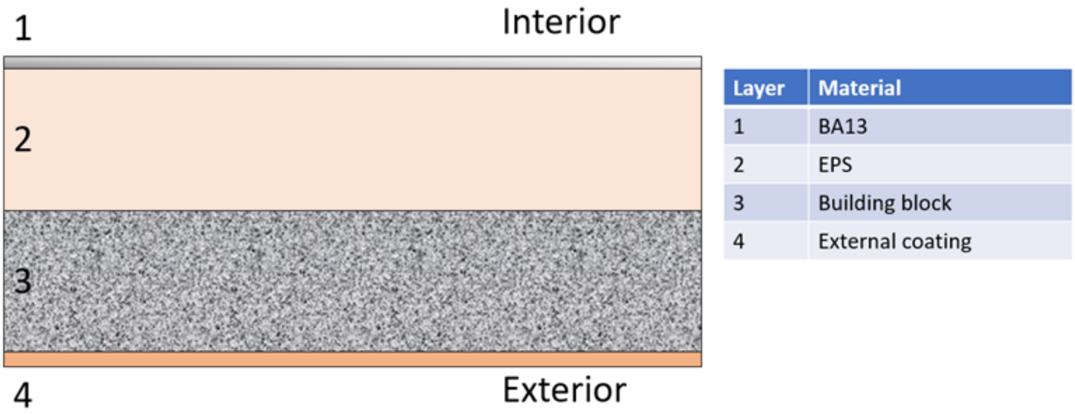

Layer	Material
1	BA13
2	EPS
3	Building block
4	External coating

Figure 5.1: General layout of the tested IWI wall.

Figure 5.2: Tested IWI wall: (left) Real views of the building block layer and (right) of the complete wall.

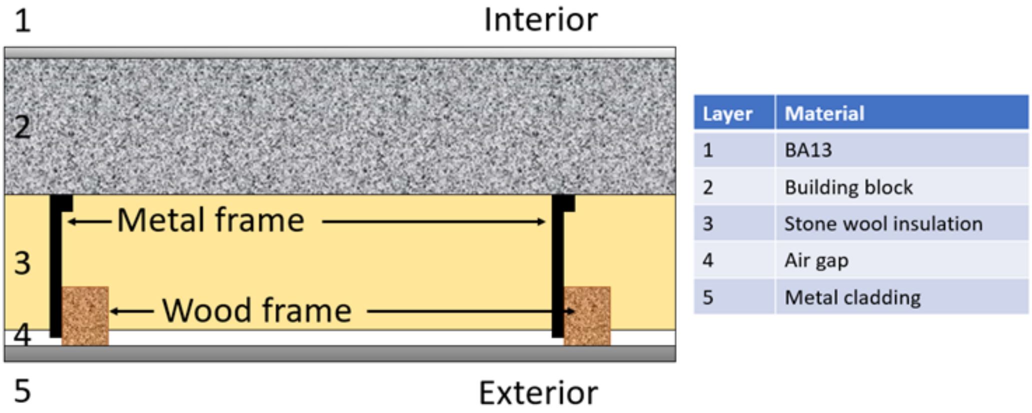

Layer	Material
1	BA13
2	Building block
3	Stone wool insulation
4	Air gap
5	Metal cladding

Figure 5.3: General layout of the tested EWI wall.

the four walls investigated in this study, the WFW wall has the most complex structure with seven layers and three structures of wood stubs (two vertical and one horizontal). A thin layer

Figure 5.4: Tested EWI wall: (left) Real view of building block layer and metal frame, (middle) of the wall without BA13 from interior view and (right) of the metal cladding of the complete wall.

of Oriented Strand Board (noted OSB) sheathing is located between both insulation layers. As in the case of EWI wall, an air gap is located between the insulation layer and external wood cladding. Moreover, this wall contains also a second air gap between the internal coating and the insulation layer (Cf. Figure 5.5).

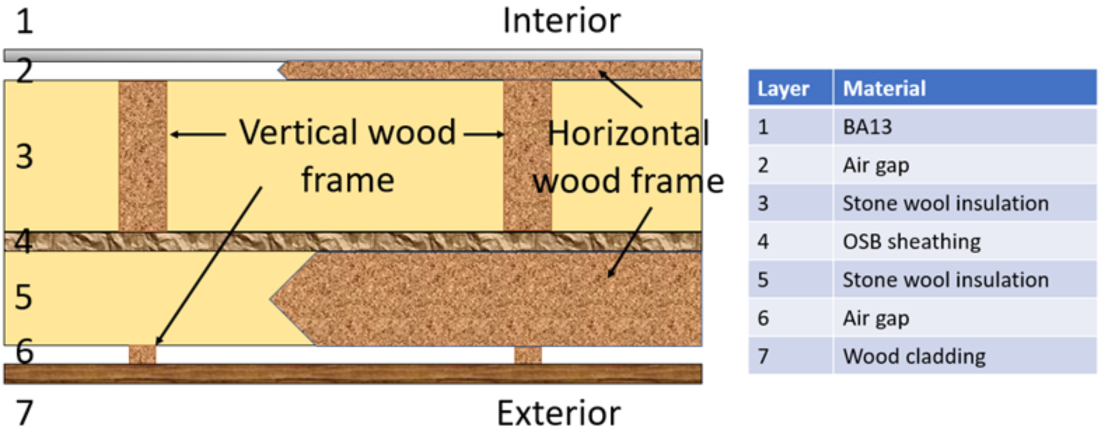

Layer	Material
1	BA13
2	Air gap
3	Stone wool insulation
4	OSB sheathing
5	Stone wool insulation
6	Air gap
7	Wood cladding

Figure 5.5: General layout of the tested WFW wall.

The last tested wall (SW) is a homogeneous concrete wall of a real building whose thickness is around 0.25 m without internal or external coating. Real views from the interior and exterior sides are shown in Figure 5.7.

Table 5.1 details the thickness and thermal conductivity of each element of the walls described above. The thermal conductivity values given in this table were determined by the Guarded Hot Plate device [85] at LNE and the Hot Disk device [86] at CEREMA, except the air

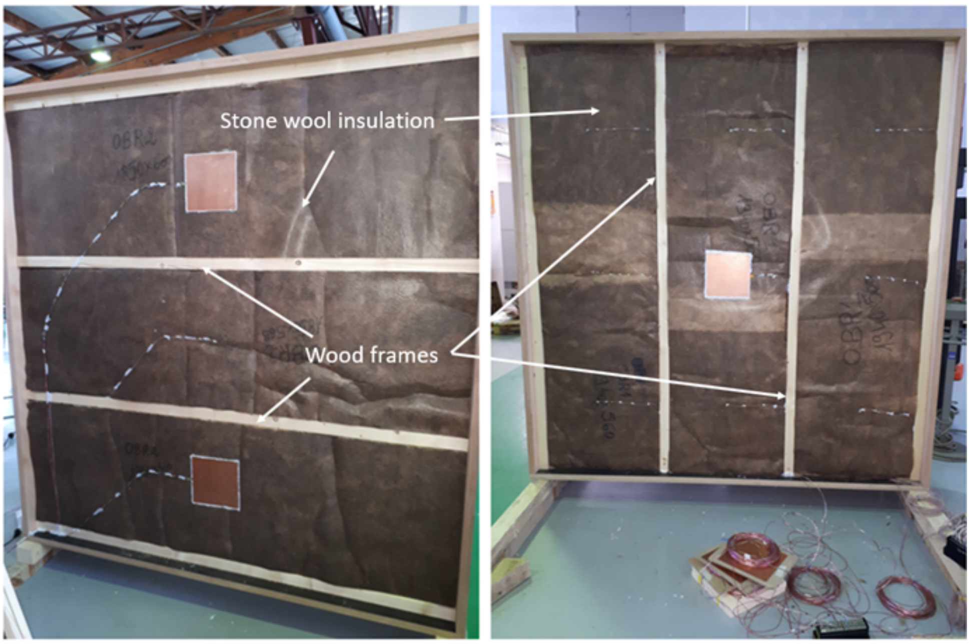

Figure 5.6: Tested WFW wall: (left) Rear and (right) front views of the insulation layer of the wall.

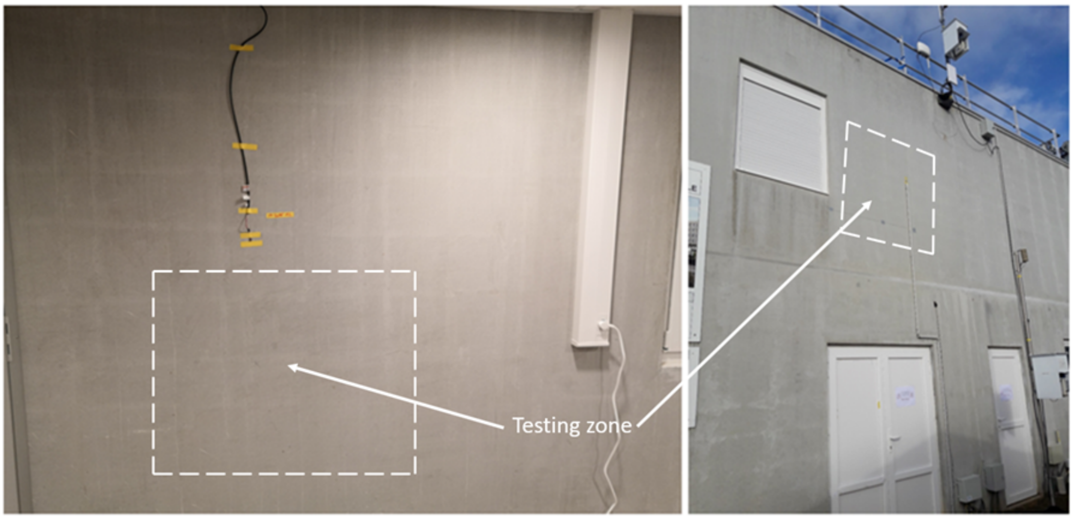

Figure 5.7: Tested SW wall: (left) Interior and (right) exterior views of the wall.

gap whose thermal resistance is calculated by applying the RT2012 [3]. These values are used to calculate the theoretical thermal resistance of each wall (see Table 5.2).

Besides, several heat flux meters and thermocouples were installed on the both surface of each layer for these wall in order to keep a close watch on the thermal evolution inside the wall during the measurement, except the SW wall.

Wall	No. of layer	Material	Thickness (m)	Thermal conductivity (W.m^{-1}.K^{-1})
IWI	1	BA13	0.013	0.242
	2	PSE	0.15	0.031
	3	Concrete	0.15	1
	4	External coating	0.015	0.931
EWI	1	BA13	0.013	0.242
	2	Concrete	0.15	1
	3	Stone wool insulation	0.15	0.035
	4	Air gap	0.02	0.16
	5	Metal cladding	0.015	205
		Metal frame	0.16	205
		Wood frame	0.065	0.141
WFW	1	BA13	0.013	0.242
	2	Air gap	0.02	0.16
	3	Stone wool insulation	0.16	0.035
	4	OSB sheathing	0.02	0.171
	5	Stone wool insulation	0.1	0.035
	6	Air gap	0.02	0.16
	7	Wood cladding	0.021	0.141
		Wood frame		0.141
SW		Concrete	0.25	1

Table 5.1: Thickness and thermal conductivity of each element of the four tested walls.

Wall	Thermal resistance (m^2.K.W^{-1})
IWI	5.06
EWI without metal frame	4.61
EWI with metal frame	0.33
WFW without wood frame	7.99
WFW with wood frame	2.45
SW	0.25

Table 5.2: Theoretical thermal resistance of the four tested walls according to Table 5.1.

5.3 Evaluation of the wall thermal resistances by the standard methods

The theoretical thermal resistance of a wall can be obtained by adding the thermal resistances of its elements. However, the real value may differ from this calculated value because there are several factors that can influence the thermal resistance of a wall (imperfect contact, imprecise measurement of thickness, thermal conductivity, etc.). Therefore, the standard measurement methods (ISO 8990 and ISO 9869-1) are chosen to evaluate this value experimentally.

5.3.1 Measurements with the Guarded Hot Box (ISO 8990)

The first three walls (IWI, EWI and WFW) were examined by a big-scale device named Guarded Hot Box (based on ISO 8990 standard [7]) at CSTB. The global view of this device is shown in Figure 5.8.

Figure 5.8: Guarded Hot Box device at CSTB [87].

This device allows determining the global U-value of a wall instead of its thermal resistance. This global value contains the proper U-value of the wall and the internal and external surface resistances. The experimental protocol to be followed with this device includes three measurement steps:

- **Step 1:** Installing the tested wall between the hot and cold sides of the device and waiting for the stability of the temperature on the both sides.

- **Step 2:** Measuring the applied heat flux from the hot side and the flux which goes through the tested wall on the cold side.

- **Step 3:** Calculating the global heat transfer coefficient of the wall including the superficial thermal resistances by using the temperature difference between hot and cold sides and the measured heat flux. The correct value of global U-value is obtained when the thermal stability inside the wall is achieved.

For each measurement, the thermal surface resistances are determined by the device calibration. Then, the wall thermal resistance value and its uncertainty is obtained by taking into account all bias factors. Three temperature levels were used for each wall because of the dependence of thermal properties of materials on operating temperature: 10°C, 20°C and 30°C.

Table 5.3 presents the measured thermal resistance of the IWI, EWI and WFW walls (without superficial thermal resistances) obtained with this method. This table shows clearly that the thermal resistance decreases when increasing the operating temperature. The GHB method can be considered as the most robust method which can determine the thermal resistance of a real wall among the two standard methods so that these results will be used as reference values for later estimations.

Wall/Temperature (°C)	Thermal resistance ($m^2.K.W^{-1}$)	Uncertainty ($m^2.K.W^{-1}$)
IWI		
10°C	3.8	0.6
20°C	3.5	0.8
30°C	3.3	0.5
EWI		
10°C	2.1	0.3
20°C	2.1	0.3
30°C	1.8	0.2
WFW		
10°C	7.6	1.8
20°C	7.1	1.6
30°C	6.7	1.5

Table 5.3: Thermal resistances of the first three tested walls obtained with the Guarded Hot Box device at CSTB under three different operating temperatures.

5.3.2 Measurements with the ISO 9869-1 standard

The last tested wall is the SW wall which is a wall of a real building. Thus, it can not be evaluated by the GHB device. Therefore, the ISO 9869-1 standard (or Heat Flux Meter method or HFM method) is chosen for measuring this wall thermal resistance. It only requires a heat flux meter on the internal surface and two thermocouples on the internal and external surfaces (see Figures 5.9) as presented in Chapter 1. These measurement data are used for the computation of the wall thermal resistance.

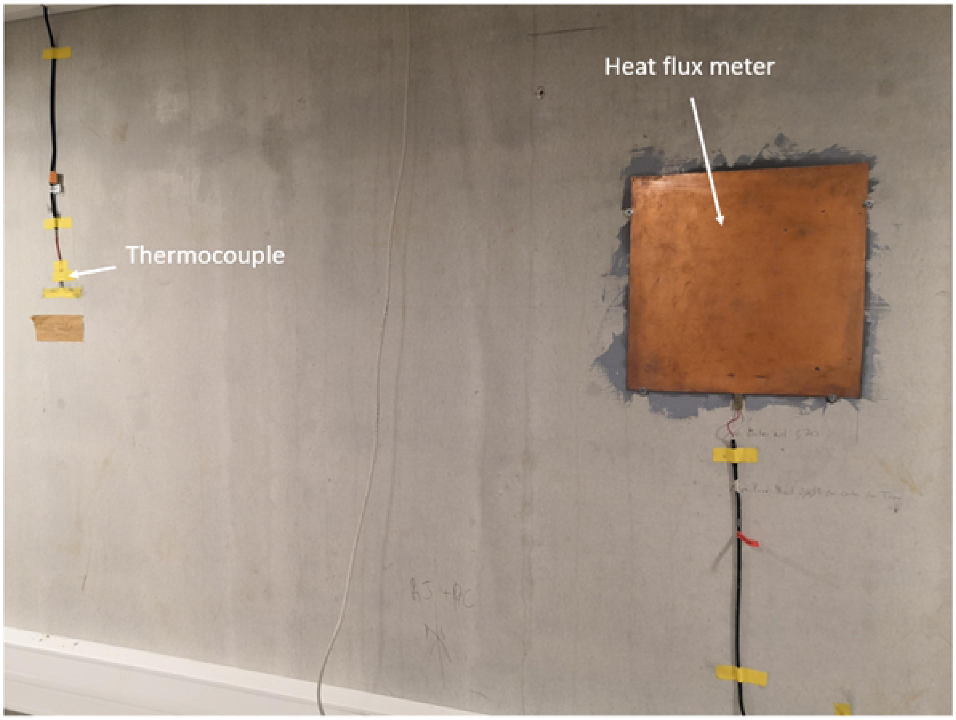

Figure 5.9: Thermal sensors on the internal surface of the tested SW wall used to apply the Heat Flux Meter method.

A monthly data of these parameters has been recorded (Cf. Figure 5.10) in order to evaluate the reference value of this wall thermal resistance. There are four series of measurement:

- The whole building stayed under natural condition during the first twelve days. Then, no control of environmental conditions was ensured (a series of strong pics of solar radiation is reported). This can be considered as realistic conditions for passive tests. A two-day data (noted series 1) is chosen to be analysed between the 150^{th} and 200^{th} hours of measurement because this period shows the weakest external condition variation during twelve days of test.

- The Sense-City climatic chamber was then installed and the air temperatures inside and outside the building were well controlled (respectively at 20°C and 5°C) and no solar radiation was applied during four days. These are perfect conditions for passive measurement. A two-day data (noted series 2) is chosen to be analysed between the 490^{th} and 540^{th} hours of measurement.

- A slight variation of environmental conditions inside the climatic chamber was finally applied during four days: the first two days with a small external air temperature variation (between the 550^{th} and 600^{th} hours, noted series 3) and the last two days with the same variation as the series 3 but a weak artificial solar flux is applied above the building roof (from the 610^{th}

hours until the end, noted series 4).

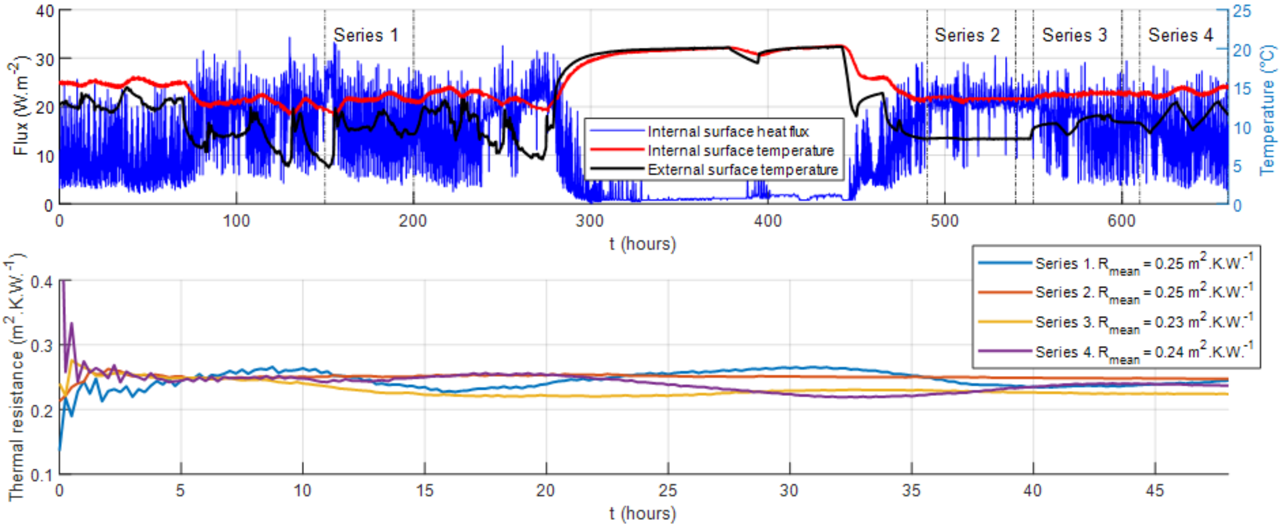

Figure 5.10: (up) Passive measurement data obtained on the tested SW wall in Sense-City and (down) wall thermal resistances computed from four series of data.

The lower part of Figure 5.10 shows the four profiles of thermal resistance obtained by passive method corresponding to the four different series. The results of the four tests are very close to each other with a very small difference (around 0.01-0.02 $m^2.K.W^{-1}$). The first series which is considered as the most realistic situation returns a similar value of thermal resistance as the second series which refers to the best controlled conditions. The results of the last two series with a small fluctuation of controlled outdoor conditions seem not far from the two others.

According to these measurements, the average value of the four cases (0.25 $m^2.K.W^{-1}$) is considered as the reference value for the SW estimation later.

5.4 Presentation of the climatic chambers

In this study, three climatic chambers at LNE, CEREMA and IFSTTAR were used. The objective of using this type of equipment is to better control the testing environment (constant and variable). Each of them has its own way for the regulation system. These chambers are used to test the real-scale walls under controlled conditions, especially the real-scale building with the chamber at IFSTTAR.

The climatic chamber at LNE is insulated by a thick insulated wall and its internal and external temperatures are controlled by a radiator and a powerful fan respectively. The tested wall is installed at the position named "Specimen" shown in Figure 5.11. The real interior and exterior views of this chamber are shown in Figure 5.12. Only constant environmental conditions are available with this chamber.

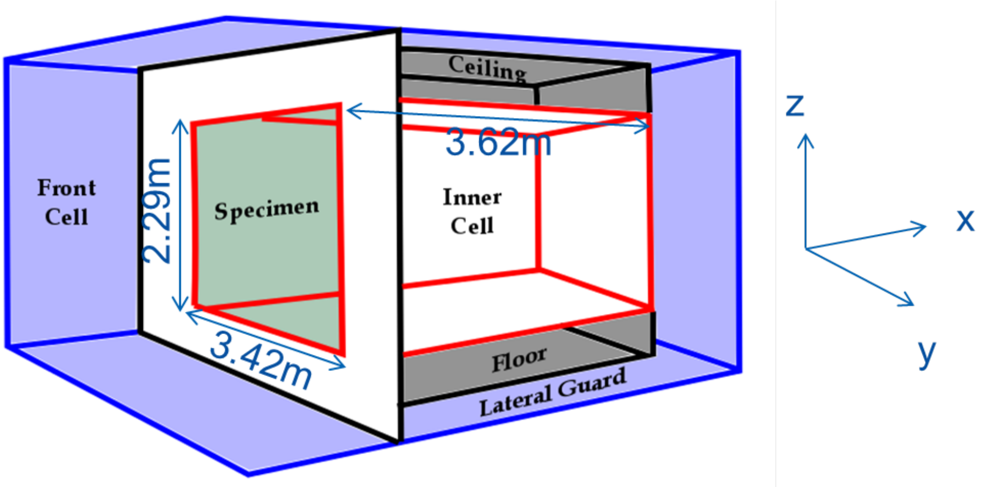

Figure 5.11: General representation of the climatic chamber at LNE [88].

Figure 5.12: (left) Interior and (right) exterior views of the climatic chamber at LNE.

The climatic chamber at CEREMA contains two parts: external and internal sides. The tested wall will be installed on their common wall. Both sides are regulated by powerful regulators which allow generating constant and variable environmental conditions. The general representation and real views of this climatic chamber are presented in Figures 5.13 to 5.15.

Sense-City is a climatic chamber of 400 m^2 which contains two separated zones (called mini-city). The internal temperature and global humidity of this chamber are controlled by a huge regulation system. There are also rain and solar systems if needed (Cf. Figure 5.16). It is possible to put the tested wall under natural conditions by removing its covering (see Figure 5.17). Multiple sensors are installed inside all buildings for studying their energetic performance

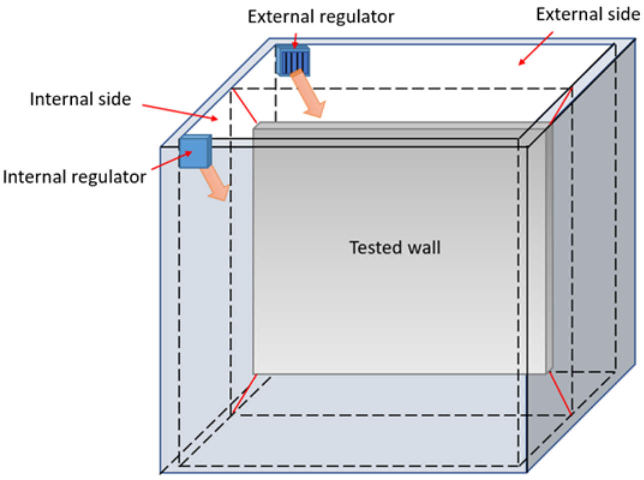

Figure 5.13: General representation of the climatic chamber at CEREMA.

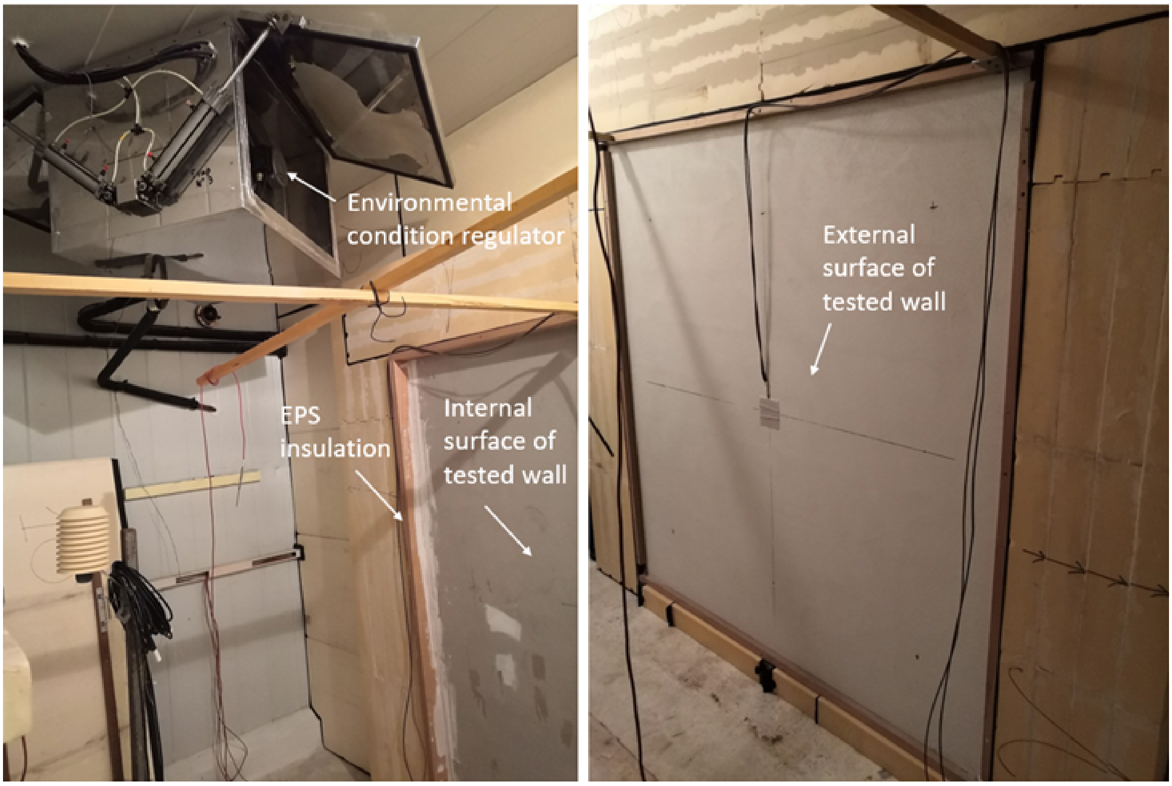

Figure 5.14: (left) Interior and (right) exterior views of the climatic chamber at CEREMA.

and the atmospheric pollution.

5.5 Testing conditions of the measurement campaigns with the third prototype

During this work, three different external conditions have been tested: constant, variable and natural. This section details the testing conditions (heating power, heating zone and external

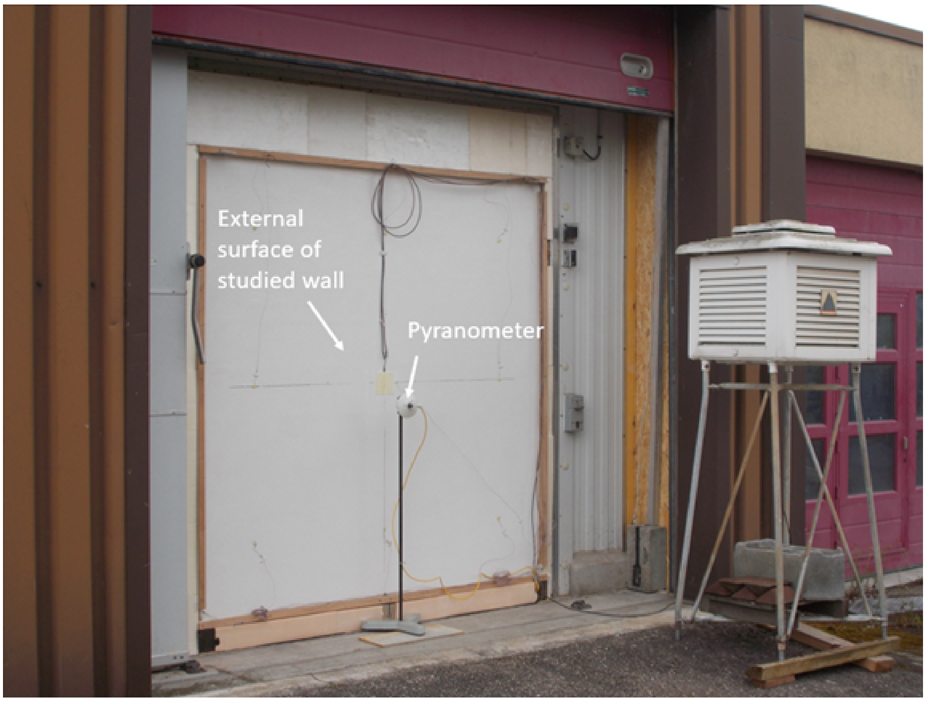

Figure 5.15: Exterior view of studied wall when testing under natural condition at CEREMA.

Figure 5.16: Regulation systems used in the climatic chamber Sense-City.

environment) for each measurement carried out on the four walls.

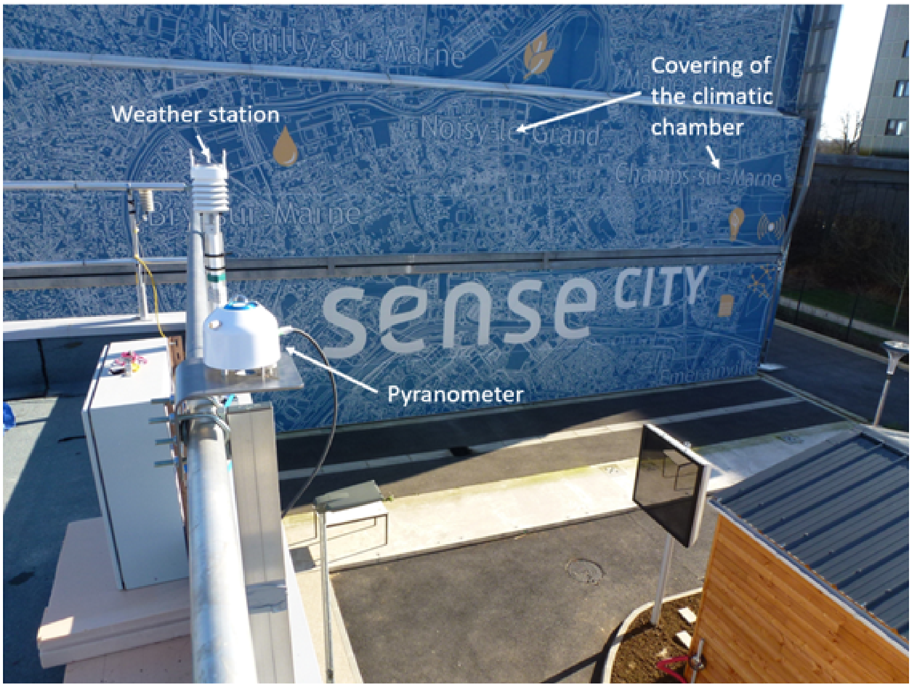

Figure 5.17: Roof of investigated building when testing under natural condition (outside the climatic chamber Sense-City) at IFSTTAR.

5.5.1 Constant conditions

With this type of condition, both internal and external environments are maintained constant by the climatic chambers. Table 5.4 details all test configurations of the four tested walls under constant conditions and their corresponding number in this study.

According to Chapter 3, the numerical study showed that it is impossible to estimate the thermal resistance of the EWI wall from inside the building due to the strong lateral diffusion through the concrete layer. Therefore, two measurements on the internal side are carried out to demonstrate this conclusion and the other tests with this wall will be performed on the external side. As presented in Figure 5.4, the external side of the tested EWI wall is covered by a metal cladding and a ventilated air gap behind. This configuration is not ideal for the thermal resistance estimation because the thermal excitation flux can not reach the insulation layer. So only one measurement on the external side of the metal cladding was launched to observe what happens when heating directly its surface, as in Figure 5.18. For the other measurements with this wall, the metal cladding is removed and the prototype is directly installed on the external surface of the insulation layer.

As observed in Figure 5.5, the WFW wall has the most complex structure with the

Figure 5.18: Prototype setup on (left) the metal cladding and (right) the external surface of insulation layer of the EWI wall.

horizontal and vertical wood frames. In order to show the influence of these thermal bridges, two tests were performed on the zone containing the thermal bridges (Cf. Figure 5.19). A zone without thermal bridge was chosen for the three others.

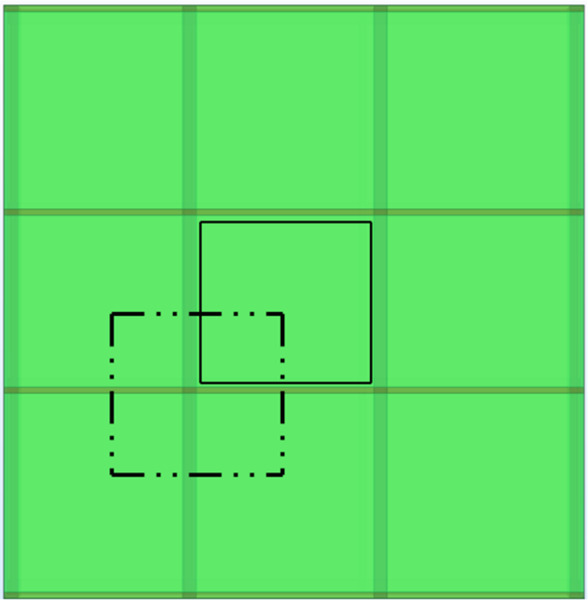

Figure 5.19: Measurement zones on the WFW wall (dash-dotted line) with the thermal bridges and (solid line) without.

Wall	Test number	Interior	Exterior	Heating power	Heating zone
IWI (at CEREMA)	1	20°C	0°C	240 W	On the wall internal surface
	2	20°C	0°C	120 W	On the wall internal surface
	3	30°C	10°C	240 W	On the wall internal surface
	4	30°C	10°C	120 W	On the wall internal surface
	5	25°C	35°C	240 W	On the wall internal surface
	6	25°C	35°C	120 W	On the wall internal surface
EWI (at LNE)	7	30°C	15°C	240 W	On the wall internal surface
	8	30°C	15°C	120 W	On the wall internal surface
	9	25°C	15°C	240 W	On the external metal cladding
	10	25°C	15°C	240 W	On the insulation external surface
	11	25°C	15°C	120 W	On the insulation external surface
	12	20°C	20°C	240 W	On the insulation external surface
	13	20°C	20°C	120 W	On the insulation external surface
	14	20°C	30°C	240 W	On the insulation external surface
	15	20°C	30°C	120 W	On the insulation external surface
	16	20°C	15°C	240 W	On the insulation external surface
	17	20°C	15°C	120 W	On the insulation external surface
SW (at Sense-City)	18	20°C	20°C	240 W	On the wall internal surface
	19	20°C	20°C	120 W	On the wall internal surface
	20	20°C	5°C	240 W	On the wall internal surface
	21	20°C	5°C	120 W	On the wall internal surface
WFW (at LNE)	22	20°C	0°C	240 W	On the wall internal surface with thermal bridge
	23	20°C	0°C	120 W	On the wall internal surface with thermal bridge
	24	20°C	0°C	240 W	On the wall internal surface without thermal bridge
	25	30°C	10°C	240 W	On the wall internal surface without thermal bridge
	26	25°C	35°C	240 W	On the wall internal surface without thermal bridge

Table 5.4: Measurement configurations for the four tested walls (IWI, EWI, SW and WFW) with the third prototype under constant conditions.

5.5.2 Variable conditions

Only the IWI and SW walls are tested under variable conditions (the reason will be described in the next sections) so that the measurement prototype is installed only on the wall internal surface. In this configuration, the internal air temperature is maintained at 20°C for all tests. Table 5.5 and Figure 5.21 give the test conditions and external air temperature profiles during these tests.

Two real records of external environment temperature in Trappes and Carpentras taken from Météo France database are used for the tests under variable conditions in the chamber at CEREMA (Cf. Figure 5.20).

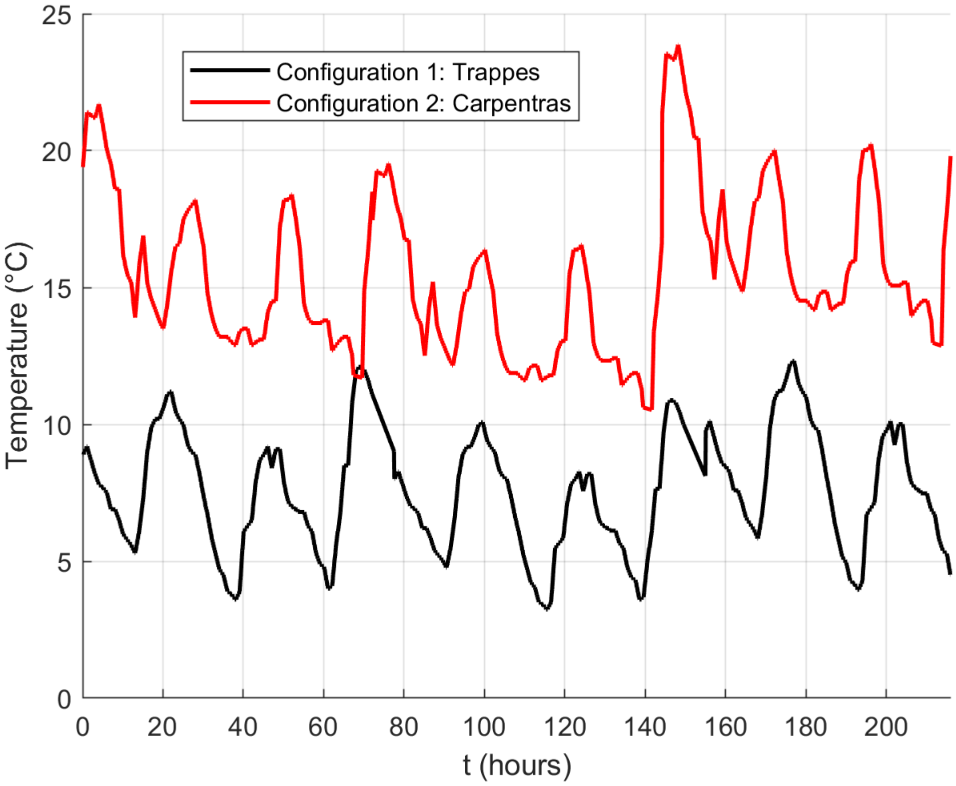

Figure 5.20: Environmental temperatures measured by Météo France.

The tests on the IWI wall are carried out at CEREMA so that it is possible to generate a complex variation of air temperature but no solar radiation control is available. Five variable conditions are proposed for this wall during some periods picked from the complete profile in Figure 5.20. Among them, the conditions T-var. 1-2 represents typical temperature profiles in winter (taken from Trappes's condition in Figure 5.20). The conditions T-var. 3-4 are spring ones (taken from Carpentras's condition in Figure 5.20). All of them have lower temperature levels than the temperature inside (20°C) then the steady-state heat flux will come from the interior to the exterior. However, a particular case T-var. 5 is tried with temperature levels higher than 20°C to inverse the heat flux and it can be considered as a day in summer (taken from Carpentras's condition and added 10°C more).

Besides, the climatic chamber at IFSTTAR allows testing with solar radiation but with a quite limited intensity. Therefore, four tests with a similar temperature ramp variation of the external environment were launched and the solar radiation was added for two of them (Cf.

Figure 5.21).

Wall	Test number	Interior	Exterior	Heating power	Remarks
IWI (at CEREMA)	27	20°C	T-Var. 1	240 W	
	28	20°C	T-Var. 1	120 W	
	29	20°C	T-Var. 2	240 W	
	30	20°C	T-Var. 2	120 W	
	31	20°C	T-Var. 3	240 W	
	32	20°C	T-Var. 3	120 W	
	33	20°C	T-Var. 4	240 W	
	34	20°C	T-Var. 4	120 W	
	35	20°C	T-Var. 5	240 W	
	36	20°C	T-Var. 5	120 W	
SW (at Sense-City)	37	20°C	T-Var. 6	240 W	
	38	20°C	T-Var. 6	120 W	
	39	20°C	T-Var. 6	240 W	Solar radiation S-Var. 1 added
	40	20°C	T-Var. 6	120 W	Solar radiation S-Var. 1 added

Table 5.5: Measurement configurations for the two tested walls (IWI and SW) with the third prototype under variable conditions.

5.5.3 Natural conditions

The IWI and SW walls are chosen to be tested under natural conditions. Here, the external side of the tested walls is subjected for several different days to an outdoor environment including solar radiation. The tests on the IWI wall were performed from 7 a.m and 7 p.m in August 2020 which corresponds to summer conditions. Besides, the SW wall was tested between 10 a.m to 10 p.m in February 2020 which corresponds to winter conditions. In addition, a local solar protection of 60×60 cm^2 was used for the IWI measurements (Cf. Figure 5.22) to study the influence of solar radiation on estimation results. Instead of fixing it directly on the external surface, there is a distance of around 5-10 cm between the protection and the wall surface in order to let the air circulate and to prevent the heating of the wall surface by the direct solar radiation. For all tests of this series, the internal air temperature is systematically maintained at 20°C.

Table 5.6 shows the details of the measurements under natural conditions for both walls and Figure 5.23 presents the external air temperature and solar radiation profiles during each test.

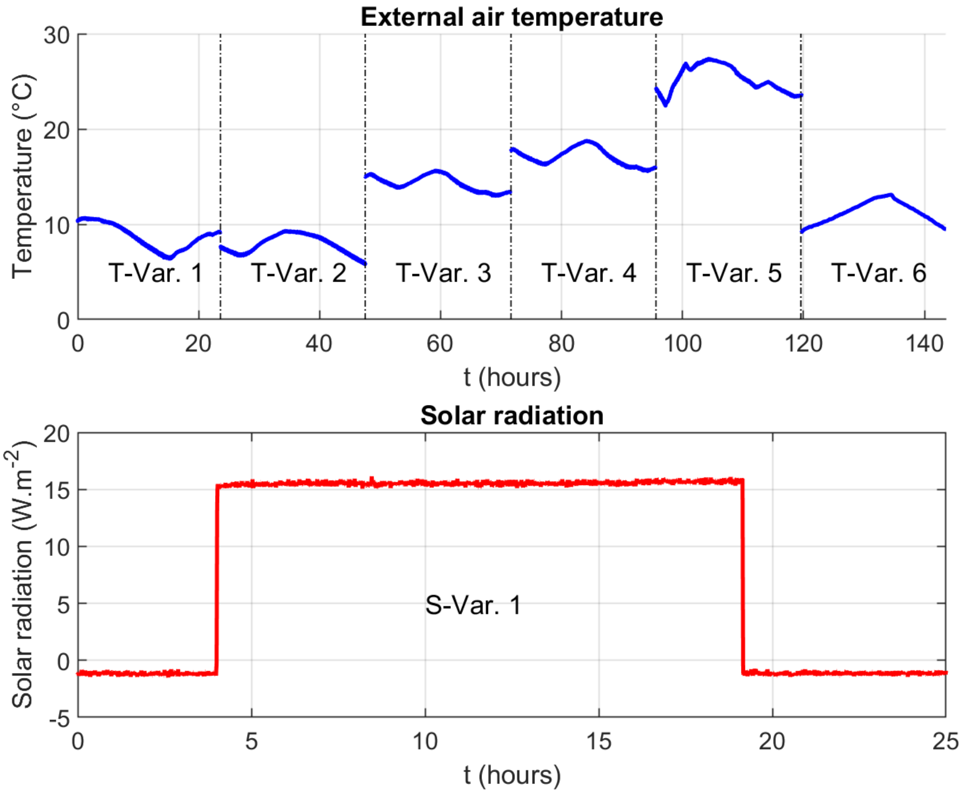

Figure 5.21: (upper) External air temperature (or T_{aE} for the tested walls) profiles and (lower) solar radiation generated by the climatic chamber during measurements with the third prototype under variable conditions.

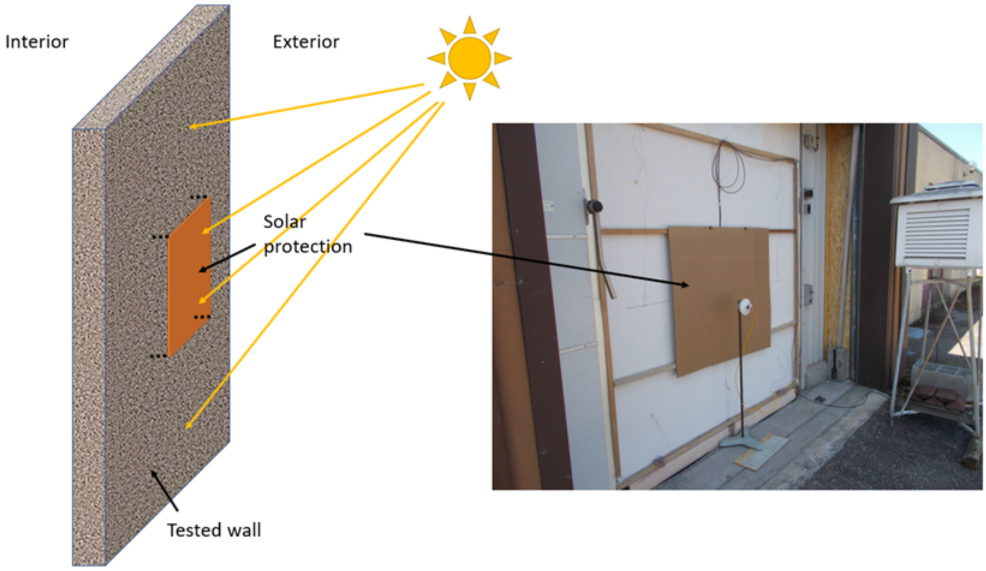

Figure 5.22: Solar protection used for the IWI tests at CEREMA.

Wall	Test number	Interior	Exterior	Heating power	Remarks
IWI (at CEREMA)	41	20°C	T-Nat. 1 S-Nat. 1	240 W	Without solar protection
	42	20°C	T-Nat. 2 S-Nat. 2	120 W	Without solar protection
	43	20°C	T-Nat. 3 S-Nat. 3	240 W	Without solar protection
	44	20°C	T-Nat. 4 S-Nat. 4	240 W	With solar protection
	45	20°C	T-Nat. 5 S-Nat. 5	120 W	With solar protection
SW (at Sense-City)	46	20°C	T-Nat. 6 S-Nat. 6	240 W	Without solar protection
	47	20°C	T-Nat. 7 S-Nat. 7	120 W	Without solar protection

Table 5.6: Measurement configurations for the two tested walls (IWI and SW) with the third prototype under natural conditions.

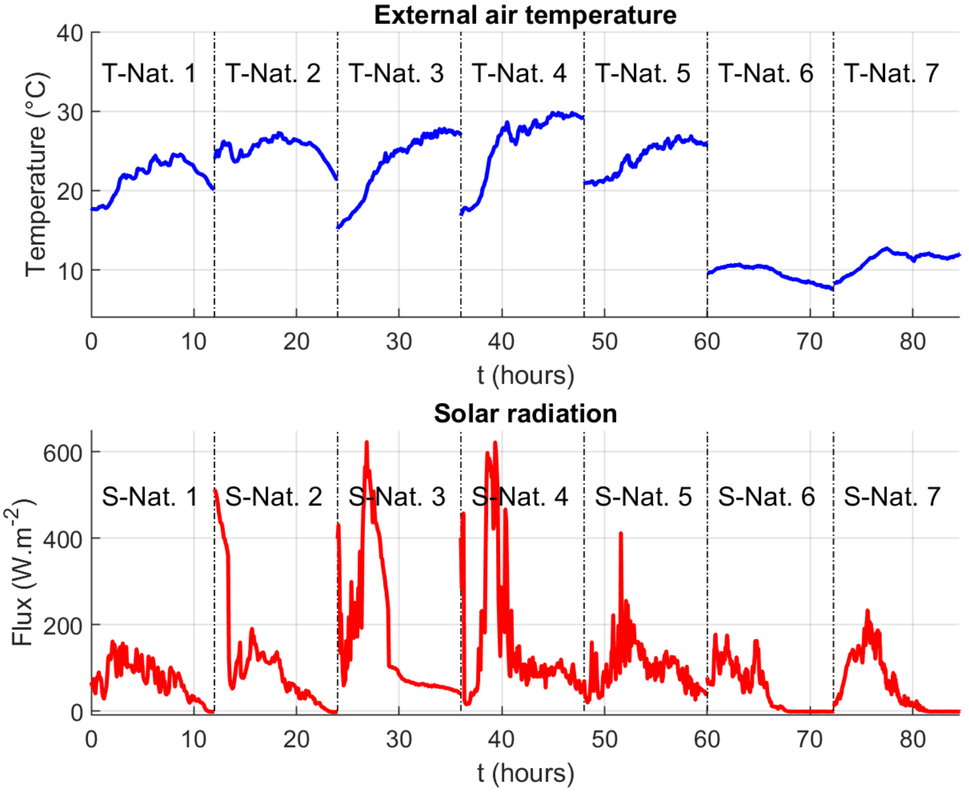

Figure 5.23: (Upper) External air temperature (or T_{aE} for the tested walls) and (lower) solar radiation measured during measurements with the third prototype under natural conditions.

5.6 Testing conditions of the measurement campaigns with the fourth prototype

With the fourth prototype, only the measurement on the IWI wall under constant and variable conditions are carried out. There is only one heating power (around 83 W). Table 5.7

details the test conditions in this series.

Wall	Test number	Interior	Exterior	Remarks
IWI (at CEREMA)	48	20°C	0°C	
	49	30°C	10°C	
	50	25°C	35°C	
	51	20°C	T-Var. 7	T-Var. 7 taken from Trappes's condition
	52	20°C	T-Var. 8	T-Var. 8 taken from Trappes's condition
	53	20°C	T-Var. 9	T-Var. 9 taken from Carpentras's condition
	54	20°C	T-Var. 10	T-Var. 10 taken from Carpentras's condition and added 10 °C more
	55	20°C	T-Var. 11	T-Var. 11 taken from Carpentras's condition and added 10 °C more
	56	Tint-Var. 1	T-Var. 12	Linear variation (5°C during 7 hours)
	57	Tint-Var. 2	T-Var. 12	Linear variation (5°C during 7 hours)
	58	Tint-Var. 2	T-Var. 13	Linear variation (5°C during 7 hours)
	59	Tint-Var. 1	T-Var. 13	Linear variation (5°C during 7 hours)

Table 5.7: Measurement configurations for the four tested walls (IWI, EWI, SW and WFW) with the fourth prototype under constant and variable conditions.

All temperature variations are presented in Figure 5.24. Here, the same variation as the ones chosen for the third prototype are used again (T-Var. from 7 to 11). Moreover, the last four test vary both the internal and external air temperatures (5°C/7 hours) to study the influence of internal air temperature variation.

5.7 Conclusions

This chapter detailed the four tested walls investigated during this thesis (Internal Wall Insulation, External Wall Insulation, Wood Frame Wall and Single Wall) and the three testing climatic chambers at LNE, CEREMA and IFSTTAR. The third and fourth measurement prototypes, which were proposed in Chapter 4, are used here.

Different environmental temperatures are applied: constant, variable and natural. With the third prototype, all of four walls are examined in using different heating power. On the other hand, only the IWI wall under constant and variable conditions was tested with the fourth prototype. The results of these tests will validate the estimation ability of the proposed prototypes when using on real walls.

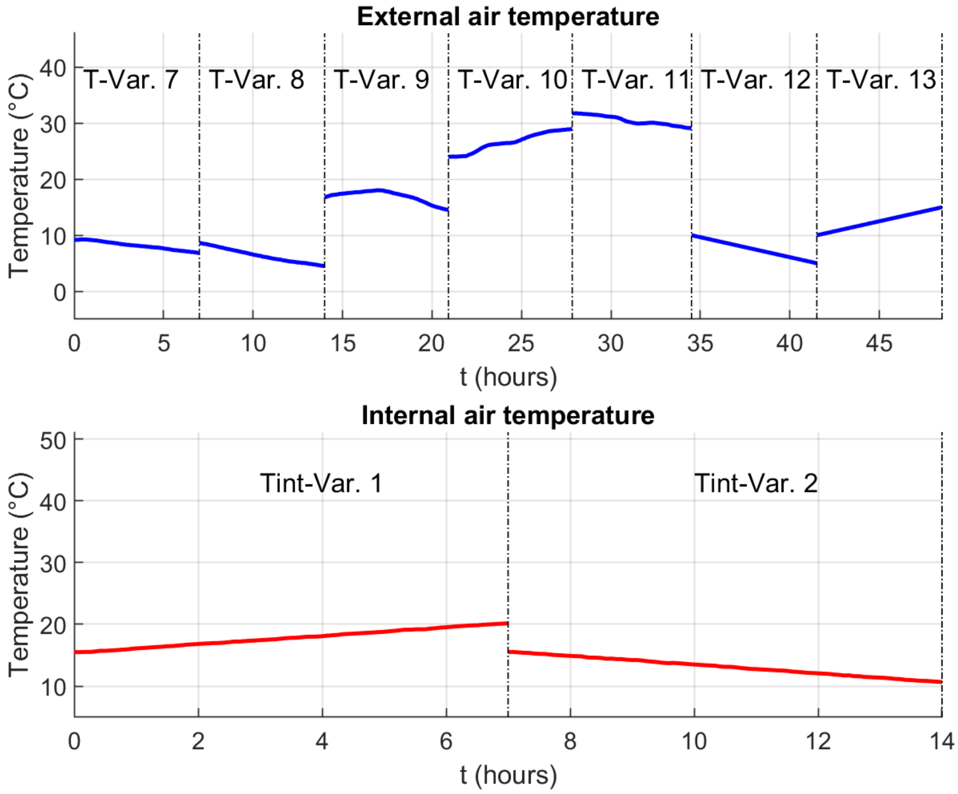

Figure 5.24: (upper) External air temperature (or T_{aE} for the tested walls) profiles and (lower) internal air temperature variation generated by the climatic chamber during measurements with the fourth prototype under variable conditions.

6 Measurement results

In this chapter, the measurement results obtained by using the third and fourth prototypes are detailed. Let us recall that the third prototype is based on using a lamp box for the thermal excitation and an aluminum plate in contact with the tested wall. In contrast, the fourth prototype uses a heating resistance integrated into the same aluminum plate. The performances of the two other prototypes being less interesting (Cf. Table 4.2), their use in measurement situations will not be studied in this last chapter. The three main sections correspond to the three different measurement conditions investigated: constant, variable, and natural. For the constant conditions, there are four separate sections for each type of tested wall. The second and third sections then present the results obtained for the IWI and SW walls, respectively, under variable and natural conditions. The estimation results in terms of thermal resistance will be compared with the reference values. The uncertainty levels on the thermal resistances obtained will also be analyzed. In Appendix A4, the residuals between measured and estimated values of minimization data (in this study, the internal surface temperature, or the external surface temperature for tests 10 to 17) of each measurement are presented.

6.1 Measurement campaign no. 1: constant conditions

6.1.1 IWI results by using the third prototype

Figure 6.1 shows the measurement data used in the thermal resistance estimation for the first six tests performed with the third prototype under constant conditions on the IWI wall. These tests were carried out in the climatic chamber at CEREMA with three different constant conditions (Cf. Table 5.4). Thanks to the insulation layer's presence, temperature and heat flux on the internal surface reached stable levels after a few hours of heating.

Table 6.1 details the estimated thermal resistances and corresponding uncertainties obtained for three different data sets: 4-hour, 6-hour and 12-hour. Figure 6.2 graphically presents these estimation results.

After six hours of measurement, the obtained estimation results with 100% of heating power are already close to the reference values. As observed in Table 6.1, Tests 1 to 5 return a thermal resistance value with a relative error from the reference value of less than 5%. However,

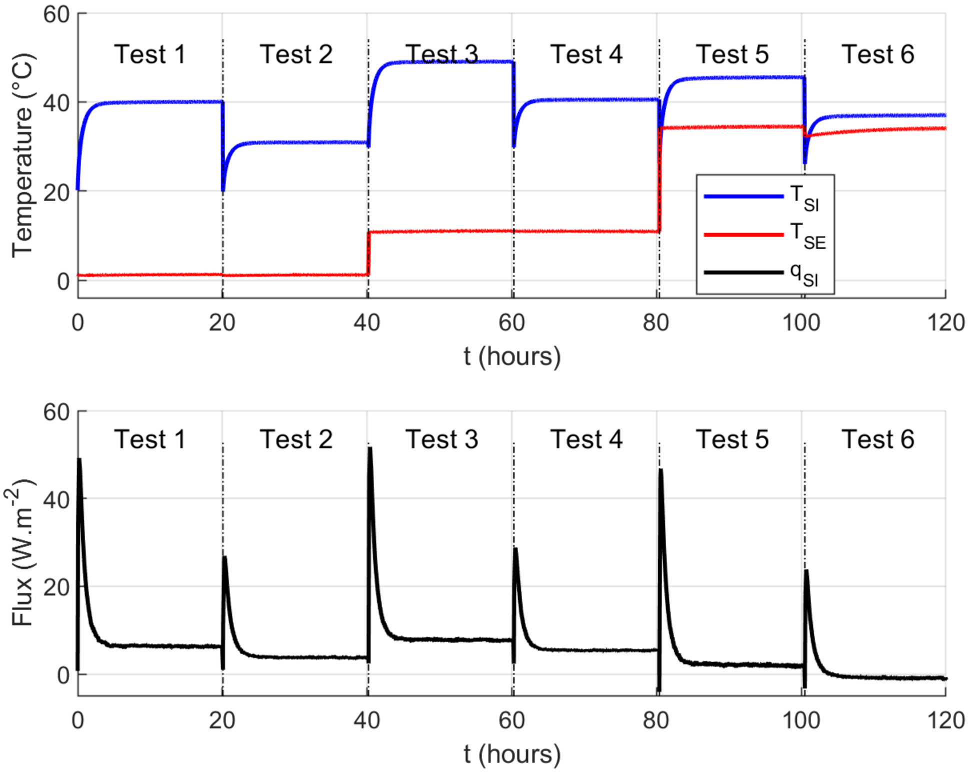

Figure 6.1: Measurement data of the IWI tests 1 to 6 under constant environmental conditions.

				Measurement duration (hours)		
Test no.	T_{aI}/T_{aE}	Power	R_{ref}	4	6	12
1	20°C/0°C	240 W (100%)	3.80	3.80 (0.01)	3.62 (0.03)	3.48 (0.01)
2	20°C/0°C	120 W (50%)	3.80	4.90 (0.85)	4.16 (0.03)	3.97 (0.01)
3	30°C/10°C	240 W (100%)	3.50	4.02 (0.13)	3.64 (0.04)	3.38 (0.01)
4	30°C/10°C	120 W (50%)	3.50	3.60 (0.32)	3.49 (0.30)	3.51 (0.45)
5	25°C/35°C	240 W (100%)	3.30	3.62 (0.06)	3.39 (0.03)	3.09 (0.01)
6	25°C/35°C	120 W (50%)	3.30	4.24 (0.10)	4.57 (0.04)	4.41 (0.03)

Table 6.1: Estimated thermal resistances and corresponding uncertainties (in m^2·K/W) for the IWI tests with the third prototype under constant environmental conditions (colors for the relative errors between $R_{estimated}$ and R_{ref}: out of 20%, 10-20%, 5-10%, <5%).

when heating for a longer duration, these estimation results drop to smaller values. The lateral diffusion causes this decrease. The insulation layer of this wall can be considered having a weak lateral effect but not completely null. Although most of the heat flux passes through the wall in the longitudinal direction, a small part of the original heat flux diffuses laterally. This lateral flux becomes more important when the heating duration is longer. However, the 1D estimation model assumes a completely longitudinal heat diffusion through the wall. With the passive method, long measurement duration is recommended, but this is not necessarily the case

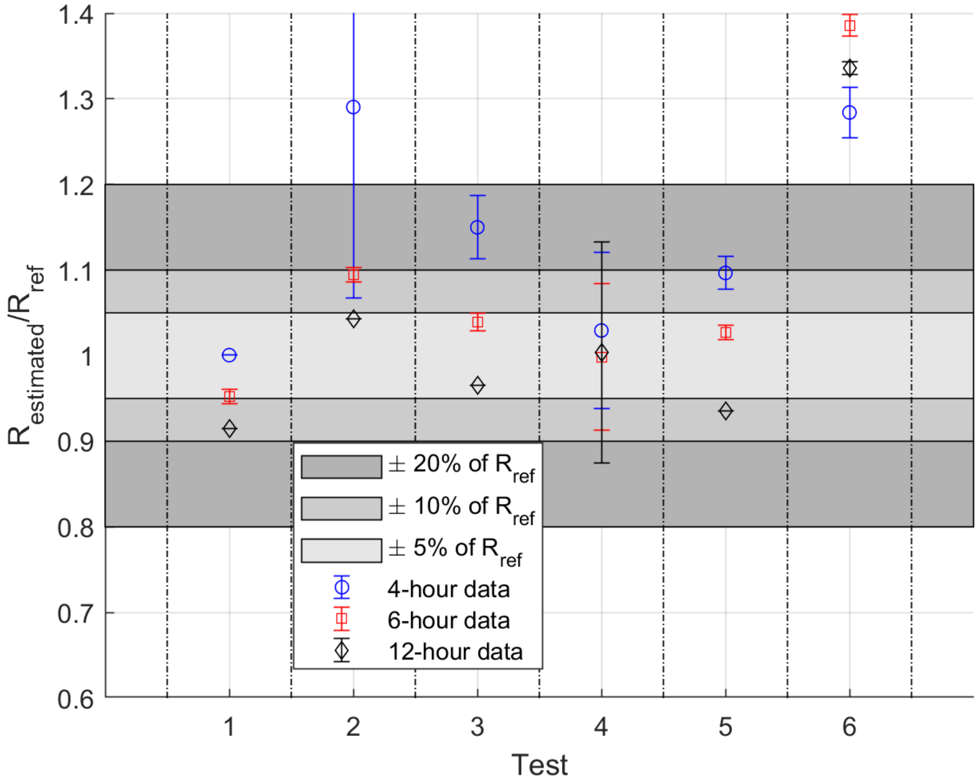

Figure 6.2: Estimated thermal resistances normalized by the reference value for the IWI tests with the third prototype under constant environmental conditions.

with an active method based on a 1D model. It can also be noted that, for these six cases, the estimation uncertainties decrease with the duration of heating. Evaluating the uncertainties does not make it possible to detect the deviation of the estimated value from the reference value when the measurement duration increases.

On the contrary, the 50% heating power seems too weak in this configuration. In the case under 20°C/0°C, it requires more time to reach the 5% zone than for the highest power. Besides, this heating power shows a more important uncertainty when comparing to the 100% one (Cf. Table 6.1). According to Appendix A4, test 2 shows important residuals during the first four hours of heating. It means that the estimation model can not return an estimated internal surface temperature good enough. Then, the estimation results for this duration has a large uncertainty, compared to others. On the other hand, test 4, which has small residuals, shows an important uncertainty for all three durations considered, even if the estimated thermal resistance is excellent. There are two reasons to explain this observation:

- The 50% heating power test has a weaker signal-to-noise ratio than the 100%.

- The use of 50% heating power limits the heating of the surrounding environment compared to the 100% case. Then, perturbations coming from the environment to the measurement are more important in this case.

Moreover, the most remarkable observation for this heating power can be made for test 6, for which the steady-state flux is opposite to the excitation one (the external air temperature is higher than the internal air temperature). The 50% of heating power is not high enough to counteract the opposite steady-state flux so that the excitation heat flux does not reach the end of the tested wall. A correct estimation of the thermal resistance with this level of power is therefore difficult in that case.

These six IWI tests under constant conditions show that a 6-hour measurement is enough to achieve a good estimation result when using the heating power of 240 W.

6.1.2 IWI results by using the fourth prototype

The measurement data of the three tests performed at CEREMA with the fourth prototype under constant conditions on the IWI wall (Cf. Table 5.7) are presented in Figure 6.3. These data are quite similar to the third prototype cases. With this prototype, the electrical power of 84 W is provided to the heating resistance. This power is weaker than the third prototype, but the wall surface's net absorbed heat flux, in this case, is stronger than the previous one. So, using the heating resistance is more efficient than using the lamps.

Figure 6.4 shows the estimation results under the three constant conditions with two data sets: 4-hour and 6-hour, and the corresponding estimated wall thermal resistances and associated uncertainties can be found in Table 6.2. These results show that the fourth prototype allows evaluating the IWI wall thermal resistance correctly with a relative error compared to the standard method less than 5%. However, the uncertainty values seem important (± 5%). This prototype's surrounding environment is less protected than with the third prototype, which uses a closed box. Moreover, the fourth prototype's internal surface temperature may not be as homogeneous as the third one because the heating resistance does not cover the plate surface totally. Then, this can explain why the uncertainty in this series is stronger than using the third prototype. To reduce the estimation uncertainty, a covering around the measurement prototype is highly recommended.

As a conclusion, if using this prototype on the IWI wall under constant conditions, it is

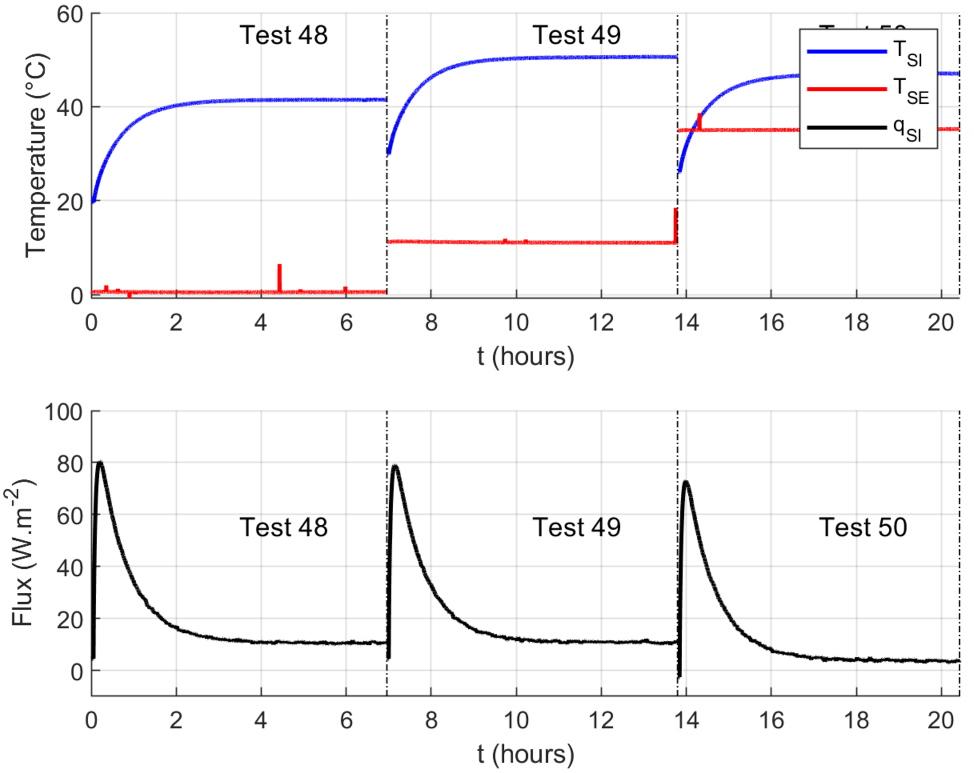

Figure 6.3: Measurement data of the IWI tests 48 to 50 under constant environmental conditions.

possible to obtain a good thermal resistance estimation after 6 hours of measurement but the uncertainties are not negligible.

			Measurement duration (hours)	
Test no.	T_{aI}/T_{aE}	R_{ref}	4	6
48	20°C/0°C	3.80	3.88 (0.13)	3.73 (0.20)
49	30°C/10°C	3.50	3.31 (0.55)	3.33 (0.42)
50	25°C/35°C	3.30	3.59 (0.16)	3.34 (0.23)

Table 6.2: Estimated thermal resistances and corresponding uncertainties (in m^2·K/W) for the IWI tests with the fourth prototype under constant environmental conditions (colors for the relative errors between $R_{estimated}$ and R_{ref}: out of 20%, 10-20%, 5-10%, <5%).

6.1.3 EWI results

Eleven tests of the EWI wall using the third prototype were carried out under constant conditions at LNE (Cf. Table 5.4). The measurement data of the tests 7 to 9 are shown in Figure 6.5. Unlike the IWI cases, the profiles of the first two tests performed directly on the internal surface of the tested wall do not reach stable levels due to the lack of internal insulation. It means that the tested wall continues to absorb and diffuse the excitation heat flux through the concrete

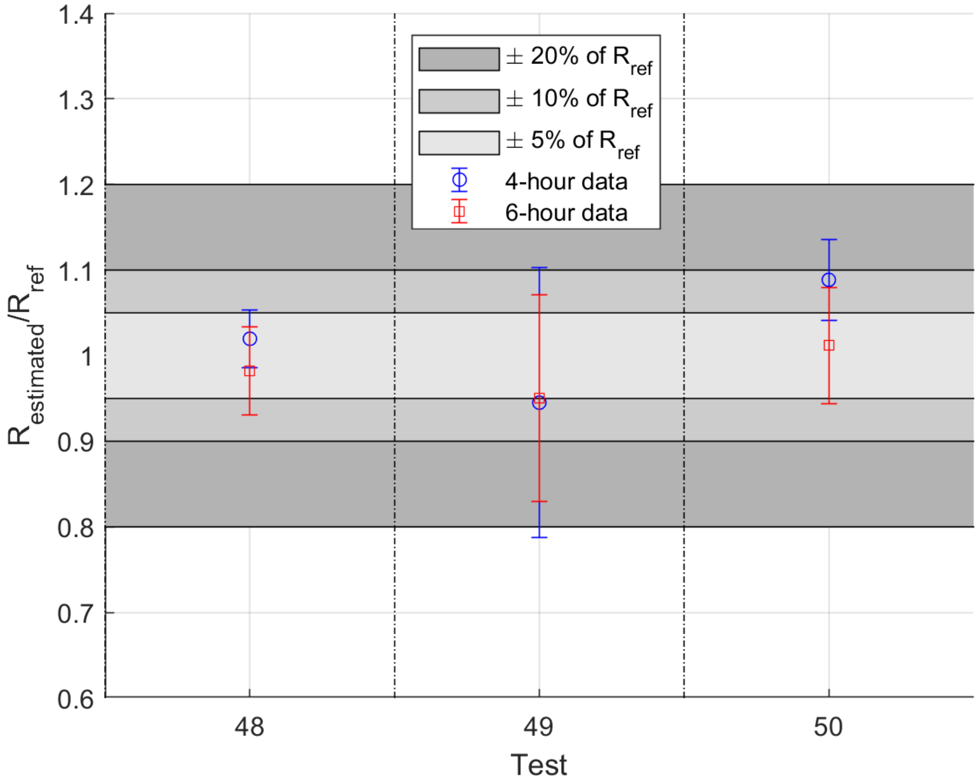

Figure 6.4: Estimated thermal resistances normalized by the reference value for the IWI tests with the fourth prototype under constant environmental conditions.

layer. On the other hand, test 9 on the external metal siding shows very stable thermal states. However, this quick evolution indicates that no thermal storage occurs and that the ventilated air gap diffuses 100% of the incoming heat flux. Besides, by removing the metal siding and installing the prototype directly on the insulation surface (Cf. Figure 5.18) for the tests 10 to 17, this wall becomes similar to the IWI case, with the same temperature evolution for the heating surface as observed in Figure 6.6).

Table 6.3 and Figure 6.7 present the estimated results for each test on this wall. As predicted in Chapter 3, the first two tests on the internal surface return a very small thermal resistance value. Moreover, the other very low resistance value obtained with the third test demonstrates that installing the measurement prototype on the external metal siding is not suitable to examine this wall due to the air gap.

The last eight measurements return a quasi-similar estimated value (around 3.4 $m^2 \cdot K/W$) after four hours of heating. These tests are carried out directly on the insulation surface (not on the internal coating as in the case of the IWI wall) so that the estimation result converges

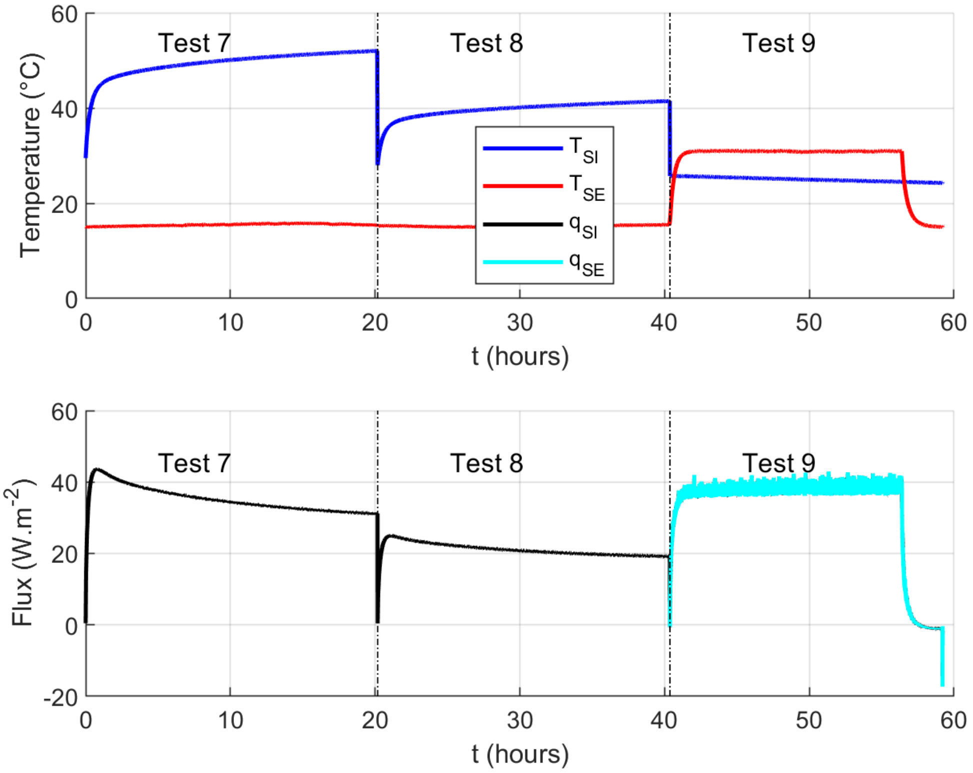

Figure 6.5: Measurement data of the EWI tests 7 to 9 under constant environmental conditions.

				Measurement duration (hours)		
Test	T_{aI}/T_{aE}	Power	Position	4	6	12
7	30°C/15°C	240 W (100%)	Internal surface	0.51 (0.02)	0.59 (0.01)	0.73 (0.01)
8	30°C/15°C	120 W (50%)	Internal surface	0.53 (0.02)	0.57 (0.01)	0.69 (0.01)
9	25°C/15°C	240 W (100%)	Metal siding surface	0.94 (0.01)	0.48 (0.07)	0.43 (0.01)
10	25°C/15°C	240 W (100%)	Ext. insulation surface	3.42 (0.01)	3.35 (0.03)	3.35 (0.01)
11	25°C/15°C	120 W (50%)	Ext. insulation surface	3.39 (0.01)	3.40 (0.01)	3.41 (0.01)
12	20°C/20°C	240 W (100%)	Ext. insulation surface	3.64 (0.02)	3.47 (0.09)	3.41 (0.05)
13	20°C/20°C	120 W (50%)	Ext. insulation surface	3.49 (0.04)	3.43 (0.08)	3.38 (0.04)
14	20°C/30°C	240 W (100%)	Ext. insulation surface	3.22 (0.10)	3.16 (0.04)	3.21 (0.04)
15	20°C/30°C	120 W (50%)	Ext. insulation surface	3.49 (0.03)	3.41 (0.02)	3.21 (0.06)
16	20°C/15°C	240 W (100%)	Ext. insulation surface	3.74 (0.04)	3.58 (0.08)	3.43 (0.02)
17	20°C/15°C	120 W (50%)	Ext. insulation surface	3.67 (0.04)	3.54 (0.03)	3.47 (0.02)

Table 6.3: Estimated thermal resistances and corresponding uncertainties (in m^2·K/W) for the EWI tests under constant environmental conditions.

faster than the IWI cases and does not change much if analyzing longer data. However, these obtained results are very far from the values of the GHB measurement R_{GHB} (Cf. Figure 6.7). The GHB device provided more heat flux with the same operating temperatures than with usual walls because of the presence of the metal frame inside the EWI wall, acting as thermal bridges.

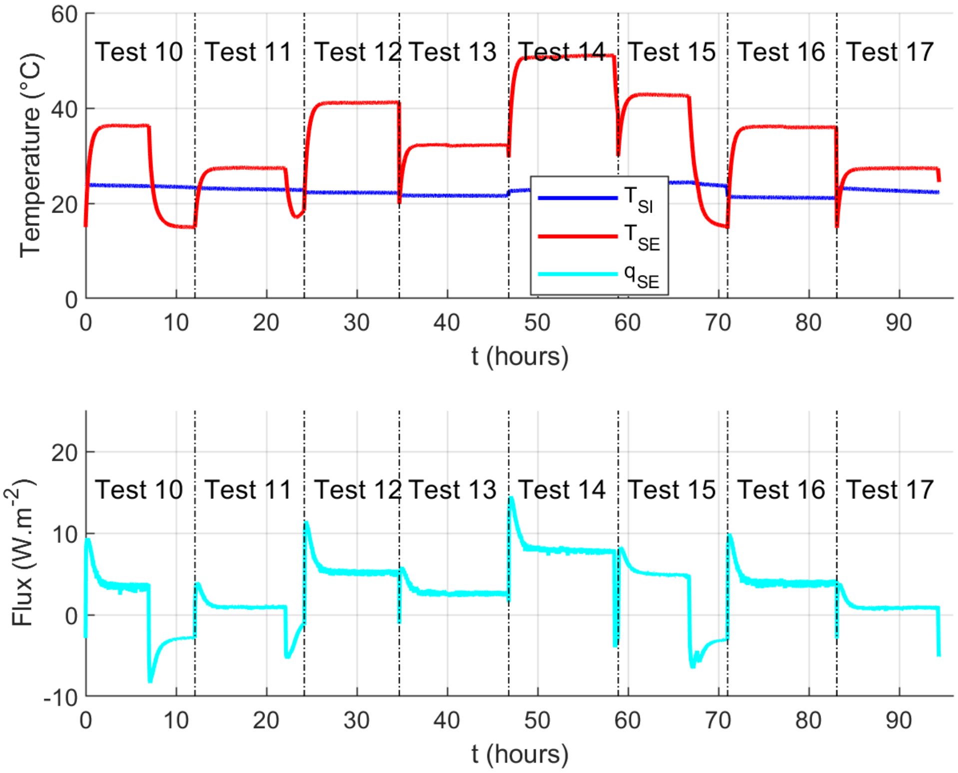

Figure 6.6: Measurement data of the EWI tests 10 to 17 under constant environmental conditions.

This decrease the thermal resistance measured with this method.

By taking into account the actual thickness of the insulation layer (0.15 m) and the thermal conductivity of the stone wool insulation (0.035 W/m·K, determined at 10°C by the Guarded Hot Plate at LNE and Hot Disk at CEREMA), the theoretical thermal resistance of this EWI wall (noted $R_{theoretical}$ in Figure 6.7) should be 4.29 m^2·K/W. However, the softness of the stone wool insulation may cause an error when measuring its thickness. The prototype must be pushed hardly to contact properly with the wall surface (without an air gap between the wall surface and the aluminum plate), then a thickness reduction of 2-3 cm may happen. This reduction in thickness could lead to a decrease of 0.6-0.9 m^2·K/W of the theoretical thermal resistance and a new theoretical value $R_{theoretical}$ between 3.48 m^2·K/W and 3.77 m^2·K/W.

Compared to $R_{theoretical}$, the estimated thermal resistance after 4 hours can be considered correct. According to Table 6.3, the estimated results respect the relationship between the thermal resistance and the operating temperatures as predicted: higher operating temperatures cause a decrease of the wall thermal resistance. Test 16, which has the smallest operating

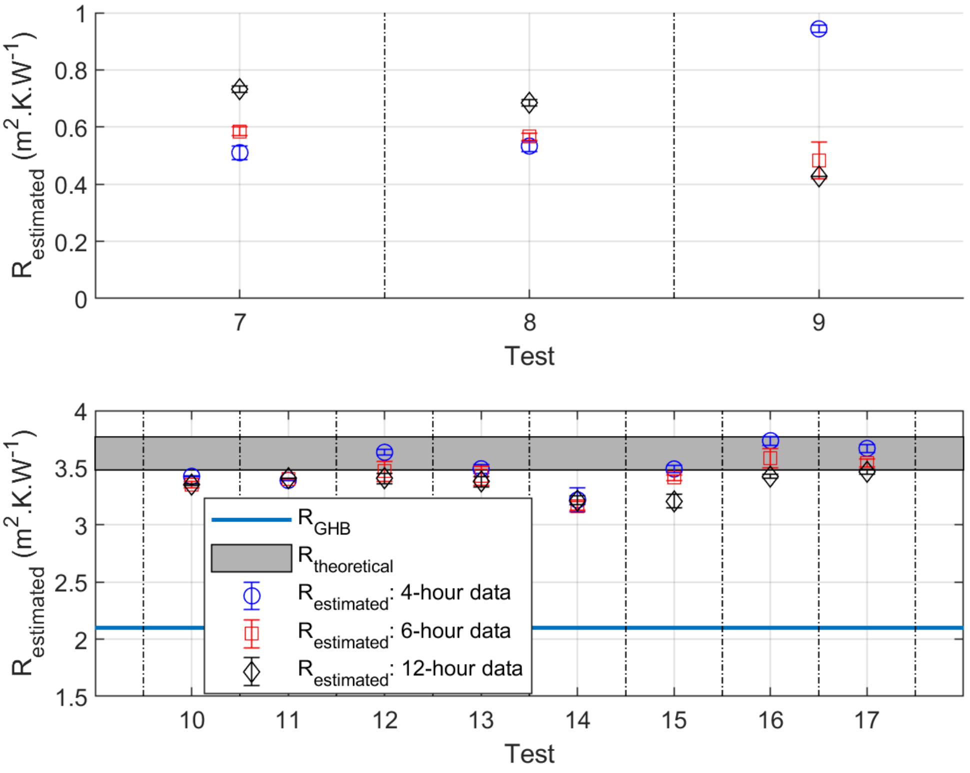

Figure 6.7: Estimated thermal resistances for the EWI tests with the third prototype under constant environmental conditions.

temperature, presents the highest estimated value. Conversely, the smallest thermal resistances are found for the test 14 under 20°C/30°C. Finally, for the majority of the tests 10 to 17, the same decrease in thermal resistance with the measurement time is observed as for the tests on the IWI wall.

Finally, in order to examine the EWI wall, the prototype should be installed on the insulation layer, as in the case of the IWI wall. Therefore, conclusions similar to those obtained for the IWI wall can be made for this wall in this configuration under constant conditions.

6.1.4 SW results

Figure 6.8 presents the measurement data on the SW wall with the third prototype under constant conditions performed at Sense-City (Cf. Table 5.4). The internal air temperature is regulated by an air conditioner installed on the wall opposite to the tested wall and operating from an On/Off control. This regulation mode explains the periodic perturbations of the internal surface temperature and internal absorbed heat flux observed in Figure 6.8, especially for tests

18 and 20 at maximum power. When the prototype is turned on, it heats both the tested surface and the surrounding environment, leading to a slight increase in the internal air temperature. So, the air conditioner is automatically turned on to cool the room. It is not ideal for testing because the amplitudes of these oscillations are quite important. However, the air conditioner is the only solution available to maintain a roughly constant temperature inside the tested building in Sense-City.

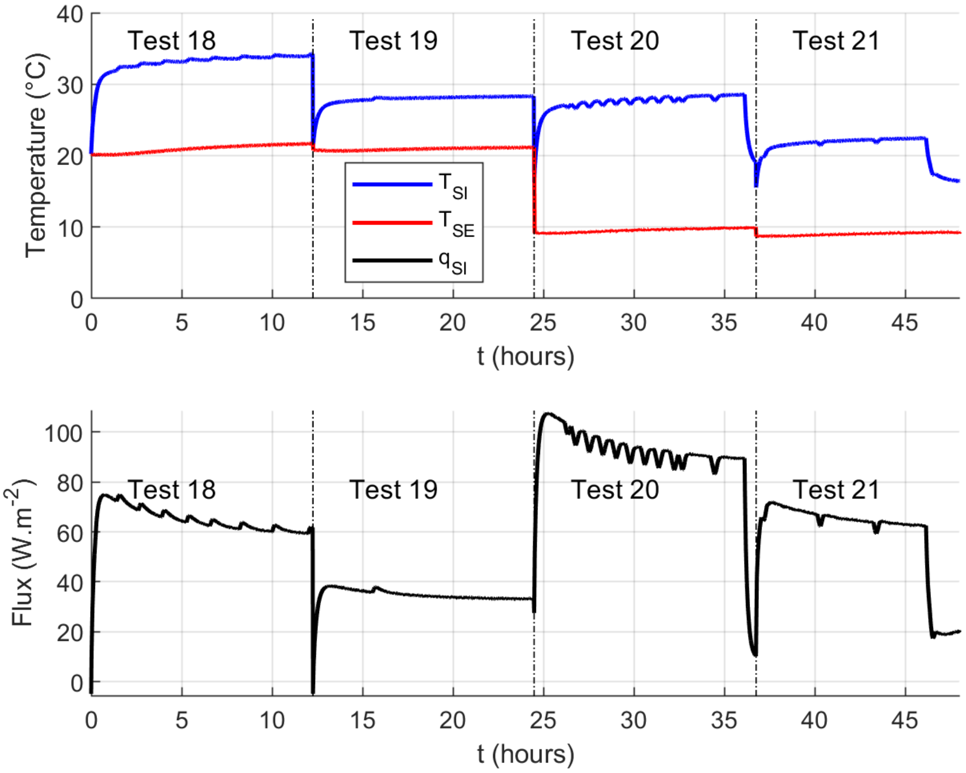

Figure 6.8: Measurement data of the SW tests 18 to 21 under constant environmental conditions.

Table 6.4 and Figure 6.9 present the estimation results of these tests and their corresponding uncertainties. According to these results, three out of four tests return an acceptable estimated thermal resistance with less than 0.05 m^2·K/W of difference compared to the reference one after 6 hours of heating. Only the test 18 (100% of heating power, under 20°C/20°C) shows an estimation result, which is two times larger than the expected value. This test produced the highest internal surface temperature. Thus, the air conditioner regulation was maximum during this test. Therefore, the measurement disturbance linked to the air conditioner was the most important in that case, which leads to a wrong estimation. Besides, the thermal inertia of this concrete wall being relatively low, the high external air temperature of tests 18 and 19 (20°C) significantly impacts the heat transfer through the wall. This is why the heating time must be longer for these tests than for the following tests 20 and 21, for which the temperature gradient between the inside and the outside helps the diffusion of the excitation heat flux.

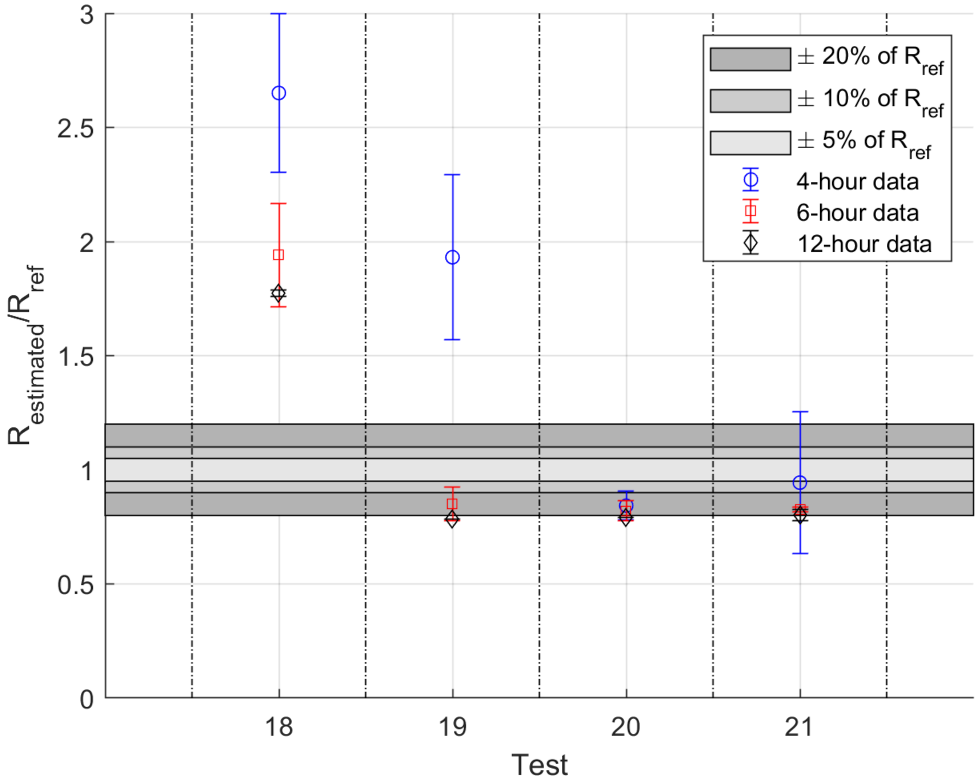

Figure 6.9: Estimated thermal resistances normalized by the reference value for the SW tests with the third prototype under constant environmental conditions.

As presented in Table 6.4, most of the obtained results are found within the 20% interval of the relative error compared to the reference value. This difference is equivalent to 0.05 m^2·K/W, which can be considered acceptable in the case of a non-insulated wall.

According to these tests, 6 hours of heating are sufficient to obtain good estimation results on that single wall. Moreover, the smallest heating power presents better results than the highest one because the internal regulation operates at a low speed with this heating level. However, this conclusion could probably be different if another type of indoor air temperature control system had been used.

6.1.5 WFW results

Figure 6.10 shows the measurement data of the five tests on the WFW wall with the third prototype at LNE under three different constant conditions (Cf. Table 5.4). According to the

				Measurement duration (hours)		
Test	T_{aI}/T_{aE}	Power	R_{ref}	4	6	12
18	20°C/20°C	240 W (100%)	0.25	0.663 (0.087)	0.485 (0.057)	0.444 (0.004)
19	20°C/20°C	120 W (50%)	0.25	0.483 (0.090)	0.213 (0.018)	0.196 (0.001)
20	20°C/5°C	240 W (100%)	0.25	0.211 (0.016)	0.205 (0.011)	0.198 (0.001)
21	20°C/5°C	120 W (50%)	0.25	0.236 (0.078)	0.207 (0.003)	0.201 (0.006)

Table 6.4: Estimated thermal resistances and corresponding uncertainties (in m^2·K/W) for the SW tests under constant environmental conditions (colors for the relative errors between $R_{estimated}$ and R_{ref}: out of 20%, 10-20%, 5-10%, <5%).

previous sections, the highest power provides the best estimation results (except for the SW tests at Sense-City due to the regulation system). Therefore, with this wall, only the heating power of 240 W is used for different constant conditions, except for the first two cases for which two heating levels are studied for the same configuration.

With the first two tests launched on the zone containing the thermal bridges (22 and 23), the surface temperature and absorbed heat flux values are much higher than for the last three cases tested in a homogeneous zone. Moreover, for these tests, internal surface temperature profiles show an increasing tendency, which is more important than the other three ones (Cf. Figure 6.5).

Figure 6.11 and Table 6.5 present the estimated thermal resistances and corresponding uncertainties for the five tests of this measurement series.

					Measurement duration (hours)		
Test	T_{aI}/T_{aE}	Power	Thermal bridge	R_{ref}	4	6	12
22	20°C/0°C	240 W (100%)	YES	7.60	1.45 (0.04)	1.70 (0.06)	1.86 (0.01)
23	20°C/0°C	120 W (50%)	YES	7.60	1.42 (0.03)	1.50 (0.03)	1.91 (0.02)
24	20°C/0°C	240 W (100%)	NO	7.60	3.38 (0.15)	3.40 (0.13)	3.59 (0.01)
25	30°C/10°C	240 W (100%)	NO	7.10	3.04 (0.23)	3.94 (0.09)	4.11 (0.04)
26	25°C/35°C	240 W (100%)	NO	6.70	3.54 (0.50)	3.55 (0.12)	3.80 (0.04)

Table 6.5: Estimated thermal resistances and corresponding uncertainties (in m^2·K/W) for the WFW tests under constant environmental conditions.

The results of the first two tests show clearly the effect of the thermal bridge. After 12 hours of measurement, only a small amount of the total thermal resistance is detected (around 25%). The thermal bridge influence is significant, as shown by the measurement data in Figure 6.10. This element disturbs the longitudinal diffusion of the excitation heat flux and accelerates the lateral one because of its high thermal conductivity. Therefore, to obtain a correct thermal

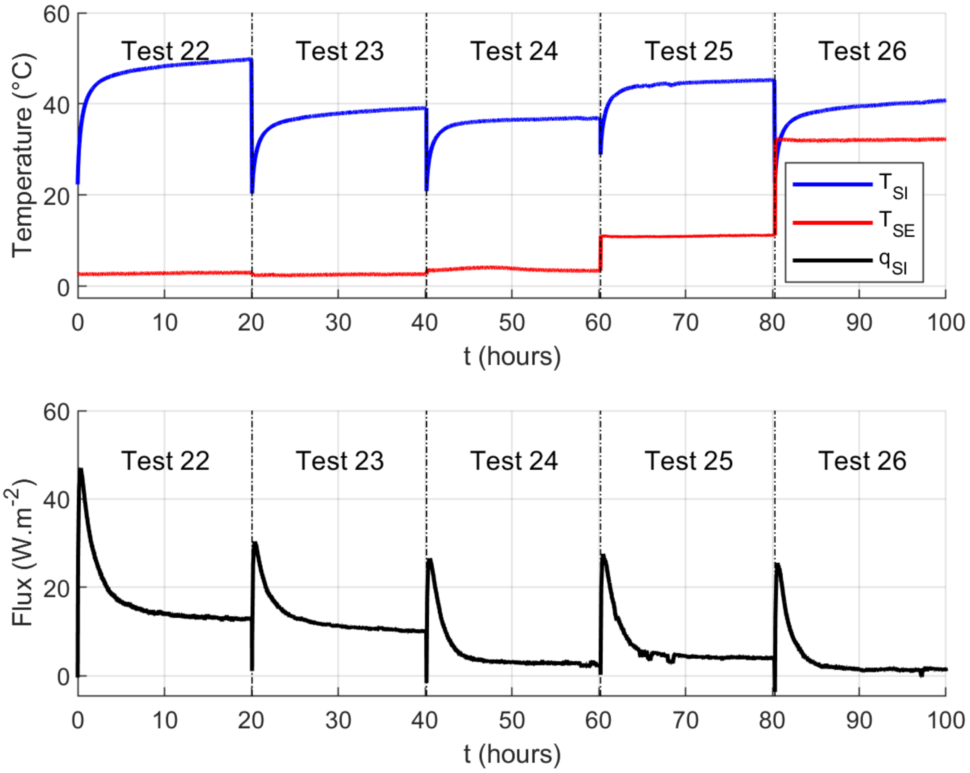

Figure 6.10: Measurement data for the WFW tests 22 to 26 under constant environmental conditions.

resistance evaluation, the thermal bridge should be avoided in the measurement area.

Besides, in the last three measurements, only half of the reference value is estimated. According to Section 5.2, this amount corresponds to the thermal resistance of the first insulation layer, so the second insulation layer is not characterized in these tests. To better understand the diffusion of heat flux inside the WFW wall during these tests, the thermal sensors measurement data integrated inside the wall are analyzed.

Figure 6.12 shows these measurement data during test 24. It indicates that there is no variation of heat flux observed in the second insulation layer. The OSB layer located between the two insulation layers diffuses mostly the heat flux from its internal surface. Therefore, the first layer is the only one that can be characterized with this configuration of WFW wall.

6.2 Measurement campaign no. 2: variable conditions

After testing our prototypes under constant conditions, variable conditions are used, and only the IWI and SW walls are investigated in this part.

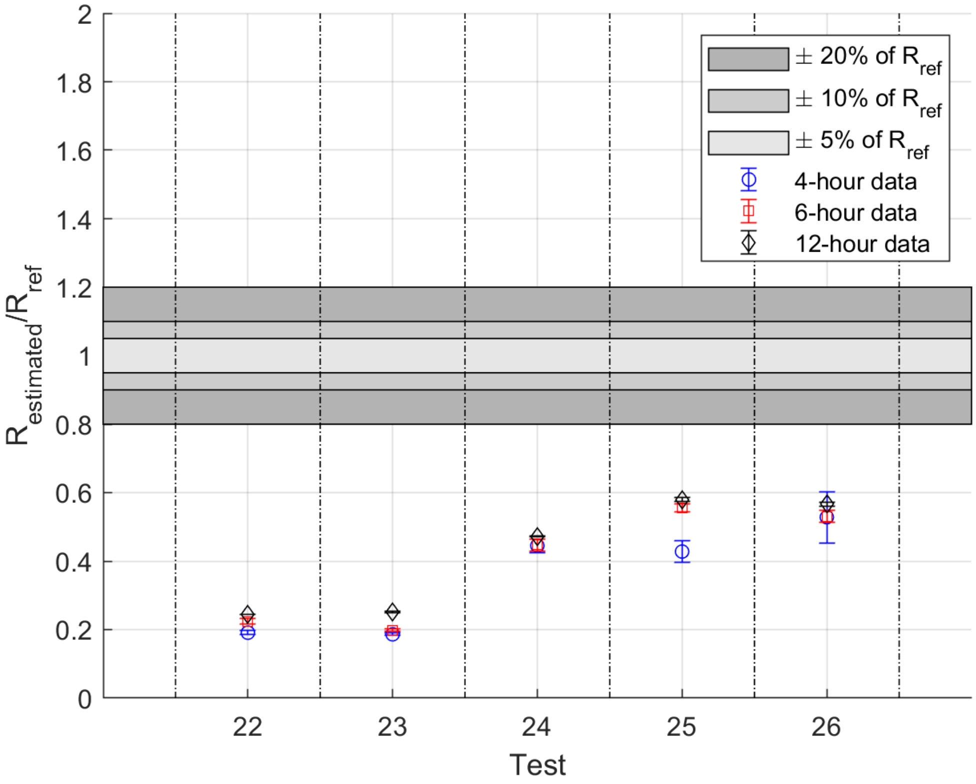

Figure 6.11: Estimated thermal resistances normalized by the reference value for the WFW tests under constant environmental conditions.

6.2.1 IWI results with the third prototype

The measurement data of the ten IWI tests under variable conditions at CEREMA (Cf. Table 5.5) with the third prototype are shown in Figure 6.13. At first sight, the variation of the external environment does not greatly influence the internal thermal states.

Figure 6.14 and Table 6.6 detail the estimation results of these tests. As observed in Table 6.6, all ten tests lead to estimation results located in a zone where the relative error is less than 10% with 4-hour and 6-hour measurement data, even with the "hot" external environment (tests 35-36). However, if the heating duration is longer, the estimated thermal resistance deviates from expected value.

This degradation of the estimation results has already been observed under constant conditions due to the lateral diffusion, but it is even more remarkable here. The variation of the external environmental conditions makes the heat transfer inside the tested wall more complex (mix of 1D and 3D fluxes), which directly affects the estimation results.

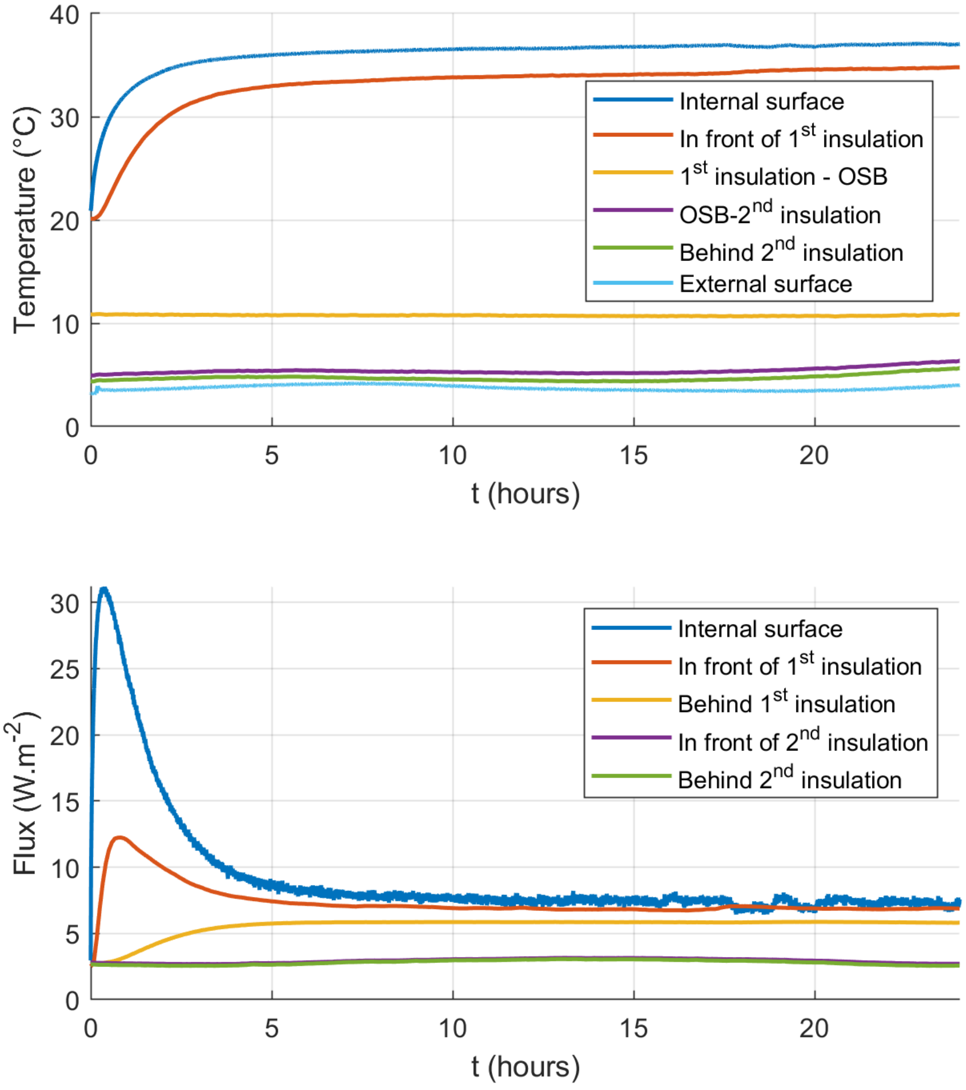

Figure 6.12: Measurement data of the thermal sensors installed inside the WFW wall during test 24.

Moreover, even both heating powers presents a good estimation with 4-hour measurement data, the use of the highest heating power seems to give better results than the lowest one under these conditions when observing the hourly estimation result profile of these tests in Appendix A4, except for test 34 for which the estimation value remains in the zone 10% but with large uncertainty. As mentioned in the IWI results under constant conditions, to obtain a good estimation result, the heating power should be important enough to eliminate the unwanted influence coming from the exterior. With the tests under variable conditions, most cases with 50% of heating power lead to an important variation of estimated thermal resistance with the heating duration.

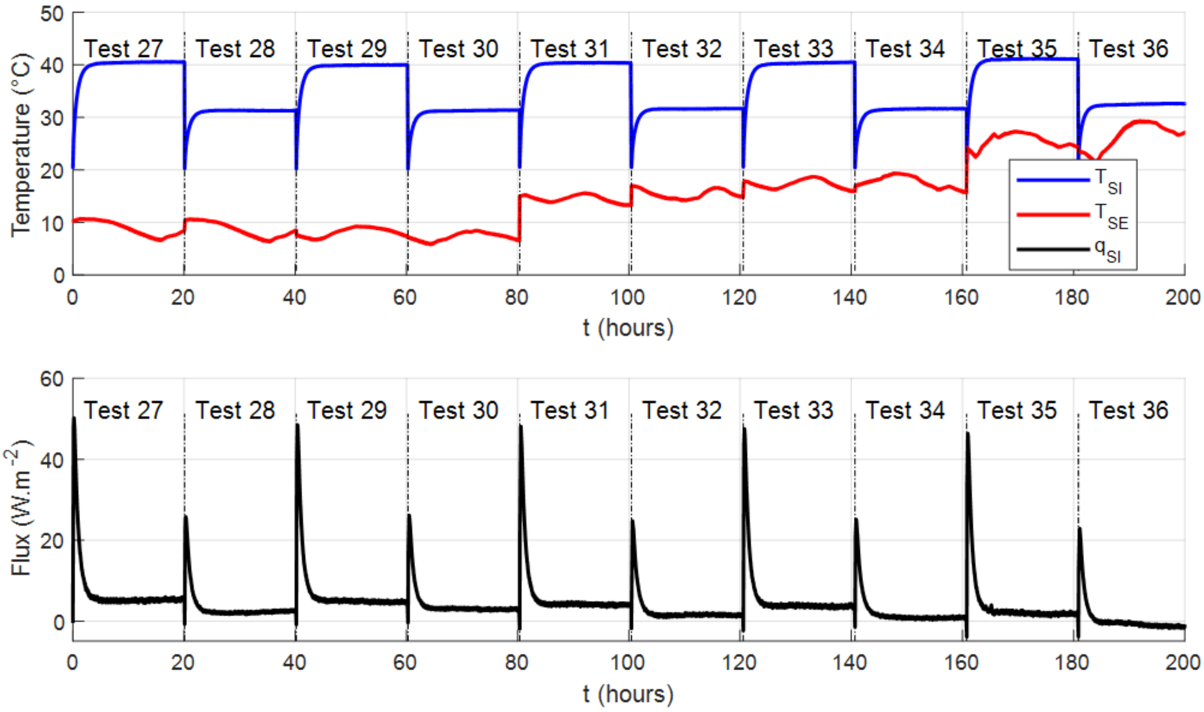

Figure 6.13: Measurement data for the IWI tests 27 to 36 with the third prototype under variable environmental conditions.

				Measurement duration (hours)		
Test	T_{aI}/T_{aE}	Power	R_{ref}	4	6	12
27	20°C/T-Var. 1	240 W (100%)	3.67	3.76 (0.05)	3.69 (0.01)	3.72 (0.02)
28	20°C/T-Var. 1	120 W (50%)	3.67	3.70 (0.01)	3.79 (0.08)	4.14 (0.10)
29	20°C/T-Var. 2	240 W (100%)	3.68	3.52 (0.29)	3.48 (0.14)	3.30 (0.16)
30	20°C/T-Var. 2	120 W (50%)	3.70	3.66 (0.18)	3.61 (0.01)	3.33 (0.17)
31	20°C/T-Var. 3	240 W (100%)	3.58	3.33 (0.01)	3.35 (0.05)	3.33 (0.17)
32	20°C/T-Var. 3	120 W (50%)	3.58	3.68 (0.14)	3.92 (0.01)	4.07 (0.01)
33	20°C/T-Var. 4	240 W (100%)	3.54	3.52 (0.01)	3.44 (0.01)	3.37 (0.07)
34	20°C/T-Var. 4	120 W (50%)	3.53	3.73 (0.10)	3.73 (0.01)	3.83 (0.07)
35	20°C/T-Var. 5	240 W (100%)	3.45	3.30 (0.01)	3.11 (0.47)	3.81 (0.19)
36	20°C/T-Var. 5	120 W (50%)	3.45	3.56 (0.01)	3.50 (0.03)	3.03 (0.03)

Table 6.6: Estimated thermal resistances and corresponding uncertainties (in m^2·K/W) for the IWI tests with the third prototype under variable environmental conditions (colors for the relative errors between $R_{estimated}$ and R_{ref}: out of 20%, 10-20%, 5-10%, <5%).

6.2.2 IWI results with the fourth prototype

Figure 6.15 shows the measurement data of the IWI tests with the fourth prototype obtained at CEREMA under variable conditions (Cf. Table 5.7). Observations similar to those obtained with the third prototype concerning the external environment's influence on the internal

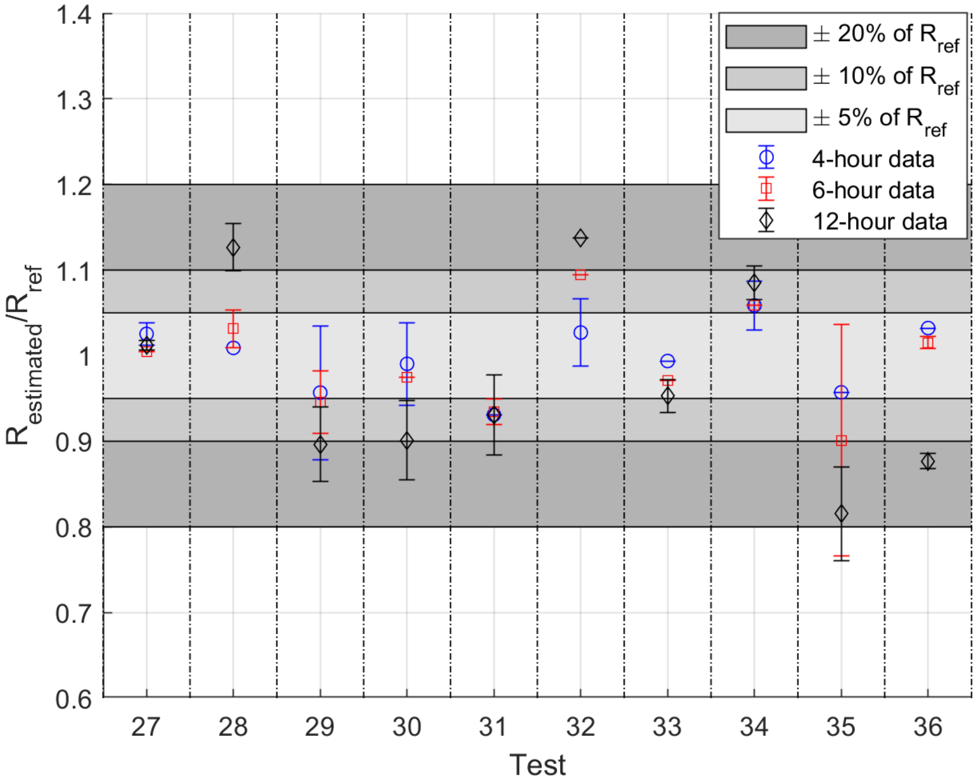

Figure 6.14: Estimated thermal resistances normalized by the reference value for the IWI tests with the third prototype under variable environmental conditions.

environment are obtained. Five quasi-identical internal surface temperature profiles are found with the first five tests 51 to 55 (constant internal air temperature and variable external air temperature). On the other hand, the variation of the internal air temperature greatly changes these data (tests 56 to 59).

Figure 6.16 and Table 6.7 detail the estimation results of these tests after analyzing 4-hour and 6-hour data sets.

The results of the first five tests (constant internal air temperature) show for each case a good estimation capability of this prototype, like when using the third one. When the interior temperature varies, 6 hours are needed to converge to a good estimated thermal resistance with this IWI wall for the tests 56 and 57. However, this is not sufficient for tests 58 and 59 (Cf. Figure 6.17). The difference between these two pairs of tests comes from the direction of variation of the external air temperature. This temperature decreases during tests 56 and 57 while it increases during tests 58 and 59. Thus, these last two tests are less favorable to the diffusion of the excitation heat flux through the wall and require a longer heating time to obtain

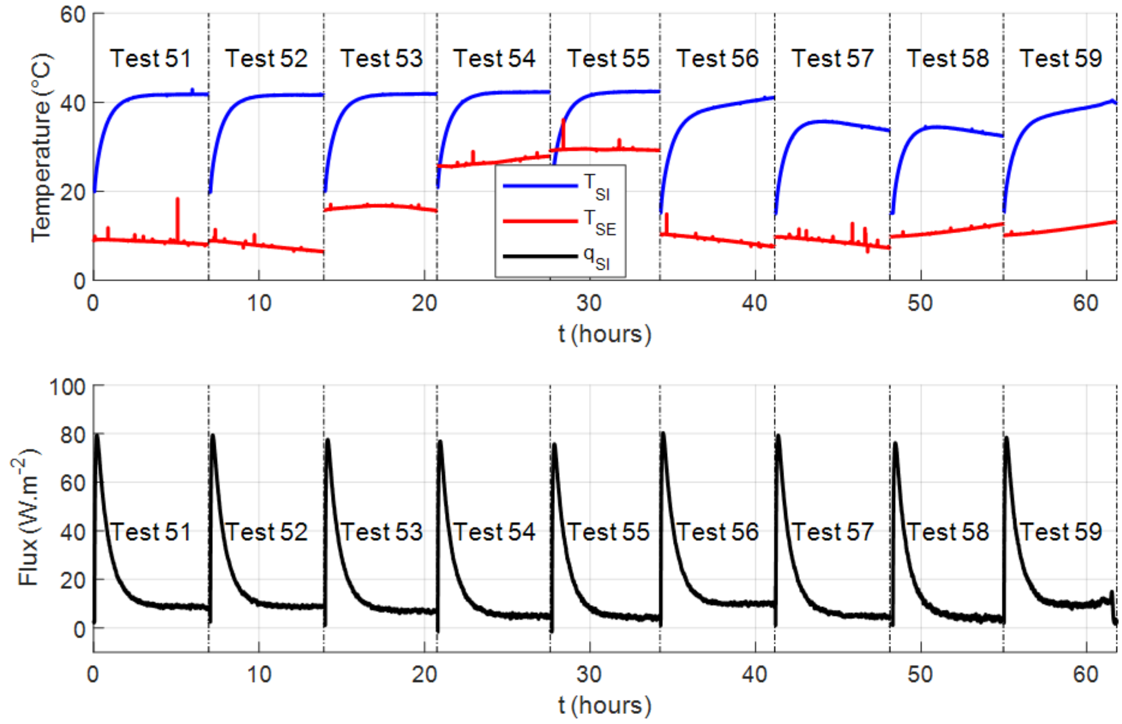

Figure 6.15: Measurement data for the IWI tests 51 to 59 with the fourth prototype under variable environmental conditions.

a satisfactory wall thermal resistance value.

There are two reasons for these results: the interior-exterior temperature gradient and the external air temperature variation. As mentioned in Chapter 1, the interior-exterior temperature gradient should be important during measurement. Then, test 58, whose temperature gradient decreases, may not be an excellent configuration. Besides, heating the external surface during the measurement is not recommended because it will create the secondary heat flux opposite to the excitation heat flux. So, tests 58 and 59 with the mix of these heat fluxes require more time to converge to an acceptable result.

6.2.3 SW results

Figure 6.18 shows the measurement data of the SW tests with the third prototype at Sense-City under variable conditions (Cf. Table 5.5). Temperature regulation inside the building only ensures a quasi constant internal air temperature. However, as presented in the previous chapter, the climatic chamber Sense-City allows controlling the external air temperature and adding artificial solar radiation on the wall's external surface. These tests are based on the same

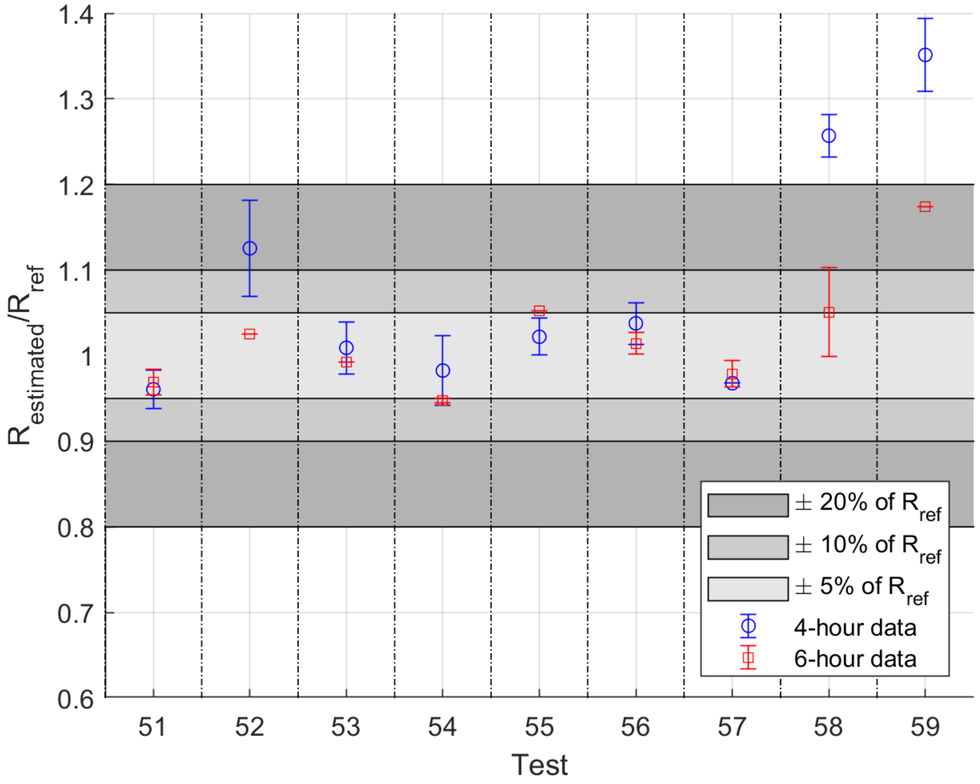

Figure 6.16: Estimated thermal resistances normalized by the reference value for the IWI tests with the fourth prototype under variable environmental conditions.

			Measurement duration (hours)	
Test no.	T_{aI}/T_{aE}	R_{ref}	4	6
51	20°C/T-var. 7	3.65	3.51 (0.08)	3.54 (0.06)
52	20°C/T-var. 8	3.65	4.11 (0.20)	3.74 (0.01)
53	20°C/T-var. 9	3.57	3.60 (0.11)	3.54 (0.01)
54	20°C/T-var. 10	3.40	3.34 (0.14)	3.22 (0.01)
55	20°C/T-var. 11	3.44	3.52 (0.07)	3.62 (0.01)
56	Tint-var. 1/T-var. 12	3.72	3.86 (0.09)	3.77 (0.05)
57	Tint-var. 2/T-var. 12	3.72	3.60 (0.01)	3.64 (0.06)
58	Tint-var. 2/T-var. 13	3.72	4.68 (0.09)	3.91 (0.19)
59	Tint-var. 1/T-var. 13	3.72	5.03 (0.16)	4.37 (0.01)

Table 6.7: Estimated thermal resistances and corresponding uncertainties (in m^2·K/W) for the IWI tests with the fourth prototype under variable environmental conditions (colors for the relative errors between $R_{estimated}$ and R_{ref}: out of 20%, 10-20%, 5-10%, <5%).

external temperature variation. However, the last two ones involve a small amount of solar radiation provided by a powerful lamp system at the ceiling of the climatic chamber. Therefore, for these last two tests, the increase of external surface temperature is greater than for the first two ones. Moreover, it can be noticed that the fluctuations due to temperature regulation inside

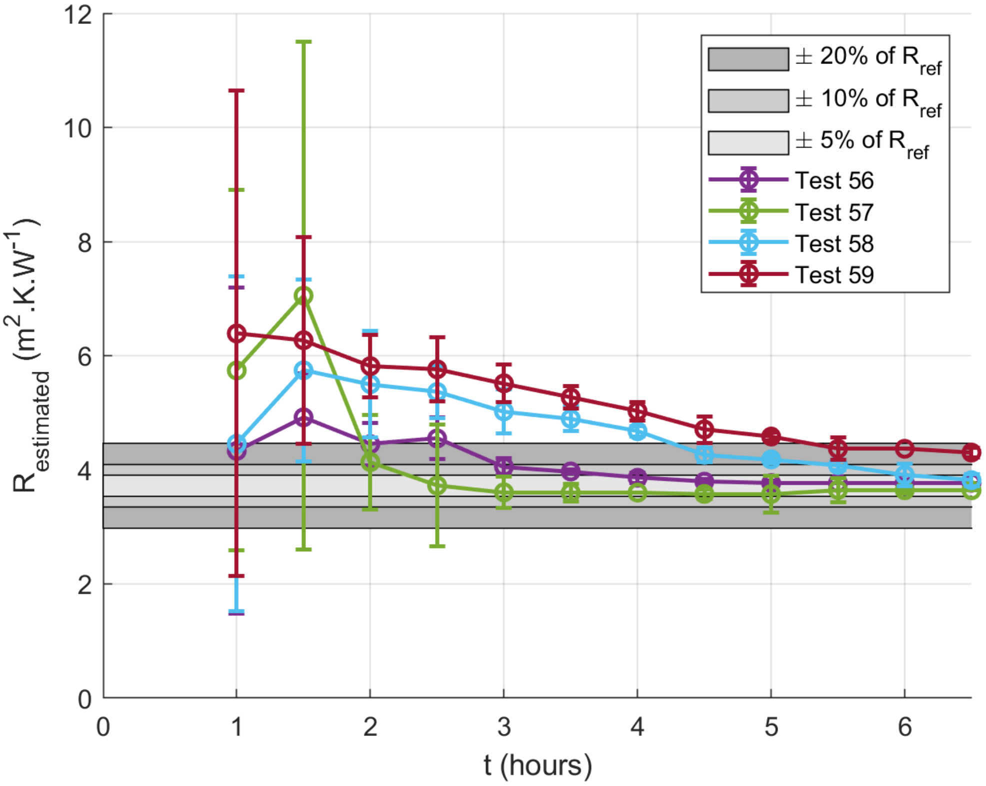

Figure 6.17: Estimated thermal resistance according to the heating time for IWI tests 56 to 59.

the building under variable conditions are more important here than under constant conditions.

The detailed estimation results are described in Figure 6.19 and Table 6.8. The estimation model quickly detects the value of the wall thermal resistance for each test, except for test 38, for which the estimation result is too large compared to the expected value. As observed in Figure 6.18, the signal to noise ratio of the measurements in test 38 is the lowest of the four tests, which could explain this incorrect estimation result. Consequently, the uncertainty values are higher for this test.

Besides, the last two cases with small solar radiation show a good estimation after 4 hours of heating. The estimated thermal resistance is still correct until 6 hours of measurement but becomes unstable for longer duration (Cf. Figure 6.20). This observation may be explained by two factors: the strong regulation of the internal temperature and the concrete wall's weak thermal inertia. Before 6 hours, the estimation model can follow the temperature regulation, the heating zone remains quite insulated, and the disturbances from other tested room areas are not significant. However, after several hours of global heating due to artificial solar radiation and the heat source of the measurement prototype, these disturbances become stronger. Due to

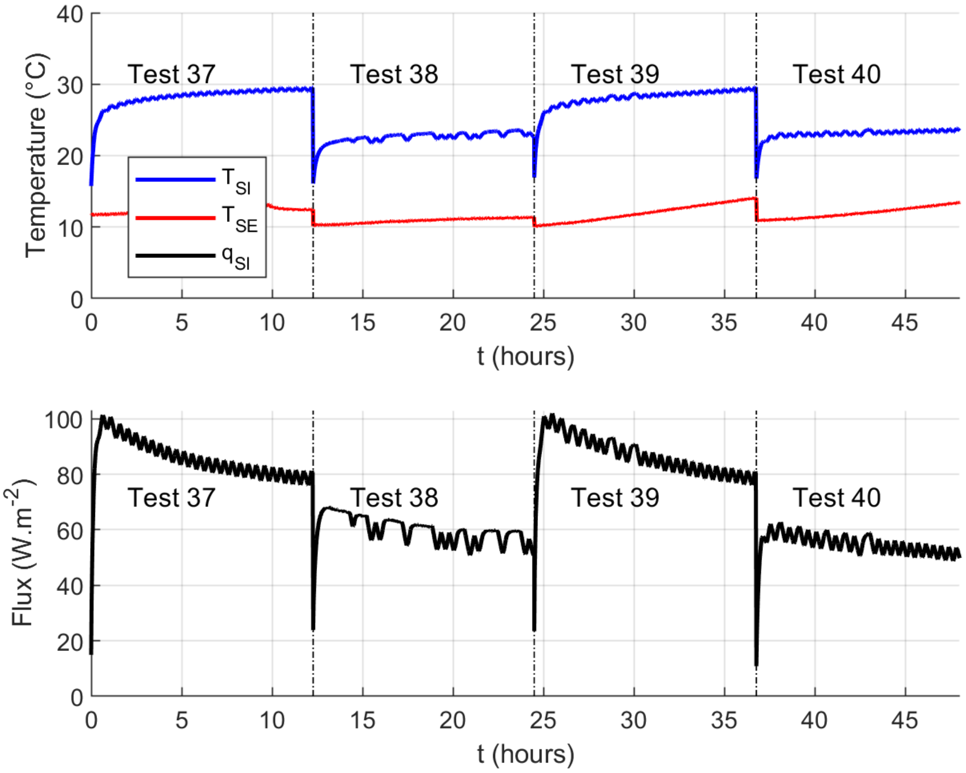

Figure 6.18: Measurement data for the SW tests 37 to 40 under variable environmental conditions.

the concrete wall's weak thermal inertia, these phenomena rapidly affect the measurement data and make it difficult to fit the estimation model output to the minimization data. As observed in Appendix A4, the residuals of these tests become stronger after 6 hours of measurement. Then, it leads to a divergence of the estimated thermal resistance since this measurement duration.

					Measurement duration (hours)		
Test	T_{aI}/T_{aE}	Power	Solar rad.	R_{ref}	4	6	12
37	20°C/T-Var. 6	240 W (100%)	0	0.25	0.230 (0.023)	0.184 (0.002)	0.198 (0.007)
38	20°C/T-Var. 6	120 W (50%)	0	0.25	0.621 (0.041)	0.343 (0.041)	0.285 (0.014)
39	20°C/T-Var. 6	240 W (100%)	S-Var. 1	0.25	0.253 (0.005)	0.248 (0.005)	0.313 (0.006)
40	20°C/T-Var. 6	120 W (50%)	S-Var. 1	0.25	0.246 (0.002)	0.236 (0.013)	0.209 (0.001)

Table 6.8: Estimated thermal resistances and corresponding uncertainties (in m^2·K/W) for the SW tests with the third prototype under variable environmental conditions (colors for the relative errors between $R_{estimated}$ and R_{ref}: out of 20%, 10-20%, 5-10%, <5%).

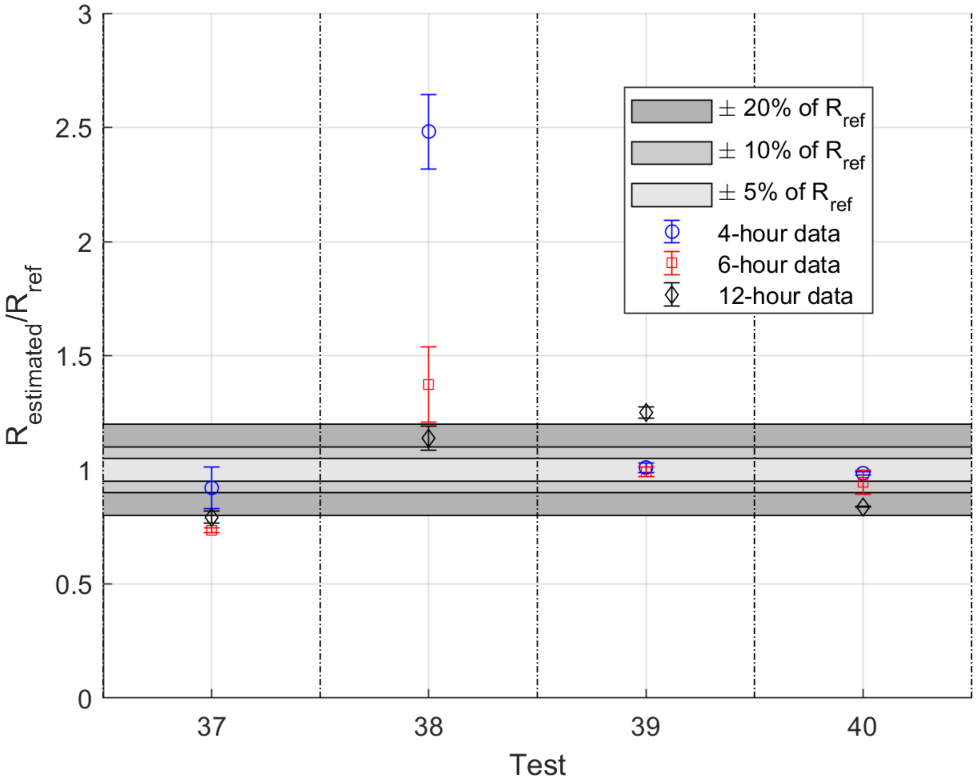

Figure 6.19: Estimated thermal resistances normalized by the reference value for the SW tests with the third prototype under variable environmental conditions.

6.3 Measurement campaign no. 3: natural conditions

The previous section showed that two prototypes developed in this study are efficient in estimating the thermal resistance of the IWI and SW walls when testing under variables conditions controlled in climatic chambers. Therefore, these two types of wall are examined here under natural conditions for which the solar radiation can sometimes be very high.

6.3.1 IWI results

Figure 6.21 shows the measurement data obtained during the IWI tests with the third prototype at CEREMA under natural conditions: two with solar protection (tests 44 and 45) and three others without (tests 41 to 43). It should be noted here that when using the climatic chamber in natural mode at CEREMA, the evaporator is regulated two times a day so that a sudden change in the measurement data is observed for all five tests. However, the estimation model in this study works on the absorbed flux. If there is a change in the testing environment, the model will follow this variation correctly. Therefore, this regulation should not have much

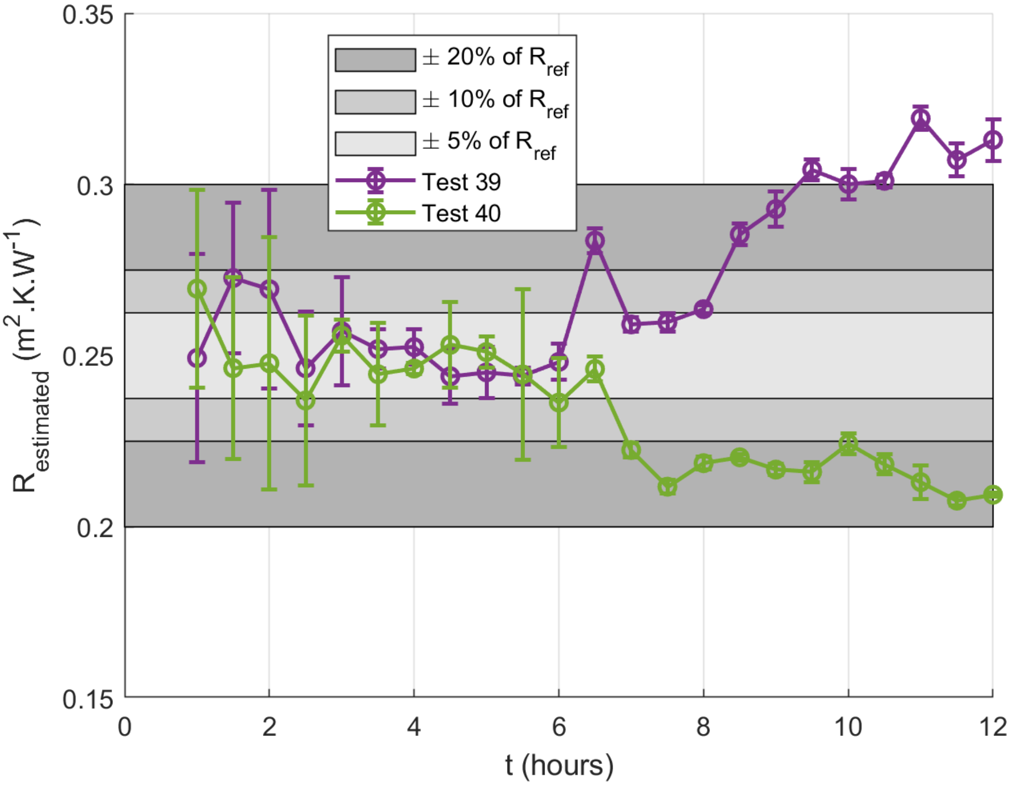

Figure 6.20: Estimated thermal resistance according to the heating time for SW tests 39 and 40.

influence on the estimation results. To validate this hypothesis, test 43 is carried out with a regulation change occurring much later than for tests 41 and 42.

The estimation results of this series of measurements are presented in Figure 6.22 and Table 6.9. When considering the tests without solar protection (no. 41 to 43), the estimation results are far from the reference resistance. Comparing the results of tests 41 and 43 (same heating power) shows that the change in regulation is probably not the cause of these bad estimations. These unsatisfactory estimation results have their origin in the influence of solar radiation. The observation of Figure 5.23 shows that the solar radiation measured on the external surface of the tested wall is much higher than the excitation heat flux (Cf. Figure 6.21). It can be considered as a second thermal source supplying heat from the exterior. Therefore, it directly disturbs the thermal diffusion inside the wall, and the 1D direct model used in the estimation is no longer suitable.

On the contrary, the two tests using the local solar protection return a good estimation after 6 hours of measurement. This protection avoids the strong disturbance due to the solar radiation on the testing area so that the estimation in 1D is still valid. According to these results,

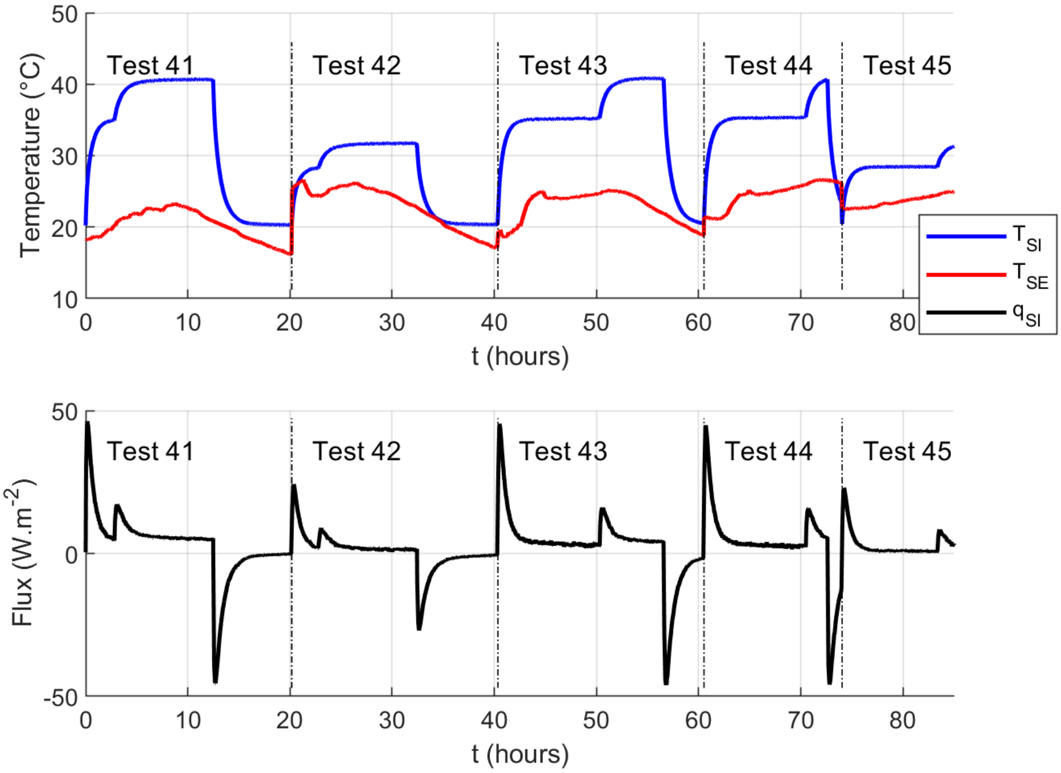

Figure 6.21: Measurement data for the IWI tests under natural environmental conditions.

the protection of 60×60 cm^2 is enough, instead of completely covering the external surface.

					Measurement duration (hours)		
Test	T_{aI}/T_{aE} /q_{solar}	Power	Solar prot.	R_{ref}	4	6	12
41	20°C/T-Rea. 1 /S-Rea. 1	240 W (100%)	NO	3.45	3.91 (0.07)	4.36 (0.24)	4.48 (0.03)
42	20°C/T-Rea. 2 /S-Rea. 2	120 W (50%)	NO	3.45	15.13 (0.73)	10.41 (1.91)	9.31 (0.09)
43	20°C/T-Rea. 3 /S-Rea. 3	240 W (100%)	NO	3.45	5.86 (0.19)	6.03 (0.01)	6.28 (0.06)
44	20°C/T-Rea. 4 /S-Rea. 4	240 W (100%)	YES	3.45	4.03 (0.11)	3.42 (0.06)	3.07 (0.01)
45	20°C/T-Rea. 5 /S-Rea. 5	120 W (50%)	YES	3.45	3.44 (0.30)	3.33 (0.06)	3.07 (0.08)

Table 6.9: Estimated thermal resistances and corresponding uncertainties (in m^2·K/W) for the IWI tests with the third prototype under natural environmental conditions (colors for the relative errors between $R_{estimated}$ and R_{ref}: out of 20%, 10-20%, 5-10%, <5%).

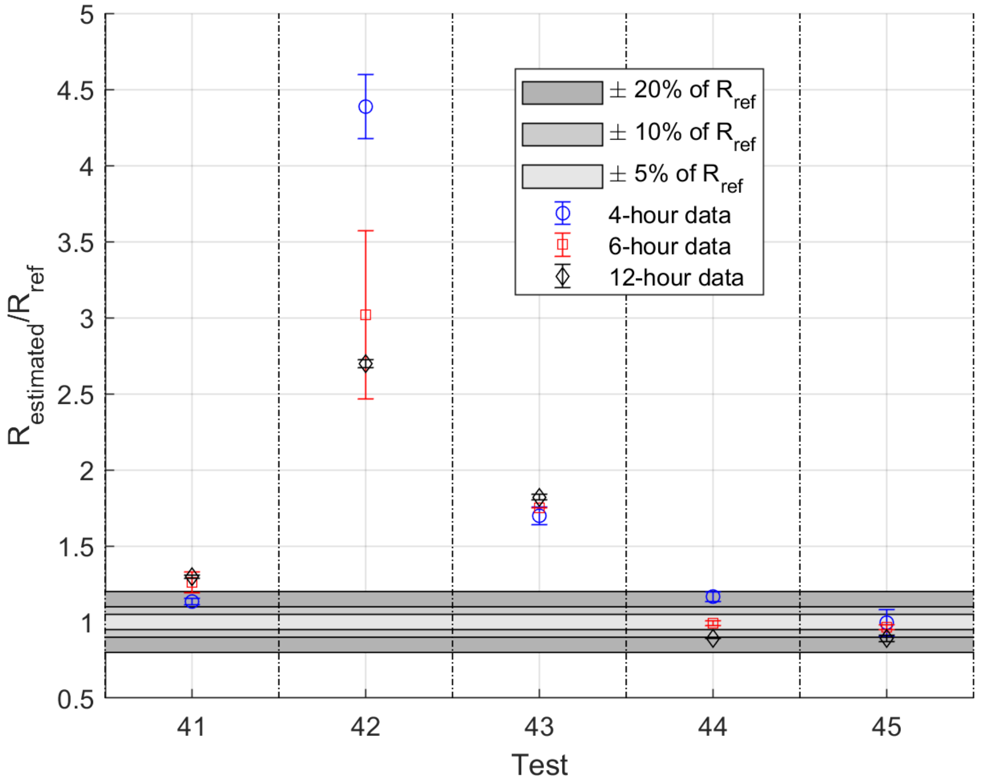

Figure 6.22: Estimated thermal resistances normalized by the reference value for the IWI tests with the third prototype under natural environmental conditions.

6.3.2 SW results

The measurement data of the SW tests with the third prototype at Sense-City under natural conditions are presented in Figure 6.23. No solar protection is used in these cases. The data sets are quite similar to the previous tests performed on this wall.

Figure 6.24 and Table 6.10 show the estimated thermal resistances obtained for these tests. None of them provides an acceptable result. The SW wall contains only a concrete layer whose thermal inertia is quite weak. Thus, significant solar radiation has a rapid impact through the wall thickness. Therefore, these measurements are less suitable to a correct estimation than those with the IWI wall. Moreover, these estimation results would be even worse if these tests had been carried out in summer. So, it appears that solar protection is essential for this type of wall under natural environmental conditions.

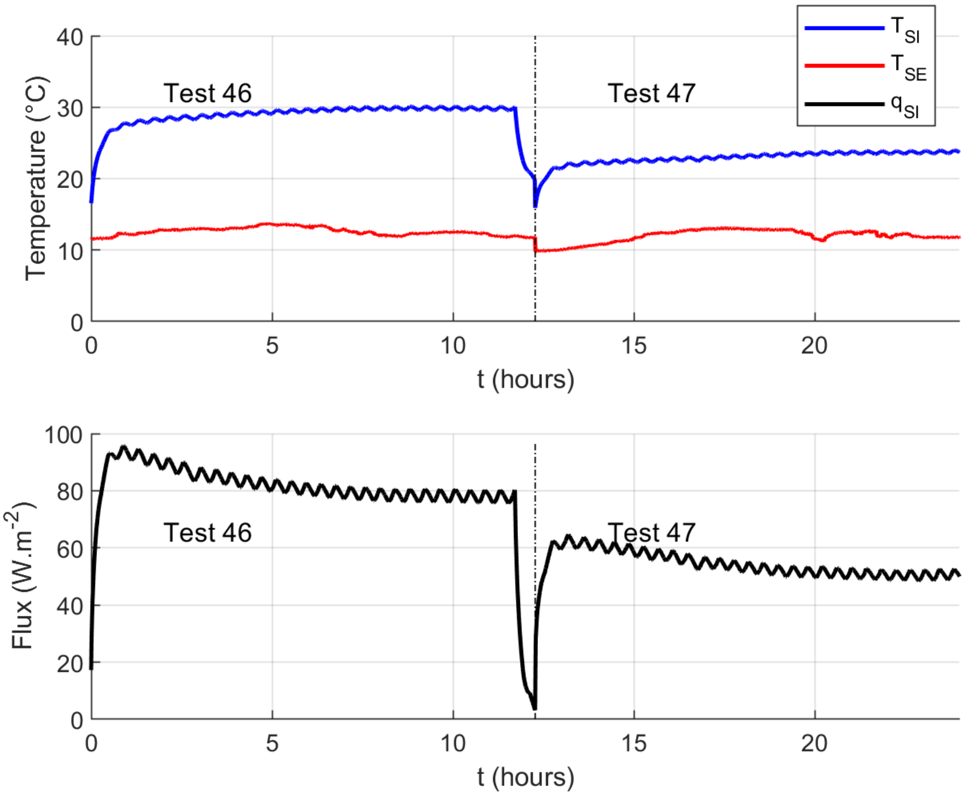

Figure 6.23: Measurement data for the SW tests under natural environmental conditions.

				Measurement duration (hours)		
Test	T_{aI}/T_{aE} /q_{solar}	Power	R_{ref}	4	6	12
46	20°C/T-Rea. 6 /S-Rea. 6	240 W (100%)	0.25	0.782 (0.047)	8.559 (3.341)	13.524 (7.270)
47	20°C/T-Rea. 7 /S-Rea. 7	120 W (50%)	0.25	0.512 (0.015)	0.557 (0.012)	1.070 (0.059)

Table 6.10: Estimated thermal resistances and corresponding uncertainties (in $m^2 \cdot K/W$) for the SW tests with the third prototype under natural environmental conditions.

6.4 Conclusions

These fifty-nine different measurement configurations on four walls among the most common in France demonstrate the third prototype's ability to estimate the thermal resistance of a wall under different environmental conditions. The estimation results obtained with this prototype are generally quite close to those resulting from standard methods. Moreover, 6 hours of measurement is likely to be sufficient with the proposed active method, while several days are needed with a passive method.

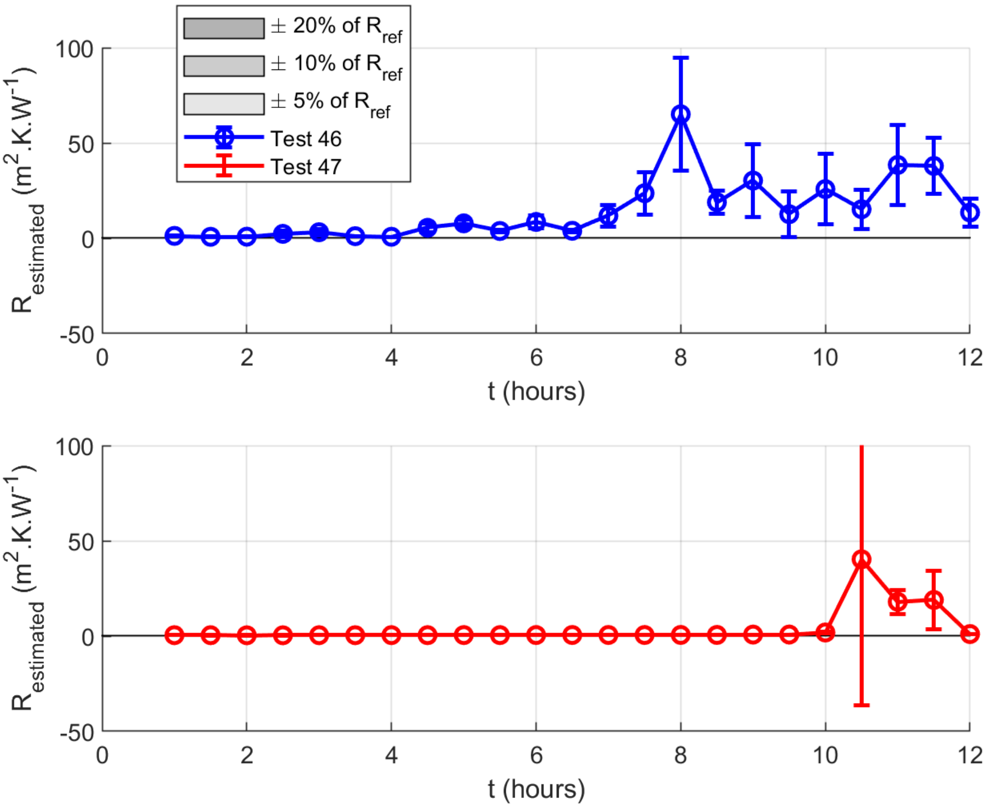

Figure 6.24: Estimated thermal resistance according to the heating time for SW tests 46 and 47.

These measurement results show that it is possible to estimate the wall thermal resistance correctly if the heating source and the insulation layer are on the same side of the wall (IWI wall when heating from the interior or EWI wall when heating from the exterior without metal siding). Moreover, if there is a diffusive layer inside the insulation layer (WFW case), only the thermal resistance from the heating surface to this diffusive layer can be estimated. Moreover, the strong heating power is recommended in order to eliminate the unwilling influences coming from the surrounding environment.

Therefore, several recommendations must be followed in order to obtain a correct estimation:

- The prototype must be installed on the same side of the wall as the insulation layer in the case of an IWI wall or EWI wall. It means that the insulation layer (with or without a coating) must be the first one heated in the wall. This recommendation does not concern the case of a single wall (or concrete wall).

- The plate of the fourth prototype should be covered by a closed box (made of plastics, for example) to protect the source and sensors from the unwilling influences coming from the environment in the testing room.

- All thermal bridges should be avoided. Therefore, a qualitative analysis using an IR camera, for instance, of the tested wall constitution is required to determine a suitable testing zone.

- The use of local solar protection on the tested wall external surface is recommended to prevent strong solar radiation when testing in the daytime. Its size should be more or less equal to 60×60 cm^2, and it should be installed at the same position as the prototype on the internal side. If it is impossible to install this protection, the measurement should be carried out during night time to avoid the solar radiation influence.

- If there is a diffusive layer inside the insulation layer (for example, the OSB sheathing layer in the WFW wall), only the part of the wall limited by this layer and the location of the prototype can be characterized because the heat flux diffuses laterally on this layer. Only a passive method, which is not concerned with lateral diffusion, may be used with this wall type.

Similar conclusions can be drawn from the use of the fourth prototype. The estimation results obtained with this prototype show good accuracy with the IWI wall after 6 hours of heating. However, there are special cases with a variation of the interior air temperature, requiring more tests to conclude on its estimation ability under this type of condition.

7 Conclusions and perspectives

The study proposed in this Ph.D. thesis has focused on the development of a novel measurement prototype to estimate the thermal resistance of an opaque wall under various conditions. The main objective was to reduce the measurement duration, which is several days for the existing techniques, without losing the computed thermal resistance accuracy. Moreover, this prototype should be usable at any time of the year and easily transportable and handled by professionals.

The literature review showed several ways to estimate a wall thermal resistance, *i.e.*, by using passive and active methods. The passive methods are the simplest techniques (installation, computation, etc.) and applicable to all wall types. However, they require several strict environmental conditions to obtain a correct thermal resistance. Some studies enhanced these techniques by considering environmental condition variations into the thermal resistance computation, but the measurement duration remains quite long. Besides, the active methods, which use an artificial thermal excitation source to create the optimal conditions, reduce significantly the measurement time by considering the tested wall's dynamic regime. Nevertheless, these methods need a physical model to simulate this dynamic regime and a least-square minimization algorithm to estimate the unknown parameters, which makes this approach more complex than the passive one. After a comparative analysis between the two methods, the active one was chosen because of its advantage in measurement duration.

The thermal quadrupole method was studied to be used as the physical model in the thermal resistance estimation process. By comparing with the COMSOL Multiphysics® commercial software, this method provided similar results for the computation of the heat transfer involved in a wall for a shorter computation time than that obtained with COMSOL. Two models were proposed in this study using different boundary conditions: Excitation With Convection (EWC) and Absorbed Flux (AbF) models. For the EWC model, the convection and the thermal excitation are both considered on the tested internal wall surface in computations (in 1D, 2D, and 3D). So, the convective heat transfer coefficient is needed. However, the model is very sensitive to this coefficient. Moreover, the heat exchange coefficient is not easy to determine experimentally. On the contrary, only the absorbed flux, which is a combination of the exchange by convection and the thermal excitation, is taken into account in the AbF model as the boundary condition on the internal wall surface. Therefore, the most sensitive parameter is eliminated. On the other hand, only the 1D AbF model is available because of mode complexity and long computation time when working with the 2D or 3D absorbed heat flux.

The wall thermal resistance is obtained by minimizing a least-square function between the measurement and model data. Several minimization algorithms were analyzed through a comparative study. The Robust Adaptive Metropolis method based on a Bayesian approach was selected because of its strong estimation ability (estimated value and uncertainty). In this identification process, the estimated parameters are the thermal effusivity and the time constant of each layer of the investigated wall. The advantage of using this representation is that these parameters are separated inside and outside the hyperbolic function in the thermal quadrupole formulation. Moreover, there are only two parameters to be estimated for each layer. This configuration improves the estimation accuracy and reduces computation time, compared to the classic formulation using thermal conductivity, volumetric heat capacity, and thickness (three parameters to be estimated for each layer).

The estimation models (EWC and AbF models) were validated by analyzing 3D numerical data generated for three different walls: Internal Wall Insulation (IWI), External Wall Insulation (EWI), and Single Wall (SW), under constant and variable boundary conditions. These results show that the IWI wall can be correctly characterized by both models with 12 hours of measurement under all conditions. In the case of SW wall, only constant and weakly varied environmental conditions lead to good estimation results. On the other hand, due to the presence of strong lateral effect, it is impossible to evaluate the thermal resistance of the EWI wall. Besides, the EWC model results are better than the one obtained when using the AbF model because of the weaker influence of the lateral heat flux in computation. However, this model requires the exact value of the convective heat transfer coefficient to obtain a good estimation, and its determination in measurement situation is challenging. Therefore, the AbF model was recommended in this study.

Four different measurement prototypes were examined in this work. They are based on different ways of applying the thermal excitation heat flux on the wall surface: using lamps or a heating resistance. After analyzing the homogeneity of the wall surface temperature and each prototype's estimation ability, two of them, which use an aluminum plate equipped with a heating resistance to deliver the heat flux, have been selected. The use of this aluminum plate in contact with the wall improves the homogeneity of the thermal excitation imposed on the wall surface. Thermal sensors (thermocouples and heat flux meters) are directly integrated in the plate's surface, which allows delivering measurement data with enhanced signal-to-noise ratio compared to other cases, for which the sensors are in contact with air. It is important to add that the installation of such a prototype is easy and fast (of the order of 5 minutes). However, these prototypes require that the aluminum plate must be in contact with the wall surface so that only flat surfaces can be tested.

To evaluate the thermal resistance estimation ability of the two prototypes, five real walls were investigated: IWI, EWI, SW, and Wood Frame Wall (WFW) under three different environmental conditions (constant, variable, and natural) in climatic chambers at LNE, CEREMA, and IFSTTAR. According to thirty-three tests performed, both prototypes show a satisfactory thermal resistance estimation for the IWI wall with 6-hour measurement data under constant, variable, and natural conditions. Under natural conditions, solar protection is highly recommended to avoid sun influence during measurements. Similar observations are found for SW cases. These tests also show that the highest heating power leads to better estimation results than the lowest one.

Nevertheless, only the first insulation and BA13 layers can be characterized in the case of the WFW wall because the Oriented Strand Board (OSB) located between two insulation layers diffuses mainly laterally the heat flux coming to the second insulation layer. Additionally, the presence of thermal bridges strongly disturb the estimation results. As expected from the numerical study results, the thermal resistance of the EWI wall is impossible to be evaluated when testing on the wall internal surface. The only solution for this wall is to apply the thermal excitation on the wall external surface.

According to the results obtained, the prototype developed in this study makes it possible to correctly assess the wall thermal resistance after 6 hours of measurement under certain conditions. Only the layers between the heating surface and a potential diffusive layer (for example, building block or OSB) can be characterized. The best hour for measurement is during the night when there is no solar radiation or strong exterior air temperature variation. In the case of measurements during the day, solar protection is recommended to protect the tested wall external surface. At the end of RESBATI project, professionals will test this prototype on building walls on site. Then, an improvement of the prototype will be possible, depending on their feedback.

Due to the unexpected epidemic of COVID, the *in-situ* measurement on the real buildings could not be carried out as scheduled. Although the climatic chambers in this study can simulate the real conditions as the *in-situ* cases, there are some influences which we can not create in a climatic chamber (for example, air temperature variation due to human activities in the testing room, influences of opening/closing windows or doors during the measurement). To validate the prototype's estimation ability proposed in this study, the *in-situ* measurements must be done. Additionally, we have only performed tests under natural conditions in summer, but not in winter. Therefore, the winter tests will be launched later to verify the estimation ability of the proposed prototype under this condition.

The presence of lateral effect is always a big problem in the thermal resistance estimation. Although we obtain acceptable results with the IWI wall, it is not completely correct because the 1D model used in the estimation does not take into account the lateral effects. This explains why the estimated resistance is reduced when increasing measurement duration. The only solution is to use the 2D direct model in the thermal resistance estimation. However, the computation time of the 2D models is much longer than the 1D one, even more than the measurement duration (3.6 hours with the EWC model and more than 20 hours with the AbF model when analyzing 6-hour measurement data). Moreover, to calculate the surface temperature correctly, the AbF model requires the horizontal and vertical heat flux measurements on the investigated wall surface. In the numerical study, these data were available. Nevertheless, during *in-situ* real measurements, it is not easy to have them. Then, there is another solution for this case. A black-box model was used to evaluate the lateral heat flux by using the absorbed heat flux measured at the center of the heating zone, the temperature of some points on the tested surface, and the current estimated thermal resistance obtained by our estimation. This model will help us to evaluate the true longitudinal heat flux rapidly. Thus, the 1D estimation will work directly with the true 1D heat flux. To well characterize the parameters of this black-box model, it is necessary to run a lot of numerical simulations and measurements on different real walls. Unfortunately, this task can not be finished during three years of my Ph.D..

Although this study mentioned that it should avoid the thermal bridges when choosing the heating zone, these irregularities may be unavoidable in some cases. If it exists a complementary method to evaluate the influence of the thermal bridges on the measurement conducted by this prototype, it is possible to remove it in the thermal resistance estimation. Then, it is possible to estimate the thermal resistance of the zone containing the thermal bridges.

References

[1] Bp Energy Outlook 2019 edition. [Online]. Available: https://www.bp.com/content/dam/bp/business-sites/en/global/corporate/pdfs/energy-economics/energy-outlook/bp-energy-outlook-2019.pdf

[2] European Statistics. [Online]. Available: https://ec.europa.eu/eurostat/web/main/home

[3] *Règlementation thermique 2012*. CSTB editor, 2012 (in French).

[4] S. M. Ocaña, I. C. Guerrero, and I. G. Requen, "Thermographic survey of two rural buildings in Spain," *Energy and Buildings*, vol. 36, pp. 515–523, 2004. [Online]. Available: https://doi.org/10.1016/j.enbuild.2003.12.012

[5] E. Barreira, R. M. Almeida, and M. Moreira, "An infrared thermography passive approach to assess the effect of leakage points in buildings," *Energy and Buildings*, vol. 140, pp. 224–235, 2017. [Online]. Available: https://doi.org/10.1016/j.enbuild.2017.02.009

[6] A. Menezes, M. G. Gomes, and I. Flores-Colen, "In-situ assessment of physical performance and degradation analysis of rendering walls," *Construction and Building Materials*, vol. 75, pp. 283–292, 2015. [Online]. Available: https://doi.org/10.1016/j.conbuildmat.2014.11.039

[7] *ISO 8990:1994. Thermal insulation - Determination of steady-state thermal transmission properties - Calibrated and guarded hot box*, ISO standard, 1994.

[8] H. Andrew and B. David, "The design and fabrication of a rotatable Guarded Hot Box (RGHB) capable of static pressure application," *ASABE Meeting Presentation*, 2013. [Online]. Available: https://doi.org/10.13031/aim.20131578832

[9] *ISO 9869-1:2014, Thermal insulation — Building elements — In-situ measurement of thermal resistance and thermal transmittance — Part 1: Heat flow meter method*, ISO standard, 2014.

[10] G. Desogus, S. Mura, and R. Ricciu, "Comparing different approaches to in situ measurement of building components thermal resistance," *Energy and Buildings*, vol. 43, pp. 2613–2620, 2011. [Online]. Available: https://doi.org/10.1016/j.enbuild.2011.05.025

[11] P. G. Cesaratto and M. D. Carli, "A measuring campaign of thermal conductance in situ and possible impacts on net energy demand in buildings," *Energy and Buildings*, vol. 59, pp. 29–36, 2013. [Online]. Available: https://doi.org/10.1016/j.enbuild.2012.08.036

[12] I. Naveros, M. Jiménez, and M. Heras, "Analysis of capabilities and limitations of the regression method based in averages, applied to the estimation of the U-value of building component tested in Mediterranean weather," *Energy and Buildings*, vol. 55, pp. 854–872, 2012. [Online]. Available: https://doi.org/10.1016/j.enbuild.2012.09.028

[13] D. Bienvenido-Huertas, J. Moyano, C. E. Rodríguez-Jiménez, and D. Marín, "Applying an artificial neural network to assess thermal transmittance in walls by means of the thermometric method," *Applied Energy*, pp. 1–14, 2019. [Online]. Available: https://doi.org/10.1016/j.apenergy.2018.10.052

[14] I. Danielski and M. Fröling, "Diagnosis of buildings' thermal performance - A quantitative

method using thermography under non-steady state heat flow," *Energy Procedia*, vol. 83, pp. 320–329, 2015. [Online]. Available: https://doi.org/10.1016/j.egypro.2015.12.186

[15] W. Jurges, *The heat transfer at a flat wall - Der Warmeubergang an einer wand.* Deihefte zum Gesundh.-Ing, 1924.

[16] S. Datcu, "Estimation des transferts convectifs par thermographie infrarouge," *Rapport d'étude CERTES-EDF*, 2003 (in French).

[17] R. Albatici and A. M. Tonelli, "Infrared thermovision technique for the assessment of thermal transmittance value of opaque building elements on site," *Energy and Buildings*, vol. 42, pp. 2177–2183, 2010. [Online]. Available: https://doi.org/10.1016/j.enbuild.2010.07.010

[18] R. Albatici, F. Passerini, A. M. Tonelli, and S. Gialanella, "Assessment of the thermal emissivity value of building materials using an infrared thermovision technique emissometer," *Energy and Buildings*, vol. 66, pp. 33–40, 2013. [Online]. Available: https://doi.org/10.1016/j.enbuild.2013.07.004

[19] R. Albatici, A. M. Tonelli, and M. Chiogna, "A comprehensive experimental approach for the validation of quantitative infrared thermography in the evaluation of building thermal transmittance," *Applied Energy*, vol. 141, pp. 218–228, 2015. [Online]. Available: https://doi.org/10.1016/j.apenergy.2014.12.035

[20] I. Nardi, S. Sfarra, and D. Ambrosini, "Quantitative thermography for the estimation of the u-value: State of the art and a case study," *Journal of Physics Conference*, vol. 547, pp. 1–8, 2014. [Online]. Available: https://doi.org/10.1088/1742-6596/547/1/012016

[21] P. A. Fokaides and S. A. Kalogirou, "Application of infrared thermography for the determination of the overall heat transfer coefficient (U-value) in building envelopes," *Applied Energy*, vol. 88, pp. 4358–4365, 2011. [Online]. Available: https://doi.org/10.1016/j.apenergy.2011.05.014

[22] *Standard test methods for measuring and compensating for reflected temperature using infrared imaging radiometers*, ASTM E1862 97-2002, 2002.

[23] *ISO 18434-1:2008, Condition monitoring and diagnostics of machines — Thermography — Part 1: General procedures*, ISO standard, 2008.

[24] A. Nowoświat, J. Skrzypczyk, P. Krause, T. Steidl, and A. Winkler-Skalna, "Estimation of thermal transmittance based on temperature measurements with the application of perturbation numbers," *Heat and Mass Transfer*, vol. 54, pp. 1477–1489, 2017. [Online]. Available: https://doi.org/10.1007/s00231-017-2233-y

[25] S. Kato, K. Kuroki, and S. Hagihara, "Method of in-situ measurement of thermal insulation performance of building elements using infrared camera," *6th IAQVEC*, 2007.

[26] *ISO 9869-2:2018, Thermal insulation — Building elements — In-situ measurement of thermal resistance and thermal transmittance — Part 2: Infrared method for frame structure dwelling*, ISO standard, 2018.

[27] D. Pajani, "Surface equivalente d'irregularité ou de défaut (SEID) et mesure du U par la méthode du SEID," *Conférence Thermogram 2011*, 2011 (in French).

[28] M. L. Youcef, V. Feuillet, L. Ibos, Y. Candau, P. Balcon, and A. Filloux, "In-situ quantitative diagnosis of insulated building walls using passive infrared thermography," *11th International Conference on Quantitative InfraRed Thermography Journal*, 2012. [Online]. Available: https://doi.org/10.21611/qirt.2012.302

[29] Z. Petojević, R. Gospavić, and G. Todorović, "Estimation of thermal impulse response of a multi-layer building wall through in-situ experimental measurements in a dynamic regime with applications," *Applied Energy*, vol. 228, pp. 468–486, 2018. [Online]. Available: https://doi.org/10.1016/j.apenergy.2018.06.083

[30] R. D. Maio, C. Mancini, C. Meola, and E. Piegari, "Numerical modeling of architectonic structures thermal response. laboratory and in-situ data analysis," *11th International Conference on Quantitative InfraRed Thermography*, 2012. [Online]. Available: https://doi.org/10.21611/qirt.2012.349

[31] F. Cerdeira, M. Vázquez, J. Collazo, and E. Granada, "Applicability of infrared thermography to the study of the behaviour of stone panels as building envelopes," *Energy and Buildings*, vol. 43, pp. 1845–1851, 2011. [Online]. Available: https://doi.org/10.1016/j.enbuild.2011.03.029

[32] C. Lerma, E. Barreira, and R. M. Almeida, "A discussion concerning active infrared thermography in the evaluation of buildings air infiltration," *Energy and Buildings*, vol. 168, pp. 56–66, 2018. [Online]. Available: https://doi.org/10.1016/j.enbuild.2018.02.050

[33] E. Sassine, "A practical method for in-situ thermal characterization of walls," *Case Studies in Thermal Engineering*, vol. 8, pp. 84–93, 2016. [Online]. Available: https://doi.org/10.1016/j.csite.2016.03.006

[34] M. L. Youcef, V. Feuillet, L. Ibos, Y. Candau, P. Balcon, and A. Filloux, "Quantitative diagnosis of insulated building walls of restored old constructions using active infrared thermography," *Quantitative InfraRed Thermography Journal*, pp. 65–87, 2011. [Online]. Available: https://doi.org/10.3166/qirt.8.65-87

[35] A. Rasooli, L. Itard, and C. I. Ferreira, "A response factor-based method for the rapid in-situ determination of wall's thermal resistance in existing buildings," *Energy and Buildings*, vol. 119, pp. 51–61, 2016. [Online]. Available: https://doi.org/10.1016/j.enbuild.2016.03.009

[36] G. Mitalas and D. Stephenson, "Room thermal response factors," *ASHRAE Trans*, 1967. [Online]. Available: http://web.mit.edu/parmstr/Public/NRCan/nrcc23302.pdf

[37] A. Rasooli and L. Itard, "In-situ rapid determination of walls' thermal conductivity, volumetric heat capacity, and thermal resistance, using response factors," *Applied Energy*, vol. 253, 2019. [Online]. Available: https://doi.org/10.1016/j.apenergy.2019.113539

[38] J. Meulemans, "An assessment of the QUB/e method for fast in situ measurements of the thermal performance of building fabrics in cold climates," *Cold Climate HVAC 2018 - The 9th International Cold Climate Conference*, 2018. [Online]. Available: https://doi.org/10.1007/978-3-030-00662-4_27

[39] I. Nardi, D. Paoletti, D. Ambrosini, T. de Rubeis, and S. Sfarra, "U-value assessment by infrared thermography: A comparison of different calculation methods in a Guarded Hot Box," *Energy and Buildings*, vol. 122, pp. 211–221, 2016. [Online]. Available: https://doi.org/10.1016/j.enbuild.2016.04.017

[40] N. Soares, C. Martins, M. Gonçalves, P. Santos, L. S. da Silva, and J. J. Costa, "Laboratory and in-situ non-destructive methods to evaluate the thermal transmittance and behavior of walls, windows, and construction elements with innovative materials: A review," *Energy and Buildings*, vol. 182, pp. 88–110, 2019. [Online]. Available: https://doi.org/10.1016/j.enbuild.2018.10.021

[41] M. Teni, H. Krstić, and P. Kosiński, "Review and comparison of current experimental approaches for in-situ measurements of building walls thermal transmittance," *Energy and Buildings*, vol. 203, 2019. [Online]. Available: https://doi.org/10.1016/j.enbuild.2019.109417

[42] J.-P. Monchau, V. Feuillet, L. Ibos, and Y. Candau, "Comparaison de méthodes de mesure de résistance thermique in-situ de parois de bâtiment : essais sur un immeuble d'habitation occupé," *Société Française de Thermique Congress*, 2015 (in French). [Online]. Available: https://www.sft.asso.fr/Local/sft/dir/user-3775/documents/actes/Congres_2015/Communications/43968-fichier4.pdf

[43] J.-P. Monchau, L. Ibos, and V. Feuillet, "Diagnosis of insulated building walls using passive infrared thermography and numerical simulations," *7th European Workshop on Structural Health Monitoring*, 2014. [Online]. Available: https://hal.inria.fr/hal-01020325/document

[44] L. Ibos, V. Feuillet, M. L. Youcef, J.-P. Monchau, A. Mazioud, and Y. Candau, "Estimation de résistance thermique de parois par thermographie active et passive: Comparaison," *Thermogram' 2013*, 2013 (in French).

[45] G. Ficco, F. Iannetta, E. Ianniello, F. R. d'Ambrosio Alfano, and M. Dell'Isola, "U-value in situ measurement for energy diagnosis of existing buildings," *Energy and Buildings*, vol. 104, pp. 108–121, 2015. [Online]. Available: https://doi.org/10.1016/j.enbuild.2015.06.071

[46] A.-H. Deconinck and S. Roels, "Comparison of characterisation methods determining the thermal resistance of building components from onsite measurements," *Energy and Buildings*, vol. 130, pp. 309–320, 2016. [Online]. Available: https://doi.org/10.1016/j.enbuild.2016.08.061

[47] CTSM-R: Continuous-Time Stochastic Modelling for R. [Online]. Available: ctsm.info

[48] E. Cuerda, O. Guerra-Santin, F. J. Neila, and N. Romero. Evaluation and comparison of building performance in use through on-site monitoring and simulation modelling. [Online]. Available: https://pdfs.semanticscholar.org/4a2c/225e1eb0ddaf95523f511268278639d3106c.pdf

[49] S.-H. Kim, J.-H. Kim, H.-G. Jeong, and K.-D. Song, "Reliability field test of the Air–Surface Temperature Ratio method for in-situ measurement of U-values," *Energies, MDPI, Open Access Journal*, vol. 11(4), pp. 1–15, 2018. [Online]. Available: https://doi.org/10.3390/en11040803

[50] *ISO 6946:2017, Building components and building elements - Thermal resistance and thermal transmittance - Calculation methods*, ISO standard, 2017.

[51] H. S. Carslaw, "Introduction to the mathematical theory of the conduction of heat in solids," *Monatsh. f. Mathematik und Physik*, vol. 32, 1921.

[52] H. Carslaw and J. Jaeger, *Conduction of heat in solids (2^{nd} edition).* Oxford University Press, New York, 1959.

[53] L. Ahlfors, *Complex analysis.* McGraw Hill, 1979.

[54] D. V. Widder, "The inversion of the Laplace integral and the related moment problem," *Transactions of the American Mathematical Society*, pp. 107–201, 1934. [Online]. Available: https://www.ams.org/journals/tran/1934-036-01/S0002-9947-1934-1501737-7/S0002-9947-1934-1501737-7.pdf

[55] H. Stehfest, "Algorithm 368: Numerical inversion of Laplace transforms," *Association for Computing Machinery*, p. 47–49, 1970. [Online]. Available: https://doi.org/10.1145/361953.361969

[56] F. R. de Hoog, J. H. Knight, and A. N. Stokes, "An improved method for numerical inversion of Laplace transforms," *SIAM Journal on Scientific and Statistical Computing*, p. 357–366, 1982. [Online]. Available: https://doi.org/10.1137/0903022

[57] K. J. Hollenbeck, "INVLAP.M: A matlab function for numerical inversion of Laplace transforms by the de Hoog algorithm," 1998. [Online]. Available: http://www.isva.dtu.dk/staff/karl/invlap.htm

[58] A. Tarantola, "Inverse problem theory and methods for model parameter estimation," *Society for Industrial and Applied Mathematics*, 2005. [Online]. Available: http://www.ipgp.fr/~tarantola/Files/Professional/Books/InverseProblemTheory.pdf

[59] Y. Jarny and K. A. W. (Ed.), *Inverse engineering handbook (Chapter 3: The adjoint method to compute the numerical solutions of inverse problems).* CRC Press, 2002.

[60] MATLAB: Least-square (Model Fitting) algorithms. [Online]. Available: https://fr.mathworks.com/help/optim/ug/lsqnonlin.html

[61] H. P. Gavin, "The Levenberg-Marquardt method for nonlinear least squares curve-fitting problems," 2013. [Online]. Available: https://pdfs.semanticscholar.org/792f/21cedf2c07c5b018c19146cad57178146054.pdf?_ga=2.236005314.296329644.1589450396-2138162943.1588512202

[62] Y. Ya-xiang, "A review of Trust region algorithms for optimization," *ICM99: Proceedings of the Fourth International Congress on Industrial and Applied Mathematics*, 1999. [Online]. Available: http://citeseerx.ist.psu.edu/viewdoc/summary?doi=10.1.1.45.9964

[63] Bayesian inference. [Online]. Available: https://datajobs.com/data-science-repo/Bayesian-Inference-[Statisticat].pdf

[64] M. Glickman and D. van Dyk, "Basic Bayesian methods," *Methods in molecular biology (Clifton, N.J.)*, 2007. [Online]. Available: http://www.glicko.net/research/glickman-vandyk.pdf

[65] J. G. Ibrahim and M.-H. Chen, "Power prior distributions for regression models," *Statistics Science*, pp. 46–60, 2000. [Online]. Available: https://doi.org/10.1214/ss/1009212673

[66] A. Gelman, A. Jakulin, M. G. Pittau, and Y.-S. Su, "A weakly informative default prior distribution for logistic and other regression models," *The Annals of Applied Statistics*, pp. 1360–1383, 2008. [Online]. Available: https://doi.org/10.1214/08-AOAS191

[67] M. Evans and G. H. Jang, "Weak informativity and the information in one prior relative to another," *Statistics Science*, pp. 423–439, 2011. [Online]. Available: https://doi.org/10.1214/11-STS357

[68] T. Z. Irony and N. D. Singpurwalla, “Non-informative priors do not exist: A dialogue with José M. Bernardo,” *Journal of Statistical Planning and Inference*, vol. 65, pp. 159–177, 1997. [Online]. Available: https://doi.org/10.1016/S0378-3758(97)00074-8

[69] S. Sarkka, *Bayesian filtering and smoothing*. Cambridge University Press, 2013.

[70] W. K. Hastings, “Monte Carlo sampling methods using Markov Chains and their applications,” *Biometrika*, pp. 97–109, 1970. [Online]. Available: https://doi.org/10.2307/2334940

[71] I. Yildirim, “Bayesian inference: Gibbs sampling,” 2012. [Online]. Available: http://www.mit.edu/~ilkery/papers/GibbsSampling.pdf

[72] R. Neal, “MCMC using Hamiltonian dynamics,” *Handbook of Markov Chain Monte Carlo*, 2012. [Online]. Available: https://arxiv.org/abs/1206.1901

[73] H. Haario, E. Saksman, and J. Tamminen, “An Adaptive Metropolis algorithm,” *Bernoulli. 7*, 2001. [Online]. Available: https://projecteuclid.org/euclid.bj/1080222083

[74] H. Haario, J. Tamminen, and E. Saksman, “Adaptive proposal distribution for random walk metropolis algorithm,” *Computational Statistics 14*, 1999. [Online]. Available: https://doi.org/10.1007/s001800050022

[75] C. Andrieu and C. Robert, “Controlled MCMC for optimal sampling,” 2001. [Online]. Available: https://pdfs.semanticscholar.org/8186/0afd9ffaf9eca3e9c52f5b3f629ba0d4771e.pdf

[76] J. Park and Y. F. Atchadé, “Markov chain Monte Carlo algorithms with sequential proposals,” 2019. [Online]. Available: https://arxiv.org/abs/1907.06544

[77] N. J.Higham. (2009) Cholesky factorization. [Online]. Available: https://www.maths.manchester.ac.uk/~higham/papers/high09c.pdf

[78] G. O. Roberts, A. Gelman, and W. R. Gilks, “Weak convergence and optimal scaling of random walk metropolis algorithms,” *Annals of Applied Probability 7*, pp. 110–120, 1997. [Online]. Available: https://doi.org/10.1214/aoap/1034625254

[79] M. Vihola, “On the stability and ergodicity of adaptive scaling Metropolis algorithms,” *Stochastic Processes and their Applications*, vol. 121, pp. 2839–2860, 2011. [Online]. Available: https://doi.org/10.1016/j.spa.2011.08.006

[80] C. Andrieu and J. Thomas, “A tutorial on adaptive MCMC,” *Statistics and Computing 18*, p. 343–373, 2008. [Online]. Available: https://doi.org/10.1007/s11222-008-9110-y

[81] M. Vihola, “Robust adaptive Metropolis algorithm with coerced acceptance rate,” *Statistics and Computing*, vol. 22, 2012. [Online]. Available: https://doi.org/10.1007/s11222-011-9269-5

[82] Light intensity. [Online]. Available: http://atj.net.au/marineaquaria/light_intensity.html

[83] User’s manual: FLIR IR Monitor. [Online]. Available: http://support.flir.com/docdownload/assets/dl/t559495-en-us$\protect\T1\textdollar$aa.pdf

[84] L. Ibos, M. L. Youcef, A. Mazioud, Y. Candau, P. Bremond, M. Piro, A. Filloux, and J. L. Bodnar, “Thermographie infrarouge appliquée au bâtiment : vers une estimation de résistance thermique de parois,” *Thermogram 2009*, 2009 (in French). [Online]. Available:

https://www.researchgate.net/publication/273383981_Thermographie_infrarouge_appliquee_au_batiment_vers_une_estimation_de_resistance_thermique_de_parois

[85] *ISO 10291:1994, Glass in building. Determination of steady-state U values (thermal transmittance) of multiple glazing. Guarded hot plate method*, ISO standard, 1994.

[86] *ISO 22007-2:2015, Plastics — Determination of thermal conductivity and thermal diffusivity — Part 2: Transient plane heat source (hot disc) method*, ISO standard, 2015.

[87] Boîte chaude gardée - Nouvel équipement au service de la transition énergétique. [Online]. Available: https://www.cstb.fr/assets/documents/cstb-boite-chaude-gardee.pdf

[88] Mesurer la performance thermique des super isolants. [Online]. Available: https://www.lne.fr/fr/lettres-information/batiment-construction/fabricants-materiaux-super-isolants

[89] List of Laplace transforms. [Online]. Available: https://en.wikipedia.org/wiki/List_of_Laplace_transforms

[90] G. Maranzana, "Modélisation thermique des composants électroniques de puissance par la méthode des quadripôles," 2005 (in French), Ph.D. thesis, Université de Lorraine.

Appendix

A1 Calculation of quadrupole transfer matrix

In Section 2.3.1, the thermal states at $x = 0$ and $x = e$ are linked together by the transfer matrix *M* which is the product of a simple matrix and the inverse of another one (Cf. equation 2.13). In this appendix, the detailed computation to obtain this transfer matrix is shown.

The original expression of the transfer matrix is:

$$M = \begin{pmatrix} 1 & 0 \\ 0 & -\lambda\sqrt{p/a} \end{pmatrix} \begin{pmatrix} ch(e\sqrt{p/a}) & sh(e\sqrt{p/a}) \\ -\lambda\sqrt{p/a}\, sh(e\sqrt{p/a}) & -\lambda\sqrt{p/a}\, ch(e\sqrt{p/a}) \end{pmatrix}^{-1} \begin{pmatrix} \theta(e,p) \\ \phi(e,p) \end{pmatrix} \tag{.1}$$

At the beginning, the second matrix of *M* should be determined first. To do that, the Gauss-Jordan elimination is used:

$$\begin{pmatrix} 1 & 0 \\ 0 & 1 \end{pmatrix} \Bigg| \begin{pmatrix} ch(e\sqrt{p/a}) & sh(e\sqrt{p/a}) \\ -\lambda\sqrt{p/a}\, sh(e\sqrt{p/a}) & -\lambda\sqrt{p/a}\, ch(e\sqrt{p/a}) \end{pmatrix}$$

After multiplying the first line by $(\lambda\sqrt{p/a}sh(e\sqrt{p/a}))/ch(e\sqrt{p/a})$ and adding it into the second line, the matrix above becomes:

$$\begin{pmatrix} 1 & 0 \\ \lambda\sqrt{p/a}\, sh(e\sqrt{p/a})/ch(e\sqrt{p/a}) & 1 \end{pmatrix} \Bigg| \begin{pmatrix} ch(e\sqrt{p/a}) & sh(e\sqrt{p/a}) \\ 0 & -\lambda\sqrt{p/a}\ /ch(e\sqrt{p/a}) \end{pmatrix}$$

Next, dividing the second line by $(-\lambda\sqrt{p/a})/ch(e\sqrt{p/a})$, a new matrix is obtained:

$$\begin{pmatrix} 1 & 0 \\ -sh(e\sqrt{p/a}) & -(\lambda\sqrt{p/a})^{-1}\, ch(e\sqrt{p/a}) \end{pmatrix} \Bigg| \begin{pmatrix} ch(e\sqrt{p/a}) & sh(e\sqrt{p/a}) \\ 0 & 1 \end{pmatrix}$$

Then, multiplying the second line by $-sh(e\sqrt{p/a})$ and adding into first line leads to:

$$\begin{pmatrix} ch^2(e\sqrt{p/a}) & (\lambda\sqrt{p/a})^{-1}\, ch(e\sqrt{p/a})sh(e\sqrt{p/a}) \\ -sh(e\sqrt{p/a}) & -(\lambda\sqrt{p/a})^{-1}\, ch(e\sqrt{p/a}) \end{pmatrix} \Bigg| \begin{pmatrix} ch(e\sqrt{p/a}) & 0 \\ 0 & 1 \end{pmatrix}$$

The last operation is the division of the first line by $ch(e\sqrt{p/a})$:

$$\begin{pmatrix} ch(e\sqrt{p/a}) & (\lambda\sqrt{p/a})^{-1}\, sh(e\sqrt{p/a}) \\ -sh(e\sqrt{p/a}) & -(\lambda\sqrt{p/a})^{-1}\, ch(e\sqrt{p/a}) \end{pmatrix} \Bigg| \begin{pmatrix} 1 & 0 \\ 0 & 1 \end{pmatrix}$$

So, the expression of the second term of equation .1 is the matrix on the left-hand side in the equation above. To obtain the transfer matrix, the last step consists in multiplying this matrix by the first term of equation .1:

$$M = \begin{pmatrix} 1 & 0 \\ 0 & -\lambda\sqrt{p/a} \end{pmatrix} \begin{pmatrix} ch(e\sqrt{p/a}) & (\lambda\sqrt{p/a})^{-1}\, sh(e\sqrt{p/a}) \\ -sh(e\sqrt{p/a}) & -(\lambda\sqrt{p/a})^{-1}\, ch(e\sqrt{p/a}) \end{pmatrix} \tag{.2}$$

Finally, the expression of matrix *M* is found:

$$M = \begin{pmatrix} ch(e\sqrt{p/a}) & (\lambda\sqrt{p/a})^{-1}\, sh(e\sqrt{p/a}) \\ \lambda\sqrt{p/a}\, sh(e\sqrt{p/a}) & ch(e\sqrt{p/a}) \end{pmatrix} \tag{.3}$$

A2 Table of Laplace transform functions for the thermal quadrupole computation

	$f(t)$	$F(p) = L(f(t))$
1	1	$1/p$
2	e^{at}	$1/(p-a)$
3	t^n	$n!/p^{n+1}$
4	$t^{\alpha}, \alpha > -1$	$\Gamma(\alpha+1)/p^{\alpha+1}$
5	$\sqrt{t}$	$\sqrt{\pi}/(2p^{3/2})$
6	$t^{n-1/2}$	$(1 \cdot 3 \cdot 5 \cdots (2n-1)\sqrt{\pi})/(2^n p^{n+1/2})$
7	$sin(at)$	$a/(p^2+a^2)$
8	$cos(at)$	$p/(p^2+a^2$
9	$tsin(at)$	$2ap/(p^2+a^2)^2$
10	$tcos(at)$	$(p^2-a^2)/(p^2+a^2)^2$
11	$sin(at) - atcos(at)$	$2a^3/(p^2+a^2)^2$
12	$sin(at) + atcos(at)$	$2ap^2/(p^2+a^2)^2$
13	$cos(at) - atsin(at)$	$p(p^2-a^2)/(p^2+a^2)^2$
14	$cos(at) + atsin(at)$	$p(p^2+3a^2)/(p^2+a^2)^2$
15	$sin(at+b)$	$(psin(b) + acos(b))/(p^2+a^2)$
16	$cos(at+b)$	$(pcos(b) - asin(b))/(p^2+a^2)$
17	$sinh(at)$	$a/(p^2-a^2)$
18	$cosh(at)$	$p/(p^2-a^2)$
19	$e^{at}sin(bt)$	$b/((p-a)^2+b^2)$
20	$e^{at}cos(bt)$	$(p-a)/((p-a)^2+b^2)$
21	$e^{et}sinh(bt)$	$b/((p-a)^2-b^2)$
22	$e^{at}cosh(bt)$	$(p-a)/((p-a)^2-b^2)$
23	$t^n e^{at}$	$n!/(p-a)^{n+1}$
24	$f(ct)$	$(1/c)F(p/c)$
25	$u_c(t) = u(t-c)$	e^{-cp}/p
26	$\delta(t-c)$	e^{-cp}
27	$u_c(t)f(t-c)$	$e^{-cp}F(p)$
28	$u_c(t)g(t)$	$e^{-cp}L(g(t+c))$
29	$e^{ct}f(t)$	$F(p-c)$
30	$t^n f(t)$	$(-1)^n F^{(n)}(p)$
31	$(1/t)f(t)$	$\int_p^{\infty} F(s)ds$
32	$\int_0^t f(v)dv$	$F(p)/p$
33	$\int_0^t f(t-\tau)g(\tau)d\tau$	$F(p)G(p)$
34	$f(t+T) = f(t)$	$(\int_0^T e^{-pt}f(t)dt)/(1-e^{-pT})$
35	$f^{'}(t)$	$pF(p) - f(0)$
36	$f^{''}(t)$	$p^2F(p) - pf(0) - f^{'}(0)$
37	$f^{(n)}(t)$	$p^nF(s) - p^{n-1}f(0) - p^{n-2}f^{'}(0) \cdots - pf^{(n-2)}(0) - f^{(n-1)}(0)$

Table A2.1: Analytical Laplace transform functions, where $n = 1, 2, 3, \cdots$, $\Gamma(x)$, $u_c(t)$, and $\delta(t)$ are the Gamma, Heaviside, and Dirac delta functions, respectively [89].

At $x = 0$	At $x = e$	Eigenvalues α_n	Eigenfunctions	Norm
$T = 0$	$T = 0$	$n\pi/e$ $(n \geq 1)$	$sin(\alpha_n x)$	$e/2$
$T = 0$	$dT/dx = 0$	$(n + 1/2)\pi/e$ $(n \geq 0)$	$sin(\alpha_n x)$	$e/2$
$T = 0$	$\lambda dT/dx$ $+hT = 0$	positive solutions of $tan(\alpha_n e) = -\lambda\alpha_n/h$	$sin(\alpha_n x)$	$\frac{e}{2}\left(1 + \frac{he/\lambda}{(he/\lambda)^2+(\alpha_n e)^2}\right)$
$dT/dx = 0$	$T = 0$	$(n + 1/2)\pi/e$ $(n \geq 0)$	$cos(\alpha_n x)$	$e/2$
$dT/dx = 0$	$dT/dx = 0$	$n\pi/e$ $(n \leq 0)$	$cos(\alpha_n x)$	e for $n = 0$ $e/2$ for $n \leq 1$
$dT/dx = 0$	$\lambda dT/dx$ $+hT = 0$	positive solutions of $cot(\alpha_n e) = \lambda\alpha_n/h$	$cos(\alpha_n x)$	$\frac{e}{2}\left(1 + \frac{he/\lambda}{(he/\lambda)^2+(\alpha_n e)^2}\right)$
$-\lambda dT/dx$ $+hT = 0$	$T = 0$	positive solutions of $tan(\alpha_n e) = -\lambda\alpha_n/h$	$sin(\alpha_n(e - x))$	$\frac{e}{2}\left(1 + \frac{he/\lambda}{(he/\lambda)^2+(\alpha_n e)^2}\right)$
$-\lambda dT/dx$ $+hT = 0$	$dT/dx = 0$	positive solutions of $cot(\alpha_n e) = \lambda\alpha_n/h$	$cos(\alpha_n(e - x))$	$\frac{e}{2}\left(1 + \frac{he/\lambda}{(he/\lambda)^2+(\alpha_n e)^2}\right)$
$-\lambda dT/dx$ $+h_1T = 0$	$\lambda dT/dx$ $+h_2T = 0$	positive solutions of $tan(\alpha_n e) = \frac{\lambda\alpha_n(h_1+h_2)}{(\lambda\alpha_n)^2-h_1h_2}$	$cos(\alpha_n x)$ $+\frac{h_1}{\lambda\alpha_n}sin(\alpha_n x)$	$\frac{1}{2e\alpha_n^2}\left(((h_1e/\lambda)^2 + (\alpha_n e)^2)(1 + \frac{h_2e/\lambda}{(h_2e/\lambda)^2+(\alpha_n e)^2}) + \frac{h_1e}{\lambda}\right)$

Table A2.2: Integral transforms in rectangular geometry [90].

A3 Noise measurement in laboratory

All measured data always contain noise due to measurement device. A noise evaluation in laboratory for all thermal sensors used in this study is carried out. This evaluation provides a real measurement noise added in the numerical study (Cf. Section 3.7) and compared with the measurement data when using the proposed prototypes in Chapter 4. Here, three measurement data should be examined: surface temperature, air temperature and surface heat flux.

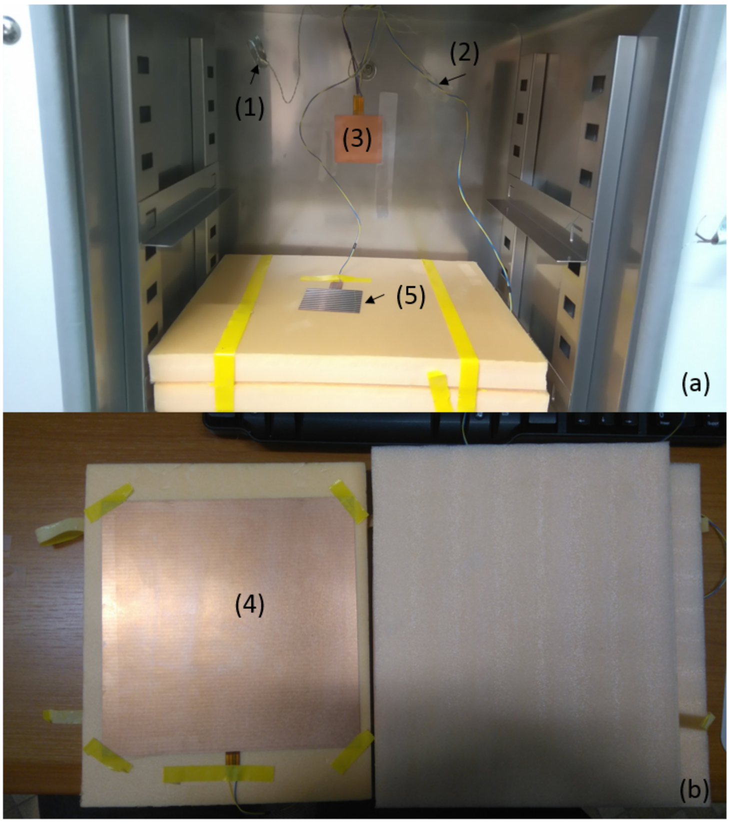

Figure A3.1: Sensors in use during noise measurement.

A thermal oven named WON 155 which allows maintaining its internal temperature constant is used during this test. Several thermal sensors are installed inside this oven: a thermocouple hanged freely in the air (1), a thermocouple (2) and a conductive heat flux meter (3) stuck on the oven surface, a radiative heat flux meter (5) on the insulation surface and a conductive heat flux meter (4) sandwiched between two insulation layers (Cf. Figure A3.1). The internal temperature is fixed to 30 °C.

However, even if this oven can maintain a relatively constant set temperature, a regulation must be activated due to heat losses on the edges. Then, when observing the raw measurement data, a small periodic fluctuation of low frequency exists as shown in Figure A3.2. So, to remove this fluctuation, the high-pass Butterworth filter of order 10 is applied to keep only variations of high frequencies that correspond to the noise. An example of filtered noise signal of air temperature is shown in Figure A3.2. The maximal value of the noise signal will be considered noise value for the studied sensor.

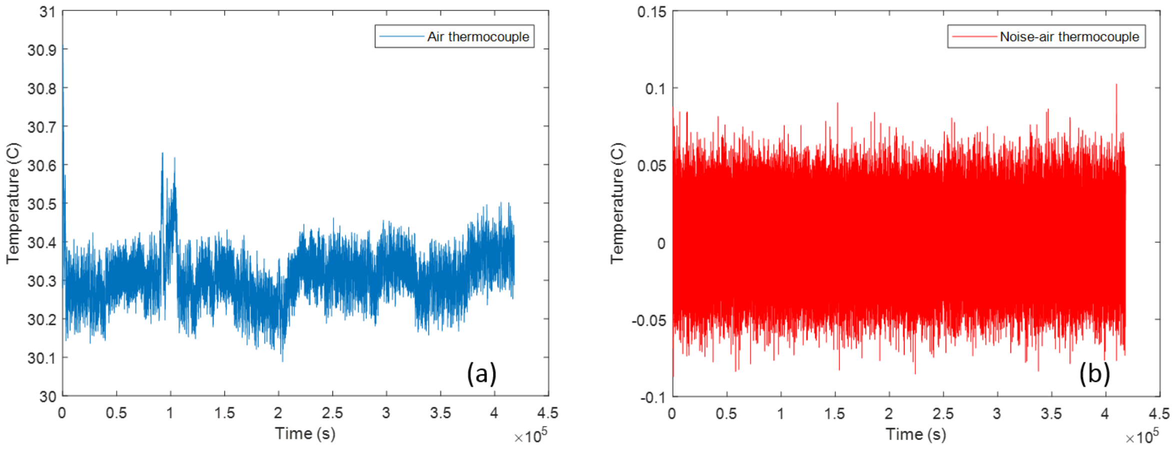

Figure A3.2: Raw measurement signal (a) and filtered signal (b).

Table A3.1 shows the noise values for the five tested sensors.

Sensor	Noise value
Thermocouple for air temperature	± 0.05°C
Thermocouple for wall surface temperature	± 0.04°C
Conductive heat flux meter	± 1.25 W.m^{-2}
Radiative heat flux meter	± 0.1 W.m^{-2}
Insulated conductive heat flux meter	± 0.004 W.m^{-2}

Table A3.1: Noise values of five thermal sensors obtained by measurement in the thermal oven.

According to these values, the conductive heat flux meter in direct contact with the air shows a high noise level. The on-site measurement, whose environment can not be controlled perfectly, may show higher noise than in this test.

A4 Residuals of thermal resistance estimations of the measurement campaigns

This appendix shows the profiles of residuals between measured and estimated minimization parameter (the internal surface temperature (or the external surface temperature for tests 10 to 17), red line) and estimation results (the estimated wall thermal resistance, blue line) of each test presented in Chapter 5. The error bars of the residuals show the maximum and minimum difference between the measurement and estimation profiles of the minimization parameter.

These figures help to understand the evolution of estimation results as a function of measurement duration and explain the results detailed in Chapter 6.

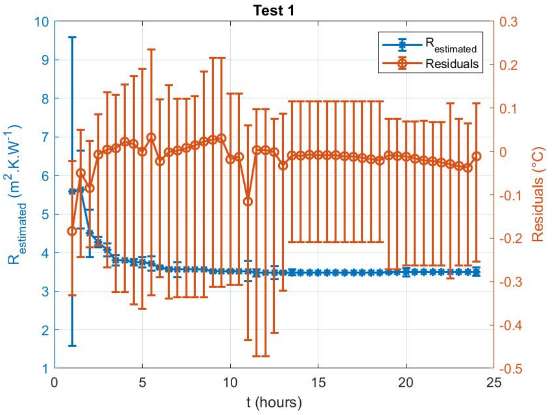

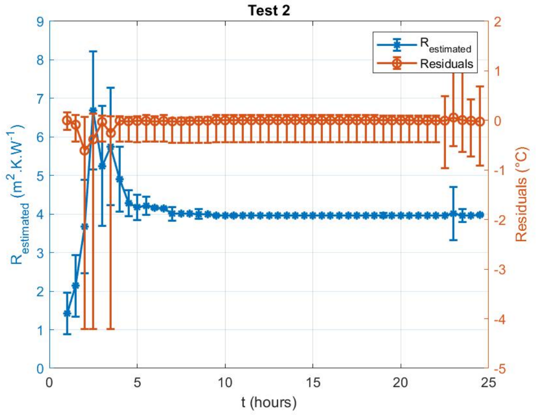

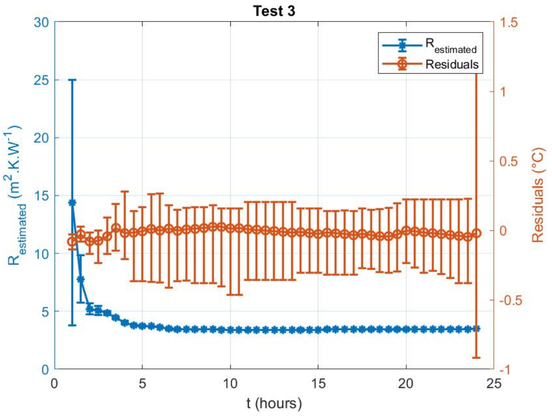

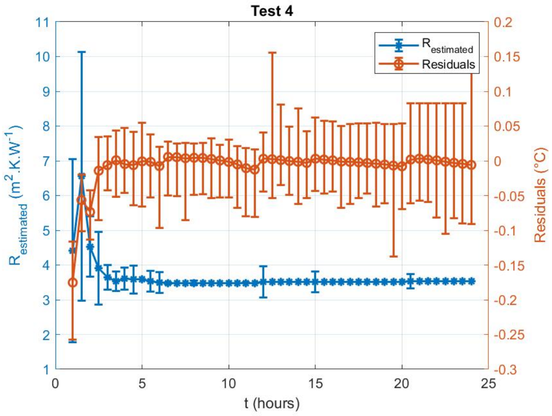

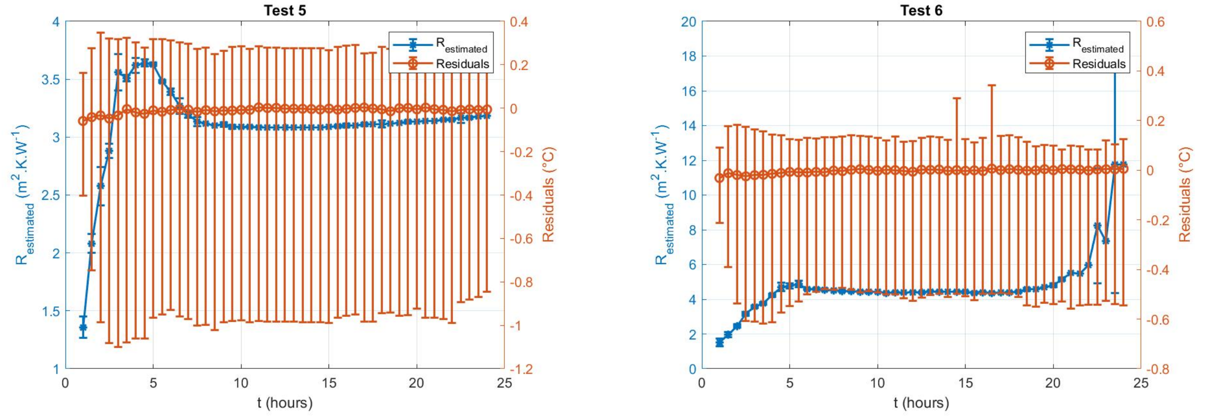

Figure A4.1: Estimated thermal resistance and residuals between measured and estimated minimization parameter for the six tests on the IWI wall under constant conditions with the third prototype.

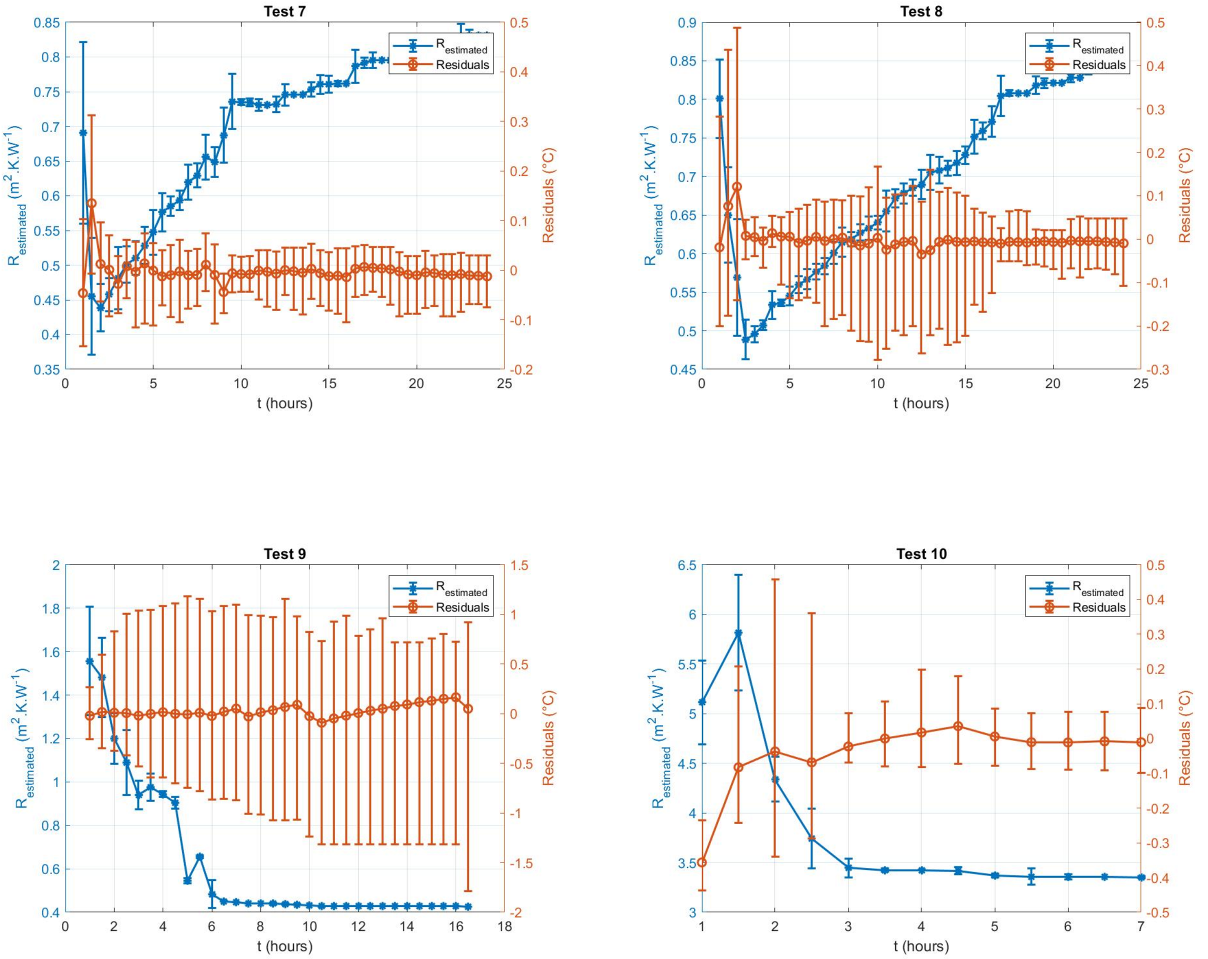

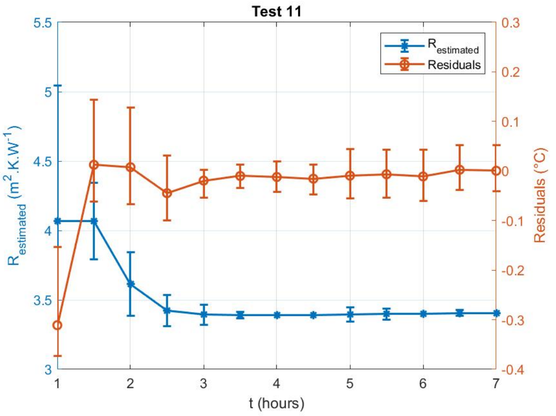
Test 11
R_estimated
Residuals
R_estimated (m².K.W⁻¹)
Residuals (°C)
t (hours)
3
3.5
4
4.5
5
5.5
-0.4
-0.3
-0.2
-0.1
0
0.1
0.2
0.3
1
2
3
4
5
6
7

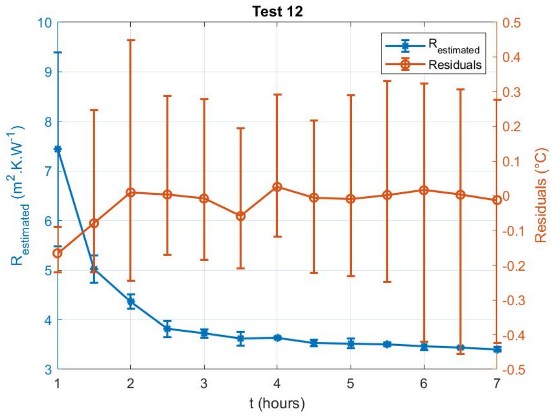
Test 12
R_estimated
Residuals
R_estimated (m².K.W⁻¹)
Residuals (°C)
t (hours)
3
4
5
6
7
8
9
10
-0.5
-0.4
-0.3
-0.2
-0.1
0
0.1
0.2
0.3
0.4
0.5
1
2
3
4
5
6
7

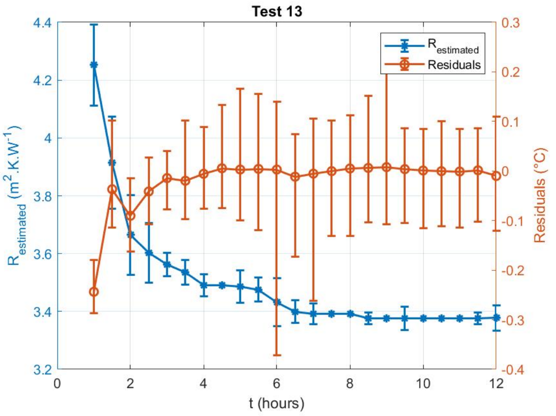
Test 13
R_estimated
Residuals
R_estimated (m².K.W⁻¹)
Residuals (°C)
t (hours)
3.2
3.4
3.6
3.8
4
4.2
4.4
-0.4
-0.3
-0.2
-0.1
0
0.1
0.2
0.3
0
2
4
6
8
10
12

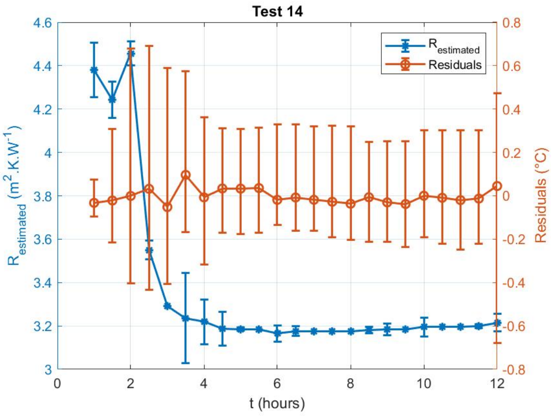
Test 14
R_estimated
Residuals
R_estimated (m².K.W⁻¹)
Residuals (°C)
t (hours)
3
3.2
3.4
3.6
3.8
4
4.2
4.4
4.6
-0.8
-0.6
-0.4
-0.2
0
0.2
0.4
0.6
0.8
0
2
4
6
8
10
12

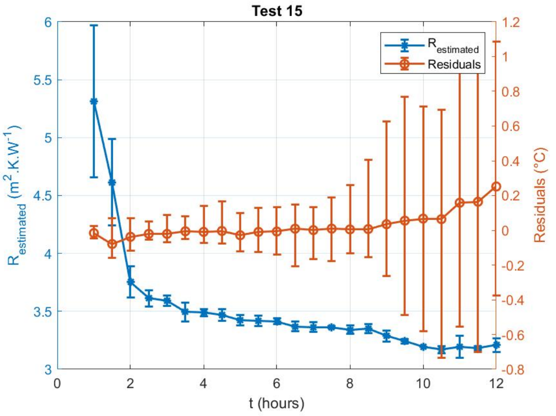
Test 15
R_estimated
Residuals
R_estimated (m².K.W⁻¹)
Residuals (°C)
t (hours)
3
3.5
4
4.5
5
5.5
6
-0.8
-0.6
-0.4
-0.2
0
0.2
0.4
0.6
0.8
1
1.2
0
2
4
6
8
10
12

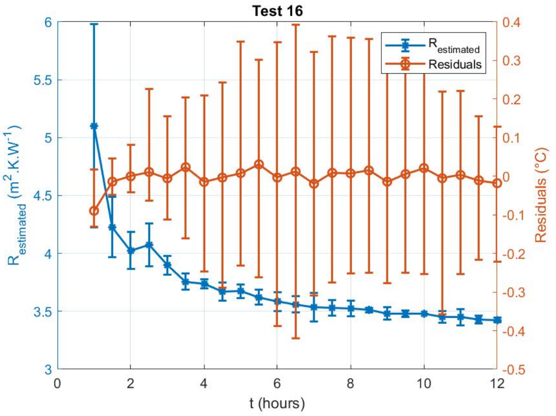
Test 16
R_estimated
Residuals
R_estimated (m².K.W⁻¹)
Residuals (°C)
t (hours)
3
3.5
4
4.5
5
5.5
6
-0.5
-0.4
-0.3
-0.2
-0.1
0
0.1
0.2
0.3
0.4
0
2
4
6
8
10
12

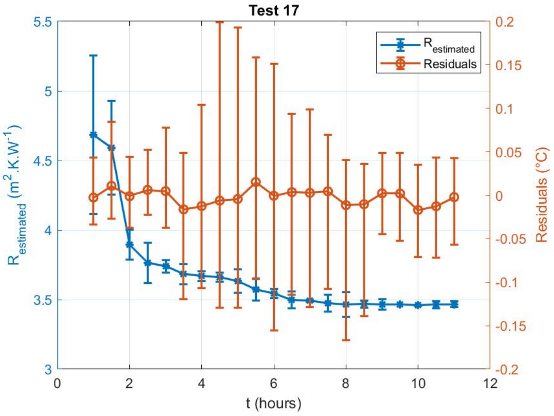

Figure A4.2: Estimated thermal resistance and residuals between measured and estimated minimization parameter for the eleven tests on the EWI wall under constant conditions with the third prototype.

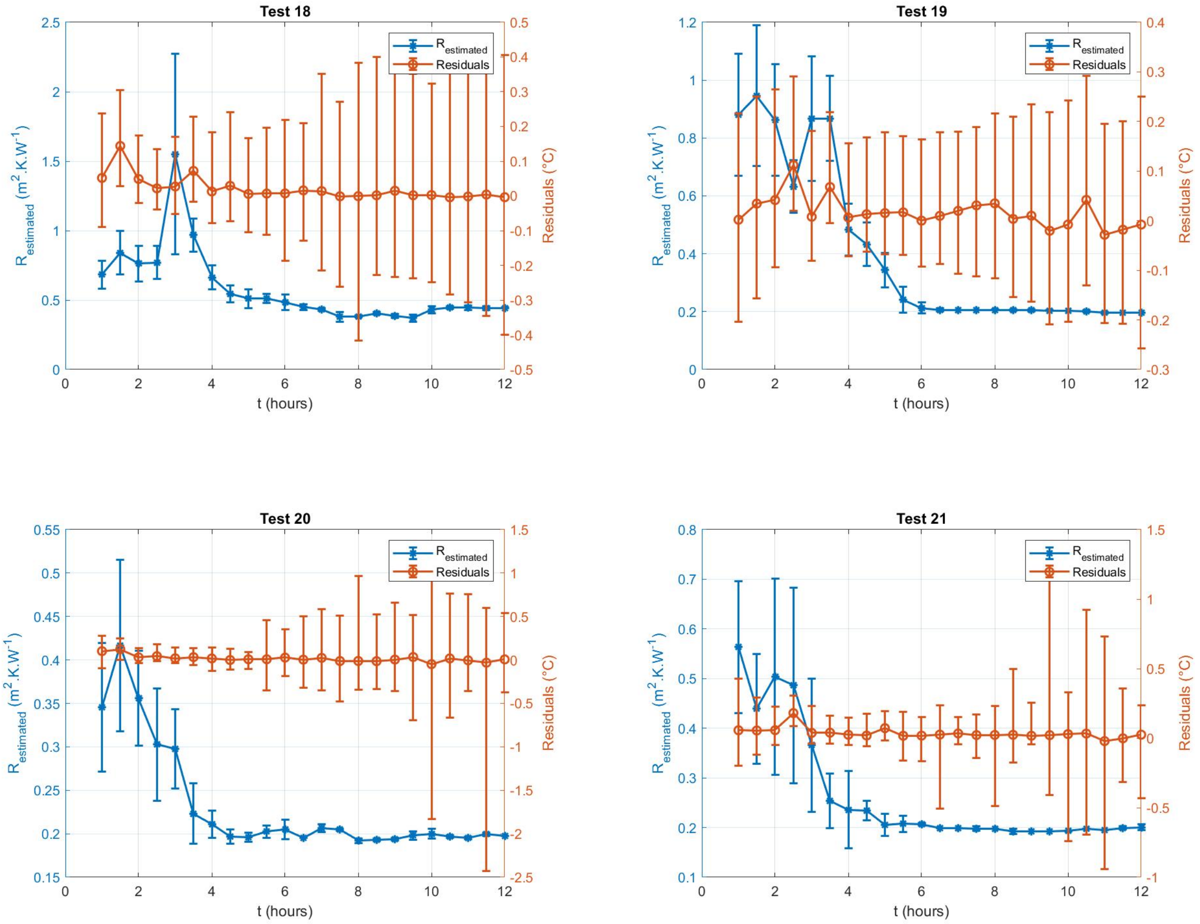

Figure A4.3: Estimated thermal resistance and residuals between measured and estimated minimization parameter for the four tests on the SW wall under constant conditions with the third prototype.

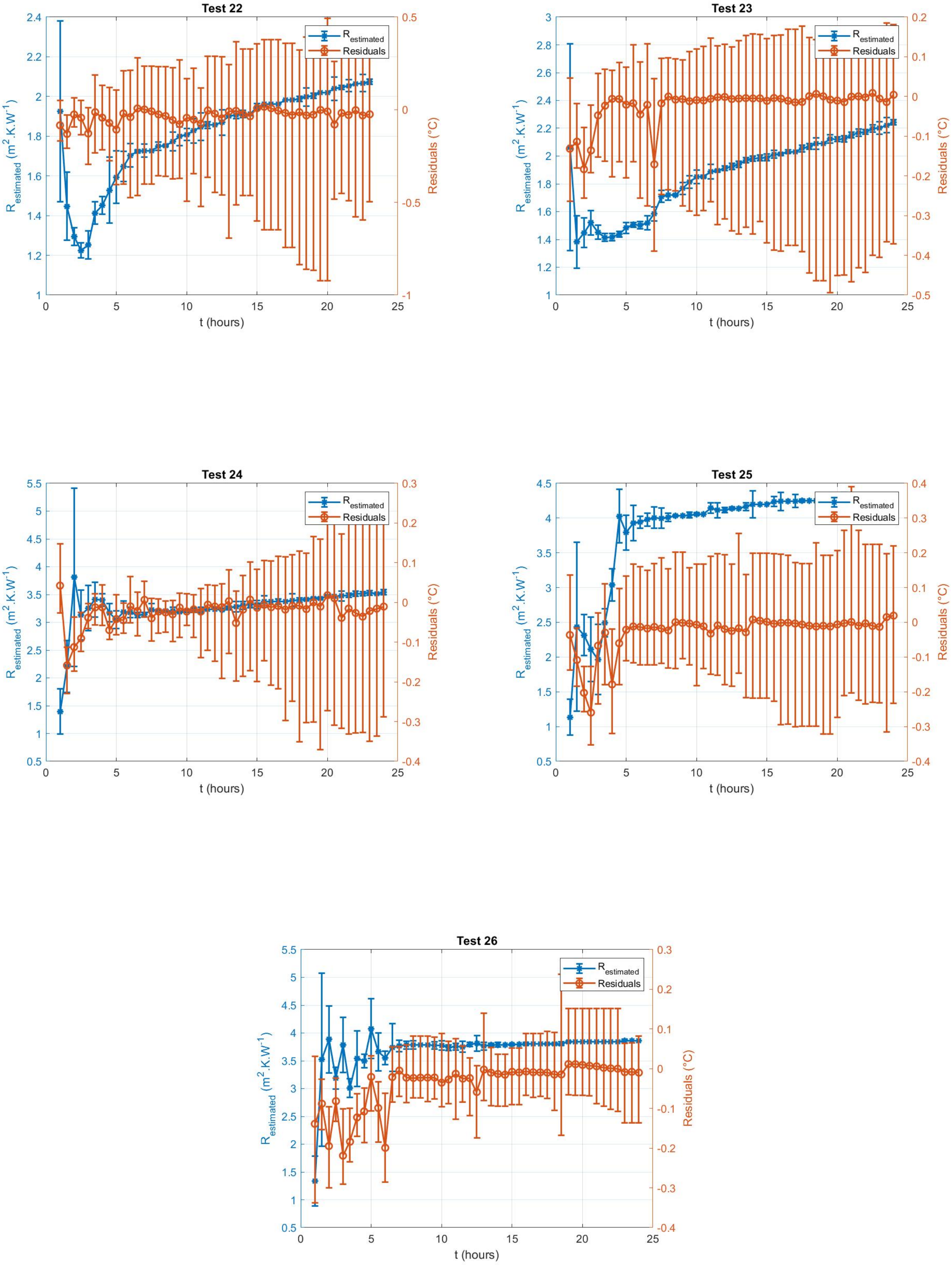

Figure A4.4: Estimated thermal resistance and residuals between measured and estimated minimization parameter during for the five tests on the WFW wall under constant conditions with the third prototype.

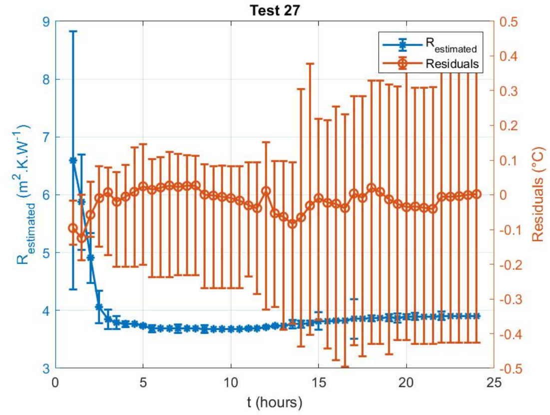
Test 27

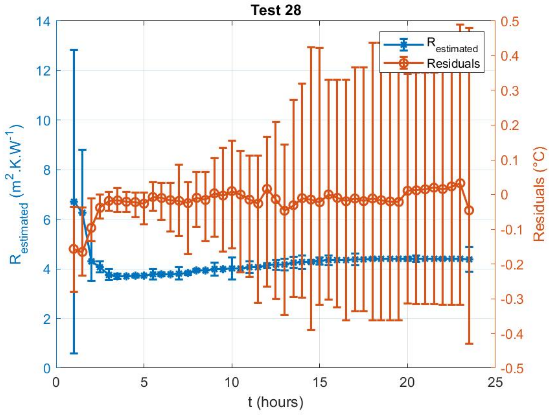
Test 28

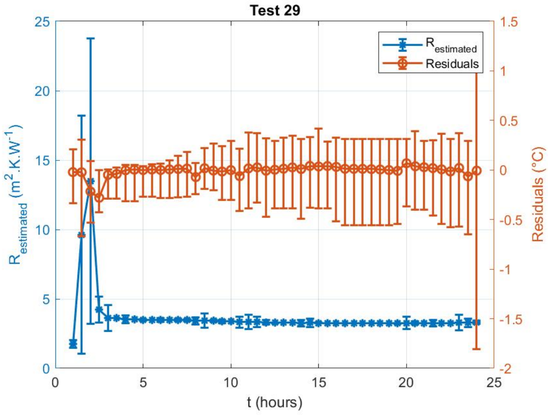
Test 29

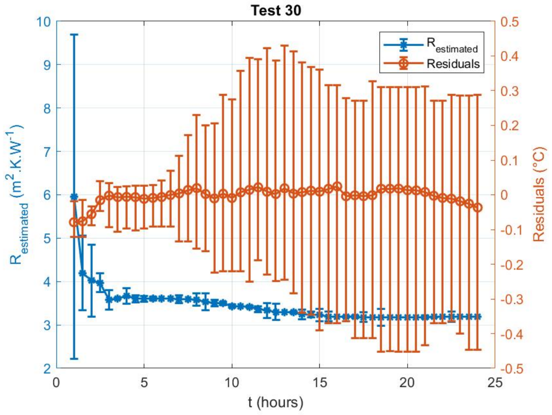
Test 30

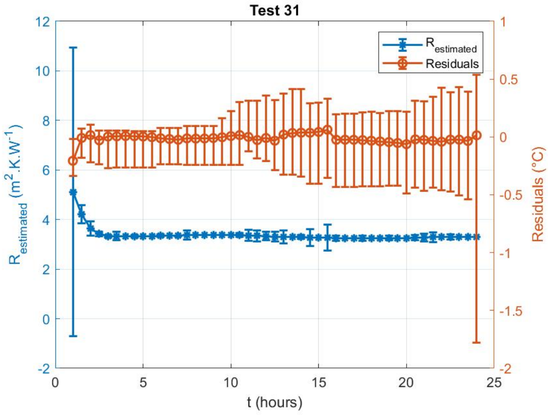
Test 31

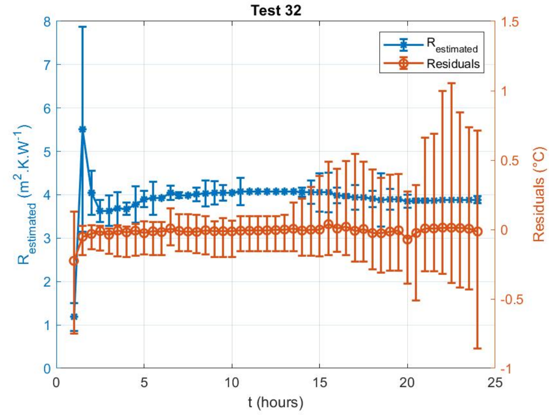
Test 32

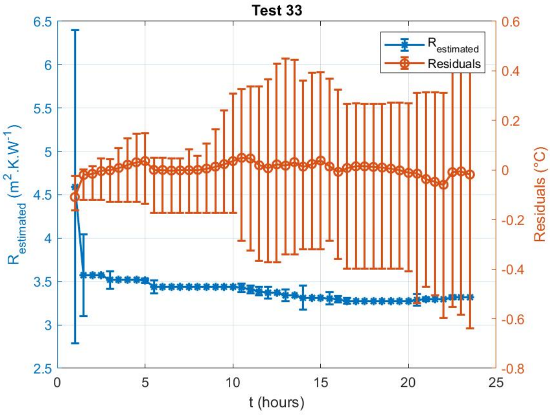
Test 33

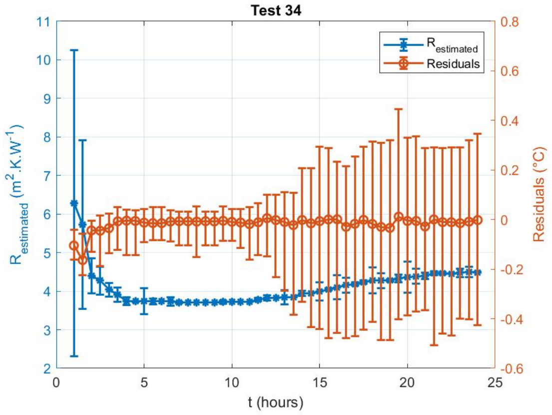
Test 34

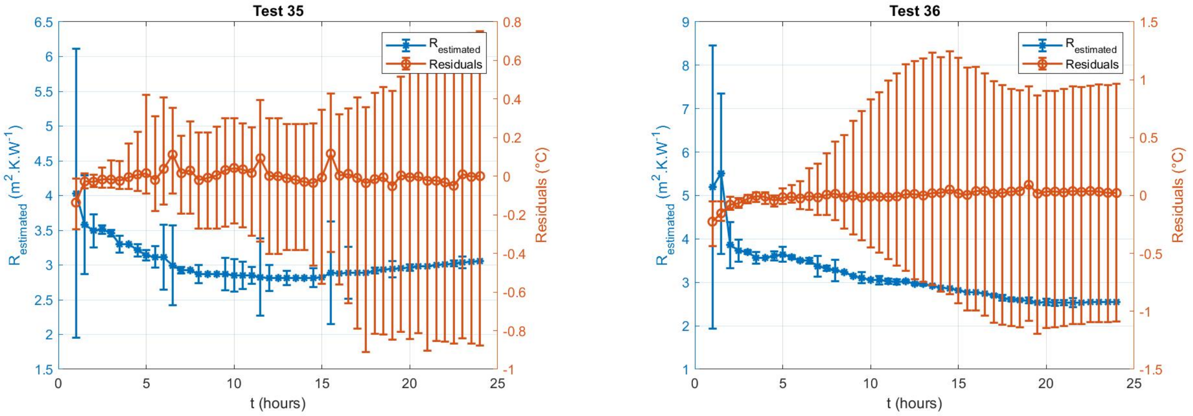

Figure A4.5: Estimated thermal resistance and residuals between measured and estimated minimization parameter during for the ten tests on the IWI wall under variable conditions with the third prototype.

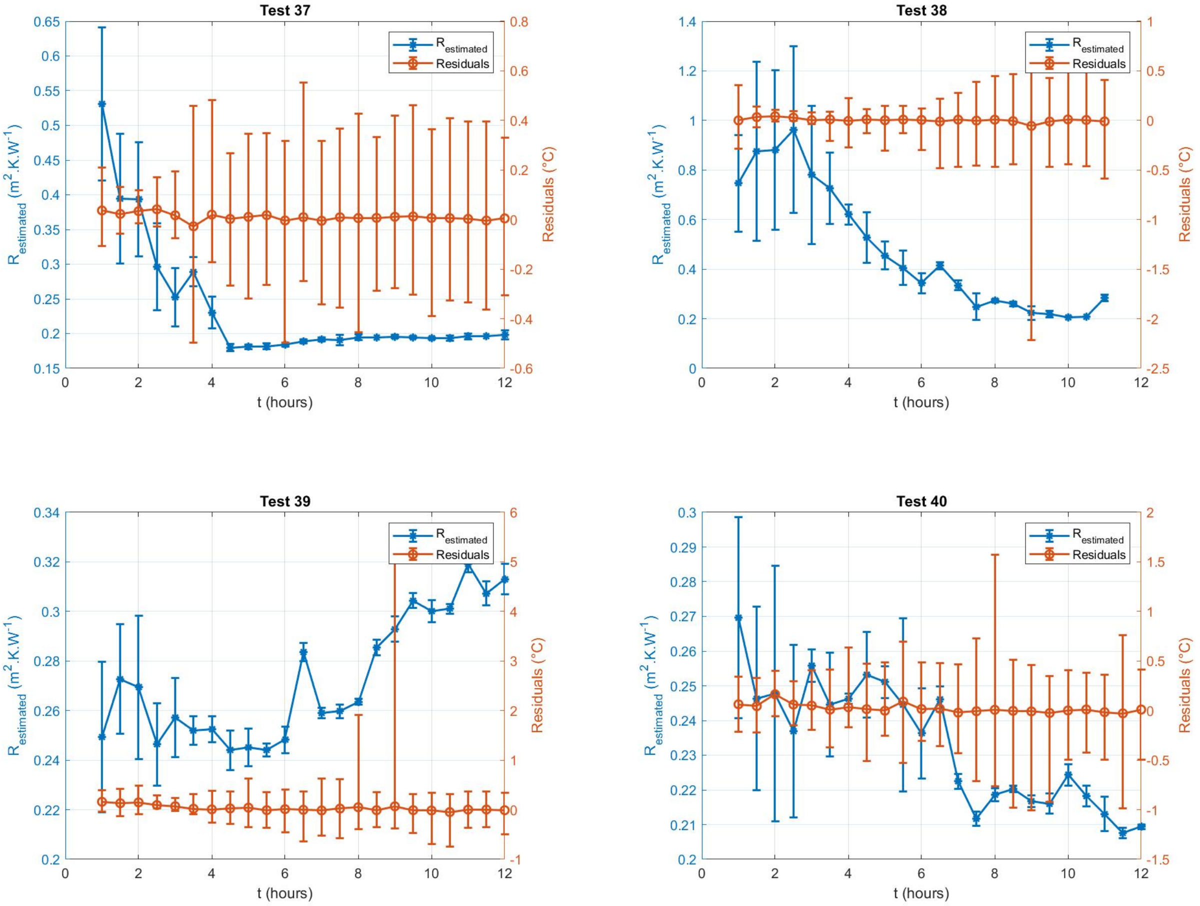

Figure A4.6: Estimated thermal resistance and residuals between measured and estimated minimization parameter for the four tests on the SW wall under variable conditions with the third prototype.

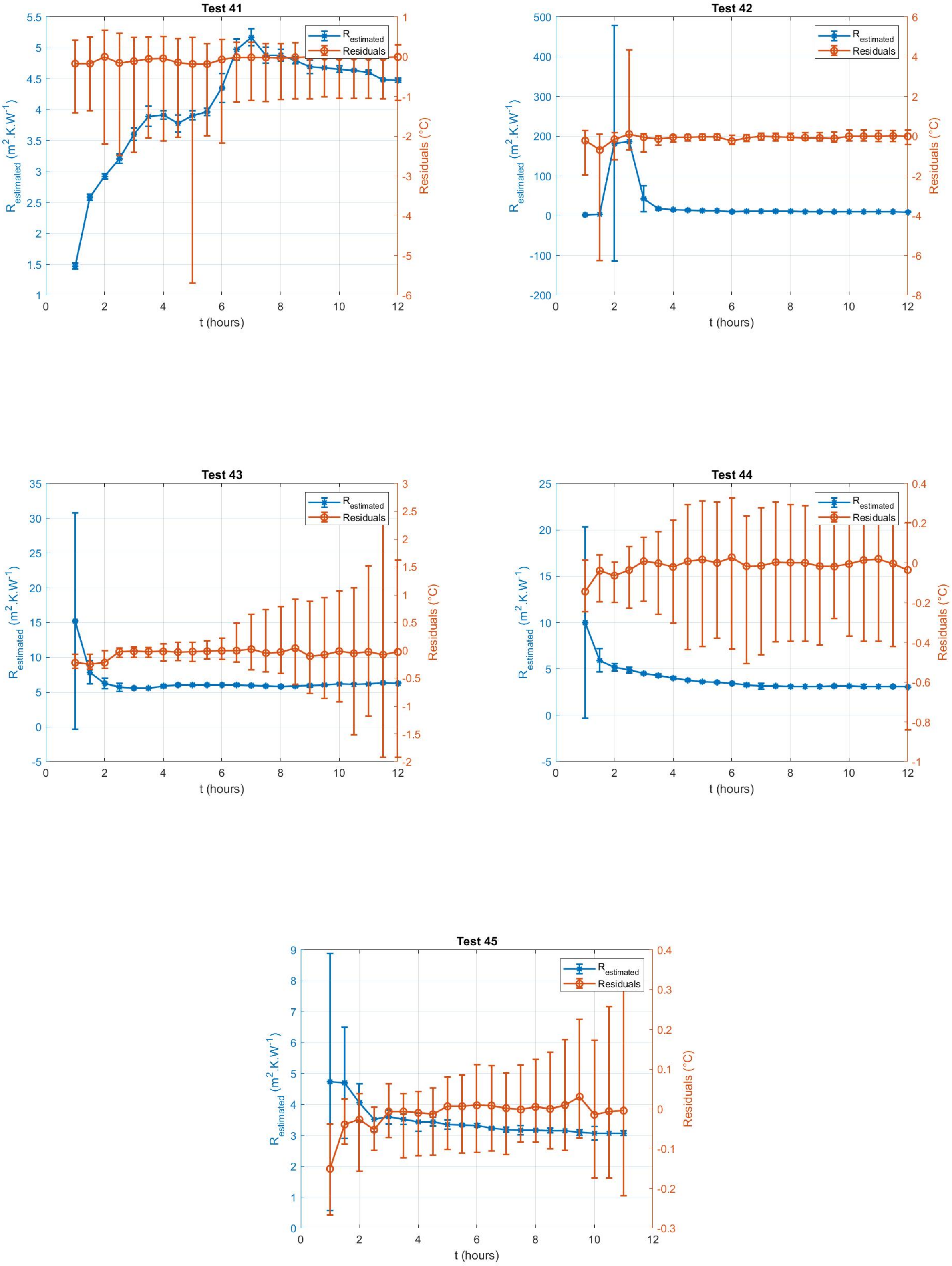

Figure A4.7: Estimated thermal resistance and residuals between measured and estimated minimization parameter during for the five tests on the IWI wall under natural conditions with the third prototype.

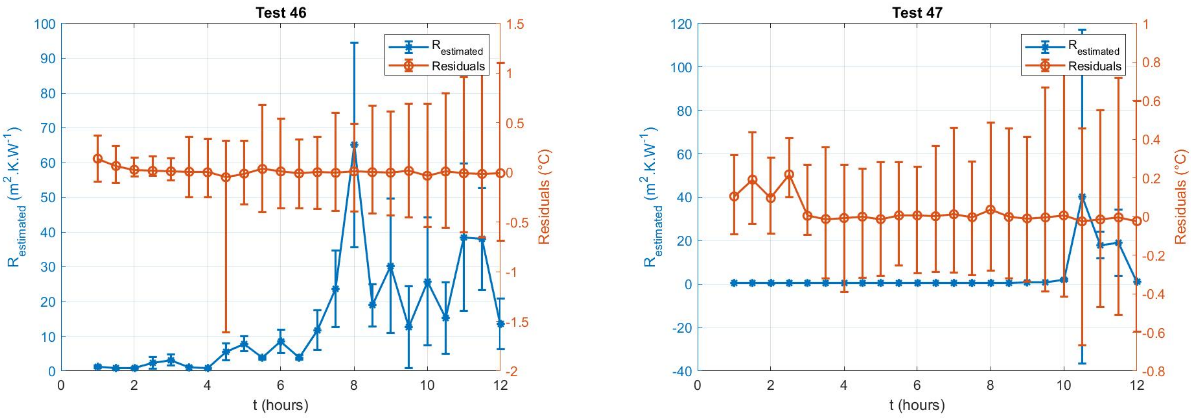

Figure A4.8: Estimated thermal resistance and residuals between measured and estimated minimization parameter for the two tests on the SW wall under natural conditions with the third prototype.

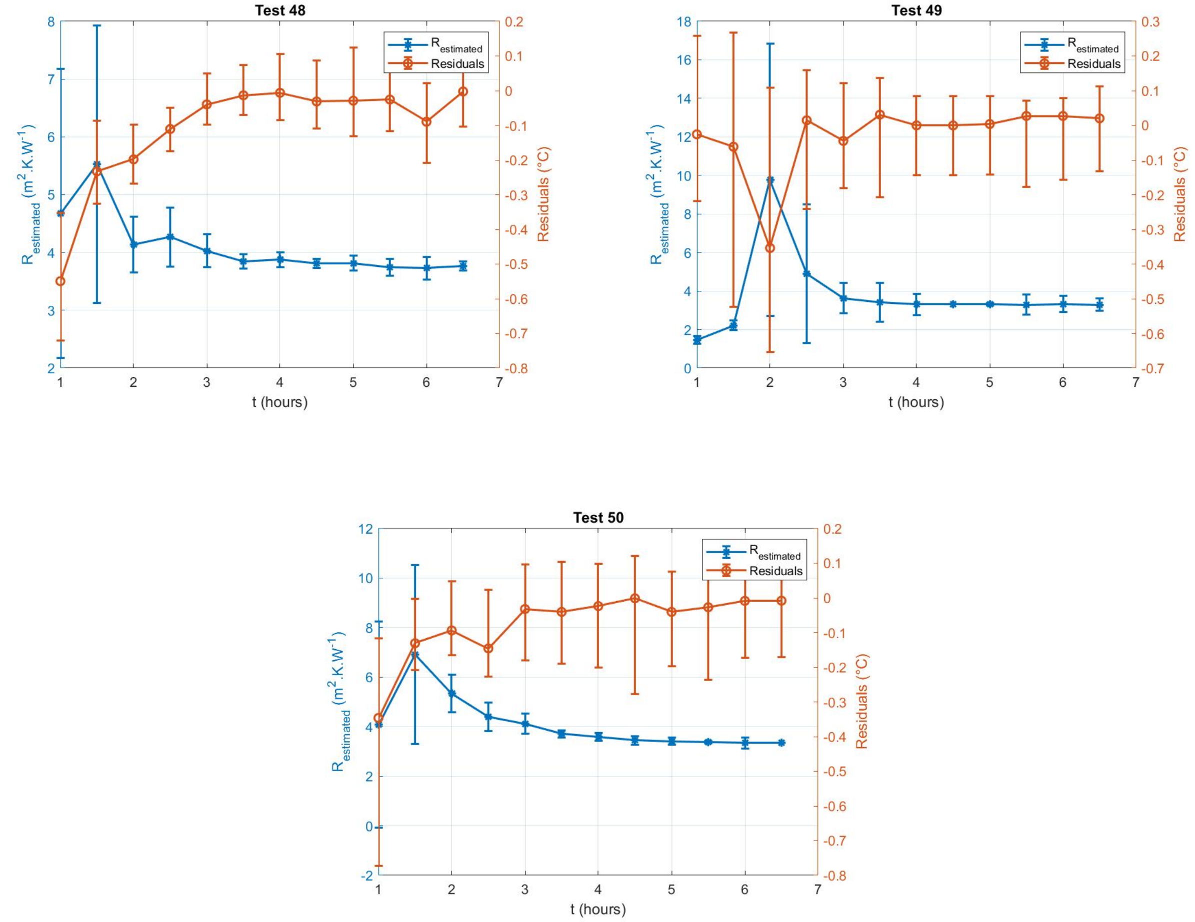

Figure A4.9: Estimated thermal resistance and residuals between measured and estimated minimization parameter for the three tests on the IWI wall under constant conditions with the fourth prototype.

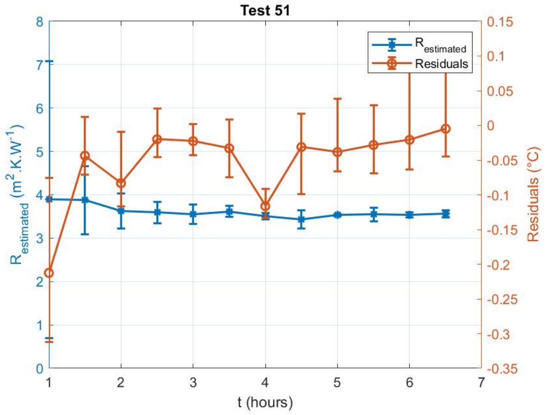
Test 51

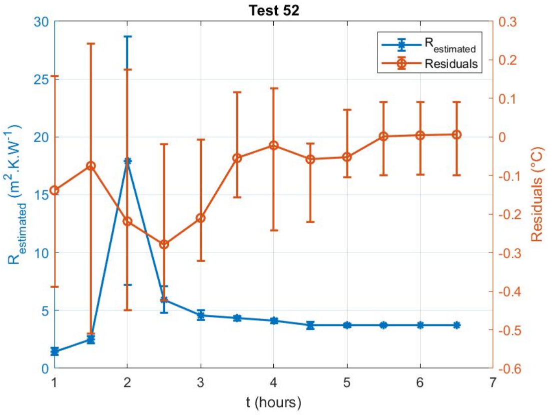
Test 52

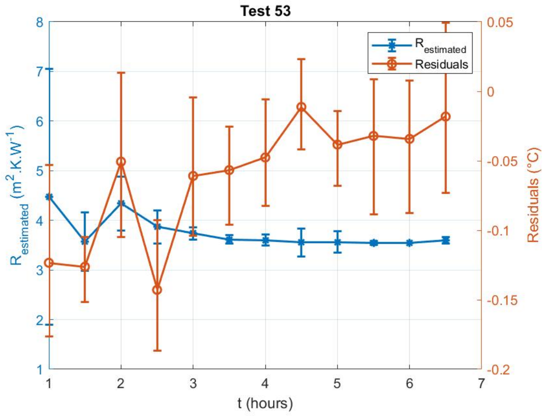
Test 53

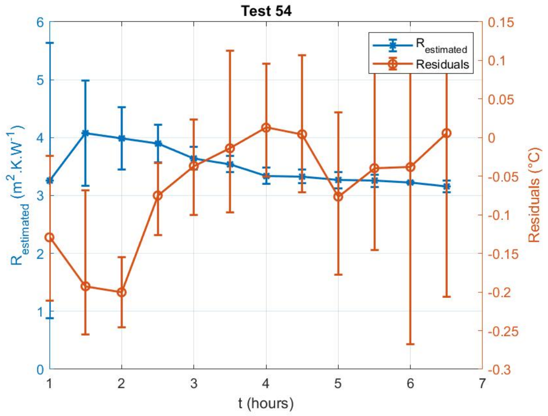
Test 54

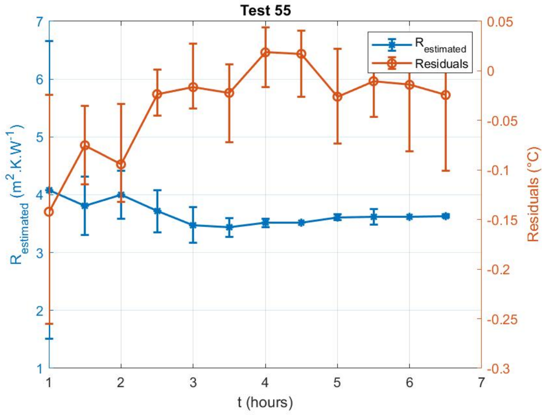
Test 55

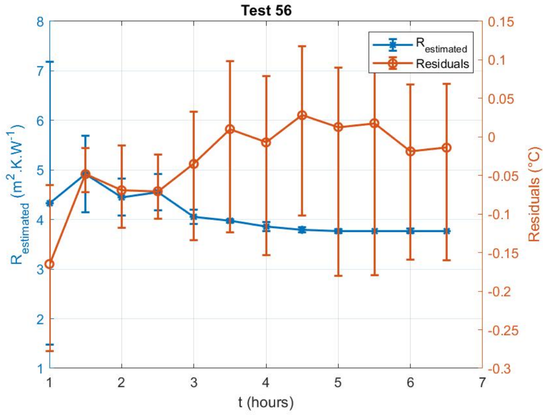
Test 56

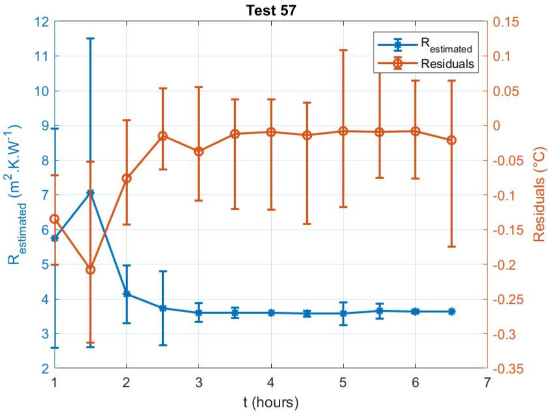
Test 57

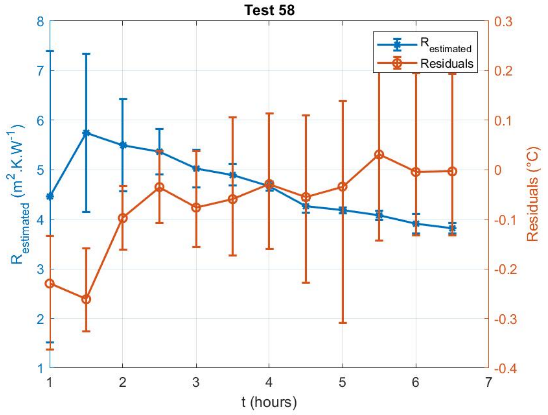
Test 58

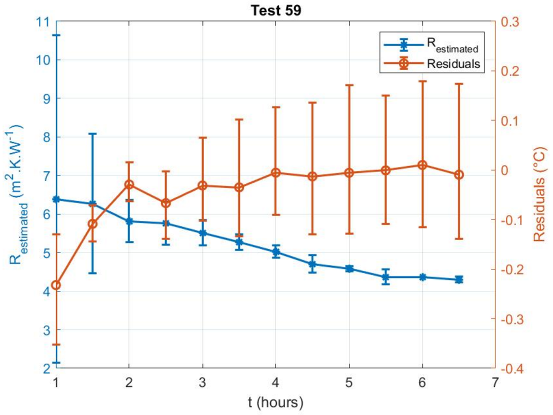

Figure A4.10: Estimated thermal resistance and residuals between measured and estimated minimization parameter for the nine tests on the IWI wall under variable conditions with the fourth prototype.